STIMULI-RESPONSIVE TARGETED THERAPEUTICS FOR TREATMENT OF PRIMARY AND METASTATIC PROSTATE CANCER

by

Zheng-Hong (Joseph) Peng

A dissertation submitted to the faculty of
The University of Utah
in partial fulfillment of the requirements for the degree of

Doctor of Philosophy

Department of Pharmaceutics and Pharmaceutical Chemistry

The University of Utah

August 2014

Copyright © Zheng-Hong (Joseph) Peng 2014

All Rights Reserved

The University of Utah Graduate School

STATEMENT OF DISSERTATION APPROVAL

The following faculty members served as the supervisory committee chair and members for the dissertation of Zheng-Hong (Joseph) Peng. Dates at right indicate the members' approval of the dissertation.

Jindřich Kopeček	, Chair	04/08/2014 Date Approved
Sung Wan Kim	, Member	04/08/2014 Date Approved
Hamid Ghandehari	, Member	04/08/2014 Date Approved
You Han Bae	, Member	04/08/2014 Date Approved
Michael Yu	, Member	04/08/2014 Date Approved

The dissertation has also been approved by David W. Grainger, Chair of the Department/School/College of Pharmaceutics and Pharmaceutical Chemistry and by David B. Kieda, Dean of The Graduate School.

ABSTRACT

Prostate cancer is the most common malignant cancer and the second leading cause of cancer-related death among men in the United States. The major aim of this dissertation was to develop stimuli-responsive, targeted therapeutics for prostate cancer treatment.

In the first part, 2-[3-(1,3-dicarboxypropyl)-ureido] pentanedioic acid (DUPA)-targeted *N*-(2-hydroxypropyl)methacrylamide (HPMA) copolymer-docetaxel (DTX) conjugates were developed for treatment of prostate cancer expressing prostate-specific membrane antigen. The in vivo results show that the spacer length between targeting moieties (DUPA) and HPMA copolymer backbone can significantly affect the treatment efficacy of DTX conjugates against C4-2 tumor bearing nu/nu mice.

In the second part, a tumor-homing peptide iRGD and histone deacetylase inhibitor valproic acid conjugate (VPA-GFLG-iRGD) was developed and its activities were tested against prostate cancer cells. The conjugate VPA-GFLG-iRGD and a mixture of valproic acid (VPA) and GFLG-iRGD have shown similar cytotoxicity against DU-145 prostate cancer cells. However, the treatment of DU-145 cells with conjugate VPA-GFLG-iRGD resulted in a decreased percentage of cells in the G2 phase, whereas the exposure of a mixture of VPA and GFLG-iRGD led to an increased percentage of cells in the G2 phase.

In the third part, tumor-homing and penetrating peptide iRGD-targeted HPMA copolymer doxorubicin conjugates (P-DOX-PLGLAG-iRGD) were developed for prostate cancer treatment. iRGD was attached to HPMA backbone via a matrix metallopeptidase 2 (MMP-2) cleavable spacer (-PLGLAG-). Doxorubicin (DOX) was conjugated to HPMA copolymer via a lysosomal cleavable tetrapeptide spacer (-GFLG-). The activities of P-DOX-PLGLAG-iRGD and related controls were assessed in both monolayer and multilayer prostate cancer cells. The results demonstrated that the conjugate P-DOX-PLGAGL-iRGD has better penetration ability than P-DOX and a mixture of P-DOX and iRGD.

In the fourth part, a HPMA copolymer CXCR-4 antagonist (BKT140) conjugate (P-PLGLAG-BKT140) was developed for inhibiting prostate cancer cell migration. BKT140 was attached to the HPMA backbone via a matrix metallopeptidase 2 (MMP-2) cleavable spacer (-PLGLAG-). The in vitro cell cytotoxicity results show that the conjugation of BKT140 to HPMA did not impact the functionality of BKT140. The migration results show that both HPMA copolymer BKT140 conjugate and free BKT140 inhibited the CXCL12 induced PC-3 prostate cancer cell migration. The conjugate P-PLGLAG-BKT140 has greater impact than that of free BKT140.

TABLE OF CONTENTS

ABSTRACT……. iii

LIST OF TABLES..……. x

LIST OF FIGURES.…… xi

ACKNOWLEDGEMENTS……. xv

Chapters

1. INTRODUCTION……. 1

1.1 Prostate Cancer……...…….. 1
1.2 Prostate Cancer Origin…….. 1
1.3 Prostate Cancer Stages and Treatment…….. 3
1.4 Physiologic Difference Between Normal and Tumor Tissues……... 3
1.5 Prostate Cancer Microenvironment……..... 6
1.5.1 Prostate cancer microenvironment-MMPs.……..... 7
1.5.2 Prostate cancer markers PSA and PSMA...……..... 9
1.6 Drug Targeting to Solid Tumor..……... 10
1.6.1 Passive targeting.…… 12
1.6.2 Active targeting…..……. 12
1.7 Drug Penetration and Cell-Penetrating Peptides...……. 16
1.7.1 Receptor-independent CPP..…… 16
1.7.2 Receptor-dependent CPPs (receptor-independent CPP + targeting ligand……..……. 25
1.7.3 Receptor-dependent CPPs (iRGD)……... 25
1.8 Cancer and Chemokines……..…….. 28
1.8.1 Chemokines and chemokine receptors..…….. 28
1.8.2 CXCL12 and CXCR4.…..…… 28
1.8.3 CXCL12/CXCR4 and cancer.…..…… 30
1.8.4 CXCR4 antagonists in clinical trial.…..……... 32
1.9 HPMA Copolymer-drug Conjugates.……..…….. 38
1.9.1 Architectures of HPMA copolymer-drug conjugates...…….. 39
1.9.2 Preparation of HPMA copolymer-drug conjugates….…… 39

1.9.3 Characterization of HPMA copolymer-drug conjugates..…….. 42
1.10 References……..……..…….. 44

2. TARGETED HPMA COPOLYMER-DOCETAXEL CONJUGATES FOR PROSTATE-SPECIFIC MEMBRANE ANTIGEN EXPRESSING PROSTATE CANCER TREATMENT……..…… 64

2.1 Summary……..... 64
2.2 Introduction…… 65
2.3 Materials and Methods…….. 68
2.3.1 Materials……. 68
2.3.2 Synthesis of *N*-methacryloylglycylphenylalanylleucylglycyl Docetaxel ……. 68
2.3.3 Synthesis of (3S,7S)-17-methyl-5,10,16-trioxo-4,6,11,15-tetraazaoctadec-17-ene-1,3,7-tricarboxylic acid.……. 70
2.3.4 Synthesis of (3S,7S)-57-methyl-5,10,50,56-tetraoxo-14,17,20,23, 26,29,32,35,38,41, 44,47-dodecaoxa-4,6,11,51,55-pentaazaocta-pentacont-57-ene-1,3,7-tricarboxylic acid (MA-EG12-DUPA)….. 77
2.3.5 Preparation of DUPA-targeted and nontargeted HPMA copolymer-DTX conjugates with RAFT polymerization..…….. 82
2.3.6 Characterization of DUPA-targeted and nontargeted HPMA copolymer-DTX conjugates.…… 88
2.3.7 Cell culture…….. 91
2.3.8 PSMA cell surface expression…..…… 92
2.3.9 In vitro cytotoxicity.……..……... 92
2.3.10 Tumor models...……..…… 93
2.3.11 In vivo anticancer efficacy of DUPA-targeted and nontargeted HPMA copolymer-DTX conjugates……..……..... 93
2.3.12 Statistical analysis……..…… 94
2.4 Results and Discussion …….. 94
2.4.1 Design, synthesis, and characterization of MA-GFLG-DTX…….. 94
2.4.2 Design, synthesis, and characterization of polymerizable DUPA derivatives with different spacer lengths…..…….... 95
2.4.3 Design, synthesis and characterization of DUPA-targeted and nontargeted HPMA copolymer-DTX conjugates…….. 97
2.4.4 In vitro cytotoxicity.…… 99
2.4.5 In vivo efficacy...……..……... 102
2.4.6 Adverse effects..……..…… 104
2.5 Conclusion....……..... 108
2.6 References.……..... 110

3. SYNTHESIS AND ACTIVITIES OF TUMOR-HOMING PEPTIDE iRGD AND HISTONE DEACETYLASE INHIBITOR VALPROIC ACID CONJUGATE ... 114

3.1 Summary.……... 114

3.2 Introduction..... 115
3.3 Materials and Methods..... 118
3.3.1 Materials..... 118
3.3.2 Synthesis of VPA-GFLG-iRGD and GFLG-iRGD..... 120
3.3.3 Purification and characterization of GFLG-iRGD and VPA-GFLG-iRGD..... 122
3.3.4 Reduction of VPA-GFLG-iRGD..... 122
3.3.5 Cell culture..... 122
3.3.6 Induction DU-145 cell cycle arrest by VPA-GFLG-iRGD, VPA, GFLG-iRGD, or a mixture of VPA and GFLG-iRGD.....124
3.3.7 Cytotoxicity of VPA-GFLG-iRGD, VPA, GFLG-iRGD, or a mixture of VPA and GFLG-iRGD 124
3.4 Results and Discussion 125
3.4.1 Synthesis and characterization of VPA-GFLG-iRGD and GFLG- iRGD 125
3.4.2 Induction of cell cycle arrest by VPA-GFLG-iRGD and controls..... 125
3.4.3 Cell cytotoxicity of VPA-GFLG-iRGD and related controls against DU-145..... 128
3.5 Conclusion 130
3.6 References 131

4. TUMOR-PENETRATING PEPTIDE TARGETED HPMA COPOLYMER DOXORUBICIN CONJUGATES FOR PROSTATE CANCER TREATMENT..... 135

4.1 Summary..... 135
4.2 Introduction..... 136
4.3 Materials and Methods..... 140
4.3.1 Materials..... 140
4.3.2 Synthesis of monomer MA-GFLG-DOX..... 141
4.3.3 Preparation of monomer MA-GG-PLGLAG-iRGD and free iRGD..... 141
4.3.4 Preparation and molecular weight (MW) measurement of polymer conjugate P-DOX..... 144
4.3.5 Synthesis and MW measurement of polymer conjugate P-DOX-PLGLAG-iRGD..... 147
4.3.6 Determination of the DOX content in conjugates P-DOX and P-DOX-PLGLAG-iRGD..... 149
4.3.7 Determination of the iRGD content in P-DOX-PLGLAG-iRGD... 149
4.3.8 Cell culture..... 149
4.3.9 In vitro Doxorubicin cellular uptake..... 150
4.3.10 Cell cycle arrest..... 150
4.3.11 Apoptosis..... 151
4.3.12 Cell cytotoxicity..... 151

4.3.13 Multicellular tumor spheroid formation..... 152
4.3.14 DOX conjugates accumulation in multicellular tumor spheroids..... 152
4.3.15 DOX conjugates penetration in multicellular tumor spheroids..... 153
4.3.16 Statistical analysis..... 153
4.4 Results and Discussion..... 153
4.4.1 Design, synthesis, and characterization of monomer MA-GFLG-DOX..... 153
4.4.2 Design, synthesis, and characterization of monomer MA-GG-PLGLAG-iRGD and free iRGD..... 154
4.4.3 Synthesis and characterization of polymer conjugates P-DOX and P-DOX-PLGLAG-iRGD..... 156
4.4.4 Cellular uptake..... 156
4.4.5 Cell cycle arrest assay..... 160
4.4.6 Apoptosis..... 160
4.4.7 In vitro cellular cytotoxicity assays..... 163
4.4.8 Accumulation of DOX conjugates and related controls in multicellular tumor spheres (MTS)..... 165
4.4.9 MTS penetration of DOX conjugates..... 165
4.5 Conclusion..... 168
4.6 References..... 169

5. HPMA COPOLYMER CXCR-4 ANTAGONIST BKT140 CONJUGATES FOR INHIBITING PROSTATE CANCER CELL MIGRATION..... 173

5.1 Summary..... 173
5.2 Introduction..... 174
5.3 Materials and Methods..... 175
5.3.1 Materials..... 175
5.3.2 Synthesis of free CXCR4 antagonist BKT140..... 176
5.3.3 Reduction of free CXCR4 antagonist BKT140..... 178
5.3.4 Synthesis of monomer MA-GG-PLGLAG-BKT140..... 178
5.3.5 Purification and characterization of BKT140 and monomer MA-GG-PLGLAG-BKT140..... 181
5.3.6 Preparation of HPMA copolymer-BKT140 conjugate..... 181
5.3.7 Purification and characterization of P-PLGLAG-BKT140..... 183
5.3.8 Cell culture..... 184
5.3.9 In vitro cleavage study..... 184
5.3.10 Cell cytotoxicity assay..... 184
5.3.11 In vitro migration assay..... 185
5.3.12 Statistical analysis..... 185
5.4 Results and Discussion..... 185
5.4.1 Design, synthesis, and characterization of BKT140 and monomer MA-GG-PLGLAG-BKT140..... 185

5.4.2 Preparation and characterization of P-PLGLAG-BKT140.....…… 186
5.4.3 In vitro cleavage results..…… 190
5.4.4 In vitro cytotoxicity results.……..……...… 194
5.4.5 In vitro migration results.……..……...… 194
5.5 Conclusion...……..…… 197
5.6 References..……..……..…… 198

6. SUMMARY, CONCLUSIONS AND FUTURE PROSPECTS.…….…….. 201

LIST OF TABLES

1.1. Representative cell-penetrating peptides and their sequences …… 19

1.2 CXCR4 antagonists in clinical trial…….…… 33

2.1 Physicochemical properties of DUPA-targeted and nontargeted DTX conjugates……...…….. 100

2.2 IC_{50} of DUPA-targeted or nontargeted DTX conjugates against C4-2 prostate cancer cells……....…….. 103

4.1 Physicochemical properties of DOX conjugates……. 158

LIST OF FIGURES

1.1. Schematic depiction of the cell types in human prostatic duct …….. 2

1.2. Clinical stages of prostate cancer and current therapeutic interventions …….... 4

1.3. Structure of proMMP-2..…… 9

1.4. Structure of PSMA……..…… 11

1.5. The distribution of doxorubicin in PC-3 tumor.……..…… 17

1.6. Proposed association mechanism between CPP and cell membrane……. 21

1.7. Possible cell penetrating peptide cellular uptake pathway……. 22

1.8. Penetration mechanism of iRGD……...……. 27

1.9. Chemokine and chemokine receptor families……...……. 29

1.10. Signal transduction pathway induced by CXCL12 binding to CXCR4……. 31

1.11. Structure of CXCR4 antagonists in clinical trials…….……. 35

1.12. Structures of T140 series peptides…….……..…… 37

1.13. Generally accepted mechanism for RAFT polymerization..…….……. 41

2.1. Synthetic scheme of monomer MA-GFLG-DTX.…….……. 69

2.2. Mass spectrum of monomer MA-GFLG-DTX….…….……. 71

2.3. Scheme for synthesis of monomer MA-DUPA....…….……. 72

2.4. Mass (A) and ^{1}H NMR (B) spectra of (S)-5-*tert*-butoxy-4-(3-((S)-1,5-di-*tert*-butoxy-1,5-dioxopentan-2-yl)ureido)-5-oxopentanoic acid..…….…… 74

2.5. ^{1}H NMR (A) and mass spectra (B) of (3S, 7S)-tri-*tert*-butyl 17-methyl-5,10,16-trioxo-4,6,11,15-tetraazaoctadec-17-ene-1,3,7-tricarboxylate…….…….. 76

2.6. ^{1}H NMR (A) and mass spectra (B) of monomer MA-DUPA…….……. 78

2.7. Synthetic scheme and structure of monomer MA-EG_{12}-DUPA...…….……. 79

2.8. Mass spectrum of compound **11** (MA-EG_{12}-DUPA(tri-*tert*-butyl))..... …… 81

2.9. Mass spectrum of monomer MA-EG_{12}-DUPA…….....……. 83

2.10. Synthetic scheme (A) and size exclusion chromatography (SEC) profile (B) of P-DTX……..……..... ……. 84

2.11. Synthetic scheme (A) and SEC profile (B) of P-DTX-DUPA……....……. 86

2.12. Synthetic scheme (A) and SEC profile (B) of P-DTX-mDUPA..…....…… 87

2.13. Synthetic scheme (A) and SEC profile (B) of P-DTX-EG_{12}-DUPA.....…… 89

2.14. Structure schematic of the DTX drug conjugates…….……....…… 98

2.15. PSMA expression on C4-2 and PC-3 cell surface...…….……....…… 101

2.16. In vivo antitumor activity of DUPA-targeted or nontargeted HPMA copolymer-DTX conjugates in nude mice bearing s.c. C4-2 prostate cancer xenografts…. 105

2.17. Percentage of mean body weight change of nu/nu mice bearing s.c. C4-2 prostate cancer xenografts following administration of saline, DTX, P-DTX, P-DTX-DUPA, P-DTX-mDUPA, and P-DTX-EG_{12}-DUPA……... 106

2.18. Histology images of major organs (heart, liver, spleen, kidney, lung) from control and treated mice.…….… 107

3.1. Structure of HDAC inhibitors...…….…..… 116

3.2. Chemical structure of VPA-GFLG-iRGD (A), VPA (B), and GFLG-iRGD (C)……. 119

3.3. Synthetic scheme of conjugate VPA-GFLG-iRGD……..... 121

3.4. Scheme for reduction of conjugate VPA-GFLG-iRGD..……..... 123

3.5. Mass spectrum of conjugate VPA-GFLG-iRGD…...……... 126

3.6. Mass spectrum of the reduced product from VPA-GFLG-iRGD…….. 126

3.7. Representative flow cytometric pictures and percentages of cells in G1 and G2 phase of the DU-145 cell cycle..……...……..... 127

3.8. Average percentage of cells in G1 (A) and G2 (B) phase of the DU-145 cell cycle……..... 127

3.9. Cytotoxicity of VPA, GFLG-iRGD, VPA-GFLG-iRGD, and a mixture of VPA and GFLG-iRGD against DU-145 prostate cancer cells..…….…..... 129

4.1. Schematic illustration of HPMA copolymer iRGD conjugate delivery.……..... 139

4.2. Synthetic scheme of monomer MA-GFLG-DOX…….……..... 142

4.3. Synthetic scheme for monomer MA-GG-PLGLAG-iRGD…….……..... 143

4.4. Synthetic scheme for free iRGD……...…….……..... 145

4.5. Synthetic scheme of polymer conjugate P-DOX.……...…….……..... 146

4.6. Synthetic scheme of polymer conjugate P-DOX-PLGLAG-iRGD….……... 148

4.7. Mass spectrum of monomer MA-GG-PLGLAG-iRGD……...….……..... 155

4.8. Mass spectrum of free iRGD…….……...….……..... 157

4.9. Uptake of DOX conjugates and controls in DU-145 cell monolayers by measuring the DOX fluorescence…….……...….……..... 159

4.10. DU-145 cell cycle distribution after treatment with DOX conjugates and related controls…….…….……...….……..... 161

4.11. Induced apoptosis in DU-145 cells after treatment with DOX conjugates and related controls.…….…….……...….……..... 162

4.12. In vitro cytotoxicity of P-DOX-PLGLAG-iRGD and related controls against DU-145 prostate cancer cells…...…….……...….……..... 164

4.13. Accumulation of DOX conjugates in DU-145 multilayer tumor cells spheroids……...…….……...….……..... 166

4.14. Penetration of DOX conjugates or controls in DU-145 MTS (surface plots of images)……..... 167

5.1. Synthetic scheme of free BKT140……..…..... 177

5.2. Scheme for reduction of free BKT140.……..…..... 179

5.3. Synthetic scheme of monomer MA-GG-PLGLAG-BKT140.……...…... 180

5.4. Synthetic scheme of polymer conjugate P-PLGLAG-BKT140……...…..... 182

5.5. Mass spectrum of monomer MA-GG-PLGLAG-BKT140....……...…..... 187

5.6. Mass spectrum of free BKT140.…….…...……...…..... 188

5.7. Mass spectrum of reduced product from free BKT140..…...……...…..... 189

5.8. Mass spectrum of cleavage product from monomer MA-GG-PLGLAG-BKT140 after incubation with PC-3 cell culture media..…...……...…..... 191

5.9. Proposed cleavage site 1 of monomer MA-GG-PLGLAG-BKT140 after incubation with PC-3 cell culture media.....…...……...…..... 192

5.10. Proposed cleavage site 2 of monomer MA-GG-PLGLAG-BKT140 after incubation with PC-3 cell culture media.....…...……...…..... 193

5.11. In vitro cytotoxicity of BKT140 and P-PLGLAG-BKT140 against PC-3 cells……..……...…...……...…..... 195

5.12. Effects of BKT140 and P-PLGLAG-BKT140 on CXCL12 induced migration of PC-3 prostate cancer cells……..……...…..... 196

ACKNOWLEDGEMENTS

I would like to express my gratitude to my supervisors, Dr. Jindřich Kopeček and Dr. Pavla Kopečková, for their guidance, support, and encouragement during my study. I would also like to thank my committee members, Dr. Sung Wan Kim, Dr. Hamid Ghandehari, Dr. You Han Bae, Dr. Michael Yu, and Dr. David Bearss, for their great mentorship and advice. I am extremely grateful to our department chair and graduate student coordinators, Dr. David Grainger, Dr. James Herron, and Dr. Carol Lim. Special thanks go to Monika Sima, Jonathan Hartley, Chris Radford, and Rui Zhang for their valuable help in the preparation of this dissertation. This research was supported in part by the NIH (USA) through grant RO1 CA132831. Finally, I wish to express heartfelt thanks to my family.

CHAPTER 1

INTRODUCTION

1.1 Prostate Cancer

Cancer accounts for 25% of the total deaths in the United States, making it the second leading cause of death (1). Prostate cancer is the most common diagnosed (except for skin cancer) and the second leading fatal cancer among men in the United States. The American Cancer Society estimated that about 233,000 men will be diagnosed with prostate cancer and about 29,480 Americans will die from this disease in 2014 (1).

1.2 Prostate Cancer Origin

As shown in Figure 1.1, the prostate epithelium consists of three differentiated cell types: luminal, basal, and neuroendocrine (2–4). The argument about prostate cancer cellular origins is still in controversy (5). Cell biologists assume that basal cells are the origin of prostate cancer because they have a more regenerative potential than luminal cells in normal prostate (5). However, most pathologists consider that prostate cancer originates from luminal cells because prostate tumor tissue consists of epithelial luminal cells and lacks epithelial basal cells (6). The difficulty in identification of the origin of prostate cancer is partly due to the fact that the prostate epithelial lineage hierarchy has not been clearly characterized (7). Shen and coworkers announce that luminal stem cells

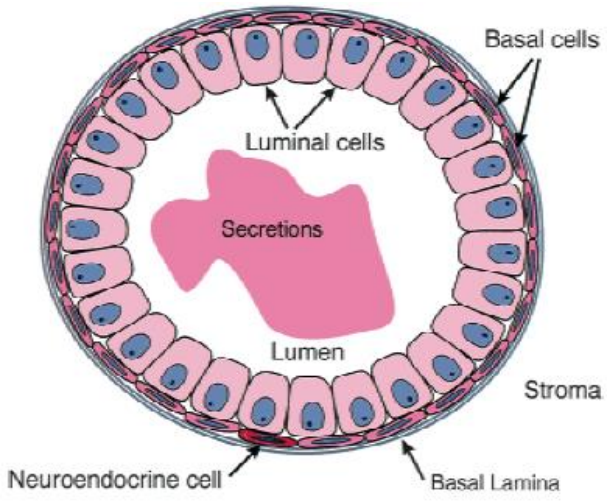

Figure 1.1: Schematic depiction of the cell types in human prostatic duct. Adapted from reference (3).

are the origin of prostate cancer (2). However, Witte and colleagues claim that basal cells are the origin of human prostate cancer (8). They further demonstrated that advanced prostate adenocarcinoma initiated in basal cells can be maintained by luminal-like tumor-propagating cells (9). Apparently, these two group's results contradict each other, but in fact, the Shen group used cells that were from an adult mouse prostate, but the Witte group used human prostate cells. Recent research found that both prostate basal and luminal cells can serve as the cellular origin of prostate cancer using a lineage tracing approach (7).

1.3 Prostate Cancer Stages and Treatment

As shown in Figure 1.2, prostate cancer progression can be divided into four stages: clinically localized disease, biochemical recurrence, castration resistant non-metastatic disease, and castration resistant metastatic disease (10). The first stage of prostate cancer (localized) can be treated with surgery and radiotherapy. The second and third stage of prostate cancer can be treated with androgen ablation (10). Finally, a small portion of prostate cancer develops to fatal, metastatic castration-resistant prostate cancer (CRPC). Although chemotherapeutic compounds (paclitaxel, docetaxel, doxorubicin, radium-223 dichloride) have been developed to treat CRPC, they can only provide medium overall survival improvement (11,12).

1.4 Physiologic Difference Between Normal and Tumor Tissues

In normal tissue, the blood vessels are well organized and most of the ~ 10^{13} cells in the human body are within a few cell diameters from a blood vessel (13). Cancer cells

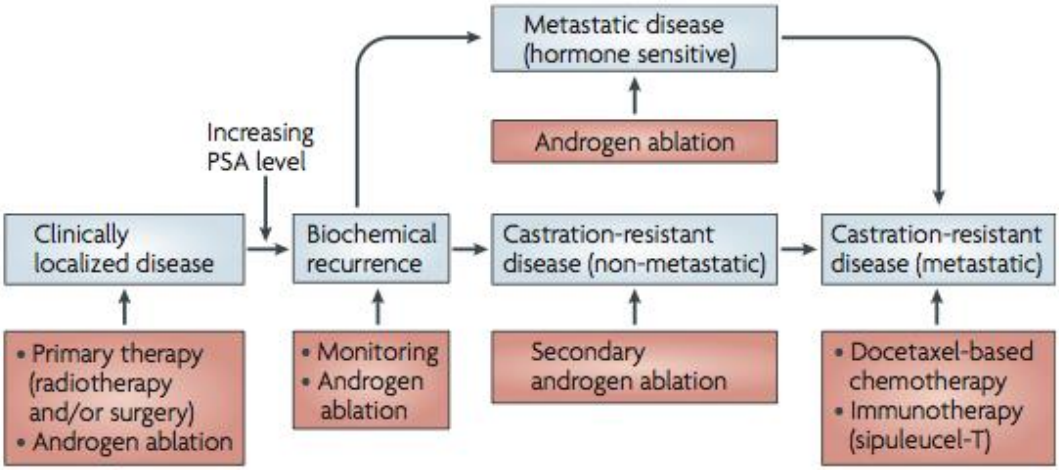

Figure 1.2: Clinical stages of prostate cancer and current therapeutic interventions. Adapted from (10).

proliferate faster than normal cells, thus the uncontrolled proliferating tumor cells compress and collapse the intratumor vessels (14). The basement membrane, endothelial cells, and pericytes in tumor vessels are disorganized and irregularly shaped. These cells are loosely connected, or overlapped or sprouted (15,16). The composition, assembly, and architecture of tumor vascular basement membrane are changed. Compared to normal vessels, tumor vessels are leaky, tortuous, and dilated, with uneven diameter, excessive branching, and shunts (17). The poorly organized, irregular blood vessels block the delivery of nutrients, oxygen, and anticancer drug to the tumor area. Furthermore, the rapidly proliferating cancer cells force vessels apart and create a population of cells distant (> 100 μm) from blood vessels (13,18).

Jain's group reported that the functional lymphatic capillaries are absent from the interior, but they are enlarged in the periphery of a solid tumor (17,19). One possible explanation is that the lack of pulsatile blood flow may inhibit the growth of lymph system (14). Perhaps the stress, which is produced by the rapidly proliferating tumor cells, prevents the formation of a functional lymphatic system (14,17,20). The enlarged lymphatics in tumor periphery may be due to the overexpression of vascular endothelial growth factor (VEGF-C) (21).

The abnormal structure and function of blood and lymphatic vessels in prostate cancer result in the formation of a prostate cancer microenvironment. The accumulation of lactic acid and CO_2 results in a low extracellular pH because the irregular tumor vasculature is insufficient to remove lactic acid and CO_2 (22). The blood-vessel leakiness, lymph-vessel abnormalities, and contraction of interstitial space most likely contributes to the elevated tumor interstitial fluid pressure (IFP) (23,24).

1.5 Prostate Cancer Microenvironment

As in other cancers, the prostate cancer microenvironment is also a complex milieu. This chapter only discusses hypoxia, matrix metalloproteinases (MMPs), prostate-specific antigen (PSA), prostate-specific membrane antigen (PSMA), and chemokines. MMPs will be discussed in Section 1.5.1. Prostate cancer unique markers including prostate-specific antigen and prostate-specific membrane antigen will be discussed in Section 1.5.2. The chemokines, which control both the growth of primary and metastatic tumor (25,26), will be discussed in Section 1.8.

Similar as in other tumors, hypoxia regions also exist in mouse, rat xenografted prostate tumors, and human prostate carcinoma (27–29). The hypoxia level is associated with prostate cancer clinical stage (30). Gerald and coworkers reported that oxygen tension in prostate cancer tissue (average media pO_2, 2.4 mmHg) is much lower than the normal tissue (muscle, average media pO_2, 30.0 mmHg) (31). Hypoxia-related genes, lysyl oxidase and glucose transporter-1 are highly expressed in prostate cancer tissue compared to benign prostatic hypertrophy (BPH) tissue (32). Immuno-histochemical analysis of 289 prostate cancer patients indicated increased expression of hypoxia marker HIF-1 alpha after surgery (33). The hypoxia microenvironment induces the high expression of CXCR4 receptor on prostate cancer cells and more stem-like tumor cells in prostate tumor (34,35). Hypoxia microenvironment in prostate cancer results in increased prostate cancer metastasis and chemotherapy resistance (36).

1.5.1 Prostate cancer microenvironment-MMPs

The MMPs are a family of zinc containing endopeptidases, and they play a critical role in the regulation of tumor invasion and metastasis (34,35). All the known 26 human MMPs contain four domains: N-terminal pro-peptide domain, catalytic domain, hinge region, and hemopexin-like C-terminal domain (39,40). Based on their specificity, MMPs are divided into four subgroups: collagenases, gelatinases, stromelysins, and matrilysins (40). The activity of MMPs is inhibited specifically and reversibly by natural tissue inhibitors of metalloproteinases (TIMPs) (38). The imbalance activity between MMPs and TIMPs causes pathological disorders (40).

Matrix metalloproteinases-2 (MMP-2), a type IV collagenase, is one of the important MMPs in drug delivery. The 2.8 Å resolution X-ray crystal structure of proMMP-2 has been analyzed and solved by Tryggvason and coworkers in 1999 (41). As shown in Figure 1.3, proMMP-2 consists of four domains: pro-domain (red), catalytic domain (blue), fibronectin domains (green) and hemopexin domain (yellow) (41). The pro-domain is a three-helix globular domain (41). The catalytic site of pro-MMP2 comprises a five-stranded β sheet and three α helices, two Zn^{2+} ions, and two Ca^{2+} ions (41). The fibronectin domain contains one α helix and two β sheets (41). The hemopexin domain is composed of four blade propeller folds (41).

MMP-2 overexpression is associated with many cancers, including prostate cancer (42,43). In normal tissue, the function of MMP-2 is to degrade extracellular matrix. As other MMPs, inhibitors of matrix metalloproteinases-2 (TIMP-2) co-exist with MMP-2. In benign prostate, the ratio of MMP-2/TIMP-2 is about one, while this ratio can increase up to 3.3 in high-grade prostate tumor. The expression of polymorphic allele in

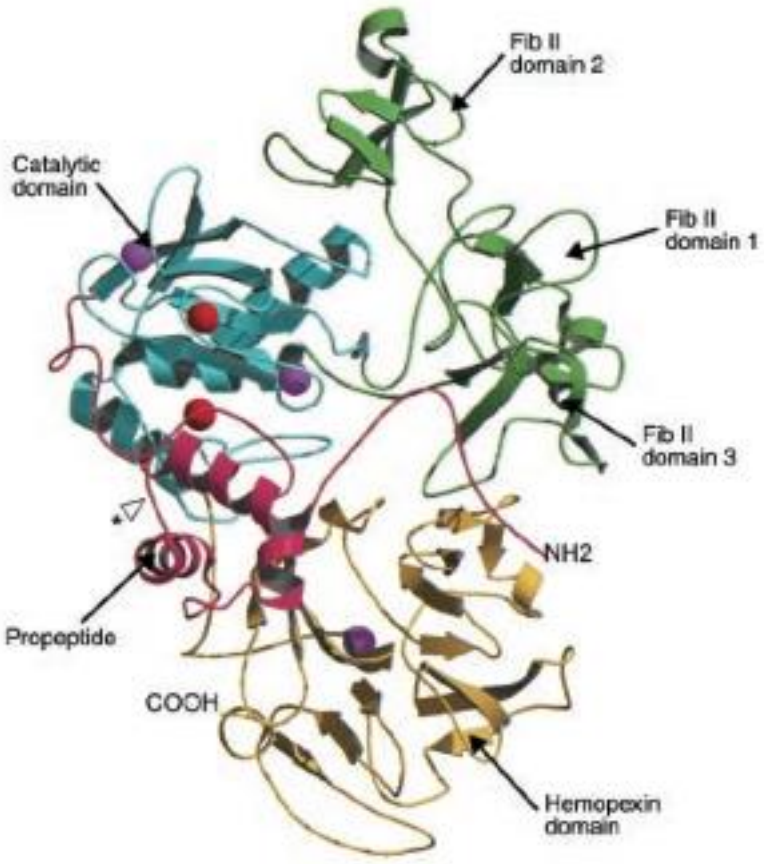

Figure 1.3: Structure of proMMP-2. The pro-domain, catalytic domain, fibronectin domains, and hemopexin domain are shown in red, blue, green, and yellow, respectively. Zn^{2+} ions are indicated in red, and Ca^{2+} are magenta. Adapted from reference (41).

the MMP2 gene increased with prostate cancer progression (43). MMP-2 is highly expressed in prostate cancer, but low in prostate hyperplasia (44). Immunohistochemical analysis of the prostate cancer tissue showed that MMP-2 expression percent in prostate cancer patients was 85.5% (53/62), while the percent was 6.7% (1/15) in BPH tissue. The MMP-9 expression in prostate cancer and BPH patients were 80.7% (50/62) and 13.3% (2/15), respectively (45). Enzyme-linked immunosorbent assay (ELISA) analysis of the active MMP-2 protein in cell culture media of PC-3 and LNCaP showed a concentration of about 2000 pg/mL, while the active MMP-2 concentration in normal prostatic epithelial cells culture media was only about 700 pg/mL (46). The MMP-2 protein concentration in plasma from PCa patients with metastasis was also higher than that of patients with BPH and healthy volunteers (47).

1.5.2 Prostate cancer markers PSA and PSMA

Prostate-specific antigen (PSA) is a 33 kDa glycoprotein secreted by the prostatic epithelium and the epithelial lining of the periurethral glands (48). PSA is a widely used marker for prostate cancer detection, but the controversy is increasing because PSA screening resulted in both false-positive and false-negative results (49).

PSMA was detected in 33/35 of primary prostate adenocarcinomas, 7/8 lymph node metastases, and 8/18 bone metastases after immunohistochemical analysis of malignant human tissue from patients with prostate cancer (50). PSMA enzyme activity in prostate cancer samples was about 10-fold higher than that in BPH and normal tissue (51). Based on the data from 136 cases of prostate cancer, PSMA expression is strongly related to the serum PSA level: the mean serum prostate-specific antigen in PSMA

overexpressing group was 18.28 ng/ml, while the mean serum PSA in non-PSMA-overexpressing group was 9.10 ng/mL. Taken together, those data implied that PSMA is an important maker for prostate cancer diagnosis and treatment (52).

PSMA is a *Mr* 100,000 type II membrane protein containing a 19-amino acid (aa) cytoplasmic fragment, a single 24-aa membrane-spanning fragment, and a 707-aa extracellular region (53,54). PSMA exists as a noncovalent homodimer on the prostate cancer cell surface, and requires dimerization to maintain its functions (54). As shown in Figure 1.4.A, the 3.5 Å crystal structure of the extracellular region of PSMA consists of three domains: a protease domain (residues 56-116 and 352-591); an apical domain (residues 117-351); and a helical domain (residues 592-750) (55).

As shown in Figure 1.4.B, the active site of PSMA is located at the interface between the three domains. A water molecule bridges two zinc ions, which are coordinated by three endogenous ligands: a histidine, a terminal aspartate or glutamate, and a bridging aspartate (55).

1.6 Drug Targeting to Solid Tumor

One of the major reasons for the low efficacy and high toxicity of systemically administered drugs is due to low accumulation in the tumor area (usually less than 5% ID) (56). The low drug accumulation in the tumor is due to two major reasons: first, the dysfunctional blood vasculature fails to deliver enough drug to the tumor area; second, the high interstitial pressure in the tumor area retards the extravasation of drug from blood vasculature to the tumor area. The advent of “nanomedicine” has the potential to revolutionize cancer therapy using passive and active targeting to improve the

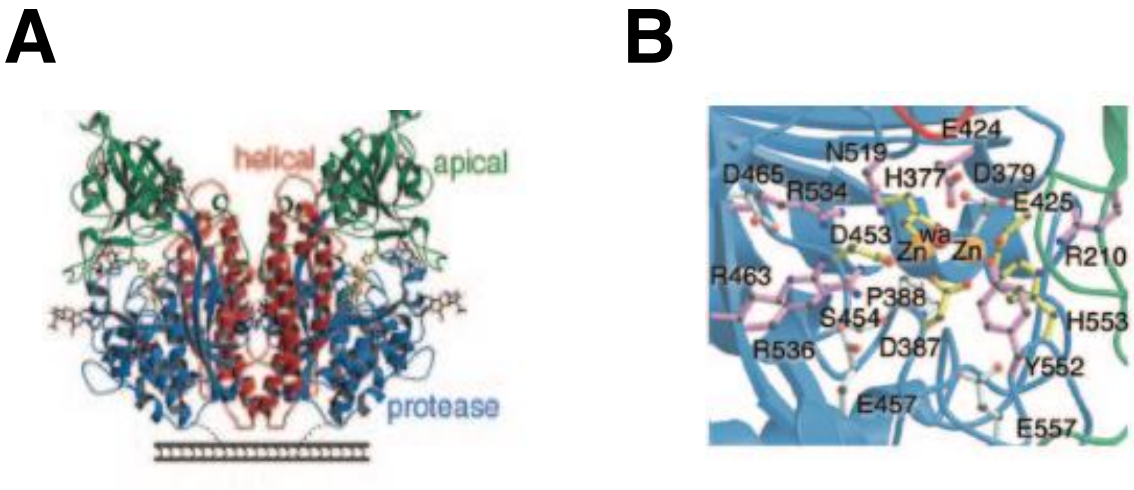

Figure 1.4: Structure of PSMA. (A) Ribbon diagrams of side views of PSMA; (B) the active site of PSMA. Adapted from reference (55).

accumulation of drugs in tumor stroma and internalization in tumor cells (57).

1.6.1 Passive targeting

The passive targeting, also called Enhanced Permeability and Retention (EPR), effect was first discovered by Maeda's group in 1986 (58,59). The EPR concept takes advantage of the irregular blood and lymphatic vessels in the tumor area (60–62). First, leaky vasculatures allow the enhanced extravasation of nanomedicines from the circulation system into the tumor. This reduces the undesirable side effect of nanomedicines. Second, the disfunctional lymphatic system in the tumor decreases the clearance of nanomedicines, thus enhancing retention time in tumor (57). Theoretically, nanomedicines can extravasate into the tumor through the leaky vessel by diffusion and convection, but the high interstitial pressure in the tumor reduces the driving force for convective movement. Thus, the extravasation of nanomedicines mainly relies on diffusion, that is, movement from a region of high concentration to a region of low concentration. This process is extremely slow. The passive delivery efficiency relies on the inherent physicochemical properties of nanomedicines (size, shape, charge, etc.) and pathophysiological features of the tumor.

1.6.2 Active targeting

The active targeting strategy is to decorate the surface of a nano-carrier with targeting moieties for binding to the overexpressing specific receptors on tumor cells. The original attempt for active targeting is to enhance the accumulation of a intravenously administered drug or imaging agent in solid tumors and lower systemic

exposure by a specific interaction between the targeting moieties and the receptors that are overexpressed or up-regulated on tumor vessels or cells (63). However, the higher binding affinity between ligands and receptors on cancer cells can only enhance the internalization of drug but not alter the accumulation of drug in tumor area (64,65). That is due to the fact that targeting moieties have no chance to interact with tumor cells until they reach the tumor (64). Despite this, active targeting still has the potential to provide safer and more effective anticancer treatment (66). Once nanomedicines arrive at the tumor, the ligand-receptor interaction can not only increase the retention time in tumor but also facilitate the uptake process (67). Currently, there are thirteen ligand-targeted nanomedicines in clinical trials (68). The active targeting strategies can be divided into two areas: (i) targeting cancer cells; (ii) targeting the tumor endothelial cells. The most popularly studied cancer cell receptors include: (1) transferrin receptor, (2) endothelial growth factors (EGF) receptor, (3) folate receptor. The two most studied tumor endothelium receptors are vascular endothelial growth factors receptors (VEGFR) and $\alpha_v\beta_3$ integrin (69). Most of the nanomedicine is to block the interaction between vascular endothelial growth factors (VEGF) and VEGFR; this is beyond the scope of this dissertation (69). Only $\alpha_v\beta_3$ integrin will be discussed in this chapter.

Transferrin receptor (TfR) is the most pertinent target for active cancer treatment in the clinic, four of the thirteen targeted nanomedicines in clinical trials (MBP-426, SGT-53, SGT-94, and CALAA-01) target transferrin receptors (68). TfR is a 180 kDa, type II transmembrane glycoprotein, which contains an intracellular domain (61aa), a transmembrane domain (28aa), and a large extracellular domain (671aa) (70). Transferrin receptor is highly expressed on cancer cells with a density of 10,000-100,000 molecules

per cancer cell, while undetectable in normal cells (71). Because transferrin is up-regulated in various types of cancer, it is possible that one targeting ligand-drug conjugate can simultaneously treat multiple cancers (72). The transferrin-targeted and nontargeted siRNA nanoparticles have similar biodistribution in a mouse tumor model, but the siRNA activity for transferrin-targeted nanoparticles is about 50% higher than that of nontargeted nanoparticles (65). The coating of transferrin on gold nanoparticles did not influence their biodistribution in tumor, but significantly increased the localization of nanoparticles in tumor cells (66).

Epidermal Growth Factor Receptor (EGFR) is another attractive target. Two EGFR targeted nanomedicines are in clinical trial (68). EGFR is frequently expressed in various types of cancer (73). The anti-EGFR antibody can enhance the internalization of nanoparticles in pancreatic cancer cells (74). The coating of anti-EGFR peptide GE11 on the surface of nanoparticles increased the biodistribution about 2-fold in a subcutaneous human pancreatic adenocarcinoma mouse model (75). The GE11 assisted delivery of sodium iodide symporter gene resulted in the specific therapy of liver cancer (76,77). The coating of anti-EGFR antibody on poly(lactic-co-glycolic acid) (PLGA) nanoparticles enhanced their uptake in breast cancer cells (73).

Folate receptor, a 38 kDa glycosyl-phosphatidylinositol-anchored glycoprotein, is overexpressed in a variety of solid tumors, including ovary, lung, breast, kidney, brain, endometrium, and colon cancer (67,69,78,79). Folate-targeted liposomes, micelles, and dendrimers have been studied for cancer treatment in mouse tumor models. The cytotoxicity of doxorubicin in folate-targeted liposomes was about 85 times greater than that in nontargeted liposomes (80). The heparin-folate-paclitaxel nanoparticles enhanced

the therapeutic efficacy of paclitaxel (81). A folate-targeted micelle containing doxorubicin prevented breast cancer metastasis compared to that of nontargeted micelles (82). Folate decorated poly(amidoamine) (PAMAM) dendrimers were able to deliver siRNA for cancer treatment (83).

The expression of integrin is associated with cancer growth and progression (84). Different from other receptors, $\alpha_v\beta_3$ integrin is overexpressed in both tumor and angiogenic endothelial cells (85). The tripeptide Arg-Gly-Asp (RGD), which was first discovered by Ruoslahti and coworkers, has high binding affinity toward integrins, especially $\alpha_v\beta_3$ (86). Now, the linear and cyclic derivatives of RGD containing peptides are commonly used for $\alpha_v\beta_3$ integrin-targeted drug and/or imaging agent delivery (84). The conjugation of CDCRGDCFC (RGD-4C) to doxorubicin significantly enhanced the efficacy of doxorubicin against MDA-MB-435 human breast cancer xenografts in nude mice and reduced the systemic toxicity of doxorubicin (87). RGD-targeted nano-medicines have shown 15-fold enhancement in treatment of pancreatic cancer metastasis (88). Inhibiting the angiogenesis in tumor blood vessels by RGD-targeted gene therapy suppressed primary and metastatic tumor growth (89). ACDCRGDCFC was conjugated to cationic polymer (PEI) to assist delivery of gene for inhibiting angiogenesis and tumor growth (90,91). The attachment of RGD targeting moieties on HPMA copolymer drug conjugates significantly increased the accumulation of drug in prostate cancer tumor (92–95). The conjugation of cRGD to zwitterionic near-infrared (NIR) fluorophore improved the ratio of tumor to background from 5.1 to 17.2 in in vivo optical imaging (96).

1.7 Drug Penetration and Cell-Penetrating Peptides

Although passive and active targeting can enhance drug accumulation in the tumor area and drug internalization in tumor cells, the drugs still need the ability to penetrate into the tumor interior to achieve efficacy (97). Some of the patients with CRPC benefit from chemotherapy, but some still die of prostate cancer because of the drug resistance (98). Resistance to chemotherapy treatment resulted from poor or limited drug distribution in solid tumors (63,99,100). Tannock and coworkers investigated the Doxorubicin (DOX) distribution in relation to tumor blood vessels in mice bearing PC-3 tumor. As shown in Figure 1.5, most of the DOX distributed around the tumor vessels and did not reach hypoxic areas (101). The Minchinton group investigated the Taxanes penetration by measuring the drug effect in HCT-116 tumor xenografts (99). The drug effect at 150 μm away from the vasculature was only about 70% of that in the tissue near the tumor vessels. In order to improve the accumulation of therapeutics in tumor area and increase the contact chance of interior tumor cells to drugs, researchers have developed cell-penetrating peptides (CPPs) to improve the penetration of drug into the solid tumor.

1.7.1 Receptor-independent CPP

The concept of CPP was inspired by Pabo's and Loewenstein's group discovery in 1988 (102,103). They found that the TAT protein from human immunodeficiency virus 1 (HIV-1) could be taken up by cells growing in tissue culture (102). The exact amino acid sequence (RKKRRQRRR), often referred to as Tat_{49-57} or the Tat 9-mer, that is responsible for the cellular uptake was first discovered by Lebleu and coworkers (104). They also demonstrated that this peptide-assisted-internalization did not involve an

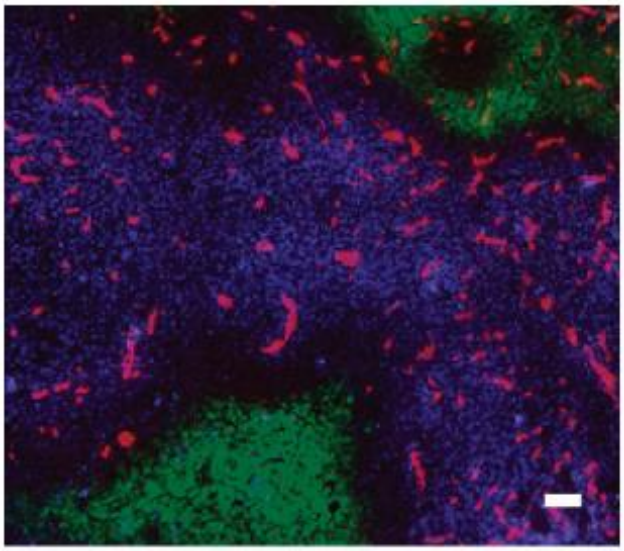

Figure 1.5: The distribution of Doxorubicin in PC-3 tumor. Adapted from reference (101).

endocytic pathway and was not energy dependent (104). The application of TAT for delivery of macromolecules to cells started in Dowdy's group. They found that TAT fused 120-kDa b-galactosidase can be delivered to each tissue in mice after being injected intraperitoneally (105). Their findings overturned the concept that only small molecules can enter into cells (106).

More CPPs were created through biomimetic or organic synthesis after the discovery of TAT. Some representative CPPs and relating sequences are shown in Table 1.1. The discovery of "Penetratin" is based on the research that the third helix of homodomain of the Antennapedia is internalized by cells (107,108). Transportan is a combination of the first 13-amino acids in N-terminus of the galanin and the first 14-amino acid in the C-terminus of mastoparan (109). VP-22 is derived from Herpesvirus structural protein (110). Xentry is derived from a N-terminal region of the X-protein of the hepatitis B virus (111). Recently, Anderson group developed a set of 50 cell penetrating peptides derived from 46 proteins that can associate with the plasma membrane (112). Organic synthesis also helped to find new CPPs by mimicking arginine or lysine-rich CPPs (113). Norbornene-based guanidine-rich polymers were developed to mimic CPPs (114). Peptoid analogues containing a six methylene spacer between the guanidine head group and backbone are better than Tat_{49-57} in penetration application (115). Although there are hydrophobic CPPs (116) and amphipathic CPPs (117), most of the CPPs can be classified into guanidinium group-rich CPPs. For the guanidinium-rich peptides, the internalization is controlled by the number and order of guanidinium groups in the peptide (118). The backbone rigidity and static presentation of guanidinium groups promote arginine-rich CPP's internalization into cells (119).

Table 1.1 Representative cell-penetrating peptides and their sequences.

Tat_{49-57}	RKKRRQRRR
R8	RRRRRRRR
Transportan	GWTLNSAGYLLGKINLKALAALAKKIL
Penetratin	RQIKIWFQNRRMKWKK
Hepatitis B Virus Translocation Motif (TLM)	PLSSIFSRIGDP
POD	GGG-$(ARKKAAKA)_4$
pVEC	LLIILRRRRIRKQAHAHSK
$ARF_{(1-22)}$	MVRRFLVTLRIRRACGPPRVRV
EB1	LIRLWSHLIHIWFQNRRLKWKKK
Rath	TPWWRLWTKWHHKRRDLPRKPE
CADY	GLWRALWRLLRSLWRLLWRA
Histatin 5	DSHAKRHHGYKRKHHSKRGY

The internalization of CPPs into cells can be divided into two steps. The first step is the association interaction between CPPs and cell membrane. The most accepted mechanism is shown in Figure 1.6. The guanidinium group can form a bidentate hydrogen bond with anionic cell surface phosphates, carboxylates, and/or sulfates to initiate cellular entry but not the ammonium group in cationic CPPs (118,120,121). The stoichiometry of peptide-heparan sulfate binding impacts the uptake efficiency of cell penetrating peptide (122).

The second step is the CPPs cellular uptake. Although many researchers try to explain the cellular uptake mechanism of CPP, the mechanism is still not fully understood. Two general uptake mechanisms were generally considered: 1) Energy-independent uptake directly across biological membranes (124); 2) Energy-dependent endocytosis. As shown in Figure 1.7, the endocytosis can be subdivided into four different pathways: macropinocytosis, clathrin-dependent endocytosis, caveolae/lipid raft-mediated endocytosis, and clathrin/caveolae-independent endocytosis. The cellular uptake mechanism of CPPs can be impacted by many factors: CPP type, attached cargo nature, cell types, or incubation condition. For example, the association of serum proteins in cell culture media with CPPs changes the cell uptake pathway (126,127). Brock's group found that Tat and Pentratin simultaneously used three endocytosis pathways to pass through cell membrane (128).

One of the most important applications of CPPs is to overcome drug resistance (129). The conjugation of octa-arginine to taxol through a disulfide spacer can overcome the ovarian cancer resistance (129). CPP-methotrexate conjugates have better cytotoxicity

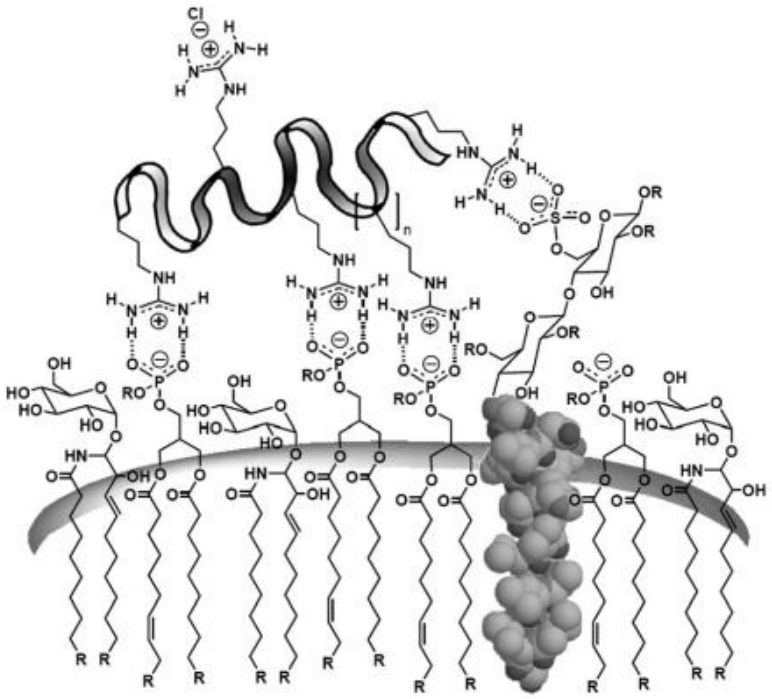

Figure 1.6: Proposed association mechanism between CPP and cell membrane. Adapted from reference (123).

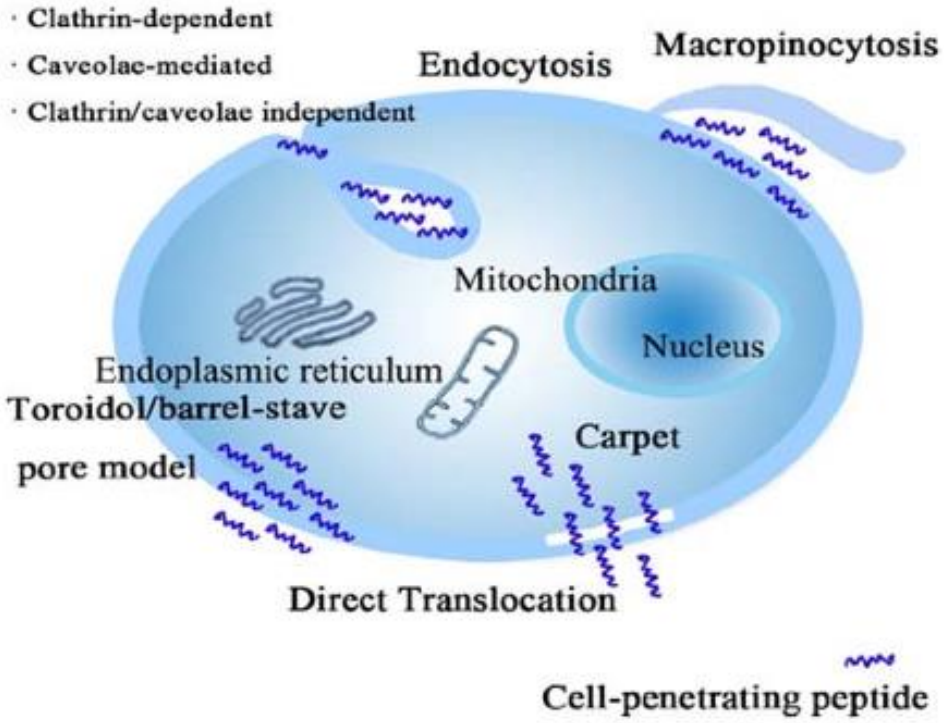

Figure 1.7: Possible cell penetrating peptide cellular uptake pathway.
Adapted from reference (125).

toward breast cancer cells compared to free methotrexate because the CPP helps to overcome drug resistance (130).

Although receptor-independent CPPs have shown promise in cell culture and animal studies, the absence of cell specificity hinders their application in clinical studies. To apply CPPs for systematic administration, their lack of cell specificity has to be bypassed. One method is to control the display of CPPs, that is, shield the CPPs with "stealth polymer" during the transport process and expose the CPPs once it arrives at the pathological sites. This method uses the tumor environment (MMPs, pH, or PSA) or extrinsic (light or heat) to trigger the exposure of CPPs.

MMPs are overexpressed in some tumors as mentioned above. Tsien and coworkers developed a MMP-2 sensitive imaging agent by conjugating CPP oligomer arginine with oligomer aspartic/glutamic acid via a -PLGLAG- linker (131). The hairpin formed by the electrostatic interaction between the polycationic and polyanionic peptide sequences can avoid the nonspecific binding of CPPs to cell membranes. The high concentration of MMP-2 in tumors will cleave the -PLGLAG- spacer. The polyanionic peptide dissociates from the CPPs, and results in recovery of CPPs's cell penetrating ability (132). Torchilin's group used a similar idea for drug delivery; they attached long poly(ethylene glycol) chain (2 kDa and 3.4 kDa) to the surface of liposomal nanocarriers via a octa-peptide (Gly-Pro-Leu-Gly-Ile-Ala-Gly-Gln) spacer to shield the TAT peptide. The octa-peptide spacer was cleaved by MMP-2 in the tumor microenvironment, and PEG was detached from the nano-carrier surface. Then, the cellular uptake ability of CPPs was recovered (133).

Using a similar strategy, Torchilin's group used the pH difference between the tumor microenvironment and circulating blood to selectively display cell-penetrating TAT peptide in the tumor microenvironment by attaching a long (2 kDa or 3.4 kDa) shielding PEG-chains on the surface of liposomes via a pH sensitive hydrazone bond (134,135). Bae's group took advantage of the acidic pH in the tumor microenvironment to display the TAT from micelles. One example is to form the PEG-poly(l-lactic acid)-TAT micelle first, then mix with poly(L-cystine bisamide-g-sulfonamide)-PEG (136). At pH 7.4, the ionic interaction between positively charged TAT and negatively charged sulfonamide resulted in the assembly of PEG on the surface of micelle to shield TAT. When the pH was decreased to 6-6.8, the sulfonamide became neutrally charged. Then, TAT was exposed on the micelle surface following the removal of poly(L-cystine bisamide-g-sulfonamide)-PEG from the micelle surface. Recently, Shen and colleagues used succinic acid to amidize the amine group in TAT (137). This amide bond was stable in blood and broken in acidic tumor microenvironment.

Another interesting stimuli-responsive CPP took advantage of the specific PSA in prostate cancer microenvironment (138). Franc group developed activatable protein transduction domain conjugates, which incorporated an r8 (positively charged) and r8 attenuating sequence (negatively charged) by a PSA cleavable linker. This conjugate was stable in serum, but disassociated by PSA (138).

The two most common used extrinsic triggers for display of CPPs are ultraviolet (UV) and temperature. One example is to modify the two ends of TAT with two alkyl chains via a UV cleavable linker first, then the modified CPPs were anchored to the liposomal surface (139). Once they reached the pathological sites, controlled release of

the TAT was achieved after the liposome was irradiated with UV. The other example is to minimize the nonspecific cellular uptake of CPP by capping the positively charged lysine with photo cleavable groups. After being irradiated with UV, the cellular uptake ability of the CPP was recovered (140). A new method used thermal triggered micelle assembly to adjust the arginine residue density in the micelle corona (141).

1.7.2 Receptor-dependent CPPs (receptor-independent CPP + targeting ligand)

Targeting moieties are used to enhance the cell specificity of CPPs. The first strategy is to decorate the traditional receptor independent CPPs or CPP conjugates with additional targeting moieties, which can recognize the receptor on the cancer cell surface. The attachment of breast tumor homing cyclic peptide cCPGPEGGAGC to the cell penetrating peptide *p*VEC improved the specific tumor uptake (142). The conjugation of anti-HER-2/neu peptide mimetic to the HIV TAT-derived CPP improved the inhibition selectivity of the therapeutic peptide STAR3BP toward cancer ErbB2-overexpressing breast cancer (143). The attachment of mAb 2C5 to the surface of liposomal nanocarrier can selectively deliver TATs to specific tumor cells (133,134). Transferrin receptor targeted cell-penetrating peptide (Transportan) is used for targeted delivery of siRNA (144).

1.7.3 Receptor-dependent CPPs (iRGD)

The second strategy is to integrate the targeting moiety (RGD) and CPP (RGDK) together. The best example is iRGD, which was first developed by Ruoslahti's group. The CPP here is the C-end rule peptides (R/KXXR/K), which bind to neuropilin-1 to

initiate internalization. This C-end peptide was discovered by mimicking the C-terminal of Vascular Endothelial Growth Factor (VEGF)-A165 (145). The carboxyl group in the C-terminal arginine plays a critical role for internalization. Blocking this carboxyl group by amidation or coupling with another amino acid will abolish the binding and penetration ability of the peptide (145).

Free iRGD is a cyclic 9-amino acid peptide, which is identified by in vivo phage display (146,147). As shown in Figure 1.8, the iRGD penetration is a three-step process (146,148). First, the RGD sequence in iRGD binds to α_v integrin. Second, the iRGD peptide is converted to cryptic CendR peptide CRGDK/R after being cleaved by cell surface associated protease(s). Third, the formed CendR peptide binds to tumor vessel signature molecule neuropilin-1 (NRP1) for mediating cell internalization.

iRGD has been used for delivery and penetration of small molecule drug, polymer conjugates, nanoparticles, and antibodies (149–155). The conjugation of iRGD to porous silicon nanoparticles enhanced their cell uptake efficiency in EA.hy926 cells (156). The attachment of iRGD on paclitaxel loaded poly(ε-caprolactone)-b-poly(N-vinylpyrrolidone) enhanced the penetration and accumulation of paclitaxel in tumor tissues (157). iRGD assisted co-delivery of Paclitaxel and survivin shRNA by micelle significantly improved the drug accumulation in lung tumor (158). iRGD was also used for optical image detection of tumor (159,160). Several conjugation methods have been developed to link iRGD to small molecule and macromolecular therapeutics. The most commonly used iRGD conjugation reaction is the thiol maleimide reaction between the thiol group in iRGD and the maleimide group on the polymer, conjugate, and

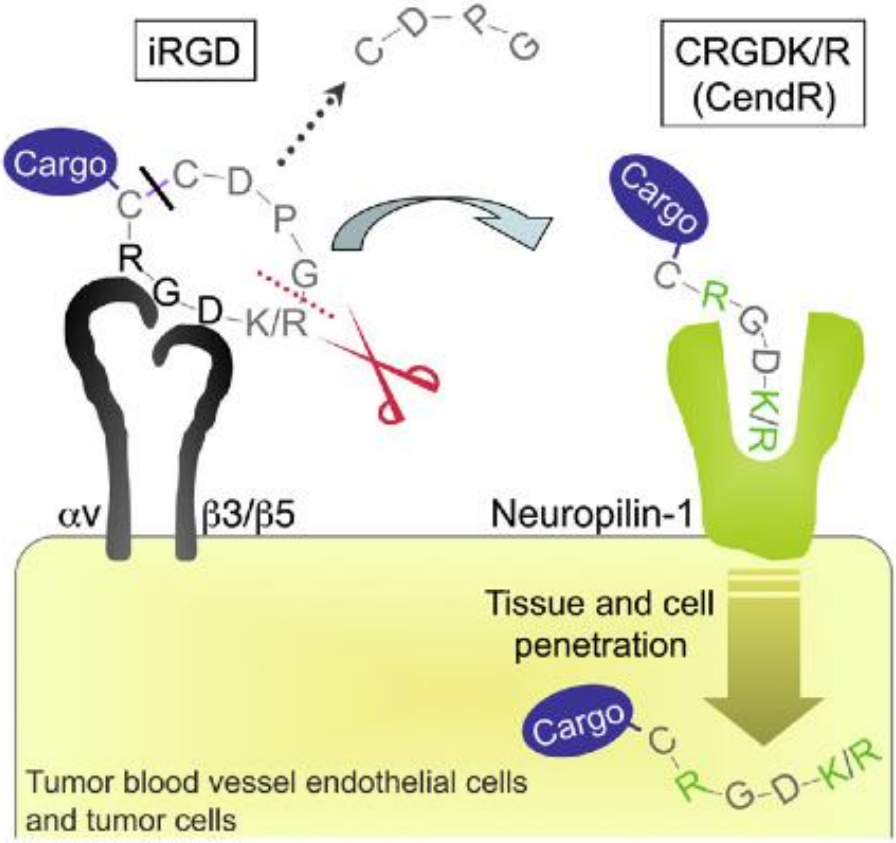

Figure 1.8: Penetration mechanism of iRGD. Adapted from reference (146).

nanoparticles (146). Also, other derivatives of iRGD are developed to diversity the iRGD conjugation (156,161).

A new peptide CRNGRGPDC was produced by altering the RGDK to RNGR in the iRGD framework, and also was able to enhance the penetration of small molecule drug and nanomedicine (162).

1.8 Cancer and Chemokines

1.8.1 Chemokines and chemokine receptors

The name of chemokine is an abbreviation of *Chemo*tactic cyto*kines*. Depending on the position of first two cysteines at the *N*-terminus, most small chemokines (8-10 kDa) are grouped into four families, that is, CXC, CC, C, and CX3 (Figure 1.9) (163). Chemokine receptors are seven transmembrane G-protein coupled receptors (GPCR), which are able to mediate the migration of cells toward a gradient of chemokines (164). Until now, more than 50 chemokines and at least 18 of their receptors have been found and investigated (163). A chemokine nomenclature system was proposed by Zlotnik and Yoshie to distinguish chemokines and receptors (165). Specific chemokine names consist of a "family name" followed by the letter "L" for ligand and a "number" for its discovery order. The corresponding, chemokine receptor name consists of "family name", followed by the letter "R" for receptor and a "number" for its discovery order (25).

1.8.2 CXCL12 and CXCR4

The chemokine CXCL12, also known as stromal cell-derived growth factor 1 (SDF-1), is the only known ligand for CXCR4. CXCR4 is a 352-amino-acid rhodophin-

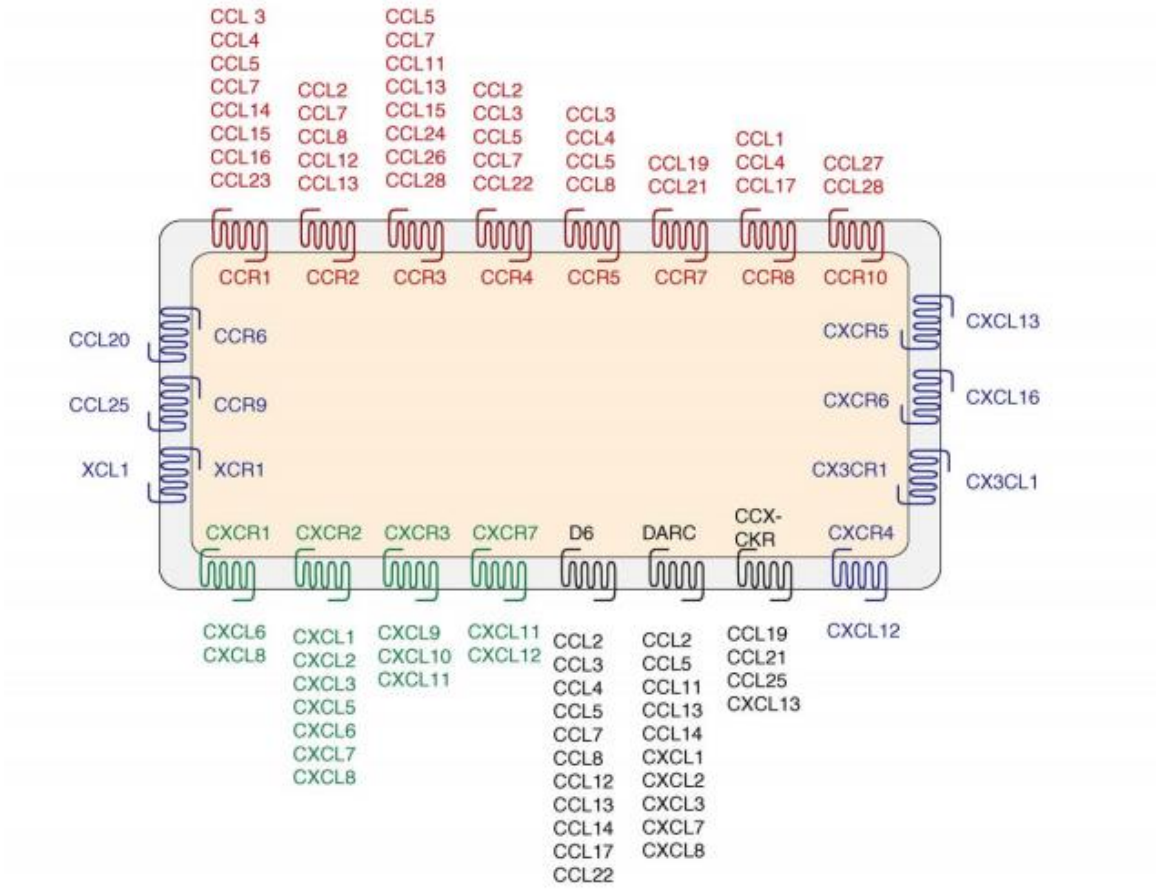

Figure 1.9: Chemokine and chemokine receptor families. Adapted from reference (166).

like seven-transmembrane GPCR (164). The specific affinity between CXCL12 and CXCR4 is due to the electrostatic interaction between the positively charged CXCL12 surface and negatively charged CXCR4 extracellular loops (167). As shown in Figure 1.10, the binding of CXCL12 results in the dimerization of CXCR4, which regulates divergent downstream signaling pathways (168).

1.8.3 CXCL12/CXCR4 and cancer

CXCR4 expression has been reported in at least 23 epithelial, mesenchymal, and hematopoietic cancers, including prostate, breast, non-small cell lung (NSCLC), and gastric cancers (169–173). The interaction between CXCR4 and CXCL12 plays a pivotal role in tumor angiogenesis, growth, and metastasis (174).

The CXCL12, which is secreted by carcinoma-associated fibroblasts in breast tumor, recruits endothelial progenitor cells (EPCs) to promote tumor angiogenesis and tumor growth (175). The treatment of CXCR4 antagonist CTCE9908 results in the disruption of tumor vasculature, lower expression of VEGF, and decreased recruitment of EPCs and neutrophils, thus inhibiting the primary tumor growth (176).

Metastases lead to more than 90% of solid cancer-related mortality (178). The formation of metastasis is a complex series of sequential events: (i) the cancer cells need to obtain the invasion ability and escape from the primary tumor; (ii) intravasate into the lymph and blood systems, (iii) survive and translocate in the circulation, (iv) extravasate (exit from the bloodstream) and adapt to the foreign microenvironment, (v) proliferate at the distant metastatic site and form macroscopic secondary tumor (179). The seed and

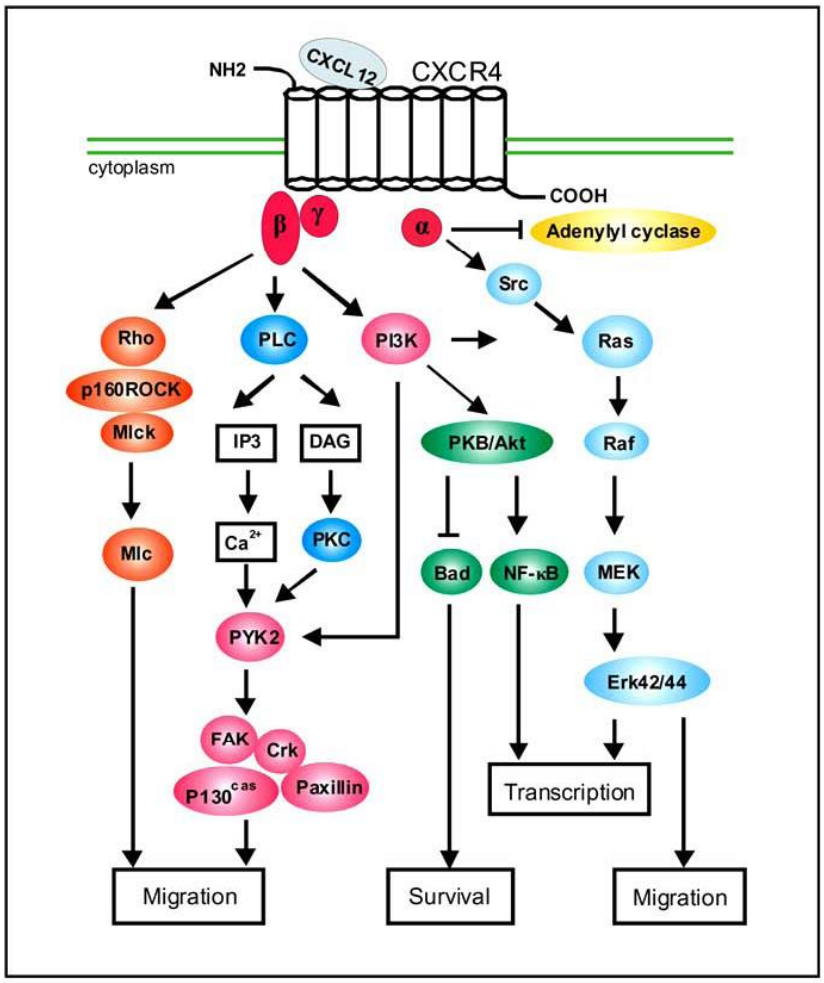

Figure 1.10: Signal transduction pathway induced by CXCL12 binding to CXCR4. Adapted from reference (177).

soil hypothesis was first proposed by Paget in 1889 to explain the cancer metastasis mechanism (179,180).

Since Muller and coworkers reported that the CXCL12/CXCR4 axis is involved in breast cancer metastasis, much effort has been made to investigate whether the CXCL12/CXCR4 is involved in other cancers (170). Quantitative RT-PCR analysis of the CXCL12 in major human organs reveals that CXCL12 is highly expressed in bone marrow, lymph nodes, liver, and lung, but has a low level of expression in prostate, brain, and muscle (170). This coincides with the fact that bone, lymph nodes, liver, and lung are the preferential sites for the formation of breast cancer metastases. Now it is believed that CXCL12/CXCR4 axis direct the cancer metastasis. The disruption of CXCR4/CXCL12 is able to inhibit cancer metastasis. The CXCL12 induced invasion ability of MDA-MB-231 decreased to 16% after silencing the CXCR 4 expression with two siRNAs. The lung metastasis in mice reduced to 22% when the injected MDA-MB-231 cells were transfected with CXCR4 siRNAs (181).

1.8.4 CXCR4 antagonists in clinical trial

Most commonly used agents to block the CXCL12/CXCR4 axis are CXCR4 antagonists (182). As shown in Table 1.2, several CXCR4 antagonists are being evaluated in clinical trials. Because the structures of TG-0054 and POL6326 are not publicly disclosed yet, only five CXCR4 antagonists are discussed below: MSX-122, CTCE9908, AMD3100, AMD070 (AMD11070), BKT140.

As shown in Figure 1.11.A, AMD3100 (Plerixafor/Mozobil^{TM}) consists of two cyclam rings, which are linked by a phenyl spacer. It is a nonpeptide CXCR4 antagonist,

Table 1.2 CXCR4 antagonists in clinical trial. Adapted from reference (188).

Agents	Phase	Indication	Sponsor
TG-0054	Phase II	Hematopoietic stem cell mobilization in patients with multiple myeloma, non-Hodgkin lymphoma or Hodgkin disease	TaiGen Biotechnology Co., Ltd
POL6326	Phase II	Cell mobilization and healing in acute myocardial infarction	Polyphor Ltd
POL6326	Phase I	Mobilization of hematopoietic stem cells in healthy volunteers	Polyphor Ltd
CTCE-9908	Phase I/II	Advanced solid tumors	Chemokine Therapeutics Co.
MSX-122	Phase I	Refractory metastatic or locally advanced solid tumor	Metastatix, Inc
Plerixafor	FDA approved	Hematopoetic stem cell mobilization in patients with non-Hodgkin's lymphoma and multiple myelome	Genozyme
Plerixafor	Phase I	Gioma, Acute Myeloid Leukemia, Chronic Lymphocytic Leukemia	Genozyme
Plerixafor	Phase I	Myelokathexis (WHIM syndrome)	Genozyme
AMD070	Phase I/II	HIV infections	National Institute of Allergy and Infectious Disease
BKT140	Phase I/II	Multiple myeloma	Biokine Therapeutics Ltd

which has been approved by the FDA to mobilize hematopoietic stem cells to the peripheral blood in combination with granulocyte colony-stimulating factor (G-CSF) (183). The specificity of AMD3100 toward CXCR4 is due to the electrostatic interaction between the positively charged nitrogen in the AMD3100 cyclam ring and the negatively charged Asp^{171}, Asp^{262}, and Glu^{288} residues in the CXCR4 receptor (184,185). The incorporation of metal ions Cu^{2+}, Zn^{2+}, or Ni^{2+} into AMD3100 significantly enhanced AMD3100's binding affinity toward CXCR4 receptor and further demonstrated the electrostatic interaction between AMD3100 and CXCR4 (186). AMD3100 inhibits the migration and invasiveness of prostate cancer cells, which was promoted by CXCL12 (44). One of the obvious limitations of AMD3100 is its short half life (3.5 to 4.9 h) (187).

AMD070 is also known as AMD11070. The structure of AMD070 is shown in Figure 1.11. B. It is the first orally bioavailable CXCR4 antagonist. Molecular modeling explained the possible interaction mechanism between AMD 070 and CXCR4 (189). The binding affinity of AMD070 and CXCR4 is from the electronic interaction between the protonated primary amine in AMD070 and one of Asp residues (Asp^{97}, Asp^{171}, Asp^{262}), and the pi stack interaction in AMD070 and Tyr^{45} and Trp^{94} residues (189). AMD 070 has shown promising in preventing melanoma metastasis to liver by blocking the CXCR4-CXCL12 axis (190). AMD070 is better than AMD3100 in blocking the CXCL12 inducing migration of human acute lymphoblastic leukemia cells (191).

MSX-122 is a novel orally bio-available small molecular weight CXCR4 antagonist. The chemical name of MSX is *N*, *N*-9-(1,4-phenylenebis(methylene)) dipyrimidine-2-amine. Shim's group reported that this antagonist can inhibit metastasis in three different metastasis animal models (192). They also demonstrated MSX-122 can

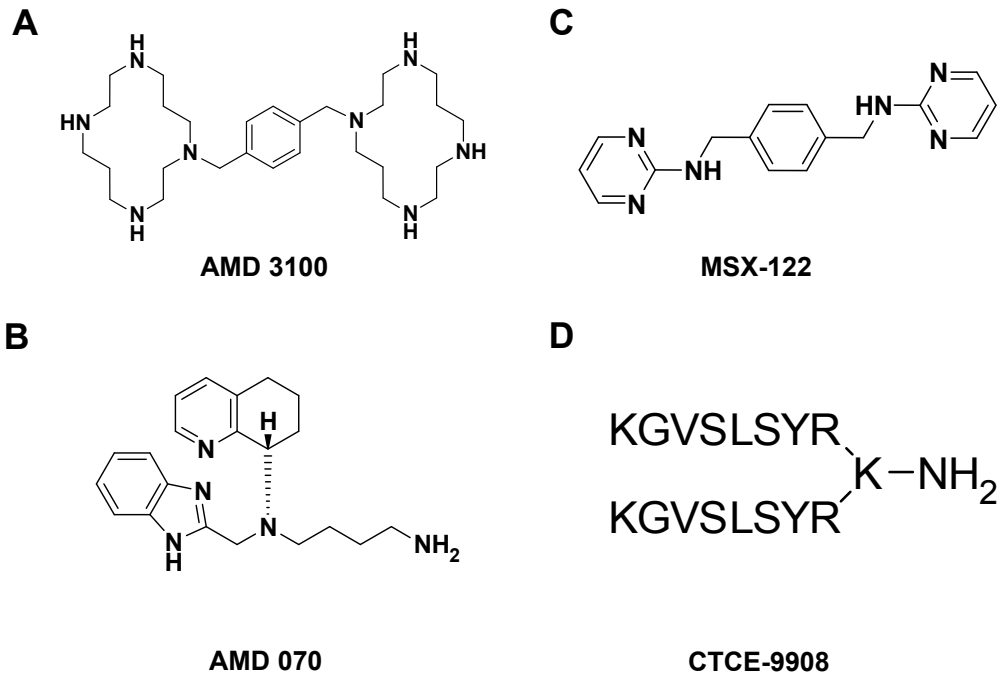

Figure 1.11: Structure of CXCR4 antagonists in clinical trials. (A) AMD3100; (B) AMD 070; (C) MSX-122; (D) CTCE-9908.

significantly reduce the formation of radiation-induced pulmonary fibrosis by disrupting the CXCL12/CXCR4 interaction (193). However, there is no reported mechanism to explain this interaction. A Phase I clinical study of MSX-122 was started in 2007, but was suspended in 2008 due to the unmanageable toxicities (188,194).

As shown in Figure 1.11.D, CTCE9908 is a dimer peptide comprised of two of the first 8 amino acids of the *N*-terminal sequence of CXCL12. Subcutaneous administration of CTCE-9908 into mice bearing MDA-MB-231 xenograft tumors reduced the growth of both primary and metastatic breast tumors (195). Systemic delivery of CTCE9908 via oncolytic vaccinia virus for treatment of BALB/c mice with 4T1 breast tumor xenograft not only inhibited the growth of orthotopic primary tumors but also reduced lung metastasis (176). CTCE-9908 also blocked the CXCL-12 induced ovarian cancer cell migration and killed the CXCR4 positive ovarian cancer cells by mitotic catastrophe (196). CTCE-9908 inhibited the proliferation of prostate cancer cells in vitro and the growth of prostate tumor in vivo (197).

BKT140 belongs to T140 series peptide (Figure 1.12). T140 peptides are another type of potent CXCR4 antagonists, which were originally developed to inhibit the T-cell line-tropic HIV infection (198). T140 series are considered to be the most active CXCR4 antagonists (199). Fujii and coworkers used the traditional Ala-subsitution scanning to investigate the structure-activity relationship between T140 peptides and CXCR4 (198). They found that four indispensable amino acid residues (Arg^2, Nal^3, Tyr^5, and Arg^{14}) are the pharmacophores of T140 peptide, which are responsible for T140 peptides' activities (198).

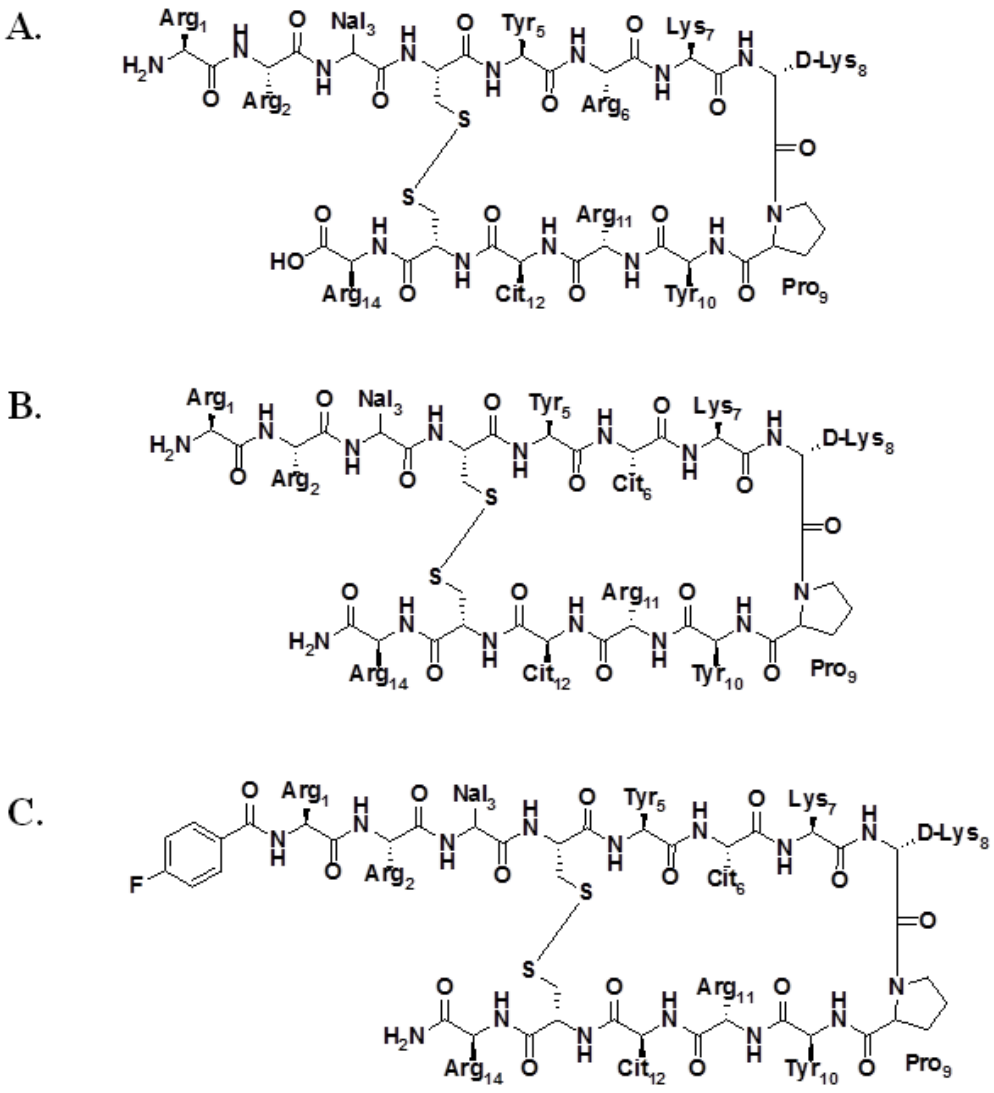

Figure 1.12: Structures of T140 series peptides. T140 (A), TN14003 (B), and BKT140 (C). Nal = L-3-(2-naphthyl)analine, Cit = L-citrulline.

However, two major drawbacks are associated with T140 peptide. First, the loss of carboxyl terminal Arg^{14} from T140 in serum results in loss of T140 activity. Second, the electrostatic interaction between the positively charged peptide (Arg^{1}, Arg^{2}, Arg^{6}, Lys^{7}, D-Lys^{8}, Arg^{11}, and Arg^{14}) and negatively charged cell membrane may lead to non-specific binding (200). To improve the serum stability and reduce the nonspecific cell cytotoxicity, another effective CXCR4 inhibitor (TN14003) was developed by C-terminal amidation and replacement of the basic Arg^{6} with non-basic Cit^{6} (201). After further modification, a new CXCR4 antagonist 4F-benzoyl-TN14003 (BKT140) with low IC_{50} (0.99 nM) was discovered (202).

1.9 HPMA Copolymer-drug Conjugates

Polymeric therapeutics belong to the first-generation nanomedicines (203). The first synthetic polymer-drug conjugates in Phase I/II clinical trial were *N*-(2-hydroxylpropyl)methacrylamide (HPMA) copolymer-doxorubicin conjugates (203). HPMA polymer was first prepared by Kopeček and coworkers in 1973, and the first HPMA copolymer drug conjugate was published in 1979 (204,205). In the past three decades, water soluble and biocompatible HPMA polymers have been utilized to deliver several anticancer drugs including doxorubicin, paclitaxel, docetaxel, camptothecin, geldanamycin, daunomycin, gemcitabine, etc. (206). The drug was conjugated to HPMA copolymer via a pH sensitive bond (hydrazone) or lysosomal cleavable tetrapeptide spacer (-GFLG-) (207–209). This section will briefly discuss the architecture, synthesis, and characterization of HPMA copolymer-drug conjugates.

1.9.1 Architectures of HPMA copolymer-drug conjugates

Since polymer conjugates' architectures determine their physicochemical properties, HPMA copolymer-drug conjugates also have been developed using various architectures including linear, branched, cross-linked, brush, etc. (210). Most of the linear HPMA copolymer-drug conjugates were random copolymers with random conformation (211–213). Some of the linear HPMA copolymers were di-block copolymers (214–216). HPMA-based di-block copolymer self-assembled to form a micelle if one block was hydrophilic and the other block was hydrophobic (214,217). Core-cross linking strategies were used to increase the stability of HPMA-based micelles during circulation (218,219). One of the typical examples of branched HPMA copolymer-drug conjugates is the star-shaped HPMA copolymer-doxorubicin (DOX) conjugate, which was formed by grafting poly(amidoamine) (PAMAM) dendrimers with semitelechelic HPMA copolymers bearing DOX (220). HPMA-oligolysine brush polymers have been used for nucleic acid delivery, and the formed polyplex morphology of brush polymers and plasmid DNA impacted nucleic acid transfection efficiency (221).

1.9.2 Preparation of HPMA copolymer-drug conjugates

HPMA copolymer-drug conjugates can be prepared via co-polymerization or polymer-analogous attachment (222,223). No matter which strategy is used for preparing HPMA copolymer-drug conjugates, radical polymerization is one of the most powerful tools to prepare HPMA copolymer-drug conjugates or their precursors. The radical polymerization consists of conventional radical polymerization and reversible-deactivation radical polymerizations (RDRP). The major RDRP includes reversible

addition-fragmentation chain transfer polymerization (RAFT), atom transfer radical polymerization (ATRP), nitroxide radical polymerization (NMP), and ring-opening polymerization (ROMP) (224). Most of the HPMA copolymer-drug conjugates were prepared by conventional radical and RAFT polymerization (223). Before the emergence of RDRP, conventional radical polymerization was the major tool for preparing HPMA copolymer-drug conjugates. However, conventional radical polymerization cannot control the molecular weight distribution, copolymer composition, and macromolecular architecture (225).

The RAFT polymerization was first reported by the scientists at Commonwealth Scientific and Industrial Research Organization (CSIRO) (Australia) in early 1998 (226). The McCormick group first utilized RAFT polymerization to prepare well-controlled HPMA polymers (Mn = 97 kDa, Mw/Mn = 1.07) (227). In addition to controlling the molecular weight and molecular weight distribution, the other advantage of RAFT polymerization is that RAFT polymerization can freely be used to prepare diblock, triblock, even multiblock HPMA copolymer drug conjugates (216,217,228). The limitation of RAFT polymerization is that its success depends upon the selection of the chain transfer agent for the monomers and reaction conditions [211]. The generally accepted RAFT polymerization mechanism is shown in Figure 1.13.

The RAFT polymerization consists of a sequence of steps: initiation, initial equilibrium, re-initiation, main equilibrium, and termination (229). The general initiation procedure starts from the decomposition of azo initiator into two radical fragments, and then reacts with monomer to produce propagating polymeric radical (P_m •) (230). In the initial equilibrium procedure, the P_m • reacts with chain transfer agent (ZC(=S)SR, 1) to

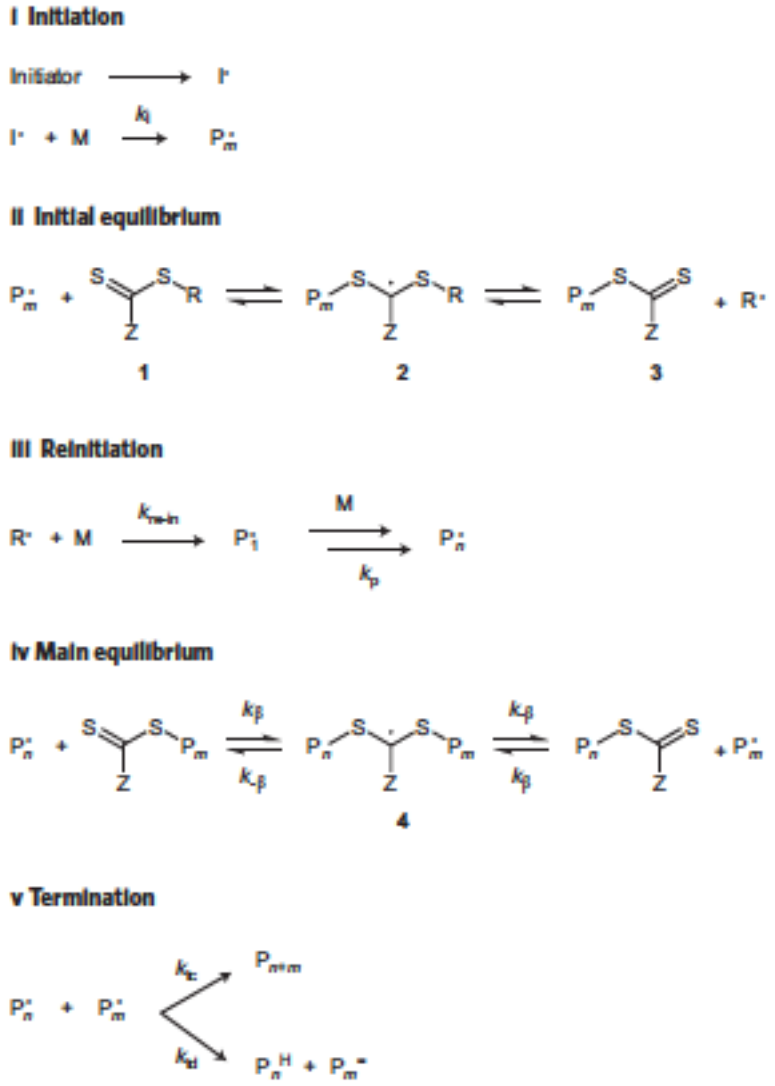

Figure 1.13: Generally accepted mechanism for RAFT polymerization (230).

form an intermediate adduct radical 2 (230). Then the intermediate radical 2 fragments to yield either the starting species or a radical (R•) and a polymeric RAFT agent (S=C(Z)S-P_m) (230). In the reinitiation procedure, the liberated radical (R•) reacts with monomer to form a new propagating radical (P_n •) (231). In the main RAFT equilibrium, propagating radical (P_n •) reacts with polymeric RAFT agent (S=C(Z)S-P_m) to form an intermediate radical 4 (232). The formation and decomposition of intermediate radical 4 is a reversible process. Importantly, the intermediate radical 4 fragment equally in either direction (232). Then all polymer chains have equal opportunities for growth, and thus narrow polydispersities (232). The termination of RAFT polymerization includes two mechanisms: coupling and disproportionation.

1.9.3 Characterization of HPMA copolymer-drug conjugates

The physicochemical properties of HPMA copolymer-drug conjugates determine the conjugates' safety/activity (233). The physicochemical properties of HPMA copolymer-drug conjugates include: molecular weight and molecular weight distribution, hydrodynamic radius, surface charge, functional groups, drug contents, morphology, etc. Size exclusion chromatography with a commercial column is usually used for measuring the molecular weight and molecular weight distribution of HPMA copolymer-drug conjugates (234). The hydrodynamic radius (R_H) of HPMA copolymer-drug conjugate is determined by dynamic light scattering (DLS) (235,236). For example, two HPMA copolymers with weight-average molecular weight (26 ± 2.0 kDa and 52 ± 5.0 kDa) had average hydrodynamic radii 1.4 ± 0.0 nm and 3.3 ± 0.2 nm, respectively [234]. The

morphology of HPMA copolymer drug conjugate core-shell nanoparticles or micelles was further measured with transmission electron microscope (TEM) (221,236).

The mechanism by which DLS can be used to measure polymer conjugates' hydrodynamic radius (R_H) will be briefly introduced. This application is based on the assumption that the conjugate molecules in solution are undergoing Brownian motion (237). The larger the conjugates, the slower the Brownian motion (diffusion velocity) will be. The hydrodynamic radius (R_H) of conjugate is calculated from its diffusion coefficient (D) using the well-known Stokes-Einstein relationship:

$$R_H=(k_BT)/6\pi\eta D$$

where k_B is the Boltzmann constant, T is the absolute temperature, and η is the viscosity of solution (238).

Overall, this section briefly introduced the architecture, preparation, and physico-chemical properties characterization of HPMA copolymer-drug conjugates.

1.10 References

1. Siegel R, Ma J, Zou Z, Jemal A. Cancer statistics, 2014. CA Cancer J Clin. 2014;64:9–29.

2. Wang X, Kruithof-de Julio M, Economides KD, Walker D, Yu H, Halili MV, et al. A luminal epithelial stem cell that is a cell of origin for prostate cancer. Nature. 2009;461:495–500.

3. Abate-Shen C, Shen MM. Molecular genetics of prostate cancer. Genes Dev. 2000;14:2410–34.

4. Shen MM, Abate-Shen C. Molecular genetics of prostate cancer: new prospects for old challenges. Genes Dev. 2010;24:1967–2000.

5. Garber K. A tale of two cells: discovering the origin of prostate cancer. J Natl Cancer Inst. 2010;102:1528–9, 1535.

6. Wojno KJ, Epstein JI. The utility of basal cell-specific anti-cytokeratin antibody (34 beta E12) in the diagnosis of prostate cancer. A review of 228 cases. Am J Surg Pathol. 1995;19:251–60.

7. Choi N, Zhang B, Zhang L, Ittmann M, Xin L. Adult murine prostate basal and luminal cells are self-sustained lineages that can both serve as targets for prostate cancer initiation. Cancer Cell. 2012;21:253–65.

8. Goldstein AS, Huang J, Guo C, Garraway IP, Witte ON. Identification of a cell of origin for human prostate cancer. Science. 2010;329:568–71.

9. Stoyanova T, Cooper AR, Drake JM, Liu X, Armstrong AJ, Pienta KJ, et al. Prostate cancer originating in basal cells progresses to adenocarcinoma propagated by luminal-like cells. Proc Natl Acad Sci U S A. 2013;110:20111–6.

10. Drake CG. Prostate cancer as a model for tumour immunotherapy. Nat Rev Immunol. 2010;10:580–93.

11. Denmeade SR, Isaacs JT. A history of prostate cancer treatment. Nat Rev Cancer. 2002;2:389–96.

12. Trewartha D, Carter K. Advances in prostate cancer treatment. Nat Rev Drug Discov. 2013;12:823–4.

13. Minchinton AI, Tannock IF. Drug penetration in solid tumours. Nat Rev Cancer. 2006;6:583–92.

14. Padera TP, Stoll BR, Tooredman JB, Capen D, di Tomaso E, Jain RK. Pathology: cancer cells compress intratumour vessels. Nature. 2004;427:695.

15. McDonald DM, Baluk P. Significance of blood vessel leakiness in cancer. Cancer Res. 2002;62:5381–5.

16. Hashizume H, Baluk P, Morikawa S, McLean JW, Thurston G, Roberge S, et al. Openings between defective endothelial cells explain tumor vessel leakiness. Am J Pathol. 2000;156:1363–80.

17. Carmeliet P, Jain RK. Angiogenesis in cancer and other diseases. Nature. 2000;407:249–57.

18. Thomlinson RH, Gray LH. The histological structure of some human lung cancers and the possible implications for radiotherapy. Br J Cancer. 1955;9:539–49.

19. Leu AJ, Berk DA, Lymboussaki A, Alitalo K, Jain RK. Absence of functional lymphatics within a murine sarcoma: a molecular and functional evaluation. Cancer Res. 2000;60:4324–7.

20. Helmlinger G, Netti PA, Lichtenbeld HC, Melder RJ, Jain RK. Solid stress inhibits the growth of multicellular tumor spheroids. Nat Biotechnol. 1997;15:778–83.

21. Jeltsch M, Kaipainen A, Joukov V, Meng X, Lakso M, Rauvala H, et al. Hyperplasia of lymphatic vessels in VEGF-C transgenic mice. Science. 1997;276:1423–5.

22. Taddei ML, Giannoni E, Comito G, Chiarugi P. Microenvironment and tumor cell plasticity: an easy way out. Cancer Lett. 2013;341:80–96.

23. Heldin C-H, Rubin K, Pietras K, Ostman A. High interstitial fluid pressure - an obstacle in cancer therapy. Nat Rev Cancer. 2004;4:806–13.

24. Kwon IK, Lee SC, Han B, Park K. Analysis on the current status of targeted drug delivery to tumors. J Control Release. 2012;164:108–14.

25. Kakinuma T, Hwang ST. Chemokines, chemokine receptors, and cancer metastasis. J Leukoc Biol. 2006;79:639–51.

26. Mantovani A. Cancer: Inflaming metastasis. Nature. 2009;457:36–7.

27. Parker C, Milosevic M, Toi A, Sweet J, Panzarella T, Bristow R, et al. Polarographic electrode study of tumor oxygenation in clinically localized prostate cancer. Int J Radiat Oncol Biol Phys. 2004;58:750–7.

28. Leith JT, Quaranto L, Padfield G, Michelson S, Hercbergs A. Radiobiological studies of PC-3 and DU-145 human prostate cancer cells: x-ray sensitivity in vitro and

hypoxic fractions of xenografted tumors in vivo. Int J Radiat Oncol Biol Phys. 1993;25:283–7.

29. Yeh KA, Biade S, Lanciano RM, Brown DQ, Fenning MC, Babb JS, et al. Polarographic needle electrode measurements of oxygen in rat prostate carcinomas: accuracy and reproducibility. Int J Radiat Oncol Biol Phys. 1995;33:111–8.

30. Movsas B, Chapman JD, Greenberg RE, Hanlon AL, Horwitz EM, Pinover WH, et al. Increasing levels of hypoxia in prostate carcinoma correlate significantly with increasing clinical stage and patient age: an Eppendorf pO(2) study. Cancer. 2000;89:2018–24.

31. Movsas B, Chapman JD, Hanlon AL, Horwitz EM, Pinover WH, Greenberg RE, et al. Hypoxia in human prostate carcinoma: an Eppendorf PO2 study. Am J Clin Oncol. 2001;24:458–61.

32. Stewart GD, Gray K, Pennington CJ, Edwards DR, Riddick ACP, Ross JA, et al. Analysis of hypoxia-associated gene expression in prostate cancer: lysyl oxidase and glucose transporter-1 expression correlate with Gleason score. Oncol Rep. 2008;20:1561–7.

33. Vergis R, Corbishley CM, Norman AR, Bartlett J, Jhavar S, Borre M, et al. Intrinsic markers of tumour hypoxia and angiogenesis in localised prostate cancer and outcome of radical treatment: a retrospective analysis of two randomised radiotherapy trials and one surgical cohort study. Lancet Oncol. 2008;9:342–51.

34. Schioppa T, Uranchimeg B, Saccani A, Biswas SK, Doni A, Rapisarda A, et al. Regulation of the chemokine receptor CXCR4 by hypoxia. J Exp Med. 2003;198:1391–402.

35. Ma Y, Liang D, Liu J, Axcrona K, Kvalheim G, Stokke T, et al. Prostate cancer cell lines under hypoxia exhibit greater stem-like properties. PloS One. 2011;6:e29170.

36. Ranasinghe WKB, Xiao L, Kovac S, Chang M, Michiels C, Bolton D, et al. The role of hypoxia-inducible factor 1α in determining the properties of castrate-resistant prostate cancers. PloS One. 2013;8:e54251.

37. Shuman Moss LA, Jensen-Taubman S, Stetler-Stevenson WG. Matrix metalloproteinases: changing roles in tumor progression and metastasis. Am J Pathol. 2012;181:1895–9.

38. Roy R, Yang J, Moses MA. Matrix metalloproteinases as novel biomarkers and potential therapeutic targets in human cancer. J Clin Oncol. 2009;27:5287–97.

39. Kessenbrock K, Plaks V, Werb Z. Matrix metalloproteinases: regulators of the tumor microenvironment. Cell. 2010;141:52–67.

40. Verma RP, Hansch C. Matrix metalloproteinases (MMPs): chemical-biological functions and (Q)SARs. Bioorg Med Chem. 2007;15:2223–68.

41. Morgunova E, Tuuttila A, Bergmann U, Isupov M, Lindqvist Y, Schneider G, et al. Structure of human pro-matrix metalloproteinase-2: activation mechanism revealed. Science. 1999;284:1667–70.

42. Talvensaari-Mattila A, Paakko P, Turpeenniemi-Hujanen T. Matrix metalloproteinase-2 (MMP-2) is associated with survival in breast carcinoma. Br J Cancer. 2003;89:1270–5.

43. Dos Reis ST, Villanova FE, Andrade PM, Pontes J Jr, de Sousa-Canavez JM, Sañudo A, et al. Matrix metalloproteinase-2 polymorphism is associated with prognosis in prostate cancer. Urol Oncol. 2010;28:624–7.

44. Zhang S, Qi L, Li M, Zhang D, Xu S, Wang N, et al. Chemokine CXCL12 and its receptor CXCR4 expression are associated with perineural invasion of prostate cancer. J Exp Clin Cancer Res. 2008;27:62.

45. Zhong W, Han Z, He H, Bi X, Dai Q, Zhu G, et al. CD147, MMP-1, MMP-2 and MMP-9 protein expression as significant prognostic factors in human prostate cancer. Oncology. 2008;75:230–6.

46. Singh S, Singh UP, Grizzle WE, Lillard JW Jr. CXCL12-CXCR4 interactions modulate prostate cancer cell migration, metalloproteinase expression and invasion. Lab Investig J Tech Methods Pathol. 2004;84:1666–76.

47. Morgia G, Falsaperla M, Malaponte G, Madonia M, Indelicato M, Travali S, et al. Matrix metalloproteinases as diagnostic (MMP-13) and prognostic (MMP-2, MMP-9) markers of prostate cancer. Urol Res. 2005;33:44–50.

48. Lilja H. A kallikrein-like serine protease in prostatic fluid cleaves the predominant seminal vesicle protein. J Clin Invest. 1985;76:1899–903.

49. Hillier SM, Kern AM, Maresca KP, Marquis JC, Eckelman WC, Joyal JL, et al. 123I-MIP-1072, a small-molecule inhibitor of prostate-specific membrane antigen, is effective at monitoring tumor response to taxane therapy. J Nucl Med. 2011;52:1087–93.

50. Silver DA, Pellicer I, Fair WR, Heston WD, Cordon-Cardo C. Prostate-specific membrane antigen expression in normal and malignant human tissues. Clin Cancer Res. 1997;3:81–5.

51. Lapidus RG, Tiffany CW, Isaacs JT, Slusher BS. Prostate-specific membrane antigen (PSMA) enzyme activity is elevated in prostate cancer cells. The Prostate. 2000;45:350–4.

52. Ross JS, Sheehan CE, Fisher HAG, Kaufman RP Jr, Kaur P, Gray K, et al. Correlation of primary tumor prostate-specific membrane antigen expression with disease recurrence in prostate cancer. Clin Cancer Res. 2003;9:6357–62.

53. Israeli RS, Powell CT, Corr JG, Fair WR, Heston WD. Expression of the prostate-specific membrane antigen. Cancer Res. 1994;54:1807–11.

54. Schülke N, Varlamova OA, Donovan GP, Ma D, Gardner JP, Morrissey DM, et al. The homodimer of prostate-specific membrane antigen is a functional target for cancer therapy. Proc Natl Acad Sci U S A. 2003;100:12590–5.

55. Davis MI, Bennett MJ, Thomas LM, Bjorkman PJ. Crystal structure of prostate-specific membrane antigen, a tumor marker and peptidase. Proc Natl Acad Sci U S A. 2005;102:5981–6.

56. Bae YH, Park K. Targeted drug delivery to tumors: myths, reality and possibility. J Control Release. 2011;153:198–205.

57. MacEwan SR, Chilkoti A. Harnessing the power of cell-penetrating peptides: activatable carriers for targeting systemic delivery of cancer therapeutics and imaging agents. Wiley Interdiscip Rev Nanomed Nanobiotechnol. 2013;5:31–48.

58. Gerlowski LE, Jain RK. Microvascular permeability of normal and neoplastic tissues. Microvasc Res. 1986;31:288–305.

59. Matsumura Y, Maeda H. A New Concept for Macromolecular Therapeutics in Cancer Chemotherapy: Mechanism of tumoritropic accumulation of proteins and the antitumor agent Smancs. Cancer Res. 1986;46:6387–92.

60. Maeda H, Wu J, Sawa T, Matsumura Y, Hori K. Tumor vascular permeability and the EPR effect in macromolecular therapeutics: a review. J Control Release. 2000;65:271–84.

61. Torchilin V. Tumor delivery of macromolecular drugs based on the EPR effect. Adv Drug Deliv Rev. 2011;63:131–5.

62. Maeda H, Nakamura H, Fang J. The EPR effect for macromolecular drug delivery to solid tumors: Improvement of tumor uptake, lowering of systemic toxicity, and distinct tumor imaging in vivo. Adv Drug Deliv Rev. 2013;65:71–9.

63. Ruoslahti E, Bhatia SN, Sailor MJ. Targeting of drugs and nanoparticles to tumors. J Cell Biol. 2010;188:759–68.

64. Kirpotin DB, Drummond DC, Shao Y, Shalaby MR, Hong K, Nielsen UB, et al. Antibody targeting of long-circulating lipidic nanoparticles does not increase tumor

localization but does increase internalization in animal models. Cancer Res. 2006;66:6732–40.

65. Bartlett DW, Su H, Hildebrandt IJ, Weber WA, Davis ME. Impact of tumor-specific targeting on the biodistribution and efficacy of siRNA nanoparticles measured by multimodality in vivo imaging. Proc Natl Acad Sci U S A. 2007;104:15549–54.

66. Choi CHJ, Alabi CA, Webster P, Davis ME. Mechanism of active targeting in solid tumors with transferrin-containing gold nanoparticles. Proc Natl Acad Sci U S A. 2010;107:1235–40.

67. Xia W, Low PS. Folate-targeted therapies for cancer. J Med Chem. 2010;53:6811–24.

68. Van der Meel R, Vehmeijer LJC, Kok RJ, Storm G, van Gaal EVB. Ligand-targeted particulate nanomedicines undergoing clinical evaluation: current status. Adv Drug Deliv Rev. 2013;65:1284–98.

69. Byrne JD, Betancourt T, Brannon-Peppas L. Active targeting schemes for nanoparticle systems in cancer therapeutics. Adv Drug Deliv Rev. 2008;60:1615–26.

70. Daniels TR, Delgado T, Rodriguez JA, Helguera G, Penichet ML. The transferrin receptor part I: Biology and targeting with cytotoxic antibodies for the treatment of cancer. Clin Immunol. 2006;121:144–58.

71. Tavano L, Muzzalupo R, Mauro L, Pellegrino M, Andò S, Picci N. Transferrin-conjugated pluronic niosomes as a new drug delivery system for anticancer therapy. Langmuir. 2013;29:12638–46.

72. Bertrand N, Wu J, Xu X, Kamaly N, Farokhzad OC. Cancer nanotechnology: the impact of passive and active targeting in the era of modern cancer biology. Adv Drug Deliv Rev. 2014;66:2–25.

73. Acharya S, Dilnawaz F, Sahoo SK. Targeted epidermal growth factor receptor nanoparticle bioconjugates for breast cancer therapy. Biomaterials. 2009;30:5737–50.

74. Bhattacharyya S, Bhattacharya R, Curley S, McNiven MA, Mukherjee P. Nanoconjugation modulates the trafficking and mechanism of antibody induced receptor endocytosis. Proc Natl Acad Sci U S A. 2010;107:14541–6.

75. Xu J, Gattacceca F, Amiji M. Biodistribution and pharmacokinetics of EGFR-targeted thiolated gelatin nanoparticles following systemic administration in pancreatic tumor-bearing mice. Mol Pharm. 2013;10:2031–44.

76. Mickler FM, Möckl L, Ruthardt N, Ogris M, Wagner E, Bräuchle C. Tuning nanoparticle uptake: live-cell imaging reveals two distinct endocytosis mechanisms

mediated by natural and artificial EGFR targeting ligand. Nano Lett. 2012;12:3417–23.

77. Klutz K, Schaffert D, Willhauck MJ, Grünwald GK, Haase R, Wunderlich N, et al. Epidermal growth factor receptor-targeted (131)I-therapy of liver cancer following systemic delivery of the sodium iodide symporter gene. Mol Ther. 2011;19:676–85.

78. Low PS, Henne WA, Doorneweerd DD. Discovery and development of folic-acid-based receptor targeting for imaging and therapy of cancer and inflammatory diseases. Acc Chem Res. 2008;41:120–9.

79. Weitman SD, Lark RH, Coney LR, Fort DW, Frasca V, Zurawski VR Jr, et al. Distribution of the folate receptor GP38 in normal and malignant cell lines and tissues. Cancer Res. 1992;52:3396–401.

80. Lee RJ, Low PS. Folate-mediated tumor cell targeting of liposome-entrapped doxorubicin in vitro. Biochim Biophys Acta. 1995;1233:134–44.

81. Wang X, Li J, Wang Y, Koenig L, Gjyrezi A, Giannakakou P, et al. A folate receptor-targeting nanoparticle minimizes drug resistance in a human cancer model. ACS Nano. 2011;5:6184–94.

82. Gao Z-G, Tian L, Hu J, Park I-S, Bae YH. Prevention of metastasis in a 4T1 murine breast cancer model by doxorubicin carried by folate conjugated pH sensitive polymeric micelles. J Control Release. 2011;152:84–9.

83. Arima H, Yoshimatsu A, Ikeda H, Ohyama A, Motoyama K, Higashi T, et al. Folate-PEG-appended dendrimer conjugate with α-cyclodextrin as a novel cancer cell-selective siRNA delivery carrier. Mol Pharm. 2012;9:2591–604.

84. Danhier F, Le Breton A, Préat V. RGD-based strategies to target alpha(v) beta(3) integrin in cancer therapy and diagnosis. Mol Pharm. 2012;9:2961–73.

85. Desgrosellier JS, Cheresh DA. Integrins in cancer: biological implications and therapeutic opportunities. Nat Rev Cancer. 2010;10:9–22.

86. Ruoslahti E, Pierschbacher MD. New perspectives in cell adhesion: RGD and integrins. Science. 1987;238:491–7.

87. Arap W, Pasqualini R, Ruoslahti E. Cancer treatment by targeted drug delivery to tumor vasculature in a mouse model. Science. 1998;279:377–80.

88. Murphy EA, Majeti BK, Barnes LA, Makale M, Weis SM, Lutu-Fuga K, et al. Nanoparticle-mediated drug delivery to tumor vasculature suppresses metastasis. Proc Natl Acad Sci U S A. 2008;105:9343–8.

89. Hood JD, Bednarski M, Frausto R, Guccione S, Reisfeld RA, Xiang R, et al. Tumor regression by targeted gene delivery to the neovasculature. Science. 2002;296:2404–7.

90. Kim WJ, Yockman JW, Lee M, Jeong JH, Kim Y-H, Kim SW. Soluble Flt-1 gene delivery using PEI-g-PEG-RGD conjugate for anti-angiogenesis. J Control Release. 2005;106:224–34.

91. Kim WJ, Yockman JW, Jeong JH, Christensen LV, Lee M, Kim Y-H, et al. Anti-angiogenic inhibition of tumor growth by systemic delivery of PEI-g-PEG-RGD/pCMV-sFlt-1 complexes in tumor-bearing mice. J Control Release. 2006;114:381–8.

92. Mitra A, Mulholland J, Nan A, McNeill E, Ghandehari H, Line BR. Targeting tumor angiogenic vasculature using polymer-RGD conjugates. J Control Release. 2005;102:191–201.

93. Borgman MP, Ray A, Kolhatkar RB, Sausville EA, Burger AM, Ghandehari H. Targetable HPMA copolymer-aminohexylgeldanamycin conjugates for prostate cancer therapy. Pharm Res. 2009;26:1407–18.

94. Borgman MP, Aras O, Geyser-Stoops S, Sausville EA, Ghandehari H. Biodistribution of HPMA copolymer-aminohexylgeldanamycin-RGDfK conjugates for prostate cancer drug delivery. Mol Pharm. 2009;6:1836–47.

95. Greish K, Ray A, Bauer H, Larson N, Malugin A, Pike D, et al. Anticancer and antiangiogenic activity of HPMA copolymer-aminohexylgeldanamycin-RGDfK conjugates for prostate cancer therapy. J Control Release. 2011;151:263–70.

96. Choi HS, Gibbs SL, Lee JH, Kim SH, Ashitate Y, Liu F, et al. Targeted zwitterionic near-infrared fluorophores for improved optical imaging. Nat Biotechnol. 2013;31:148–53.

97. Mura S, Nicolas J, Couvreur P. Stimuli-responsive nanocarriers for drug delivery. Nat Mater. 2013;12:991–1003.

98. Seruga B, Ocana A, Tannock IF. Drug resistance in metastatic castration-resistant prostate cancer. Nat Rev Clin Oncol. 2011;8:12–23.

99. Kyle AH, Huxham LA, Yeoman DM, Minchinton AI. Limited tissue penetration of taxanes: a mechanism for resistance in solid tumors. Clin Cancer Res. 2007;13:2804–10.

100. Tannock IF, Lee CM, Tunggal JK, Cowan DSM, Egorin MJ. Limited penetration of anticancer drugs through tumor tissue: a potential cause of resistance of solid tumors to chemotherapy. Clin Cancer Res. 2002;8:878–84.

101. Primeau AJ, Rendon A, Hedley D, Lilge L, Tannock IF. The Distribution of the anticancer drug Doxorubicin in relation to blood vessels in solid tumors. Clin Cancer Res. 2005;11:8782–8.

102. Frankel AD, Pabo CO. Cellular uptake of the tat protein from human immunodeficiency virus. Cell. 1988;55:1189–93.

103. Green M, Loewenstein PM. Autonomous functional domains of chemically synthesized human immunodeficiency virus tat trans-activator protein. Cell. 1988;55:1179–88.

104. Vivès E, Brodin P, Lebleu B. A truncated HIV-1 Tat protein basic domain rapidly translocates through the plasma membrane and accumulates in the cell nucleus. J Biol Chem. 1997;272:16010–7.

105. Schwarze SR, Ho A, Vocero-Akbani A, Dowdy SF. In vivo protein transduction: delivery of a biologically active protein into the mouse. Science. 1999;285:1569–72.

106. Van de Waterbeemd H, Camenisch G, Folkers G, Chretien JR, Raevsky OA. Estimation of blood-brain barrier crossing of drugs using molecular size and shape, and H-bonding descriptors. J Drug Target. 1998;6:151–65.

107. Derossi D, Joliot AH, Chassaing G, Prochiantz A. The third helix of the Antennapedia homeodomain translocates through biological membranes. J Biol Chem. 1994;269:10444–50.

108. Derossi D, Calvet S, Trembleau A, Brunissen A, Chassaing G, Prochiantz A. Cell internalization of the third helix of the Antennapedia homeodomain is receptor-independent. J Biol Chem. 1996;271:18188–93.

109. Pooga M, Hällbrink M, Zorko M, Langel U. Cell penetration by transportan. FASEB J. 1998;12:67–77.

110. Elliott G, O'Hare P. Intercellular trafficking and protein delivery by a herpesvirus structural protein. Cell. 1997;88:223–33.

111. Montrose K, Yang Y, Sun X, Wiles S, Krissansen GW. Xentry, a new class of cell-penetrating peptide uniquely equipped for delivery of drugs. Sci Rep. 2013;3:1661.

112. Karagiannis ED, Urbanska AM, Sahay G, Pelet JM, Jhunjhunwala S, Langer R, et al. Rational design of a biomimetic cell penetrating peptide library. ACS Nano. 2013;7:8616–26.

113. Futaki S, Suzuki T, Ohashi W, Yagami T, Tanaka S, Ueda K, et al. Arginine-rich peptides. An abundant source of membrane-permeable peptides having potential as carriers for intracellular protein delivery. J Biol Chem. 2001;276:5836–40.

114. Som A, Tezgel AO, Gabriel GJ, Tew GN. Self-activation in de novo designed mimics of cell-penetrating peptides. Angew Chem Int Ed Engl. 2011;50:6147–50.

115. Wender PA, Mitchell DJ, Pattabiraman K, Pelkey ET, Steinman L, Rothbard JB. The design, synthesis, and evaluation of molecules that enable or enhance cellular uptake: peptoid molecular transporters. Proc Natl Acad Sci U S A. 2000;97:13003–8.

116. Watkins CL, Brennan P, Fegan C, Takayama K, Nakase I, Futaki S, et al. Cellular uptake, distribution and cytotoxicity of the hydrophobic cell penetrating peptide sequence PFVYLI linked to the proapoptotic domain peptide PAD. J Control Release. 2009;140:237–44.

117. Pujals S, Giralt E. Proline-rich, amphipathic cell-penetrating peptides. Adv Drug Deliv Rev. 2008;60:473–84.

118. Stanzl EG, Trantow BM, Vargas JR, Wender PA. Fifteen years of cell-penetrating, guanidinium-rich molecular transporters: basic science, research tools, and clinical applications. Acc Chem Res. 2013;46:2944–54.

119. Lättig-Tünnemann G, Prinz M, Hoffmann D, Behlke J, Palm-Apergi C, Morano I, et al. Backbone rigidity and static presentation of guanidinium groups increases cellular uptake of arginine-rich cell-penetrating peptides. Nat Commun. 2011;2:453.

120. Sandgren S, Cheng F, Belting M. Nuclear targeting of macromolecular polyanions by an HIV-Tat derived peptide. Role for cell-surface proteoglycans. J Biol Chem. 2002;277:38877–83.

121. Nakase I, Akita H, Kogure K, Gräslund A, Langel U, Harashima H, et al. Efficient intracellular delivery of nucleic acid pharmaceuticals using cell-penetrating peptides. Acc Chem Res. 2012;45:1132–9.

122. Wallbrecher R, Verdurmen WPR, Schmidt S, Bovee-Geurts PH, Broecker F, Reinhardt A, et al. The stoichiometry of peptide-heparan sulfate binding as a determinant of uptake efficiency of cell-penetrating peptides. Cell Mol Life Sci. 2013.

123. Wender PA, Galliher WC, Goun EA, Jones LR, Pillow TH. The design of guanidinium-rich transporters and their internalization mechanisms. Adv Drug Deliv Rev. 2008;60:452–72.

124. Fonseca SB, Pereira MP, Kelley SO. Recent advances in the use of cell-penetrating peptides for medical and biological applications. Adv Drug Deliv Rev. 2009;61:953–64.

125. Wang F, Wang Y, Zhang X, Zhang W, Guo S, Jin F. Recent progress of cell-penetrating peptides as new carriers for intracellular cargo delivery. J Control Release. 2013;174C:126–36.

126. Jones AT, Sayers EJ. Cell entry of cell penetrating peptides: tales of tails wagging dogs. J Control Release. 2012;161:582–91.

127. Kosuge M, Takeuchi T, Nakase I, Jones AT, Futaki S. Cellular internalization and distribution of arginine-rich peptides as a function of extracellular peptide concentration, serum, and plasma membrane associated proteoglycans. Bioconjug Chem. 2008;19:656–64.

128. Duchardt F, Fotin-Mleczek M, Schwarz H, Fischer R, Brock R. A comprehensive model for the cellular uptake of cationic cell-penetrating peptides. Traffic. 2007;8:848–66.

129. Dubikovskaya EA, Thorne SH, Pillow TH, Contag CH, Wender PA. Overcoming multidrug resistance of small-molecule therapeutics through conjugation with releasable octaarginine transporters. Proc Natl Acad Sci U S A. 2008;105:12128–33.

130. Lindgren M, Rosenthal-Aizman K, Saar K, Eiríksdóttir E, Jiang Y, Sassian M, et al. Overcoming methotrexate resistance in breast cancer tumour cells by the use of a new cell-penetrating peptide. Biochem Pharmacol. 2006;71:416–25.

131. Jiang T, Olson ES, Nguyen QT, Roy M, Jennings PA, Tsien RY. Tumor imaging by means of proteolytic activation of cell-penetrating peptides. Proc Natl Acad Sci U S A. 2004;101:17867–72.

132. Nguyen QT, Olson ES, Aguilera TA, Jiang T, Scadeng M, Ellies LG, et al. Surgery with molecular fluorescence imaging using activatable cell-penetrating peptides decreases residual cancer and improves survival. Proc Natl Acad Sci U S A. 2010;107:4317–22.

133. Zhu L, Kate P, Torchilin VP. Matrix metalloprotease 2-responsive multifunctional liposomal nanocarrier for enhanced tumor targeting. ACS Nano. 2012;6:3491–8.

134. Koren E, Apte A, Jani A, Torchilin VP. Multifunctional PEGylated 2C5-immunoliposomes containing pH-sensitive bonds and TAT peptide for enhanced tumor cell internalization and cytotoxicity. J Control Release. 2012;160:264–73.

135. Apte A, Koren E, Koshkaryev A, Torchilin VP. Doxorubicin in TAT peptide-modified multifunctional immunoliposomes demonstrates increased activity against both drug-sensitive and drug-resistant ovarian cancer models. Cancer Biol Ther. 2013;15.

136. Sethuraman VA, Bae YH. TAT peptide-based micelle system for potential active targeting of anti-cancer agents to acidic solid tumors. J Control Release. 2007;118:216–24.

137. Jin E, Zhang B, Sun X, Zhou Z, Ma X, Sun Q, et al. Acid-active cell-penetrating peptides for in vivo tumor-targeted drug delivery. J Am Chem Soc. 2013;135:933–40.

138. Goun EA, Shinde R, Dehnert KW, Adams-Bond A, Wender PA, Contag CH, et al. Intracellular cargo delivery by an octaarginine transporter adapted to target prostate cancer cells through cell surface protease activation. Bioconjug Chem. 2006;17:787–96.

139. Hansen MB, van Gaal E, Minten I, Storm G, van Hest JCM, Löwik DWPM. Constrained and UV-activatable cell-penetrating peptides for intracellular delivery of liposomes. J Control Release. 2012;164:87–94.

140. Shamay Y, Adar L, Ashkenasy G, David A. Light induced drug delivery into cancer cells. Biomaterials. 2011;32:1377–86.

141. Macewan SR, Chilkoti A. Digital switching of local arginine density in a genetically encoded self-assembled polypeptide nanoparticle controls cellular uptake. Nano Lett. 2012;12:3322–8.

142. Myrberg H, Zhang L, Mäe M, Langel U. Design of a tumor-homing cell-penetrating peptide. Bioconjug Chem. 2008;19:70–5.

143. Tan M, Lan K-H, Yao J, Lu C-H, Sun M, Neal CL, et al. Selective inhibition of ErbB2-overexpressing breast cancer in vivo by a novel TAT-based ErbB2-targeting signal transducers and activators of transcription 3-blocking peptide. Cancer Res. 2006;66:3764–72.

144. Youn P, Chen Y, Furgeson DY. A myristoylated cell-penetrating peptide bearing a transferrin receptor-targeting sequence for neuro-targeted siRNA delivery. Mol Pharm. 2014;11:486–95.

145. Teesalu T, Sugahara KN, Kotamraju VR, Ruoslahti E. C-end rule peptides mediate neuropilin-1-dependent cell, vascular, and tissue penetration. Proc Natl Acad Sci U S A. 2009;106:16157–62.

146. Sugahara KN, Teesalu T, Karmali PP, Kotamraju VR, Agemy L, Girard OM, et al. Tissue-penetrating delivery of compounds and nanoparticles into tumors. Cancer Cell. 2009;16:510–20.

147. Teesalu T, Sugahara KN, Ruoslahti E. Tumor-penetrating peptides. Front Oncol. 2013;3:216.

148. Pang H-B, Braun GB, She Z-G, Kotamraju VR, Sugahara KN, Teesalu T, et al. A free cysteine prolongs the half-life of a homing peptide and improves its tumor-penetrating activity. J Control Release. 2014;175:48–53.

149. Yu K-F, Zhang W-Q, Luo L-M, Song P, Li D, Du R, et al. The antitumor activity of a doxorubicin loaded, iRGD-modified sterically-stabilized liposome on B16-F10 melanoma cells: in vitro and in vivo evaluation. Int J Nanomedicine. 2013;8:2473–85.

150. Liu Y, Ji M, Wong MK, Joo K-I, Wang P. Enhanced Therapeutic Efficacy of iRGD-Conjugated Crosslinked Multilayer Liposomes for Drug Delivery. BioMed Res Int. 2013. DOI:10.1155/2013/378380.

151. Song W, Li M, Tang Z, Li Q, Yang Y, Liu H, et al. Methoxypoly(ethylene glycol)-block-poly(L-glutamic acid)-loaded cisplatin and a combination with iRGD for the treatment of non-small-cell lung cancers. Macromol Biosci. 2012;12:1514–23.

152. Wang X, Zhen X, Wang J, Zhang J, Wu W, Jiang X. Doxorubicin delivery to 3D multicellular spheroids and tumors based on boronic acid-rich chitosan nanoparticles. Biomaterials. 2013;34:4667–79.

153. Su S, Wang H, Liu X, Wu Y, Nie G. iRGD-coupled responsive fluorescent nanogel for targeted drug delivery. Biomaterials. 2013;34:3523–33.

154. Tian Y, Li S, Song J, Ji T, Zhu M, Anderson GJ, et al. A doxorubicin delivery platform using engineered natural membrane vesicle exosomes for targeted tumor therapy. Biomaterials. 2014;35:2383–90.

155. Ren Y, Cheung HW, von Maltzhan G, Agrawal A, Cowley GS, Weir BA, et al. Targeted tumor-penetrating siRNA nanocomplexes for credentialing the ovarian cancer oncogene ID4. Sci Transl Med. 2012;4:147ra112.

156. Wang C-F, Mäkilä EM, Kaasalainen MH, Liu D, Sarparanta MP, Airaksinen AJ, et al. Copper-free azide-alkyne cycloaddition of targeting peptides to porous silicon nanoparticles for intracellular drug uptake. Biomaterials. 2014;35:1257–66.

157. Zhu Z, Xie C, Liu Q, Zhen X, Zheng X, Wu W, et al. The effect of hydrophilic chain length and iRGD on drug delivery from poly(ε-caprolactone)-poly(N-vinylpyrrolidone) nanoparticles. Biomaterials. 2011;32:9525–35.

158. Shen J, Meng Q, Sui H, Yin Q, Zhang Z, Yu H, et al. iRGD Conjugated TPGS mediates codelivery of Paclitaxel and Survivin shRNA for the reversal of lung cancer resistance. Mol Pharm. 2013. DOI: 10.1021/mp400576f

159. Ye Y, Zhu L, Ma Y, Niu G, Chen X. Synthesis and evaluation of new iRGD peptide analogs for tumor optical imaging. Bioorg Med Chem Lett. 2011;21:1146–50.

160. Ye Y, Xu B, Nikiforovich GV, Bloch S, Achilefu S. Exploring new near-infrared fluorescent disulfide-based cyclic RGD peptide analogs for potential integrin-targeted optical imaging. Bioorg Med Chem Lett. 2011;21:2116–20.

161. Alves NJ, Champion MM, Stefanick JF, Handlogten MW, Moustakas DT, Shi Y, et al. Selective photocrosslinking of functional ligands to antibodies via the conserved nucleotide binding site. Biomaterials. 2013;34:5700–10.

162. Alberici L, Roth L, Sugahara KN, Agemy L, Kotamraju VR, Teesalu T, et al. De novo design of a tumor-penetrating peptide. Cancer Res. 2013;73:804–12.

163. Balkwill F. Cancer and the chemokine network. Nat Rev Cancer. 2004;4:540–50.

164. Furusato B, Mohamed A, Uhlén M, Rhim JS. CXCR4 and cancer. Pathol Int. 2010;60:497–505.

165. Zlotnik A, Yoshie O. Chemokines: a new classification system and their role in immunity. Immunity. 2000;12:121–7.

166. Lazennec G, Richmond A. Chemokines and chemokine receptors: new insights into cancer-related inflammation. Trends Mol Med. 2010;16:133–44.

167. Dealwis C, Fernandez EJ, Thompson DA, Simon RJ, Siani MA, Lolis E. Crystal structure of chemically synthesized [N33A] stromal cell-derived factor 1alpha, a potent ligand for the HIV-1 "fusin" coreceptor. Proc Natl Acad Sci U S A. 1998;95:6941–6.

168. Wong D, Korz W. Translating an antagonist of chemokine receptor CXCR4: from bench to bedside. Clin Cancer Res. 2008;14:7975–80.

169. Sun Y-X, Wang J, Shelburne CE, Lopatin DE, Chinnaiyan AM, Rubin MA, et al. Expression of CXCR4 and CXCL12 (SDF-1) in human prostate cancers (PCa) in vivo. J Cell Biochem. 2003;89:462–73.

170. Müller A, Homey B, Soto H, Ge N, Catron D, Buchanan ME, et al. Involvement of chemokine receptors in breast cancer metastasis. Nature. 2001;410:50–6.

171. Scotton CJ, Wilson JL, Milliken D, Stamp G, Balkwill FR. Epithelial cancer cell migration: a role for chemokine receptors? Cancer Res. 2001;61:4961–5.

172. Su L, Zhang J, Xu H, Wang Y, Chu Y, Liu R, et al. Differential expression of CXCR4 is associated with the metastatic potential of human non-small cell lung cancer cells. Clin Cancer Res. 2005;11:8273–80.

173. Ying J, Xu Q, Zhang G, Liu B, Zhu L. The expression of CXCL12 and CXCR4 in gastric cancer and their correlation to lymph node metastasis. Med Oncol. 2012;29:1716–22.

174. Teicher BA, Fricker SP. CXCL12 (SDF-1)/CXCR4 pathway in cancer. Clin Cancer Res. 2010;16:2927–31.

175. Orimo A, Gupta PB, Sgroi DC, Arenzana-Seisdedos F, Delaunay T, Naeem R, et al. Stromal fibroblasts present in invasive human breast carcinomas promote tumor growth and angiogenesis through elevated SDF-1/CXCL12 secretion. Cell. 2005;121:335–48.

176. Gil M, Seshadri M, Komorowski MP, Abrams SI, Kozbor D. Targeting CXCL12/CXCR4 signaling with oncolytic virotherapy disrupts tumor vasculature and inhibits breast cancer metastases. Proc Natl Acad Sci U S A. 2013;110:E1291–1300.

177. Liekens S, Schols D, Hatse S. CXCL12-CXCR4 axis in angiogenesis, metastasis and stem cell mobilization. Curr Pharm Des. 2010;16:3903–20.

178. Gupta GP, Massagué J. Cancer metastasis: building a framework. Cell. 2006;127:679–95.

179. Fidler IJ. The pathogenesis of cancer metastasis: the “seed and soil” hypothesis revisited. Nat Rev Cancer. 2003;3:453–8.

180. Paget S. The distribution of secondary growths in cancer of the breast. 1889. Cancer Metastasis Rev. 1989;8:98–101.

181. Liang Z, Yoon Y, Votaw J, Goodman MM, Williams L, Shim H. Silencing of CXCR4 blocks breast cancer metastasis. Cancer Res. 2005;65:967–71.

182. Zlotnik A, Burkhardt AM, Homey B. Homeostatic chemokine receptors and organ-specific metastasis. Nat Rev Immunol. 2011;11:597–606.

183. Brave M, Farrell A, Ching Lin S, Ocheltree T, Pope Miksinski S, Lee S-L, et al. FDA review summary: Mozobil in combination with granulocyte colony-stimulating factor to mobilize hematopoietic stem cells to the peripheral blood for collection and subsequent autologous transplantation. Oncology. 2010;78:282–8.

184. Rosenkilde MM, Gerlach L-O, Hatse S, Skerlj RT, Schols D, Bridger GJ, et al. Molecular mechanism of action of monocyclam versus bicyclam non-peptide antagonists in the CXCR4 chemokine receptor. J Biol Chem. 2007;282:27354–65.

185. Gerlach LO, Skerlj RT, Bridger GJ, Schwartz TW. Molecular interactions of cyclam and bicyclam non-peptide antagonists with the CXCR4 chemokine receptor. J Biol Chem. 2001;276:14153–60.

186. Gerlach LO, Jakobsen JS, Jensen KP, Rosenkilde MR, Skerlj RT, Ryde U, et al. Metal ion enhanced binding of AMD3100 to Asp262 in the CXCR4 receptor. Biochemistry (Mosc). 2003;42:710–7.

187. Hendrix CW, Flexner C, MacFarland RT, Giandomenico C, Fuchs EJ, Redpath E, et al. Pharmacokinetics and safety of AMD-3100, a novel antagonist of the CXCR-4 chemokine receptor, in human volunteers. Antimicrob Agents Chemother. 2000;44:1667–73.

188. Debnath B, Xu S, Grande F, Garofalo A, Neamati N. Small molecule inhibitors of CXCR4. Theranostics. 2013;3:47–75.

189. Wong RSY, Bodart V, Metz M, Labrecque J, Bridger G, Fricker SP. Comparison of the potential multiple binding modes of bicyclam, monocylam, and noncyclam small-molecule CXC chemokine receptor 4 inhibitors. Mol Pharmacol. 2008;74:1485–95.

190. O'Boyle G, Swidenbank I, Marshall H, Barker CE, Armstrong J, White SA, et al. Inhibition of CXCR4-CXCL12 chemotaxis in melanoma by AMD11070. Br J Cancer. 2013;108:1634–40.

191. Parameswaran R, Yu M, Lim M, Groffen J, Heisterkamp N. Combination of drug therapy in acute lymphoblastic leukemia with a CXCR4 antagonist. Leukemia. 2011;25:1314–23.

192. Liang Z, Zhan W, Zhu A, Yoon Y, Lin S, Sasaki M, et al. Development of a unique small molecule modulator of CXCR4. PloS One. 2012;7:e34038.

193. Shu H-KG, Yoon Y, Hong S, Xu K, Gao H, Hao C, et al. Inhibition of the CXCL12/CXCR4-axis as preventive therapy for radiation-induced pulmonary fibrosis. PloS One. 2013;8:e79768.

194. Ziarek JJ, Liu Y, Smith E, Zhang G, Peterson FC, Chen J, et al. Fragment-based optimization of small molecule CXCL12 inhibitors for antagonizing the CXCL12/CXCR4 interaction. Curr Top Med Chem. 2012;12:2727–40.

195. Huang EH, Singh B, Cristofanilli M, Gelovani J, Wei C, Vincent L, et al. A CXCR4 antagonist CTCE-9908 inhibits primary tumor growth and metastasis of breast cancer. J Surg Res. 2009;155:231–6.

196. Kwong J, Kulbe H, Wong D, Chakravarty P, Balkwill F. An antagonist of the chemokine receptor CXCR4 induces mitotic catastrophe in ovarian cancer cells. Mol Cancer Ther. 2009;8:1893–905.

197. Porvasnik S, Sakamoto N, Kusmartsev S, Eruslanov E, Kim W-J, Cao W, et al. Effects of CXCR4 antagonist CTCE-9908 on prostate tumor growth. The Prostate. 2009;69:1460–9.

198. Tamamura H, Omagari A, Oishi S, Kanamoto T, Yamamoto N, Peiper SC, et al. Pharmacophore identification of a specific CXCR4 inhibitor, T140, leads to development of effective anti-HIV agents with very high selectivity indexes. Bioorg Med Chem Lett. 2000;10:2633–7.

199. Burger JA, Peled A. CXCR4 antagonists: targeting the microenvironment in leukemia and other cancers. Leukemia. 2008;23:43–52.

200. Tamamura H, Hiramatsu K, Kusano a S, Terakubo S, Yamamoto N, Trent JO, et al. Synthesis of potent CXCR4 inhibitors possessing low cytotoxicity and improved biostability based on T140 derivatives. Org Biomol Chem. 2003;1:3656–62.

201. Tamamura H, Omagari A, Hiramatsu K, Gotoh K, Kanamoto T, Xu Y, et al. Development of specific CXCR4 inhibitors possessing high selectivity indexes as well as complete stability in serum based on an anti-HIV peptide T140. Bioorg Med Chem Lett. 2001;11:1897–902.

202. Tamamura H, Hori A, Kanzaki N, Hiramatsu K, Mizumoto M, Nakashima H, et al. T140 analogs as CXCR4 antagonists identified as anti-metastatic agents in the treatment of breast cancer. FEBS Lett. 2003;550:79–83.

203. Duncan R, Vicent MJ. Polymer therapeutics-prospects for 21st century: the end of the beginning. Adv Drug Deliv Rev. 2013;65:60–70.

204. Kopeček J, Bažilová H. Poly[N-(2-hydroxypropyl)methacrylamide]—I. Radical polymerization and copolymerization. Eur Polym J. 1973;9:7–14.

205. Obereigner B, Burešová M, Vrána A, Kopeček J. Preparation of polymerizable derivatives of N-(4-aminobenzenesulfonyl)-N-(n-butylurea). J Polym Sci Polym Symp. 1979;66:41–52.

206. Minko T. HPMA copolymers for modulating cellular signaling and overcoming multidrug resistance. Adv Drug Deliv Rev. 2010;62:192–202.

207. Ray A, Larson N, Pike DB, Grüner M, Naik S, Bauer H, et al. Comparison of active and passive targeting of docetaxel for prostate cancer therapy by HPMA copolymer-RGDfK conjugates. Mol Pharm. 2011;8:1090–9.

208. Etrych T, Subr V, Laga R, Říhová B, Ulbrich K. Polymer conjugates of doxorubicin bound through an amide and hydrazone bond: Impact of the carrier structure onto synergistic action in the treatment of solid tumours. Eur J Pharm. 2014;58:1–12.

209. Malugin A, Kopečková P, Kopeček J. HPMA copolymer-bound doxorubicin induces apoptosis in ovarian carcinoma cells by the disruption of mitochondrial function. Mol Pharm. 2006;3:351–61.

210. Qiu LY, Bae YH. Polymer architecture and drug delivery. Pharm Res. 2006;23:1–30.

211. Shi J, Johnson RN, Schellinger JG, Carlson PM, Pun SH. Reducible HPMA-co-oligolysine copolymers for nucleic acid delivery. Int J Pharm. 2012;427:113–22.

212. Ren K, Dusad A, Yuan F, Yuan H, Purdue PE, Fehringer EV, et al. Macromolecular prodrug of dexamethasone prevents particle-induced peri-implant osteolysis with reduced systemic side effects. J Control Release Off J Control Release Soc. 2014;175:1–9.

213. Nakamura H, Etrych T, Chytil P, Ohkubo M, Fang J, Ulbrich K, et al. Two step mechanisms of tumor selective delivery of N-(2-hydroxypropyl)methacrylamide copolymer conjugated with pirarubicin via an acid-cleavable linkage. J Control Release. 2014;174:81–7.

214. Allmeroth M, Moderegger D, Gündel D, Buchholz H-G, Mohr N, Koynov K, et al. PEGylation of HPMA-based block copolymers enhances tumor accumulation in vivo: a quantitative study using radiolabeling and positron emission tomography. J Control Release. 2013;172:77–85.

215. Duvall CL, Convertine AJ, Benoit DSW, Hoffman AS, Stayton PS. Intracellular delivery of a proapoptotic peptide via conjugation to a RAFT synthesized endosomolytic polymer. Mol Pharm. 2010;7:468–76.

216. Qin Z, Liu W, Li L, Guo L, Yao C, Li X. Galactosylated N-2-hydroxypropyl methacrylamide-b-N-3-guanidinopropyl methacrylamide block copolymers as hepatocyte-targeting gene carriers. Bioconjug Chem. 2011;22:1503–12.

217. Barz M, Armiñán A, Canal F, Wolf F, Koynov K, Frey H, et al. P(HPMA)-block-P(LA) copolymers in paclitaxel formulations: polylactide stereochemistry controls micellization, cellular uptake kinetics, intracellular localization and drug efficiency. J Control Release. 2012;163:63–74.

218. Zhou Z, Li L, Yang Y, Xu X, Huang Y. Tumor targeting by pH-sensitive, biodegradable, cross-linked N-(2-hydroxypropyl) methacrylamide copolymer micelles. Biomaterials. 2014;35:6622–35.

219. Wei R, Cheng L, Zheng M, Cheng R, Meng F, Deng C, et al. Reduction-responsive disassemblable core-cross-linked micelles based on poly(ethylene glycol)-b-poly(N-2-hydroxypropyl methacrylamide)-lipoic acid conjugates for triggered intracellular anticancer drug release. Biomacromolecules. 2012;13:2429–38.

220. Etrych T, Kovář L, Strohalm J, Chytil P, Říhová B, Ulbrich K. Biodegradable star HPMA polymer-drug conjugates: Biodegradability, distribution and anti-tumor efficacy. J Control Release. 2011;154:241–8.

221. Shi J, Choi JL, Chou B, Johnson RN, Schellinger JG, Pun SH. Effect of polyplex morphology on cellular uptake, intracellular trafficking, and transgene expression. ACS Nano. 2013;7:10612–20.

222. Nuhn L, Barz M, Zentel R. New Perspectives of HPMA-based Copolymers Derived by Post-Polymerization Modification. Macromol Biosci. 2014;14:607–18.

223. Kopeček J, Kopečková P. HPMA copolymers: origins, early developments, present, and future. Adv Drug Deliv Rev. 2010;62:122–49.

224. Matyjaszewski K. Atom Transfer Radical Polymerization (ATRP): Current Status and Future Perspectives. Macromolecules. 2012;45:4015–39.

225. Moad G, Rizzardo E, Thang SH. Toward Living Radical Polymerization. Acc Chem Res. 2008;41:1133–42.

226. Le TP, Moad G, Rizzardo E, Thang SH. Polymerization with living characteristics. 2010. Patent: US7714075 B1.

227. Scales CW, Vasilieva YA, Convertine AJ, Lowe AB, McCormick CL. Direct, controlled synthesis of the nonimmunogenic, hydrophilic polymer, poly(N-(2-hydroxypropyl)methacrylamide) via RAFT in aqueous media. Biomacromolecules. 2005;6:1846–50.

228. Treat NJ, Smith D, Teng C, Flores JD, Abel BA, York AW, et al. Guanidine-Containing Methacrylamide (Co)polymers via aRAFT: Toward a Cell Penetrating Peptide Mimic. ACS Macro Lett. 2012;1:100–4.

229. Moad G, Rizzardo E, Thang SH. Radical addition–fragmentation chemistry in polymer synthesis. Polymer. 2008;49:1079–131.

230. Semsarilar M, Perrier S. “Green” reversible addition-fragmentation chain-transfer (RAFT) polymerization. Nat Chem. 2010;2:811–20.

231. Chong Y. K., Le TPT, Moad G, Rizzardo E, Thang SH. A more versatile route to block copolymers and other polymers of complex architecture by living radical polymerization: The RAFT Process. Macromolecules. 1999;32:2071–4.

232. York AW, Kirkland SE, McCormick CL. Advances in the synthesis of amphiphilic block copolymers via RAFT polymerization: stimuli-responsive drug and gene delivery. Adv Drug Deliv Rev. 2008;60:1018–36.

233. Duncan R. Development of HPMA copolymer-anticancer conjugates: clinical experience and lessons learnt. Adv Drug Deliv Rev. 2009;61:1131–48.

234. Liu J, Kopečková P, Pan H, Sima M, Bühler P, Wolf P, et al. Prostate-cancer-targeted N-(2-hydroxypropyl)methacrylamide copolymer/docetaxel conjugates. Macromol Biosci. 2012;12:412–22.

235. Sadekar S, Ray A, Janàt-Amsbury M, Peterson CM, Ghandehari H. Comparative biodistribution of PAMAM dendrimers and HPMA copolymers in ovarian-tumor-bearing mice. Biomacromolecules. 2011;12:88–96.

236. Jäger E, Jäger A, Chytil P, Etrych T, Říhová B, Giacomelli FC, et al. Combination chemotherapy using core-shell nanoparticles through the self-assembly of HPMA-based copolymers and degradable polyester. J Control Release. 2013;165:153–61.

237. Yu Z, Reid JC, Yang Y-P. Utilizing dynamic light scattering as a process analytical technology for protein folding and aggregation monitoring in vaccine manufacturing. J Pharm Sci. 2013;102:4284–90.

238. Kostka L, Konák Č, Šubr V, Špírková M, Addadi Y, Neeman M, et al. Removable nanocoatings for siRNA polyplexes. Bioconjug Chem. 2011;22:169–79.

CHAPTER 2

TARGETED HPMA COPOLYMER-DOCETAXEL CONJUGATES FOR PROSTATE-SPECIFIC MEMBRANE ANTIGEN EXPRESSING PROSTATE CANCER TREATMENT [1]

2.1 Summary

Combination of targeted delivery and controlled release is a powerful technique for cancer treatment. Here, we describe the design, synthesis, structure validation, and biological properties of targeted and nontargeted *N*-(2-hydroxypropyl)methacrylamide (HPMA) copolymer docetaxel conjugates. Docetaxel (DTX) was conjugated to HPMA copolymer via a tetrapeptide spacer (-GFLG-). 3-(1,3-dicarboxypropyl)-ureido]pentanedioic acid (DUPA) was used as the targeting moiety to actively deliver DTX for treatment of Prostate-Specific Membrane Antigen (PSMA) expressing prostate cancer. Short and long spacer DUPA monomers were prepared, and four HPMA copolymer-DTX conjugates (nontargeted, two targeted with short spacer, and targeted with long spacer) were prepared via Reversible Addition-Fragmentation Chain Transfer

---

[1] This chapter has been modified with permission from the following publication: Peng ZH, Sima M, Salama ME, Kopečková P, Kopeček J. Spacer length impacts the efficacy of targeted docetaxel conjugates in prostate-specific membrane antigen expressing prostate cancer. *J Drug Target*. 2013, 21(10): 968-80.

(RAFT) copolymerization. Following confirmation of PSMA expression on C4-2 cell line, the DTX conjugates' in vitro cytotoxicity was tested against C4-2 tumor cells and their anticancer efficacies were assessed in nude mice bearing *s.c.* human prostate adenocarcinoma C4-2 xenografts. The in vivo results show that the spacer length between targeting moieties and HPMA copolymer backbone can significantly affect the treatment efficacy of DTX conjugates against C4-2 tumor bearing nu/nu mice. Moreover, histological analysis indicated that the DUPA targeted DTX conjugate with longer spacer had no toxicity in major organs of treated mice.

2.2 Introduction

Prostate cancer is the most common malignant cancer and the second leading cause of cancer-related death among men in the United States. It was estimated that 238,590 Americans will be newly diagnosed with prostate cancer and 29,720 Americans will die from prostate cancer in 2013 (1). Although several therapeutic strategies, including radical prostatectomy, androgen deprivation, chemotherapy, bone-directed therapy, and radiation therapy have been available for prostate cancer treatment, they are ineffective against advanced prostate cancer and also associated with severe side effects (2). DTX, the first line chemotherapy for prostate cancer treatment, is associated with fatigue, nausea or vomiting or both, alopecia, diarrhea, nail changes, sensory neuropathy, anorexia, changes in taste, stomatitis, dyspnea, tearing, peripheral edema, and epistaxis (3). One of the major reasons for these side effects is that DTX distributes indiscriminately into all cells of the body and causes damage to malignant and healthy cells alike. Although DTX benefit for patients with metastatic castration-resistant prostate

cancer (CRPC), the overall survival improvement is mild (~ 2.5 months) (4). The significant mortality and morbidity of prostate cancer urgently require development of novel, safer, and more potent formulations of DTX therapeutics. The recently developed nano-medicine technology can help to mitigate the off-target and dose limiting effects of small molecule therapeutics and enhance antitumor efficacy through polymer conjugate delivery system, especially decoration of the conjugate with a targeting ligand can provide the most effective therapy (5,6).

The most appealing antigen for treatment and diagnosis of prostate cancer is prostate-specific membrane antigen (PSMA) because: (*i*) PSMA presented at the cell surface but not shed into the circulation; (*ii*) PSMA enzyme activity in prostate cancer sample was about 10-fold higher than that in benign prostatic hyperplasia (BPH) and normal tissue (7); (*iii*) its expression on prostate cancer was about 1000-fold higher than the minimal expression in other tissues such as kidney, proximal small intestine, salivary gland (8); (*iii*) its expression increased with disease progression (9).

Therefore, several classes of ligands including aptamers (10–12), antibodies (13–16), peptides (17,18), and small molecules (19,20) have been developed to deliver therapeutics (21) and imaging agents (22–24) for diagnosis and treatment of PSMA expressing prostate cancer. Phosphoramidate and glutamate ureas are two major classes of small-molecule ligands that can bind PSMA selectively and with high affinity (25,26). However, the majority of their applications focus on imaging prostate cancer on murine models (22–24). Few efforts have used small-molecule anti-PSMA ligands for treatment studies in mice models, maybe due to the challenging chemistry for small molecule ligands modification (21,27,28).

In the present study, we choose 3-(1,3-dicarboxypropyl)-ureido]pentanedioic acid (DUPA) as the targeting moiety because of its favorable characteristics: multivalency, low cost, reproducible chemical synthesis, nonimmunogenicity, high permeability in solid tumors, and fast clearance from normal tissue. DUPA belongs to a class of glutamate ureas (19,20); it is comparatively easy to modify the R group at C-2 position. We therefore reasoned that we might be able to incorporate a spacer at this position to connect the polymer-drug conjugate and DUPA targeting moiety. Because the active site of PSMA is about 20 Å depth in the PSMA, we hypothesized a reasonable length of spacer is required between DUPA targeting moiety and drug carrier (29,30).

Based on the above considerations, we were interested in using DUPA as the targeting moiety to actively deliver DTX for treatment of PSMA expressing prostate cancer. DUPA and DTX were incorporated into the uncharged, hydrophilic, and biocompatible HPMA copolymer via a suitable spacer length linker and lysosomally degradable spacer (-GFLG-), respectively (31,32). We hypothesized that conjugation of the targeting moiety DUPA to HPMA copolymer will enhance the ligands opportunity to bind to PSMA by increasing the circulation time of DUPA. The overall goal of the combination of targeted delivery and controlled release of DTX is to enhance its antitumor efficacy and lower its toxicity. Herein, we designed, synthesized, and characterized polymerizable derivatives of DTX and DUPA (short and long spacer). We synthesized the DUPA targeted or nontargeted HPMA copolymer - DTX conjugates and assessed their anticancer efficacies in nude mice bearing *s.c.* human prostate adenocarcinoma C4-2 xenografts. We also tested the toxicity of DTX conjugates by monitoring mice body weight changes and using a histological assay.

2.3 Materials and Methods

2.3.1 Materials

DTX was purchased from AK Scientific (Union City, CA). *N*-(3-aminopropyl) methacrylamide (APMA) was purchased from PolySciences (Warrington, PA). Initiator 2,2'-azobis(2,4-dimethylvaleronitrile) (V-65) and azobisisobutyronitrile (AIBN) were purchased from Wako Pure Chemicals (Richmond, VA). *L*-glutamate di-*tert*-butyl ester hydrochloride, *O*-(7-azabenzotriazol-1-yl)-*N*,*N*,*N*',*N*'-tetramethyluronium hexafluoro - phosphate (HATU), 4-dimethylaminopyridine (DMAP), and 1-ethyl-3-(3-dimethylaminopropyl)carbodiimide hydrochloride (EDC) were purchased from AAPPTec (Louisville, KY). L-glutamic acid benzyl ester α-tert-butyl ester was purchased from Chem-Impex International (Wood Dale, IL). 1-(9H-fluoren-9-yl)-3-oxo-2,7,10,13,16,19,22,25,28,31,34,37,40-tridecaoxa-4-azatritetracontan-43-oic acid (Fmoc-NH-EG_{12}-COOH) was purchased from Peptides International (Louisville, KY). Monomer HPMA (33), *N*-methacryloyl-Gly-Phe-Leu-Gly-OH (MA-GFLG-OH) (34), and chain transfer agent 4-cyanopentanoic acid dithiobenzoate (CPAD) (35) were prepared as described in the literature. All other reagents were purchased from Sigma Aldrich (St. Louis, MO) if not otherwise mentioned.

2.3.2 Synthesis of *N*-methacryloylglycylphenylalanylleucylglycyl-Docetaxel

The scheme for synthesis of *N*-methacryloylglycylphenylalanylleucylglycyl Docetaxel (MA-GFLG-DTX) is shown in Figure 2.1. A solution of MA-GFLG-OH (920.5 mg, 2 mmol), DTX (807.4 mg, 1 mmol), and DMAP (146.6 mg, 1.2 mmol) in dichloromethane (DCM) (5 mL) was cooled to 0°C in an ice bath, then EDC (230 mg, 1.2

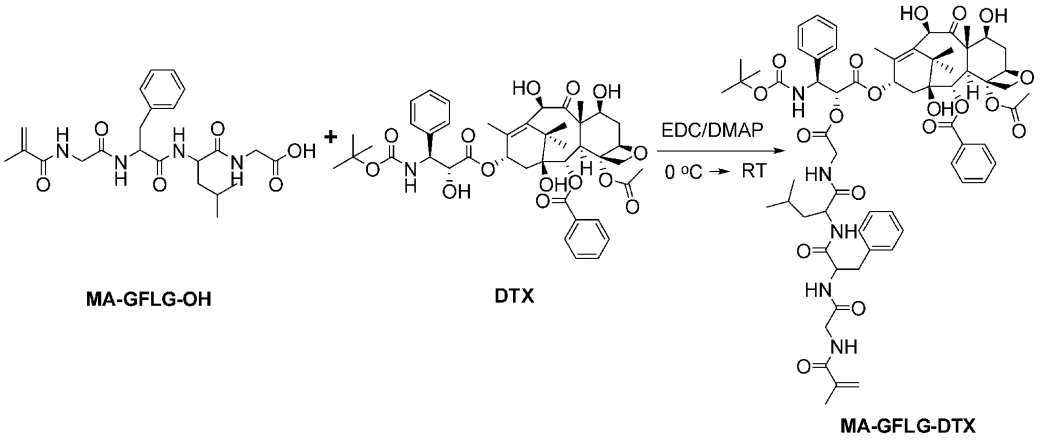

Figure 2.1: Synthetic scheme of monomer MA-GFLG-DTX.

mmol) was added at 0°C. The reaction mixture was stirred at 0°C for 2 h, then allowed to warm to room temperature and stirred at room temperature for additional 22 h. The reaction mixture was washed with water three times, brine once, and dried over anhydrous sodium sulfate. After removing the solvent under reduced pressure, the crude residue was purified by column chromatography (silica gel 60 Å, 200-400 mesh; ethyl acetate: hexane = 1:4, 1:1, 100% ethyl acetate) to obtain 800 mg pure product with 64% yield. The structure of the product was validated by matrix assisted laser desorption/ionization-time of flight (MALDI-TOF) mass spectroscopy (MS) (Figure 2.2). MALDI-TOF MS: calcd for $C_{66}H_{83}N_5NaO_{19}$ ($[M + Na]^+$) 1273.4, found 1273.8; calcd for $C_{66}H_{83}N_5KO_{19}$ ($[M + K]^+$), 1289.5, found 1289.8.

2.3.3 Synthesis of (3S,7S)-17-methyl-5,10,16-trioxo-4,6,11,15-tetraazaoctadec-17-ene-1,3,7-tricarboxylic acid

The synthesis procedure of (3S,7S)-17-methyl-5,10,16-trioxo-4,6,11,15-tetraazaoctadec-17-ene-1,3,7-tricarboxylic acid (MA-DUPA) is schematically shown in Figure 2.3. Numbers of compounds used in the description below also relate to Figure 2.3.

2.3.3.1 Synthesis of ((S)-5-benzyl 1-tert-butyl 2-(3-((S)-1,5-di-tert-butoxy-1,5-dioxopentan-2-yl)ureido) pentanedioate) (Compound 4)

To a dried three-neck flask was added *L*-glutamate di-*tert*-butyl ester hydrochloride (**1**; 2.5 g, 8.45 mmol) and 100 mL of DCM under nitrogen atmosphere. After the solution was cooled to -65 ^{o}C, triphosgene (**2**; 830 mg, 2.8 mmol) and 2.5 mL of triethylamine were added. Then this solution was stirred for 5 h and temperature

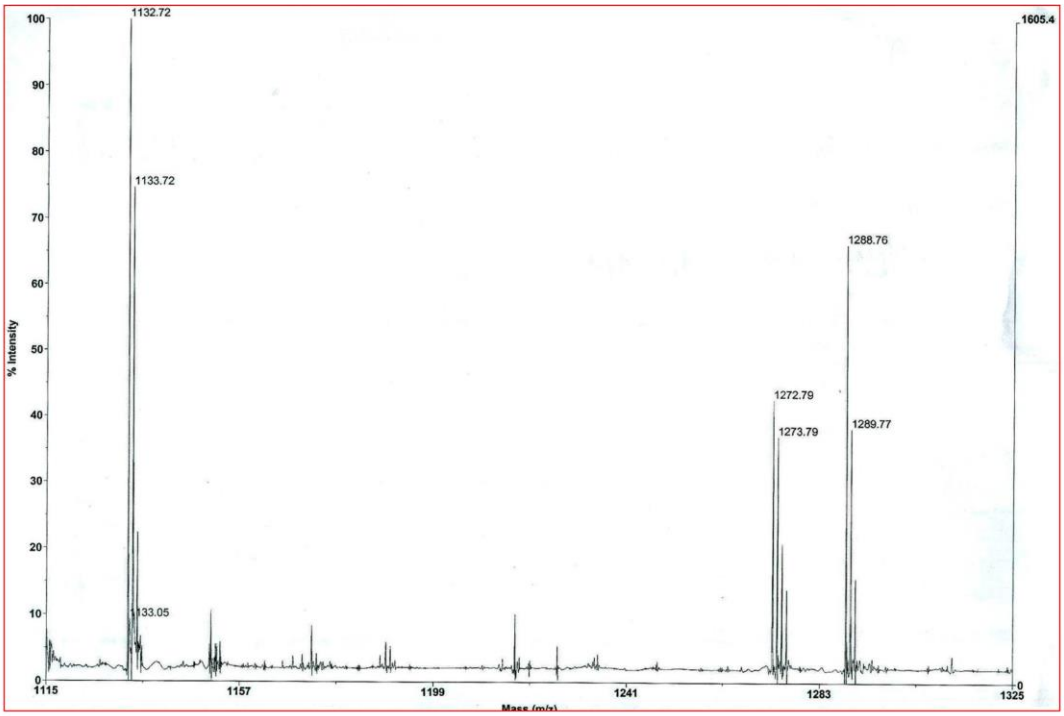

Figure 2.2: Mass spectrum of monomer MA-GFLG-DTX.

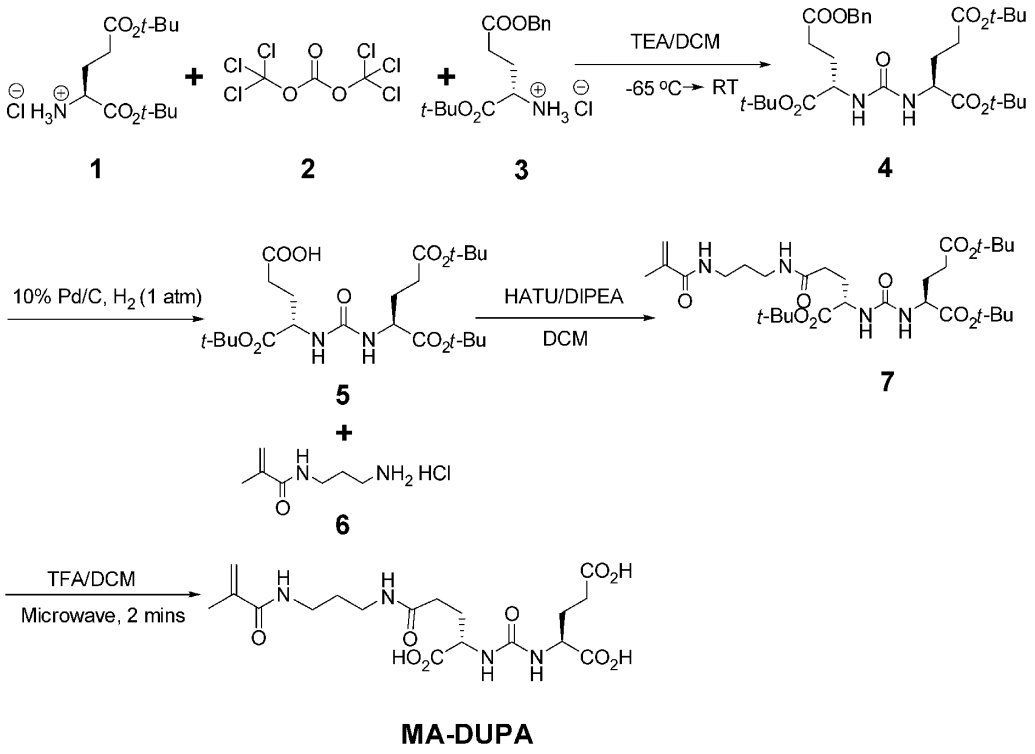

Figure 2.3: Scheme for synthesis of monomer MA-DUPA.

gradually raised from -65 ^{o}C to 10 ^{o}C under the protection of nitrogen. The solution was recooled to -65 ^{o}C before adding a solution of L-Glu(OBn)-O^{t}Bu (**3**; 3 g, 9.1 mmol) and triethylamine (1.5 mL) in DCM (50 mL). The reaction mixture was allowed to increase to room temperature over a period of 2 h and stirred at room temperature overnight. The reaction was quenched with 1 M HCl, and the organic layer was washed with water, brine, and dried over anhydrous sodium sulfate. The crude product was purified using flash chromatography to obtain 2.95 g (60.3%) of product as colorless oil.

2.3.3.2 Synthesis of (S)-5-*tert*-butoxy-4-(3-((S)-1,5-di-tert-butoxy-1,5-dioxopentan-2-yl)ureido)-5-oxopentanoic acid (Compound 5)

((S)-5-benzyl 1-*tert*-butyl 2-(3-((S)-1,5-di-tert-butoxy-1, 5-dioxopentan-2-yl)ureido) pentanedioate) (**4**; 1 g, 1.73 mmol) was dissolved in 30 mL of DCM, then 10% Pd/C (200 mg) was added into this solution. The reaction mixture was hydrogenated at 1 atm for 28 h at room temperature. Pd/C was filtered through a Celite pad and washed with DCM. The crude product was purified by using flash chromatography (silica gel; hexane: ethyl acetate = 4:1, 2:1, 1:1) to obtain the desired product as white solid (590 mg, 70% yield). The product was checked with ^{1}H NMR (Figure 2.4A) and MS (Figure 2.4B). ^{1}H NMR ($CDCl_3$): δ 6.0 (d, J = 8.4 Hz, 1H); 5.52 (d, J = 8.4 Hz, 1H); 4.51-4.42 (m, 1H); 4.34-4.28 (m, 1H); 2.47-2.35 (m, 2H); 2.34-2.26 (m, 2H); 2.18-2.04 (m, 2H); 1.94-1.78 (m, 2H); 1.48 (s, 9H), 1.45 (s, 9H); 1.42 (s, 9H). High resolution mass spectrometry (HRMS) (ESI+): calcd for $C_{23}H_{40}N_2O_9Na$ $[M+Na]^+$, 511.2631; found, 511.2643.

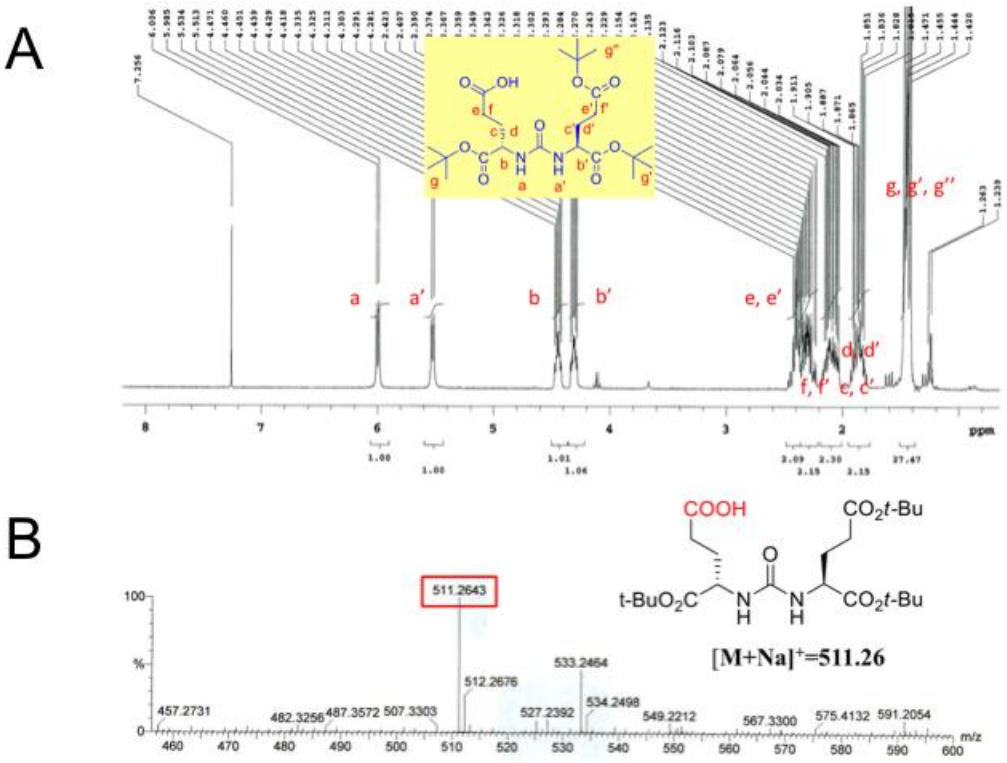

Figure 2.4: Mass (A) and ^{1}H NMR (B) spectra of (S)-5-*tert*-butoxy-4-(3-((S)-1,5-di-*tert*-butoxy-1,5-dioxopentan-2-yl)ureido) -5-oxopentanoic acid (Compound 5)

2.3.3.3 Synthesis of (3S, 7S)-tri-*tert*-butyl 17-methyl-5,10,16-trioxo-4,6,11,15-tetraazaoctadec-17-ene-1,3,7-tricarboxylate (Compound 7)

(S)-5-tert-butoxy-4-(3-((S)-1,5-di-*tert*-butoxy-1,5-dioxopentan-2-yl)ureido)-5-oxopentanoic acid (**5;** 817 mg, 1.67 mmol), APMA (**6**; 329 mg, 1.84 mmol), HATU (700 mg, 1.84 mmol), *N*, *N*-diisopropylethylamine (DIPEA) (321 μL, 1.84 mmol), and DCM were added into 50 mL flask, then this mixture was stirred at room temperature overnight. Water was added into this mixture, then the organic phase was washed with water and brine. Then the organic phase was dried over anhydrous sodium sulfate, filtered, and concentrated under vacuum. The crude product was loaded on silica gel and was purified using flash chromatography (silica gel; hexane: ethyl acetate=1:1; 100% of ethyl acetate; 30% methanol in DCM) to obtain 841 mg (yield = 82.2%) of product. The product was characterized with ^{1}H NMR (Figure 2.5A) and MS (Figure 2.5B). ^{1}H NMR (400 MHz, D_2O): δ 7.29 (t, *J* = 6 Hz, *J* = 6.4 Hz, 1H), 7.02 (t, *J* = 6 Hz, *J* = 6.4 Hz, 1H), 5.79 (s, 1H), 5.57 (d, *J* = 8 Hz, 1H), 5.47 (d, *J* = 8 Hz, 1H), 5.33 (s, 1H), 4.32-4.25 (m, 2H), 3.38-3.26 (m, 4H), 2.39-2.22 (m, 4H), 2.20-2.02 (m, 2H), 1.98 (s, 3H), 1.85-1.75 (m, 2H), 1.72-1.64 (m, 2H), 1.47 (s, 9H), 1.44 (s, 9H); 1.42 (s, 9H). HRMS (ESI+): calcd for $C_{30}H_{52}N_4O_9Na$ $[M+Na]^+$, 635.3632; found, 635.3641.

2.3.3.4 Deprotection of compound 7 to produce MA-DUPA

To a microwave reaction tube was added (3S, 7S)-tri-*tert*-butyl 17-methyl-5,10,16-trioxo-4,6,11,15-tetraazaoctadec-17-ene-1,3,7-tricarboxylate (**7**; 150 mg, 0.245 mmol), 1 mL of DCM, 2 mL of trifluoroacetic acid (TFA), and stirrer bar. The tube was sealed and subjected to microwave irradiation (Biotage, Charlotte, NC) at 70 ^{o}C (150 W)

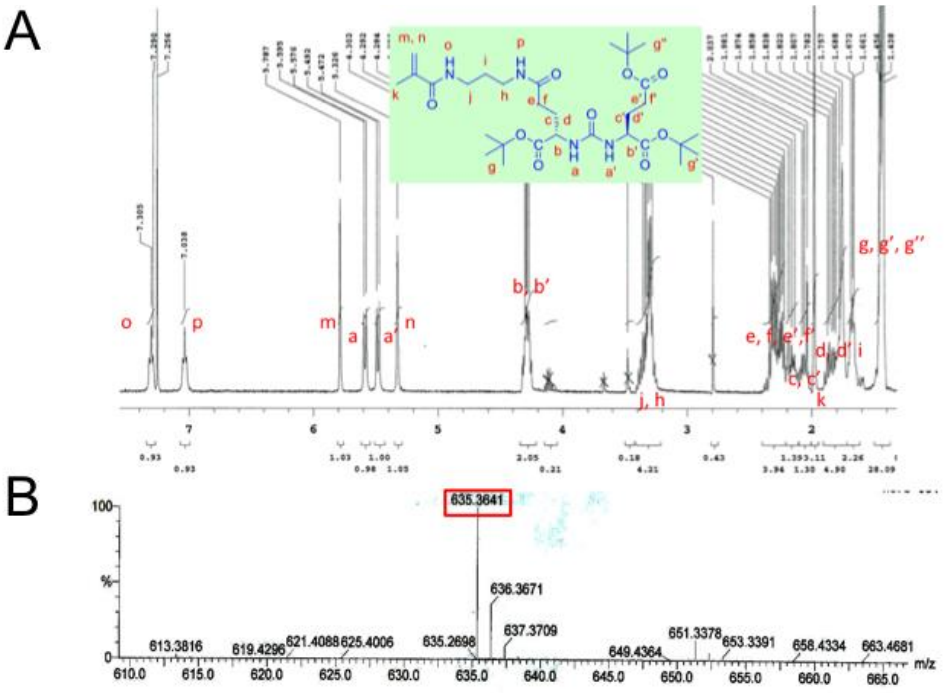

Figure 2.5: ^{1}H NMR (A) and mass (B) spectra of (3S, 7S)-tri-*tert*-butyl 17-methyl-5,10,16-trioxo-4,6,11,15-tetraazaoctadec-17-ene-1,3,7-tricarboxylate (Compound 7).

for 2.5 min. After being cooled to room temperature and concentrated under reduced pressure, the crude product was precipitated in diethyl ether. After being dried under air and purified with HPLC, 79.3 mg (72.9%) of pure product was obtained. The product was characterized with ^{1}H NMR (Figure 2.6A) and MS (Figure 2.6B). ^{1}H NMR (400 MHz, D_2O): δ 5.51 (s, 1H), 5.27 (s, 1H), 4.10 (dd, *J* = 9.2 Hz, 5.2 Hz, 1H), 4.03 (dd, *J* = 9.2 Hz, 4.4 Hz, 1H), 3.10 (t, *J* = 7.2 Hz, 2H), 3.05 (t, *J* = 6 Hz, 2H), 2.35 (t, *J* = 6 Hz, 2H), 2.20 (t, *J* = 6.8 Hz, 2H), 2.08-1.96 (m, 2H), 1.86-1.76 (m, 2H), 1.75 (s, 3H), 1.60-1.52 (m, 2H). MS (ESI+): calcd for $C_{18}H_{28}N_4NaO_9$ ($[M + Na]^+$) 467.2, found 467.3.

2.3.4 Synthesis of (3S,7S)-57-methyl-5,10,50,56-tetraoxo 14,17,20,23,26,29,32, 35,38,41, 44,47-dodecaoxa-4,6,11,51,55-pentaazaoctapentacont-57-ene-1,3,7-tricarboxylic acid (MA-EG_{12}-DUPA)

The synthesis procedure of (3S,7S)-57-methyl-5,10,50,56-tetraoxo-14,17,20,23,26,29, 32,35,38,41,44,47-dodecaoxa-4,6,11,51,55-pentaazaoctapentacont-57-ene-1,3,7-tricarboxylic acid (MA-EG_{12}-DUPA) is schematically shown in Figure 2.7. Numbers of compounds used in the description below also relate to Figure 2.7.

2.3.4.1 Synthesis of 1-amino-*N*-(3-methacrylamidopropyl)-3,6,9,12,15,18,21,24,27,30, 33,36-dodecaoxanonatriacontan-39-amide (MA-EG_{12}-NH_2)

To a carefully dried three-neck flask was added Fmoc-NH-EG_{12}-COOH (**8**; 90 mg, 0.11 mmol), HATU (82 mg, 0.22 mmol), and 2 mL DCM, and then the mixture was stirred for about 2 h. Then APMA (**6**; 38 mg, 0.22 mmol) and DIPEA (56 μL, 0.33 mmol) were added and stirred overnight. The crude product was washed with water three times,

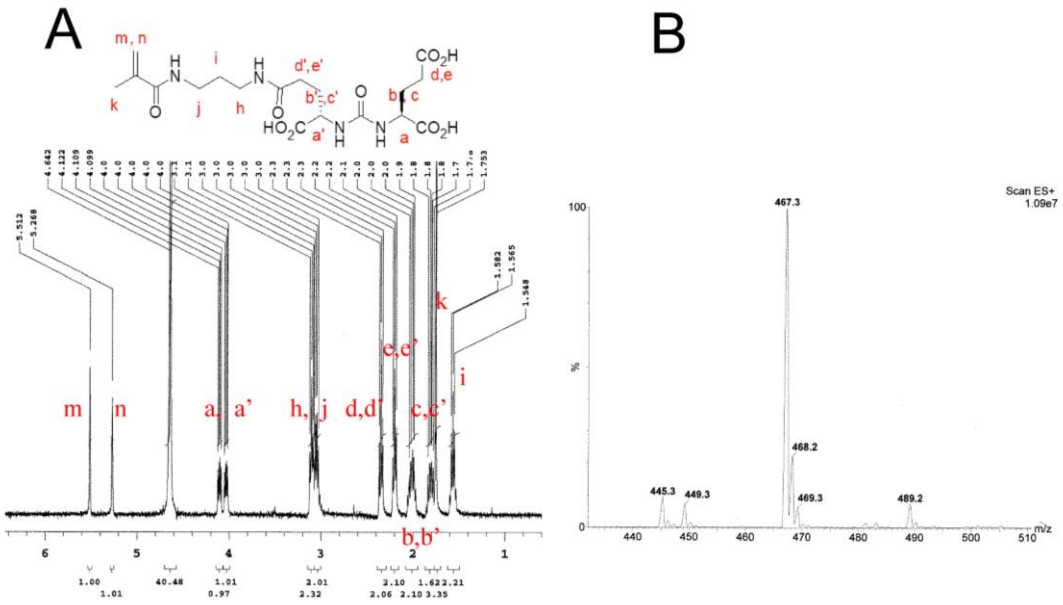

Figure 2.6: ^{1}H NMR (A) and mass spectra (B) of monomer MA-DUPA

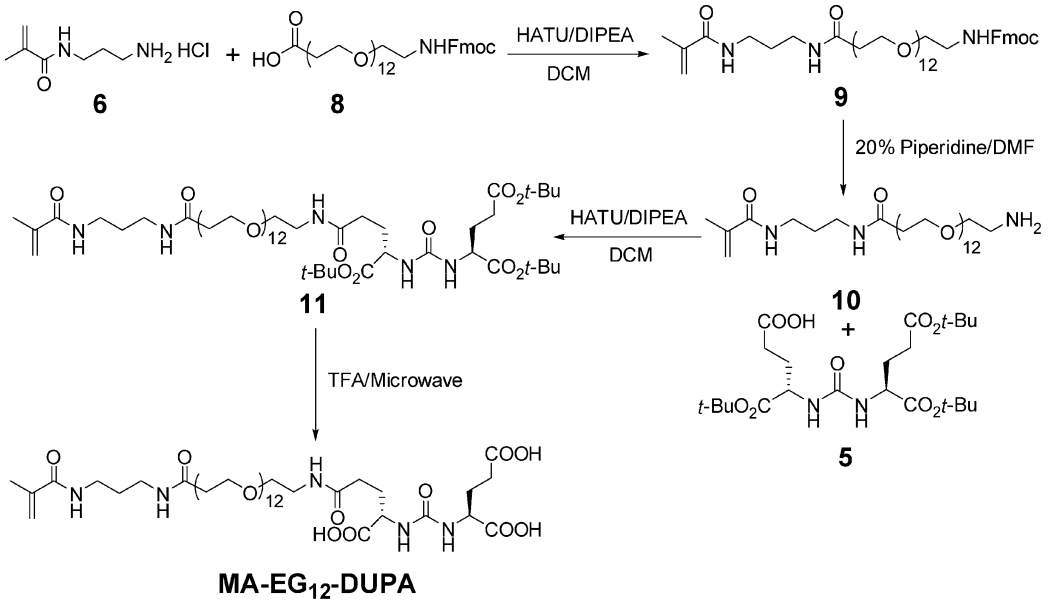

Figure 2.7: Synthetic scheme and structure of monomer MA-EG_{12}-DUPA.

brine once, and dried over anhydrous sodium sulfate. The product MA-EG_{12}-NHFmoc (**9,** 43 mg) was obtained with a yield 41%.

The obtained 43 mg of MA-EG_{12}-NHFmoc was redissolved in a mixture of DMF (1 mL) and piperidine (0.25 mL), then this mixture was stirred at room temperature for about 8 h. After removing the solvent, the remaining crude product was purified with flash chromatography on silica gel using methanol/DCM as eluent to provide the product MA-EG_{12}-NH_2 (**10**; 10 mg, 33%).

2.3.4.2 Synthesis of (3S,7S) tri-*tert*-butyl 57-methyl-5,10,50,56-tetraoxo-14,17,20,23,26,29,32,35,38,41,44,47-dodecaoxa-4,6,11,51,55-pentaazaoctapentacont-57-ene-1,3,7-tricarboxylate (MA-EG_{12}-DUPA(tri-*tert*-butyl); 11)

To a carefully dried three-neck flask was added (S)-5-*tert*-butoxy-4-(3-((S)-1,5-di-*tert*-butoxy-1,5-dioxopentan-2-yl)ureido)-5-oxopentanoic acid (**5**; 658.5 mg, 1.35 mmol), HATU (512.4 mg, 1.35 mmol), and 2 mL DCM, then the mixture was stirred for about 30 min. Then MA-EG_{12}-NH_2 (**10**; 500 mg, 0.67 mmol) and DIPEA (352 μL, 2.02 mmol) were added and stirred overnight. After removing the solvent, the crude product was purified with silica gel column with gradient solvent to afford 600 mg of desired products with the yield of 81.3%. The product was characterized with mass spectroscopy (Figure 2.8). TOF-MS (ESI+): calcd for $C_{57}H_{106}N_5O_{22}$ ($[M + H]^+$), 1212.7, found 1212.8; calcd for $C_{57}H_{109}N_6O_{22}$ ($[M + NH_4]^+$), 1229.8, found 1229.8; calcd for $C_{57}H_{105}N_5NaO_{22}$ ($[M + Na]^+$), 1234.7, found 1234.7.

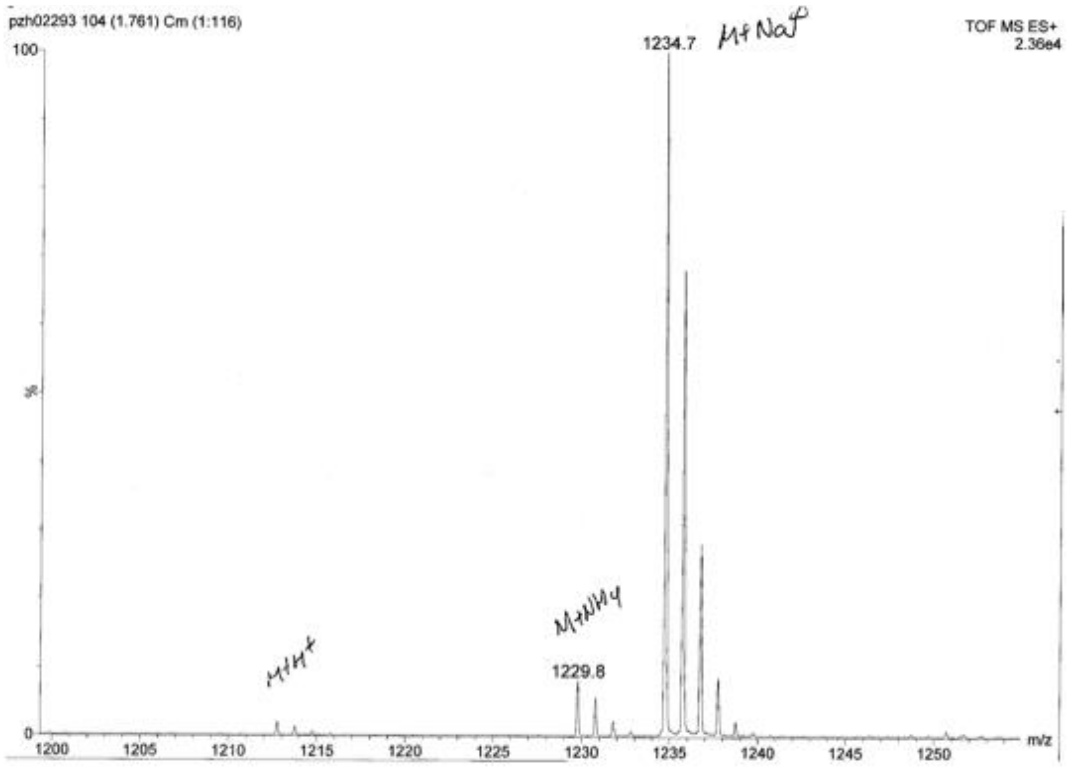

Figure 2.8: Mass spectrum of compound **11** (MA-EG_{12}-DUPA(tri-*tert*-butyl).

2.3.4.3 Deprotection of compound 11 to produce MA-EG_{12}-DUPA

MA-EG_{12}-DUPA(tri-*tert*-butyl) (**11**; 100 mg, 0.082 mmol) in a mixture of solvent (DCM/TFA=1/2) (3mL) was kept in a microwave reaction sealed tube. After being prestirred for 30 sec, the reaction was conducted at 50 ^{o}C for 2 min in a microwave reactor. After removing the solvent under reduced pressure, the remaining crude product was precipitated in diethyl ether. After being purified with semipreparative HPLC, pure product (42 mg) was obtained in 48.8% yield. The product was characterized with mass spectroscopy (Figure 2.9). ESI^-: calcd for $C_{45}H_{80}N_5O_{22}$ ($[M-H]^-$), 1042.5. Found: 1042.5.

2.3.5 Preparation of DUPA-targeted and nontargeted HPMA copolymer-DTX conjugates

DUPA-targeted and nontargeted HPMA copolymer-DTX conjugates were prepared with RAFT polymerization.

2.3.5.1 Preparation of nontargeted HPMA copolymer-DTX conjugate P-DTX

The scheme for preparation of nontargeted HPMA copolymer-DTX conjugate P-DTX is shown in Figure 2.10. To an ampoule was added monomer HPMA (357 mg, 2.496 mmol), MA-GFLG-DTX (80 mg, 0.064 mmol), CPAD (0.716 mg), azobisisobutyronitrile (AIBN) (0.084 mg), and methanol (1.5 mL). Then this mixture was bubbled with nitrogen for 30 min and the ampoule was sealed. The RAFT copolymerization was conducted at 55 °C for 79 h. The resulting copolymer was precipitated in diethyl ether and purified by preparative FPLC. After freeze-drying, 84.7 mg of product was obtained (18.4% in yield).

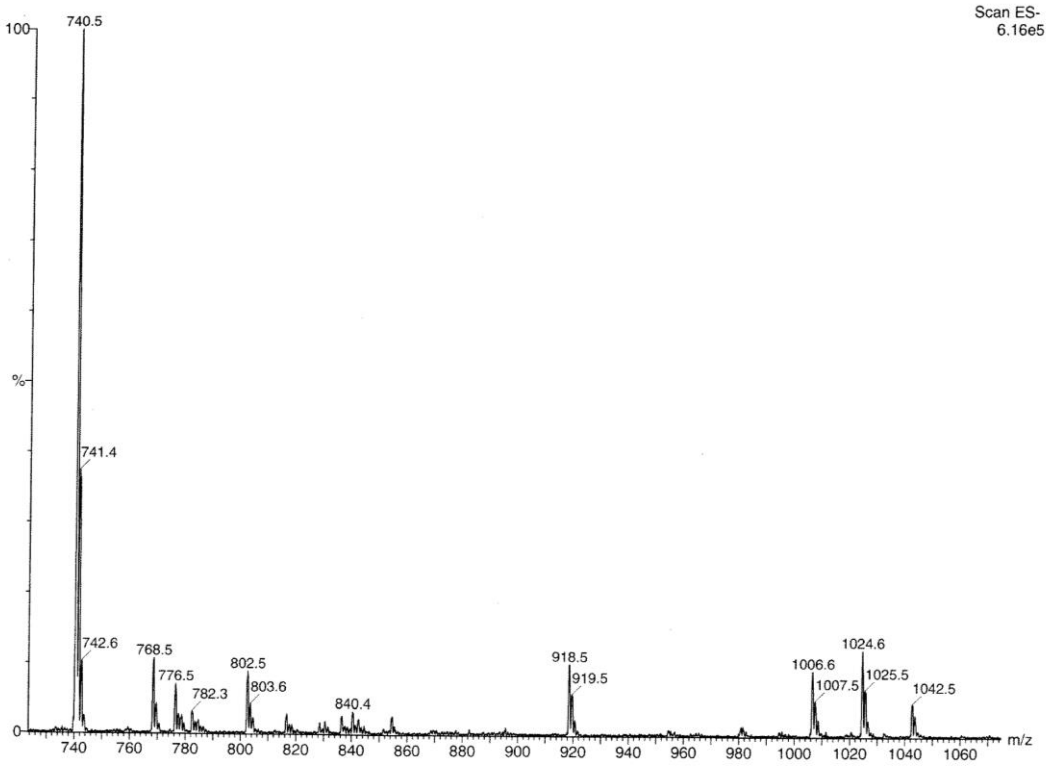

Figure 2.9: Mass spectrum of monomer MA-EG_{12}-DUPA.

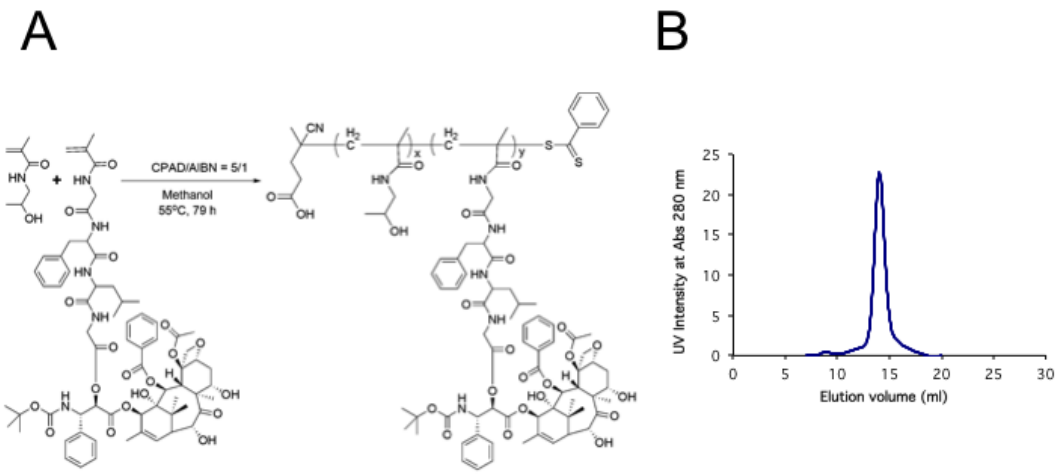

Figure 2.10: Synthetic scheme (A) and size exclusion chromatography (SEC) profile (B) of P-DTX.

2.3.5.2 Preparation of DUPA-targeted HPMA copolymer-DTX conjugate P-DTX-DUPA (Low MW)

The synthetic scheme for preparing low molecular weight DUPA-targeted HPMA copolymer-DTX conjugate P-DTX-DUPA is shown in Figure 2.11. To an ampoule was added monomer HPMA (238.7 mg, 1.667 mmol), MA-GFLG-DTX (56.7 mg, 0.045 mmol), MA-DUPA (47 mg, 0.106 mmol), and a solution of 0.9 mg CPAD or 0.167 mg of V-65 in DMSO. Then more of DMSO and DI water were added until the final volume of DMSO and DI water were 1.8 mL and 1.2 mL, respectively. The mixture was bubbled with nitrogen for 30 min before sealing the ampoule. The RAFT copolymerization was conducted at 52 °C for 36 h. The resulting copolymer was precipitated in diethyl ether and purified by preparative FPLC. After freeze-drying, 110 mg of product was obtained (32% in yield).

2.3.5.3 Preparation of DUPA-targeted HPMA copolymer-DTX conjugate P-DTX-mDUPA (High MW)

The scheme for preparing DUPA-targeted HPMA copolymer-DTX conjugate P-DTX-mDUPA with high molecular weight is shown in Figure 2.12. To an ampoule was added monomer HPMA (338.8 mg, 2.366 mmol), MA-GFLG-DTX (80 mg, 0.064 mmol), MA-DUPA (57.58 mg, 0.130 mmol), CPAD (0.716 mg), azobisisobutyronitrile (AIBN) (0.084 mg), and methanol (1.5 mL). Then this mixture was bubbled with nitrogen for 30 min and the ampoule was sealed. The RAFT copolymerization was conducted at 55 °C for 79 h. The resulting copolymer was precipitated in diethyl ether and purified by preparative FPLC. After freeze-drying, 174 mg of product was obtained (36.5% in yield).

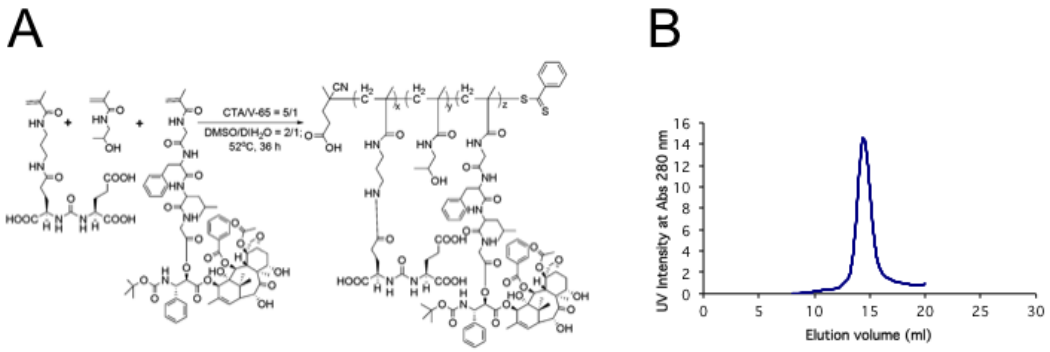

Figure 2.11: Synthetic scheme (A) and SEC profile (B) of P-DTX-DUPA.

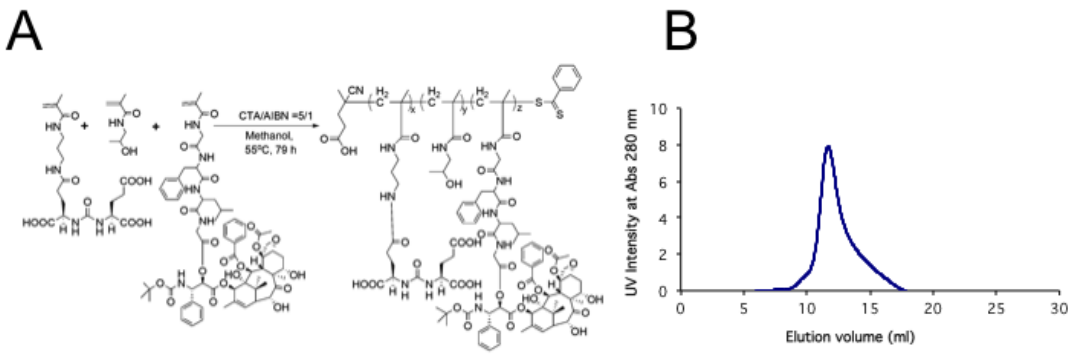

Figure 2.12: Synthetic scheme (A) and SEC profile (B) of P-DTX-mDUPA.

2.3.5.4 Preparation of DUPA-targeted HPMA copolymer-DTX conjugate P-DTX-EG_{12}-DUPA

The synthetic scheme for preparing DUPA-targeted HPMA copolymer-DTX conjugate P-DTX-EG_{12}-DUPA is shown in Figure 2.13. The general procedure is: (*i*) added monomer HPMA (238.7 mg, 1.667 mmol), MA-EG_{12}-DUPA (100 mg, 0.096 mmol), and MA-GFLG-DTX (56.7 mg, 0.045 mmol) into an ampoule; (*ii*) added a solution of 0.9 mg CPAD in DMSO and 0.167 mg of V-65 in DMSO; (*iii*) added more of DMSO and DI water until the final volume of DMSO was 1.8 mL and final volume of DI water was 1.2 mL; (*iv*) bubbled the mixture with nitrogen for 30 min before sealing the ampoule; (*iv*) the RAFT copolymerization was conducted at 52 °C for 36 h. The resulting copolymer was precipitated in diethyl ether and purified by preparative FPLC. After freeze-drying, 138 mg of product was obtained (35% in yield).

2.3.6 Characterization of DUPA-targeted and nontargeted HPMA copolymer-DTX conjugates

The number average molecular weight (M_n), weight average molecular weight (M_w) and polydispersity (M_w/M_n) of DUPA-targeted or non-targeted HPMA copolymer-DTX conjugates were analyzed by size exclusion chromatography using a Superose 6 HR10/30 analytical column on an AKTA FPLC system (Pharmacia) equipped with refractive index (Optilab rEX) and light scattering MiniDawn TREOS detectors (Wyatt Technology Inc, Santa Barbara). The buffer with 0.1 M of sodium acetate in a mixture of 30% acetonitrile/70% DI water (v/v) (pH = 6.5) was used as the eluant, and the flow rate

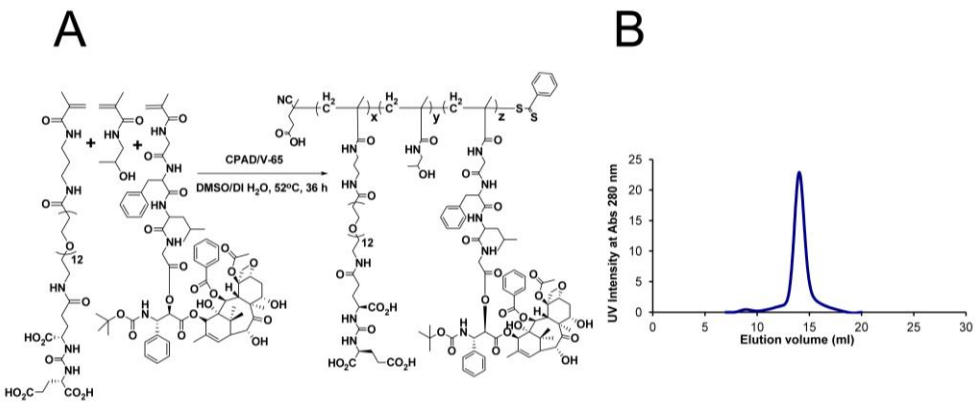

Figure 2.13: Synthetic scheme (A) and SEC profile (B) of P-DTX-EG_{12}-DUPA.

was 0.4 mL/min. HPMA homopolymer fractions were used as molecular weight standards.

The DTX content in DUPA-targeted or nontargeted HPMA copolymer-DTX conjugates was determined by using HPLC after complete enzymatic hydrolysis of DTX from DUPA targeted or nontargeted HPMA copolymer-DTX conjugates with excess of papain. The general procedure to measure the DTX content in conjugate: (*i*) to a 1 mL of Eppendorf vial was added 10 μL of 20 mg/mL of DTX conjugate in DMSO solution; (*ii*) added 100 μL of 10 mM glutathione in Mcllvaine's buffer (50 mM citrate/0.1 M phosphate pH 6.0); (*iii*) added 20 μL of 25 mg/mL papain in Mcllvaine's buffer; (*iv*) the mixture was incubated at 37 °C for 12 h; (*v*) the reaction was terminated by addition of 10 μL of $3*10^{-3}$ M sodium iodoacetate (enzyme inhibitor) solution and 280 μL of 0.02% of acetic acid in methanol. The amount of released DTX in the final mixture was measured by analytical HPLC (Agilent Technologies 1100 series, Zorbax C8 column 4.6 X 150 mm) using gradient elution from 30% to 90% of buffer B in 30 min (Buffer A: 0.1% TFA in DI water; Buffer B: 0.1% TFA in acetonitrile), and the flow rate was 1.0 mL/min. Free DTX was used for standard curve calibration generated under the same conditions as the assay.

The DUPA content in DUPA-targeted HPMA copolymer-DTX conjugates was determined by amino acid analysis. The general procedure for measuring DUPA content in DUPA targeted HPMA copolymer-DTX conjugates: (*i*) 2 mg of DUPA targeted HPMA copolymer-DTX conjugates and 0.5 mL of 6 M HCl in a sealed ampule were heated at 110 ^{o}C for 24 h, (*ii*) the solvent was removed under reduced pressure and the residue was redissolved in 100 μL of DI water; (*iii*) derivatization of hydrolyzed amino

acid by sequential addition: 20 μL of potassium tetraborate in distilled water (150 μg/μL), 20 μL of o-phthaldialdehyde in methanol (50 μg/μL), 20 μL of mercaptopropionic acid in distilled water (0.05 mL/1 mL), 20 μL of sample solution; (*iv*) the mixture was vortexed for 1 min and was added 0.5 mL of 0.1 M sodium acetate buffer, and then filtered; (*v*) the fluorescence (E_x = 229 nm, E_m = 450 nm) of the hydrolyzed amino acid derivatives was measured by analytical HPLC (Agilent Technologies 1100 series, XDB-C8, 5 μm, column 4.6 X 150 mm) using gradient elution (0-2 min, 10% buffer B; 2-10 min, 10%-50% buffer B; 10-20 min, 50%-60% buffer B; 20-25 min, 60% buffer B; 25-30 min, 60%-70% buffer B; 30-35 min, 70%-90% buffer B; 35-40 min, 90% buffer B) (Buffer A: 0.05 M sodium acetate in 25 mL of acetonitrile and 975 mL of DI water, pH 6; Buffer B: 0.05 M sodium acetate in 300 mL of DI water and 700 mL of methanol, pH 6), and the flow rate was 1.0 mL/min. Monomer MA-DUPA was used for standard curve calibration.

2.3.7 Cell culture

LNCaP-derived androgen-independent C4-2 cell line was kindly provided by Dr. Elsässer-Beile (University of Karlsruhe). PC-3 cell line was purchased from American Type Culture Collection (ATCC) (Manassas, VA). Cells were maintained in RPMI-1640 medium (Sigma-Aldrich, St. Louis, MO) supplemented with 10% (v/v) fetal bovine serum (FBS), 100 U/ml penicillin, and 100 μg/mL streptomycin (Gibco, Carlsbad, CA). Cells were incubated at 37 ^{o}C in a humidified atmosphere of 5% CO_2 (v/v). Cells were passaged every 3-4 d and stopped at passage 20.

2.3.8 PSMA cell surface expression

The PSMA surface expression on C4-2 and PC-3 cells was measured by flow cytometry. The cells were detached from flask with 0.05% of trypsin in ethylenediaminetetraacetic acid (EDTA), centrifuged at 1000 rpm, and washed three times with PBS. After cooling the cells and solutions to 4 ^{o}C, about 200,000 cells were re-suspended in 100 μL staining buffer (PBS solution containing 3% FBS and 0.1 % NaN_3). Then to each vial was added 100 μL of 10 μg/mL primary antibody 3F/11 (provided by Dr. Elsässer-Beile). The final 3/F11 concentration was 5 μg/mL. After being incubated for 30 min at 4 ^{o}C, the cells were washed three times with 1 mL of staining buffer. Following incubation with a 1:500 dilution of secondary antibody (Alexa Fluor 488 goat anti-mouse IgG (H+L), 4 μg / mL) (Life Technologies, Grand Island, NY) at 4 ^{o}C for 30 min, the cells were washed three times with staining buffer and kept in 250 μL of staining buffer for flow cytometry study. No-staining cells were used as the negative control.

2.3.9 In vitro cytotoxicity

The cytotoxicity of DTX conjugates against C4-2 human prostate cancer cells was measured by Cell Counting Kit-8 assay (CCK-8, Dojindo, Japan). The C4-2 cells were seeded in 96-well plates at a density of 5,000 cells/well in 100 μL RMPI-1640 media containing 10% fetal bovine serum. After 24 h, old media were removed and replaced with a series concentration of DTX conjugates in 100 μL media. After 72 h, 50 μL of 1:5 diluted original CCK-8 solution was added and incubated for 1-2 h. The absorbance of the reduced product formazan at 450 nm (630 nm as reference) was measured with a

microplate reader (Bio-Rad, Hercules, CA). The data were analyzed using GraphPad Prism v. 5.03 (GraphPad Software Inc., La Jolla, CA).

2.3.10 Tumor models

All animals were handled in compliance with the Institutional Animal Care and Use Committee (IACUC) guidelines in University of Utah. All works were conducted under the protocol (#10-10006) approved by University of Utah IACUC. Male nu/nu mice (about 6 weeks of age) were obtained from Charles River (Wilmington, MA) and housed in BPRB Rm#28 with a controlled environment (24°C); 12:12-h light dark cycle) under specific-pathogen free conditions with water and food provided *ad libitum*. In this study, male nu/nu mice were inoculated subcutaneously with two millions of C4-2 cells in 200 μL of a mixture of Matrigel/medium =1/1 in the right flank.

2.3.11 In vivo anticancer efficacy of DUPA-targeted and nontargeted HPMA copolymer-DTX conjugates

The efficacies of DTX conjugates were assessed in six groups of nu/nu mice bearing C4-2 prostate cancer xenografts. When the tumor volume reached approximately 100-200 mm^3, the mice were administered three dosages of 3 mg/kg DTX equivalent DUPA targeted and nontargeted HPMA copolymer-DTX conjugates, free DTX, and saline via tail vein once per week (days 0, 7, and 14). After the first dose, the mice weight was monitored everyday and tumor growth was monitored three times per week. The perpendicular diameters (length and width) of the tumors were measured by digital calipers, and the tumor volume was calculated by the following formula: (3.14 * $Width^2$ *

Length)/6. Mice were euthanized when the tumor weight reached 10% of the predosing weight. Individual tumor volume relative to initial size was calculated. At study end points, mice were euthanized and their tumors as well as organs were excised. The tumors and organs were stored in 10% of formalin and embedded in paraffin, cryosectioned, and stained with hematoxylin and eosin (H&E) for histological analysis. The slices were examined with fluorescence microscope.

2.3.12 Statistical analysis

Data values were expressed as the mean ± standard error of the mean (SEM). Difference between means was assessed by one-way analysis of variance (ANOVA) and Dunnett's test using GraphPad Prism software. P values ≤ 0.05 were considered statistically significant.

2.4. Results and Discussion

2.4.1 Design, synthesis, and characterization of MA-GFLG-DTX

There are two common ways to prepare drug conjugates: one way is to prepare the conjugate precursor first, then attach the drug into the conjugate; the other way is to prepare a monomer form of drug, then copolymerize with comonomers to prepare the drug conjugates. Compared with the former method, the latter method has several advantages: (*i*) flexible to control the drug content by adjusting the monomer drug content in feed; (*ii*) easier to obtain the pure product when the drug has several reactive groups. As there are three hydroxyl groups in DTX at the C-7, C-10, and C-2' positions, respectively, we prefer to prepare monomer MA-GFLG-DTX first and then polymerize

the comonomers. The tetrapeptide (-GFLG-) was used as the spacer to conjugate the drug DTX into HPMA copolymer as this peptide is degraded in the lysosomes (34,36,37). Thus the free drug DTX will be released from the HPMA copolymer in the lysosomal compartment. The design and synthesis of MA-GFLG-DTX is shown in Figure 2.1. The monomer MA-GFLG-DTX was prepared by coupling MA-GFLG-OH with DTX at 0 ^{o}C in the presence of DMAP and EDC in DCM. The coupling reaction occurred preferentially at the C-2' hydroxyl position since the steric hindrance reduces the hydroxyl group reactivity at both C-7 and C-10 positions. Furthermore, the coupling reaction selectivity among those hydroxyl groups was enhanced by lowering the reaction temperature to 0^{o}C. The mass spectrum of MA-GFLG-DTX is shown in Figure 2.2.

2.4.2 Design, synthesis, and characterization of polymerizable DUPA derivatives with different spacer lengths

Using similar rationale as for MA-GFLG-DTX, the targeting moiety DUPA was also converted to a polymerizable form. We designed and synthesized two kinds of DUPA monomer, MA-DUPA (Figure 2.3) and MA-EG_{12}-DUPA (Figure 2.7). Because the modification at C2 position in DUPA results in minimal loss of binding affinity (28), the monomer forms of DUPA were prepared by conjugation at this position. To make sure the targeting moiety can reach the active site of PSMA, we incorporated twelve ethylene glycol units as a spacer between the DUPA and methacryloyl group in the monomer MA-EG_{12}-DUPA. This > 47 Å spacer should be long enough to easily access the PSMA binding site via the funnel-shaped tunnel (30). To evaluate whether the spacer

length between targeting moiety and polymer drug carrier can affect the efficacy of drug conjugates, we prepared monomer MA-DUPA with short spacer as a control.

The preparation of monomer (MA-DUPA) is shown in Figure 2.3. The core ligand, 2-[3-(1,3-bis-*tert*-butoxycarbonyl-propyl)-ureido] pentanedioic acid 1-*tert*-butyl ester, was synthesized according to the literature (20). It started from reaction of L-glutamate di-*tert*-butyl ester hydrochloride, triphosgene, and γ-benzoylated glutamic acid to obtain 2-[3-(3-benzyloxycarbonyl-1-*tert*-butoxycarbonyl-propyl)-ureido] pentanedioic acid di-*tert*-butyl ester (Compound **4**). The benzyl group was selectively removed with activated palladium-carbon to obtain the 2-[3-(1,3-bis-*tert*-butoxycarbonyl-propyl)-ureido] pentanedioic acid 1-*tert*-butyl ester (Compound **5**). Then the carboxylic acid **5** was coupled with APMA to obtain (3S, 7S)-tri-*tert*-butyl-17-methyl-5,10,16-trioxo-4,6,11,15-tetraazaoctadec-17-ene-1,3,7-tricarboxylate (Compound **7**). Under acid assisted microwave irradiation, three *tert*-butyl groups in Compound **7** were removed to obtain monomer MA-DUPA. After being purified with RP-HPLC, the monomer MA-DUPA was characterized with both ^{1}H NMR and MS (Figure 2.6).

As shown in Figure 2.7, the preparation of monomer MA-EG_{12}-DUPA started from the coupling of APMA with Fmoc-NH-EG_{12}-COOH in the presence of HATU and DIPEA in DCM. After the Fmoc group in the MA-EG_{12}-NHFmoc was removed with 20% piperidine in DMF, the amine **10** was coupled with carboxylic acid **5** to obtain MA-EG_{12}-DUPA(tri-*tert*-butyl). The next step is to remove the three *tert*-butyl groups. First, we tried the same reaction condition as used in the preparation of monomer MA-DUPA. From the mass spectrum, several water molecules were lost from the desired product. Then we optimized the reaction condition by lowering the reaction temperature from

70^{o}C to 50 ^{o}C. After being purified with RP-HPLC, the desired product MA-EG_{12}-DUPA with correct mass spectrum was obtained (Figure 2.9).

2.4.3 Design, synthesis, and characterization of DUPA targeted and nontargeted HPMA copolymer-DTX conjugates

RAFT polymerization has been widely applied for preparation of drug delivery systems due to its unique advantages: precise control of the molecular weight of the product, less by-products, opportunity to synthesize telechelic polymers, and possibility to polymerize in aqueous environment. RAFT polymerization required all the monomers, initiator, and CTA to be soluble, and reaction kinetics to be reasonable. A mixture of DMSO and DI water was used as the solvent for these RAFT polymerizations because all the monomers, initiator, and CTA were soluble in DMSO, and DI water was added to facilitate the RAFT polymerization.

The DUPA targeted and nontargeted HPMA copolymer-DTX conjugates were prepared by RAFT polymerization of comonomers: MA-GFLG-DTX, MA-EG_{12}-DUPA, and HPMA for P-DTX-EG_{12}-DUPA; MA-GFLG-DTX, MA-DUPA, and HPMA for P-DTX-DUPA and P-DTX-mDUPA; MA-GFLG-DTX and HPMA for P-DTX. The schematic structure of the DUPA targeted and nontargeted DTX drug conjugates is shown in Figure 2.14. For all the DTX conjugates, degradable linker is the lysosomally degradable tetrapeptide spacer "-GFLG-". For P-DTX, Z is "0", that means no targeting moiety DUPA in this conjugate. For P-DTX-DUPA, the spacer between targeting moiety and polymer backbone is short, that is, three methylene groups. In P-DTX-DUPA, Z is "~7.9". This means that the number of average targeting moieties in one polymer chain is

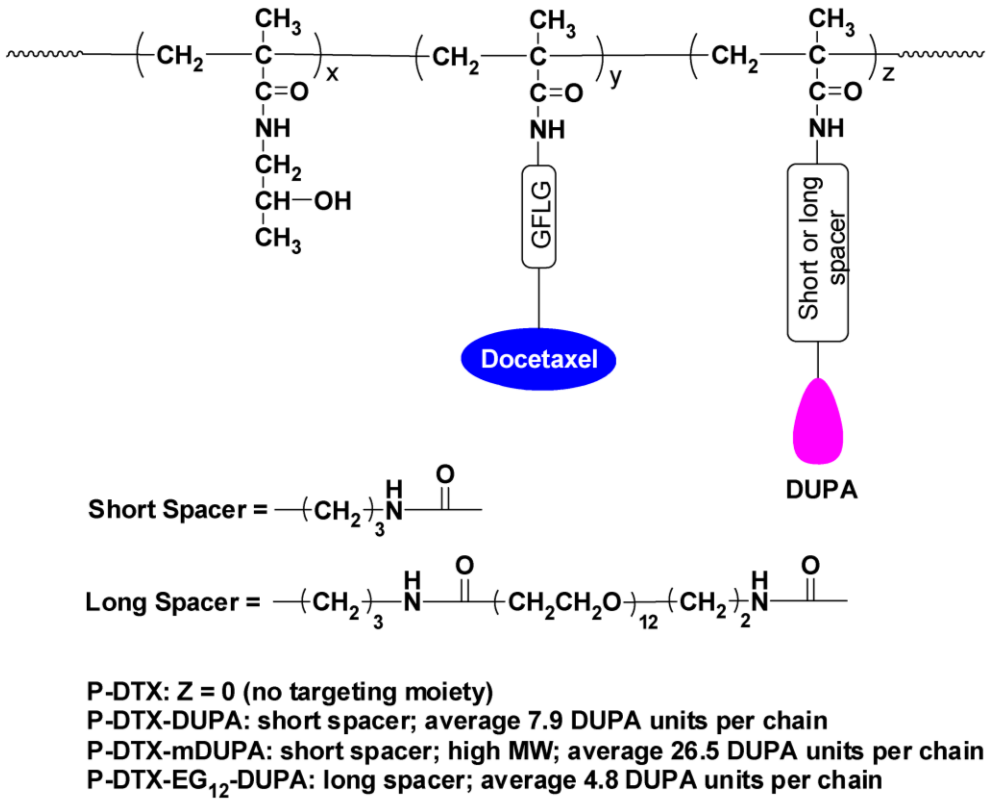

Figure 2.14: Structure schematic of the DTX drug conjugates.

about 7.9. For P-DTX-mDUPA, the spacer between targeting moiety and polymer backbone is the same as that of in P-DTX-DUPA. The difference is that there are more targeting moieties (Z = ~26.5) in P-DTX-mDUPA polymer chain. For P-DTX-EG_{12}-DUPA, the spacer between targeting moiety and polymer backbone is long, including five methylene groups and twelve ethylene glycol groups. In P-DTX-EG_{12}-DUPA, Z is "~4.8", that means there are about 4.8 targeting moieties in one polymer chain. Figure 2.13 shows the structure and synthetic scheme of P-DTX-EG_{12}-DUPA. CPAD and V-65 were used as the CTA and initiator, respectively. The structure, synthetic scheme, and SEC profile of P-DTX, P-DTX-DUPA, and P-DTX-mDUPA are shown in Figures 2.10, 2.11, and 2.12, respectively. Table 2.1 summarizes the molecular weights, polydispersities, DTX and DUPA content in DUPA-targeted and nontargeted HPMA copolymer-DTX conjugates. The molecular weights of all polymer conjugates are well controlled with low polydispersities.

2.4.4 In vitro cytotoxicity

To check whether the C4-2 cell lines are PSMA positive, C4-2 prostate cancer cells and the negative control PC-3 prostate cancer cells were successively incubated with primary mouse anti-PSMA human antibody and secondary goat anti-mouse IgG (H+L) antibody with Alexa Fluor 488. Then those cells were analyzed by flow cytometry. Unstained cells were used as the control. In Figure 2.15, the red line indicates the unstained cells and the blue line indicates the stained cells. The flow cytometry results show that PSMA are expressed on C4-2 cells but not on PC-3. After confirmation of the PSMA cell surface expression on C4-2 cells, we evaluated the in vitro cytotoxicity of

Table 2.1 Physicochemical properties of DUPA-targeted

and nontargeted DTX conjugates.

DTX Conjugate	Spacer Length	Mn (kDa)	Mw (kDa)	Mw/Mn	DTX (wt%)	DUPA Units Per Polymer Chain
P-DTX	N/A	50	59	1.18	5.30	N/A
P-DTX-DUPA	Short	48	64	1.34	5.86	7.9
P-DTX-mDUPA	Short	115	142	1.24	3.93	26.5
P-DTX-EG_{12}-DUPA	Long	70	81	1.16	3.84	4.8

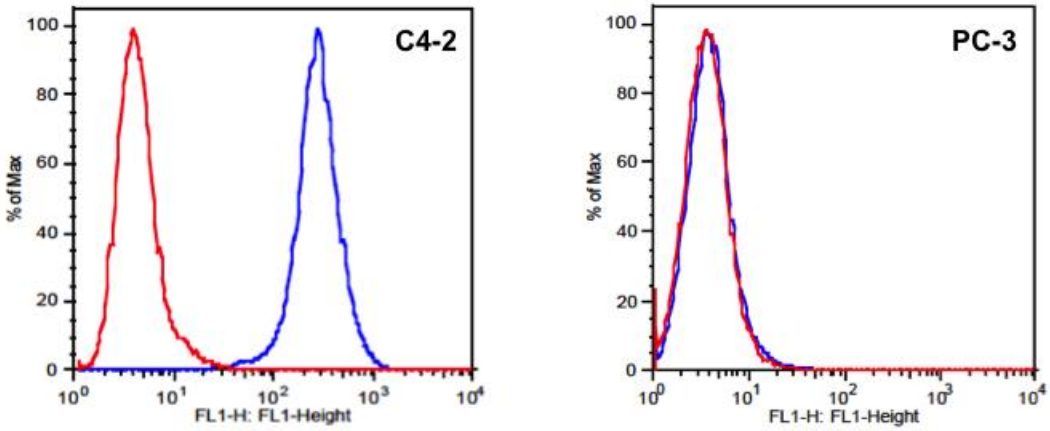

Figure 2.15: PSMA expression on C4-2 and PC-3 cell surface. The red line shows the unstained cells. The blue line shows the cells that had been stained with primary anti-PSMA antibody and secondary antibody.

DUPA targeted and nontargeted HPMA copolymer-DTX conjugates toward C4-2 human prostate cancer cells. As shown in Table 2.2, P-DTX, P-DTX-DUPA, P-DTX-mDUPA, and P-DTX-EG_{12}-DUPA all possess strong cytotoxicity toward C4-2 cells (IC_{50} = 4.14±1.03 nM, 2.99±1.09 nM, 3.32±1.00 nM, 3.18±0.42 nM, respectively. The data are presented as mean ± SEM. n = 3.). The similar IC_{50} doses can be explained by the presence of ester bond between DTX and HPMA copolymer backbone; part of the DTX was released from the conjugates during 72 h incubation in cell culture media. Consequently, C4-2 cells were exposed to a mixture of free and polymer-bound DTX. This is consistent with another other research group's results (38).

2.4.5 In vivo efficacy

Among prostate cancer tumor models, the C4-2 tumor model mimics closely human prostate cancer growth (39). Therefore, the antitumor activities of DUPA-targeted and nontargeted HPMA copolymer-DTX conjugates were tested in six groups of nu/nu mice bearing C4-2 prostate cancer xenografts (n = 4-6): untreated control (saline), free DTX, nontargeted conjugate (P-DTX), and DUPA-targeted conjugates (P-DTX-DUPA, P-DTX-mDUPA, and P-DTX-EG_{12}-DUPA). Based on preliminary experiments, dosage (3 mg/kg) was enough to control C4-2 tumor growth (unpublished data). Three doses of 3 mg/kg DTX equivalent were administered *via* tail vein once per week (days 0, 7, and 14). At study end points, mice were euthanized and their tumors as well as organs were excised. As shown in Figure 2.16.A, the targeted DTX conjugate with longer spacer (P-DTX-EG_{12}-DUPA) was significantly more efficacious in tumor size reduction than P-DTX-DUPA, P-DTX-mDUPA, P-DTX, free DTX, and saline. Typical images of excited

Table 2.2 IC_{50} of DUPA-targeted or nontargeted DTX

conjugates against C4-2 prostate cancer cells.

	P-DTX	P-DTX-DUPA	P-DTX-mDUPA	P-DTX-EG_{12}-DUPA
IC_{50} (nM)	4.14±1.03	2.99±1.09	3.32±1.00	3.18±0.42

tumors at the end points for DTX conjugates treated groups are shown in Figure 2.16.B. For the treated group of P-DTX, P-DTX-mDUPA, and P-DTX-EG_{12}-DUPA at day 42 after the first treatment, the mean relative tumor percents ((final tumor size/initial size)*100) were (1590 ± 208)%, (1193 ± 285)%, and (810 ± 160)%, respectively (mean ± SEM). Consistent with our hypothesis that the spacer length is important for DUPA attachment to the PSMA binding site, the efficacy of P-DTX-EG_{12}-DUPA was the highest of all conjugates studied; there was no significant difference in the efficacy of P-DTX, P-DTX-DUPA, and P-DTX-mDUPA. Interestingly, the P-DTX-mDUPA possessed lesser efficacy than that P-DTX at early stages, but more efficacy in later stages of the experiment although the difference is not statistically significant.

2.4.6 Adverse effects

To evaluate whether the DUPA-targeted or nontargeted DTX conjugates have nonspecific toxicities, the weight of treated and nontreated mice was monitored everyday. As shown in Figure 2.17, both treated and nontreated mice exhibited a slight weight loss maybe due to the bearing of tumor. However, there was no significant difference between treated and nontreated mice groups.

To further test whether the DTX conjugates have toxicity or not, we analyzed the histology of major organs (heart, liver, spleen, kidney, lung) after the mice were sacrificed. As shown in Figure 2.18, histologic examination of H&E stained sections from paraffin embedded tissue of organs in treated and nontreated groups indicated no pathologic changes or end organ damage. Histologic sections from the heart and liver showed cardiomyocytes and hepatocytes within normal limits compared to saline treated

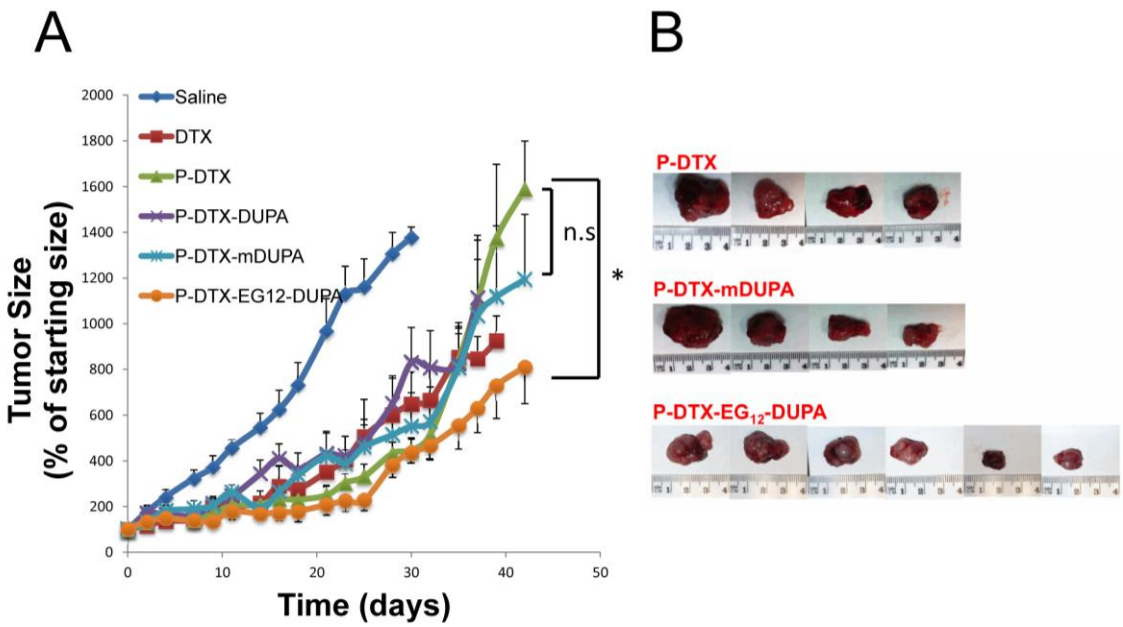

Figure 2.16: In vivo antitumor activity of DUPA-targeted or nontargeted HPMA copolymer-DTX conjugates in nude mice bearing s.c. C4-2 prostate cancer xenografts. (A) C4-2 tumor growth curve after treatment with three doses of DTX, P-DTX, P-DTX-DUPA, P-DTX-mDUPA, and P-DTX-EG_{12}-DUPA (3 mg equivalent DTX/kg at days 0, 7, and 14). Control mice were administered saline. The data are presented as mean ± SEM (n =4-6; $^{*}P<0.05$; ns, not significant). (B) Images of excised tumors from mice, which were treated by P-DTX, P-DTX-mDUPA, and P-DTX-EG_{12}-DUPA, respectively. Those mice were sacrificed at day 42 after the first injection.

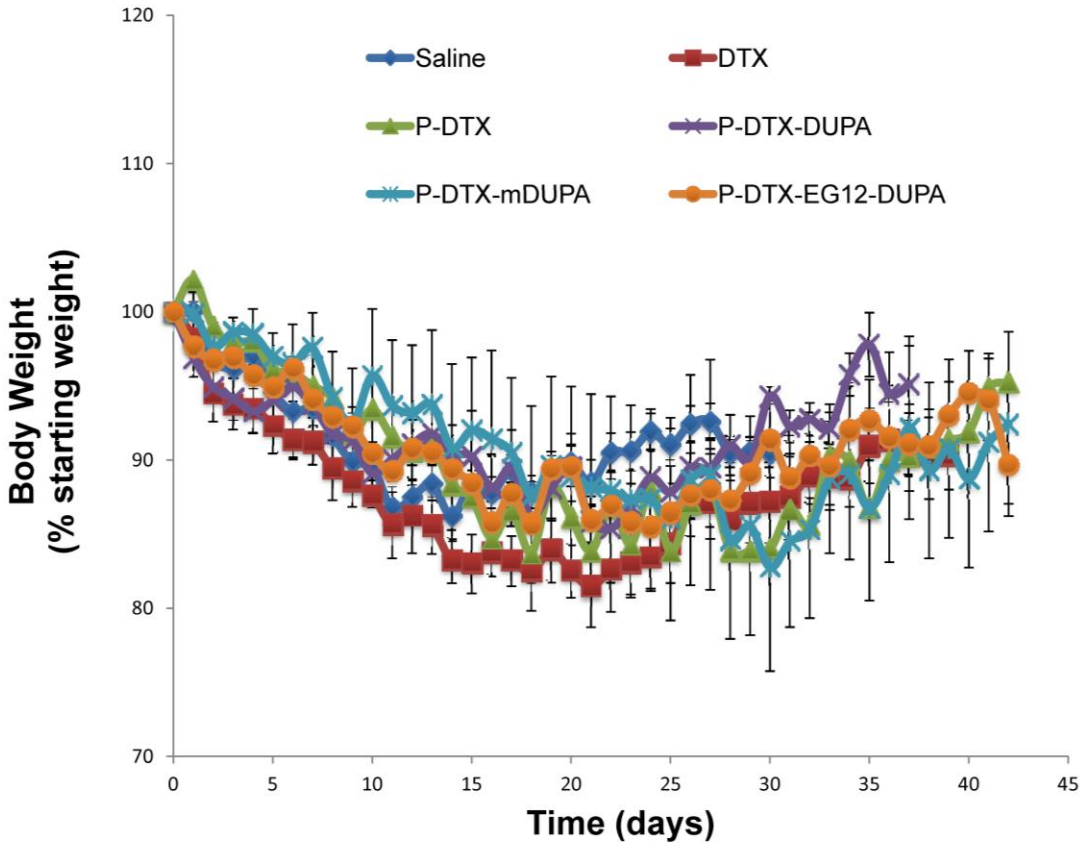

Figure 2.17: Percentage of mean body weight change of nu/nu mice bearing s.c. C4-2 prostate cancer xenografts following administration of saline, DTX, P-DTX, P-DTX-DUPA, P-DTX-mDUPA, and P-DTX-EG_{12}-DUPA (3 mg equivalent DTX/kg at days 0, 7, and 14). The data are presented as mean ± SEM (n =4-6).

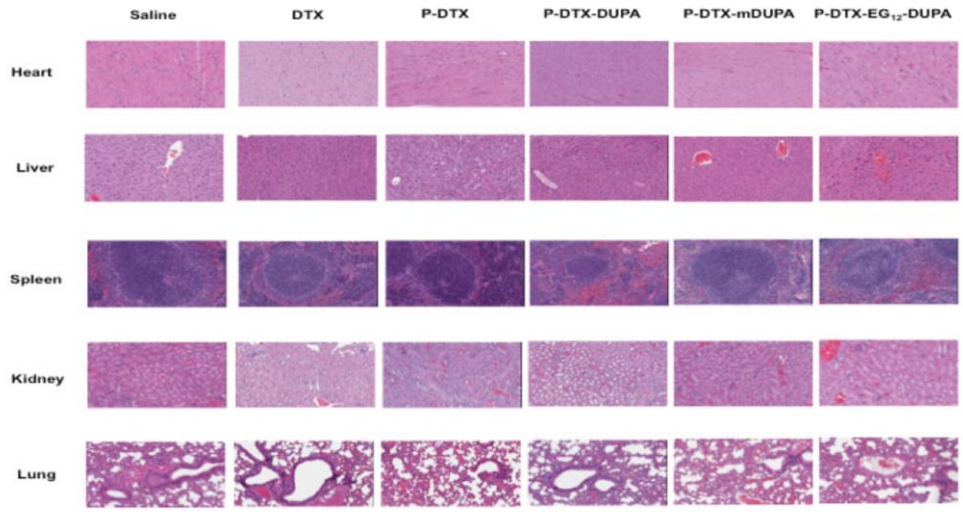

Figure 2.18: Histology images of major organs (heart, liver, spleen, kidney, lung) from control and treated mice.

control samples. White and red bulb of the spleen also did not show histopathologic differences. Similarly section of the kidney showed normal glomeruli without evidence of tubular necrosis in any of the groups. Compared to the control group, there was no significant histologic difference in the lung tissue from the treated group.

2.5 Conclusion

In summary, we examined the targeting effect of DUPA and the spacer length effect in the treatment of PSMA expressing prostate cancer. Two polymerizable forms of DUPA with different spacer length were prepared and characterized. DUPA targeted and nontargeted HPMA copolymer - DTX conjugates with well-controlled molecular weight and molecular weight distribution were efficiently prepared by RAFT polymerization. To our knowledge, this is the first time to directly incorporate the targeting moiety DUPA into drug delivery system by polymerization. Importantly, the general approach to prepare monomer form of DUPA can be extended to a wide variety of other PSMA targeting moieties such as phosphoramidates and peptides. Importantly, the P-DTX-mDUPA and P-DTX-EG_{12}-DUPA treated groups exhibited better tumor regression than that of the P-DTX treated group at the study end point. This might be attributed to the targeting effect of DUPA toward PSMA on tumor cells. Furthermore, P-DTX-EG_{12}-DUPA exhibited better C4-2 tumor regression than that of P-DTX-mDUPA even though the P-DTX-mDUPA contains more targeting moieties than P-DTX-EG_{12}-DUPA. These in vivo results show that the spacer length between targeting moieties and HPMA copolymer backbone affects the DUPA's targeting effect, and concomitantly the treatment efficacy of DTX conjugates against C4-2 tumor bearing nu/nu mice. However,

it is also possible that the enhanced treatment effect of P-DTX-EG_{12}-DUPA result from other factors such as the change of morphology and enhanced water solubility of conjugates. Moreover, histology study showed that the DUPA-targeted DTX conjugate exhibited no nonspecific toxicity to the treated mice. This formulation design provides a promising targeted therapeutics for PSMA expressing prostate cancer treatment. The results of this study demonstrated the importance of spacer length in targeted drug delivery, especially when the size of targeting moiety is small. Further modifications, such as optimizing the targeting moieties distribution and increasing the number of targeting moieties per polymer chain, should further enhance the DUPA targeting effect.

2.6 References

1. Siegel R, Naishadham D, Jemal A. Cancer statistics, 2013. CA Cancer J Clin. 2013;63:11–30.

2. Olson WC, Heston WDW, Rajasekaran AK. Clinical trials of cancer therapies targeting prostate-specific membrane antigen. Rev Recent Clin Trials. 2007;2:182–90.

3. Tannock IF, de Wit R, Berry WR, Horti J, Pluzanska A, Chi KN, et al. Docetaxel plus prednisone or mitoxantrone plus prednisone for advanced prostate cancer. N Engl J Med. 2004;351:1502–12.

4. Corcoran C, Rani S, O'Brien K, O'Neill A, Prencipe M, Sheikh R, et al. Docetaxel-resistance in prostate cancer: evaluating associated phenotypic changes and potential for resistance transfer via exosomes. PloS One. 2012;7:e50999.

5. Yu MK, Park J, Jon S. Targeting strategies for multifunctional nanoparticles in cancer imaging and therapy. Theranostics. 2012;2:3–44.

6. Duncan R. Polymer therapeutics as nanomedicines: new perspectives. Curr Opin Biotechnol. 2011;22:492–501.

7. Lapidus RG, Tiffany CW, Isaacs JT, Slusher BS. Prostate-specific membrane antigen (PSMA) enzyme activity is elevated in prostate cancer cells. The Prostate. 2000;45:350–4.

8. Ghosh A, Heston WDW. Tumor target prostate specific membrane antigen (PSMA) and its regulation in prostate cancer. J Cell Biochem. 2004;91:528–39.

9. Ross JS, Sheehan CE, Fisher HAG, Kaufman RP Jr, Kaur P, Gray K, et al. Correlation of primary tumor prostate-specific membrane antigen expression with disease recurrence in prostate cancer. Clin Cancer Res. 2003;9:6357–62.

10. Ni X, Zhang Y, Ribas J, Chowdhury WH, Castanares M, Zhang Z, et al. Prostate-targeted radiosensitization via aptamer-shRNA chimeras in human tumor xenografts. J Clin Invest. 2011;121:2383–90.

11. Dassie JP, Liu X-Y, Thomas GS, Whitaker RM, Thiel KW, Stockdale KR, et al. Systemic administration of optimized aptamer-siRNA chimeras promotes regression of PSMA-expressing tumors. Nat Biotechnol. 2009;27:839–49.

12. Bagalkot V, Farokhzad OC, Langer R, Jon S. An aptamer-doxorubicin physical conjugate as a novel targeted drug-delivery platform. Angew Chem Int Ed Engl. 2006;45:8149–52.

13. Henry MD, Wen S, Silva MD, Chandra S, Milton M, Worland PJ. A prostate-specific membrane antigen-targeted monoclonal antibody-chemotherapeutic

conjugate designed for the treatment of prostate cancer. Cancer Res. 2004;64:7995–8001.

14. Moffatt S, Papasakelariou C, Wiehle S, Cristiano R. Successful in vivo tumor targeting of prostate-specific membrane antigen with a highly efficient J591/PEI/DNA molecular conjugate. Gene Ther. 2006;13:761–72.

15. Elsässer-Beile U, Reischl G, Wiehr S, Bühler P, Wolf P, Alt K, et al. PET imaging of prostate cancer xenografts with a highly specific antibody against the prostate-specific membrane antigen. J Nucl Med. 2009;50:606–11.

16. Evans MJ, Smith-Jones PM, Wongvipat J, Navarro V, Kim S, Bander NH, et al. Noninvasive measurement of androgen receptor signaling with a positron-emitting radiopharmaceutical that targets prostate-specific membrane antigen. Proc Natl Acad Sci U S A. 2011;108:9578–82.

17. Aggarwal S, Singh P, Topaloglu O, Isaacs JT, Denmeade SR. A dimeric peptide that binds selectively to prostate-specific membrane antigen and inhibits its enzymatic activity. Cancer Res. 2006;66:9171–7.

18. Rege K, Patel SJ, Megeed Z, Yarmush ML. Amphipathic peptide-based fusion peptides and immunoconjugates for the targeted ablation of prostate cancer cells. Cancer Res. 2007;67:6368–75.

19. Kularatne SA, Venkatesh C, Santhapuram H-KR, Wang K, Vaitilingam B, Henne WA, et al. Synthesis and biological analysis of prostate-specific membrane antigen-targeted anticancer prodrugs. J Med Chem. 2010;53:7767–77.

20. Kularatne SA, Wang K, Santhapuram H-KR, Low PS. Prostate-specific membrane antigen targeted imaging and therapy of prostate cancer using a PSMA inhibitor as a homing ligand. Mol Pharm. 2009;6:780–9.

21. Sanna V, Pintus G, Bandiera P, Anedda R, Punzoni S, Sanna B, et al. Development of polymeric microbubbles targeted to prostate-specific membrane antigen as prototype of novel ultrasound contrast agents. Mol Pharm. 2011;8:748–57.

22. Maresca KP, Hillier SM, Femia FJ, Keith D, Barone C, Joyal JL, et al. A series of halogenated heterodimeric inhibitors of prostate specific membrane antigen (PSMA) as radiolabeled probes for targeting prostate cancer. J Med Chem. 2009;52:347–57.

23. Humblet V, Misra P, Bhushan KR, Nasr K, Ko Y-S, Tsukamoto T, et al. Multivalent scaffolds for affinity maturation of small molecule cell surface binders and their application to prostate tumor targeting. J Med Chem. 2009;52:544–50.

24. Banerjee SR, Pullambhatla M, Byun Y, Nimmagadda S, Foss CA, Green G, et al. Sequential SPECT and optical imaging of experimental models of prostate cancer with a dual modality inhibitor of the prostate-specific membrane antigen. Angew Chem Int Ed Engl. 2011;50:9167–70.

25. Liu T, Nedrow-Byers JR, Hopkins MR, Berkman CE. Spacer length effects on in vitro imaging and surface accessibility of fluorescent inhibitors of prostate specific membrane antigen. Bioorg Med Chem Lett. 2011;21:7013–6.

26. Zhou J, Neale JH, Pomper MG, Kozikowski AP. NAAG peptidase inhibitors and their potential for diagnosis and therapy. Nat Rev Drug Discov. 2005;4:1015–26.

27. Jayaprakash S, Wang X, Heston WD, Kozikowski AP. Design and synthesis of a PSMA inhibitor-doxorubicin conjugate for targeted prostate cancer therapy. ChemMedChem. 2006;1:299–302.

28. Zhang AX, Murelli RP, Barinka C, Michel J, Cocleaza A, Jorgensen WL, et al. A remote arene-binding site on prostate specific membrane antigen revealed by antibody-recruiting small molecules. J Am Chem Soc. 2010;132:12711–6.

29. Davis ME, Chen ZG, Shin DM. Nanoparticle therapeutics: an emerging treatment modality for cancer. Nat Rev Drug Discov. 2008;7:771–82.

30. Mesters JR, Barinka C, Li W, Tsukamoto T, Majer P, Slusher BS, et al. Structure of glutamate carboxypeptidase II, a drug target in neuronal damage and prostate cancer. EMBO J. 2006;25:1375–84.

31. Kopeček J, Kopečková P. HPMA copolymers: origins, early developments, present, and future. Adv Drug Deliv Rev. 2010;62:122–49.

32. Kopeček J. Polymer-drug conjugates: origins, progress to date and future directions. Adv Drug Deliv Rev. 2013;65:49–59.

33. Kopeček J, Bažilová H. Poly[N-(2-hydroxypropyl)methacrylamide]—I. Radical polymerization and copolymerization. Eur Polym J. 1973;9:7–14.

34. Rejmanová P, Kopeček J, Pohl J, Baudyš M, Kostka V. Polymers containing enzymatically degradable bonds, 8. Degradation of oligopeptide sequences in N-(2-hydroxypropyl)methacrylamide copolymers by bovine spleen cathepsin B. Makromol Chem. 1983;184:2009–20.

35. Mitsukami Y, Donovan MS, Lowe AB, McCormick CL. Water-Soluble Polymers. 81. Direct Synthesis of Hydrophilic Styrenic-Based Homopolymers and Block Copolymers in Aqueous Solution via RAFT. Macromolecules. 2001;34:2248–56.

36. Satchi-Fainaro R, Puder M, Davies JW, Tran HT, Sampson DA, Greene AK, et al. Targeting angiogenesis with a conjugate of HPMA copolymer and TNP-470. Nat Med. 2004;10:255–61.

37. Liu J, Kopečková P, Pan H, Sima M, Bühler P, Wolf P, et al. Prostate-cancer-targeted N-(2-hydroxypropyl)methacrylamide copolymer/docetaxel conjugates. Macromol Biosci. 2012;12:412–22.

38. Etrych T, Šírová M, Starovoytova L, Říhová B, Ulbrich K. HPMA copolymer conjugates of paclitaxel and docetaxel with pH-controlled drug release. Mol Pharm. 2010;7:1015–26.

39. Thalmann GN, Anezinis PE, Chang SM, Zhau HE, Kim EE, Hopwood VL, et al. Androgen-independent cancer progression and bone metastasis in the LNCaP model of human prostate cancer. Cancer Res. 1994;54:2577–81.

CHAPTER 3

SYNTHESIS AND ACTIVITIES OF TUMOR-HOMING PEPTIDE iRGD AND HISTONE DEACETYLASE INHIBITOR VALPROIC ACID CONJUGATE[1]

3.1 Summary

In this chapter, we present a concise strategy to prepare a conjugate of the tumor-homing peptide iRGD and histone deacetylase inhibitor Valproic acid (VPA), VPA-GFLG-iRGD. Conjugates VPA-GFLG-iRGD and GFLG-iRGD were prepared by solid phase synthesis. The activities of VPA-GFLG-iRGD and related controls against DU-145 prostate cancer cells were tested by both cell cytotoxicity and cell cycle arrest assays. The conjugate VPA-GFLG-iRGD and a mixture of VPA and GFLG-iRGD have shown similar cytotoxicity against DU-145 prostate cancer cells. However, the treatment of DU-145 cells with conjugate VPA-GFLG-iRGD resulted in a decreased percentage of cells in the G2 phase, whereas the exposure of a mixture of VPA and GFLG-iRGD led to an increased percentage of cells in the G2 phase. We also found that GFLG-iRGD possessed cytotoxicity at the tested concentrations.

---

[1] This chapter has been modified with permission from the following the publication: Peng ZH, Kopeček J. Synthesis and activity of tumor-homing peptide iRGD and histone deacetylase inhibitor Valproic acid conjugate. *Bioorg. Med. Chem. Lett*. 2014, 2014, 24(8):1928-33.

3.2 Introduction

Epigenetic therapy has shown promise in the treatment of cancer (1). Manipulation of the histone acetylation by histone acetyltransferases (HATs) and histone deacetylases (HDACs) regulate epigenetics gene expression. HDACs catalyze the removal of acetyl groups from amino terminal lysine residue in histones; the resulting ionic interactions between the positively charged histones and the negatively charged DNA induce transcriptional repression through chromatin condensation (2–5). HDACs activities in prostate cancer cell lines are two to three folds higher than that in benign prostatic hyperplasia (BPH) cell line (6,7). HDAC isoforms are strongly expressed in majority of the prostate carcinomas (HDAC1: 69.8%, HDAC2: 74%, HDAC3: 94.8%) (8). In the last decade, HDAC inhibitors (HDACi) have shown promise in the treatment of cancers, including prostate cancer. As shown in Figure 3.1, HDCAi are classified into four subtypes: hydroxamate, cyclic peptide, short-chain fatty acid, and benzamide (9). HDACi have shown promising in antiproliferative and apoptotic properties on various cancer cells, including prostate cancer cells (10). Vorinostat and romidepsin have been approved by United States Food and Drug Administration for treating cutaneous and peripheral T-cell lymphoma, respectively, and several HDACi have entered clinical trial. However, HDACi are not satisfactory for solid tumor treatment. For example, Vorinostat has significant toxicities in clinical trial in patients with metastatic castration resistant prostate cancer (11,12). Targeting strategies have been used to improve the efficacy of HDACi and lower their toxicities (12).

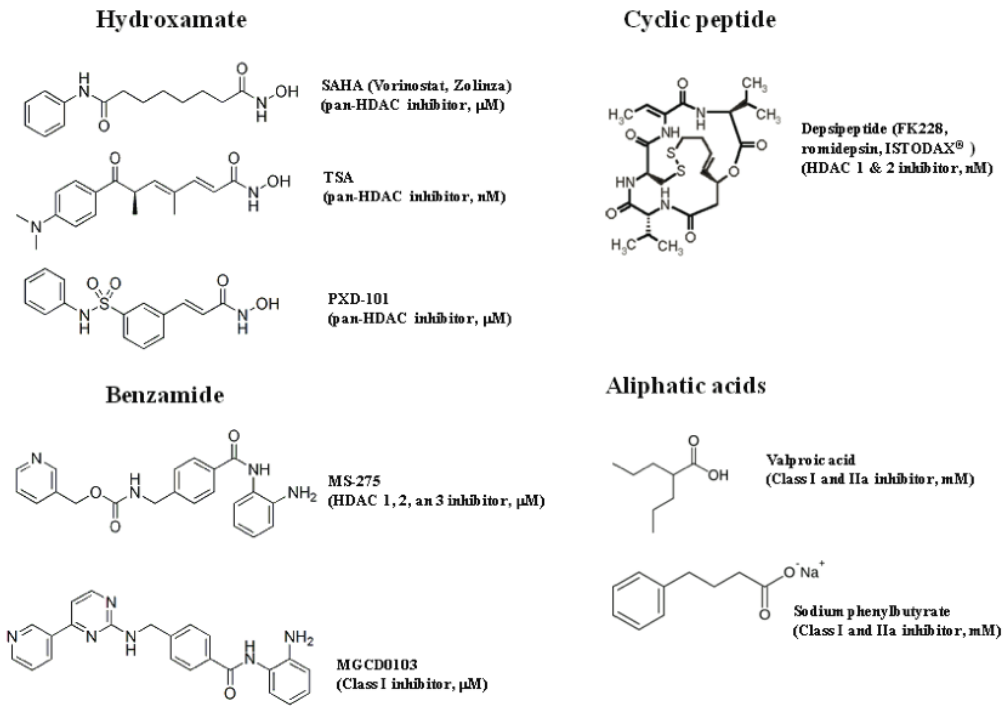

Figure 3.1: Structure of HDAC inhibitors. Adapted from reference (13).

Valproic acid (VPA, 2-propylpentanoic acid) is a short-chain branched fatty acid, which has been used as an anticonvulsant for more than four decades. Now VPA has shown promise for inhibiting tumor growth and metastasis. VPA inhibits HDACs and causes histone hyperacetylation at therapeutic concentrations (14,15). VPA selectively decreases HDAC expression in human ovarian cancer cells, causes tumor cell growth arrest, and inhibits HeLa cervical cancer cell growth (14–18). The combination of VPA with other drugs has enhanced anticancer effect. Specifically, its combination with cyclin-dependent kinase (CDK) inhibitor is effective in treatment of lung tumor xenograft in SCID mice (19). In addition, VPA and Aspirin have synergistic cytotoxicity against hepatocellular cancer cells (20). Aurora Kinase Inhibitors can also enhance the cytotoxicity of VPA against gynecologic cancer cells (21). VPA enhanced the sensitivity of anaplastic thyroid cancer cells toward doxorubicin (22). Exposure to VPA enhanced the radiosensitivity of prostate cancer (23). Chronic administration of VPA caused the increase of acetylation of histone H3, cancer cell cycle arrest, and reduction of tumor xenograft (24,25). Furthermore, VPA has the potential to inhibit prostate cancer metastasis by inhibiting prostate cancer migration through up-regulating E-cadherin expression (26).

Protein transduction domains (PTDs) or cell-penetrating peptides (CPPs) are often attached to therapeutics to enhance their cellular uptake (27,28). However, most CPPs cause undesired toxicities because they cannot distinguish between normal and tumor cells. Targeted drug delivery strategies are often used to reduce therapeutics' side effects in normal cells (29–32). Targeting moieties have been also attached to CPPs or CPP conjugates to improve CPP's selectivity (33,34). Recently, Ruoslahti and

coworkers discovered that a specific tumor-homing peptide iRGD, which combines a targeting peptide and a cell-penetrating peptide, can significantly improve drug uptake into specific tumors (35,36).

In this study, we designed, prepared and tested a novel drug conjugate VPA-GFLG-iRGD. The structure of VPA-GFLG-iRGD is composed of three components (Figure 3.2.A): cell-penetrating peptide iRGD, VPA, and lysosomally degradable tetrapeptide (-GFLG-) spacer. The RGD sequence in the VPA-GFLG-iRGD will recognize the integrin receptor on the prostate cancer cell surface. The RGD-integrin interaction will assist the uptake of conjugate VPA-GFLG-iRGD into prostate cancer cells.

3.3 Materials and Methods

3.3.1 Materials

Protected amino acids and Rink amide MBHA resin were purchased from AAPPTEC (Louisville, KY). 1-[Bis(dimethylamino)methylene]-1H-1,2,3-triazolo[4,5-b]pyridinium 3-oxid hexafluorophosphate (HATU) was purchased from P3bioSystems (Shelbyville, KY). Thallium (III) trifluoroacetate ($Tl(OOCF_3)_3$), piperidine, *N*-methylmorpholine (NMM), and triisopropylsilane (TIPS) were purchased from Sigma Aldrich (St. Louis, MO). Tris(2-carboxyethyl) phosphine hydrochloride (TCEP) was purchased from Thermo Scientific (Waltham, MA). Dimethylformamide (DMF), acetonitrile (ACN) and methanol were purchased from Fisher Scientific (Fair Lawn, NJ). Trifluoroacetic acid (TFA) was purchased from Acros (Fair Lawn, NJ).

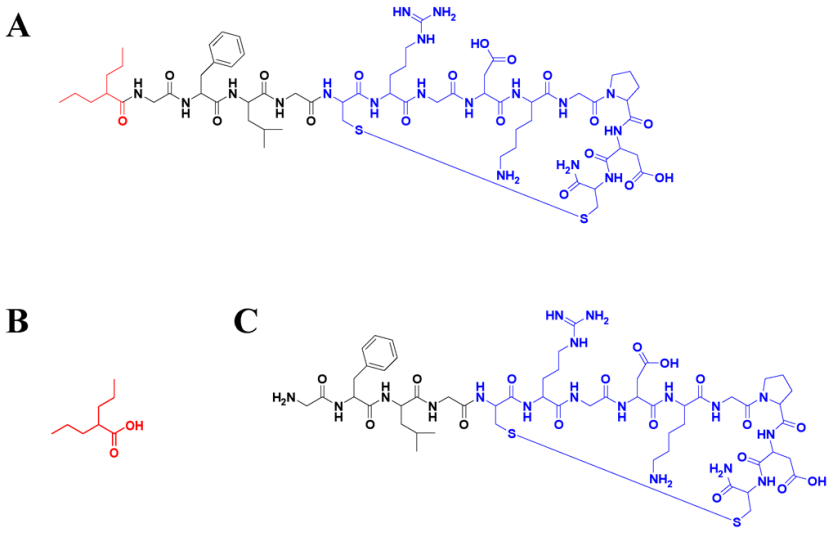

Figure 3.2: Chemical structure of VPA-GFLG-iRGD (A),
VPA (B) and GFLG-iRGD (C).

3.3.2 Synthesis of VPA-GFLG-iRGD and GFLG-iRGD

As shown in Figure 3.3, the conjugate VPA-GFLG-iRGD was prepared by solid phase synthesis. The first step was to prepare the linear conjugate VPA-Gly-Phe-Leu-Gly-Cys(Acm)-Arg(Pbf)-Gly-Asp(OBu^t)-Lys(Boc)-Gly-Pro-Asp(OBu^t)-Cys(Acm) on the MBHA Rink amide resin (37). The general procedure for stepwise attachment of each protected amino acid (Fmoc-Cys(Acm)-OH, Fmoc-Asp(OBu^t)-OH, Fmoc-Pro-OH, Fmoc-Gly-OH, Fmoc-Lys(Boc)-OH, Fmoc-Asp(OBu^t)-OH, Fmoc-Gly-OH, Fmoc-Arg(Pbf)-OH, Fmoc-Cys(Acm)-OH, Fmoc-Gly-OH, Fmoc-Leu-OH, Fmoc-Phe-OH, Fmoc-Gly-OH) (468 μmol), and VPA (468 μmol) on MBHA Rink amide resin (300 mg, 156 μmol) includes two parts: (i) 20% of piperidine in DMF was mixed with resin for 5 min to remove Fmoc protecting group; (ii) the Fmoc protected amino acid or VPA was dissolved in a mixture of 0.4 mM *N*-methylmorpholine (NMM) and DMF then incubated with the resin for 20 min at room temperature. 1-[Bis(dimethylamino)methylene]-1H-1,2,3-triazolo[4,5-b]pyridinium 3-oxid hexafluoro phosphate (HATU) was used as the coupling agent.

The second step was to cyclize the iRGD peptide via a disulfide bridge by treating the resin bound peptide with a solution of $Tl(OOCCF_3)_3$ in DMF (38). Finally, the peptide conjugate was cleaved from the resin by using a mixture of H_2O/TIPS/TFA = 2.5/2.5/95. Other acid labile protecting groups (Bu^t on Asp, Boc on Lys, and Pbf on Arg) were also removed during the cleavage process.

The preparation of GFLG-iRGD is similar as that of VPA-GFLG-iRGD except that no VPA was added during the coupling procedure.

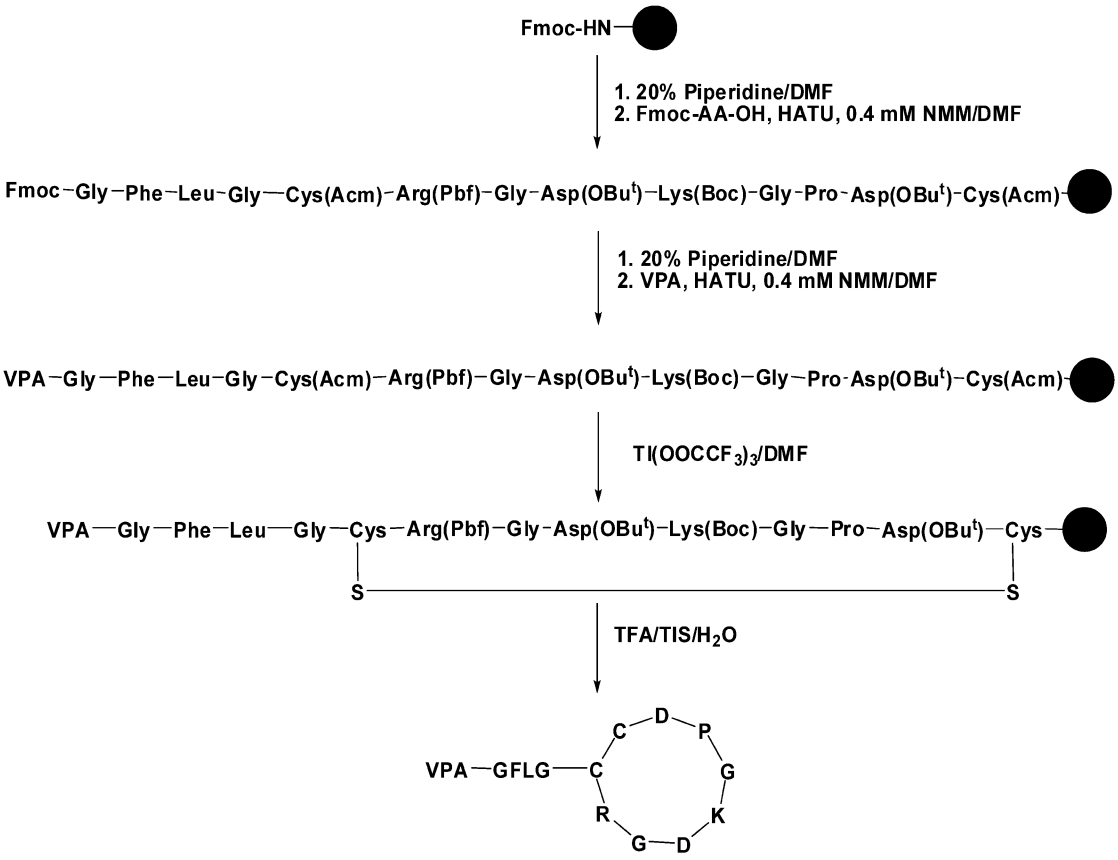

Figure 3.3: Synthetic scheme of conjugate VPA-GFLG-iRGD.

3.3.3 Purification and characterization of GFLG-iRGD and VPA-GFLG-iRGD

Both conjugates were purified by RP-HPLC (Agilent 1100 series) equipped with a semipreparative ZORBAX 300SB-C18 column (5 μm, 9.4*250 mm) from Agilent Technologies (Santa Clara, CA). The purity of conjugates were checked with analytical ZORBAX 300SB-C18 column (5 μm, 4.6*250 mm) in the same instrument as used for purification. Two buffers were used as elution agents: buffer A (0.1% TFA in DI water), buffer B (0.1% TFA in acetonitrile). The structures of these two conjugates were measured by MALDI-TOF mass spectrometry (Voyager-DE STR Biospectromety Workstation, Perseptive Biosystems, Framingham, MA).

3.3.4 Reduction of VPA-GFLG-iRGD

The reduction scheme of VPA-GFLG-iRGD is shown in Figure 3.4. To a vial was added 0.2 mg of conjugate VPA-GFLG-iRGD and 0.5 mL of 10 mM TCEP in 10 mM PBS buffer with 1 mM EDTA. The mixture solution was incubated at 37 ^{o}C for 2 h. The reduced product was analyzed with MALDI-TOF mass spectrometry (Voyager-DE STR Biospectromety Workstation, Perseptive Biosystems, Framingham, MA).

3.3.5 Cell culture

DU-145 prostate cancer cells (ATCC, Manassas, VA) were grown in RPMI-1640 media (Sigma-Aldrich, St. Louis, MO) supplemented with 10% (v/v) FBS, 100 U/ml penicillin, and 100 μg/mL streptomycin (Gibco, Carlsbad, CA) at 37 ^{o}C in a humidified atmosphere of 5% CO2 (v/v). Cells were passaged every 3-4 d and stopped at passage 20.

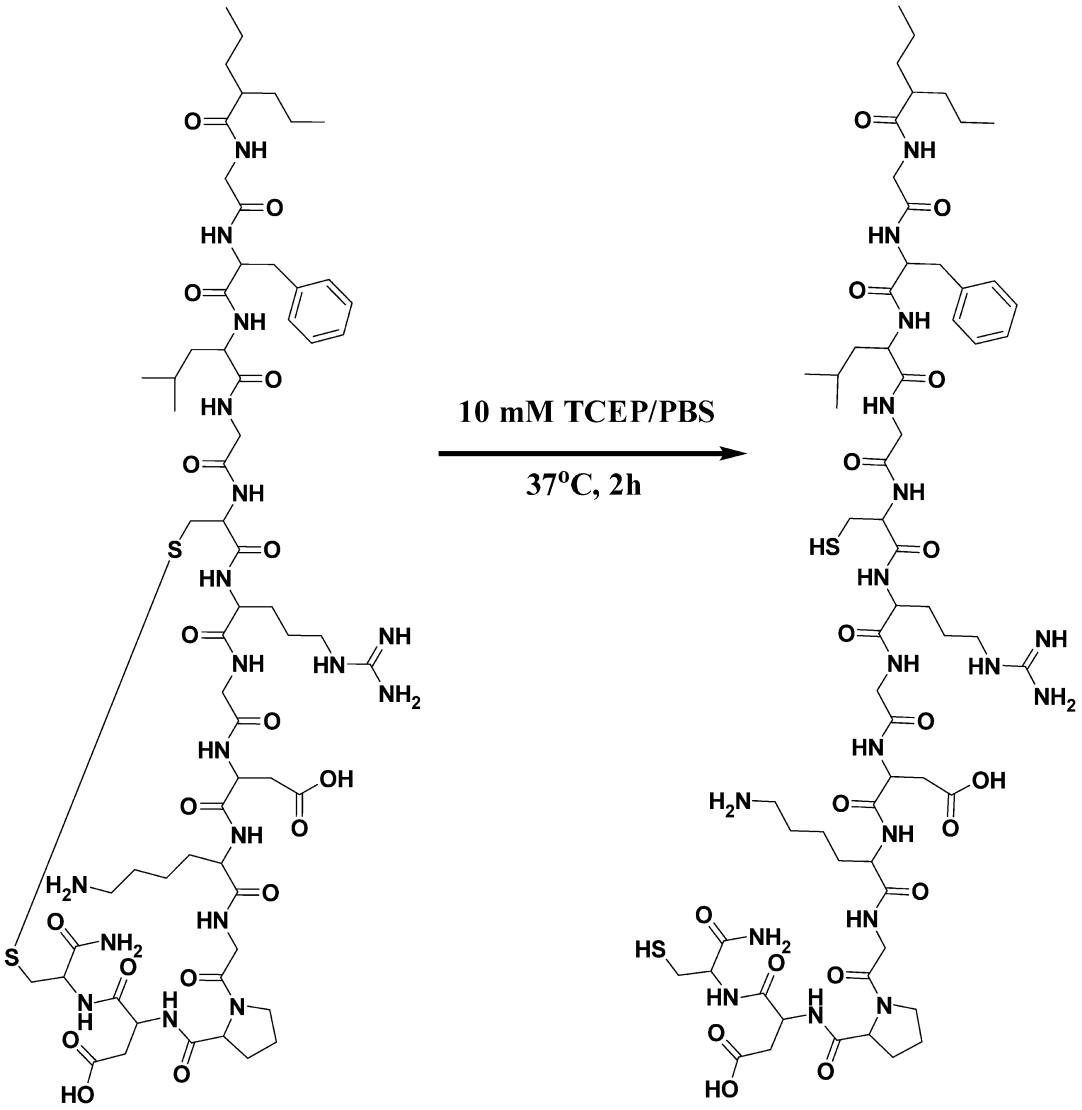

Figure 3.4: Scheme for reduction of conjugate VPA-GFLG-iRGD.

3.3.6 Induction of DU-145 cell cycle arrest by VPA-GFLG-iRGD, VPA, GFLG-iRGD or a mixture of VPA and GFLG-iRGD

In the cell cycle arrest experiments, the following steps were performed: (I) DU-145 cells were seeded at a density of $5*10^5$cells/well in 6-well plates for 24 h; (II) the media was replaced with 1.5 mM of VPA, GFLG-iRGD, VPA-GFLG-iRGD, or a mixture of VPA and GFLG-iRGD, then incubated for another 24 h; (III) the media was removed, and the cells were washed with PBS; (IV) the cells were detached from 6-well plates, and transferred to 1.5 mL Eppendorf vials; (V) after removing the supernatant, the cells were resuspended in 100 µL PBS; (VI) added 400 µL of ice cold 100% ethanol to each vial and kept at room temperature for 2 h; (VII) added 1 mL of PBS to cells and spun for 5 min, then aspirated and washed with 1 mL PBS; (VIII) resuspended cells in 500 µL of propidium iodide (PI) staining solution (50 µg/mL PI, 200 µg/mL RNase); (IX) covered with foil and analyzed on flow cytometer. The cell cycle arrest assay was repeated four times.

3.3.7 Cytotoxicity of VPA-GFLG-iRGD, VPA, GFLG-iRGD or a mixture of VPA and GFLG-iRGD

The DU-145 cells were seeded in 96-well plates at a density of 3,500 cell/well in 100 µL RMPI-1640 media containing 10% fetal bovine serum. After incubating at 37 ^oC for 24 h, media was removed and replaced with 1.5 mM of VPA, GFLG-iRGD, VPA plus GFLG-iRGD or VPA-GFLG-iRGD. After incubation at 37 ^oC for 72 h, 50 µL of 1:5 diluted original Cell Counting Kit-8 (CCK-8) (Dojindo, Japan) solution was added and incubated at 37 ^oC for 1-2 h. The absorbance of the reduced product formazan at

450 nm (630 nm as reference) was measured with a microplate reader (Bio-Rad, Hercules, CA). The data were analyzed with One-Way ANOVA plus Turkey's post-hoc test by using Prism 5 software.

3.4 Results and Discussion

3.4.1 Synthesis and characterization of VPA-GFLG-iRGD and GFLG-iRGD

The structure of the VPA-GFLG-iRGD conjugate was confirmed by MALDI-TOF (matrix-assisted laser desorption ionization, time-of-flight) mass spectroscopy. As shown in Figure 3.5, the peaks at m/z 1447.69 correspond to the desired product ($[M+H]^+$). The elution time of VPA-GFLG-iRGD and its reduced product on an HPLC analytical column (Agilent, 300SB-C18, 4.6 * 250 mm, 5 μm) were 14.12 and 14.53 min, respectively, when using a gradient solvent from 10% Buffer B to 100% Buffer B in 30 min (Buffer A and Buffer B are the same as used in Section 3.3.3). The reduction of the disulfide bond produced two sulfhydryl groups, which should result in a mass 2 Da higher than the original VPA-GFLG-iRGD. As shown in Figure 3.6, the peak at m/z (MALDI-TOF) 1449.56 corresponds to the reduced product $[M_1+H]^+$. Mass spectrum peaks $[M_1+Na]^+$ and $[M_1+K]^+$ at m/z 1471.54 and 1487.49, respectively, support the structure of the reduced product.

3.4.2 Induction of cell cycle arrest by VPA-GFLG-iRGD and controls

Representative cell cycle arrest results are shown in Figure 3.7, and the average cell cycle arrest results are shown in Figure 3.8. The treatment with VPA-GFLG-iRGD or a mixture of VPA and GFLG-iRGD showed a statistically significant difference in the

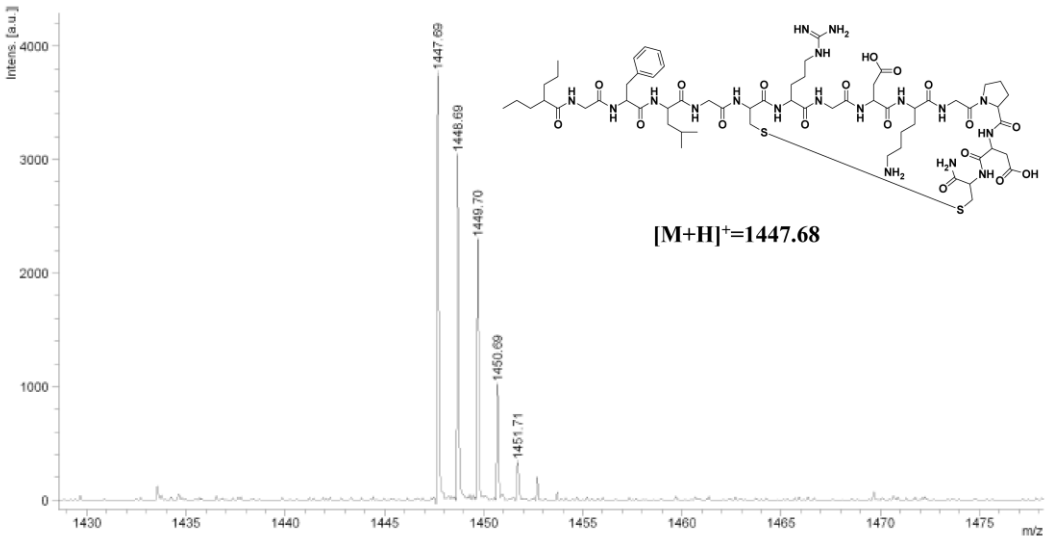

Figure 3.5: Mass spectrum of conjugate VPA-GFLG-iRGD.

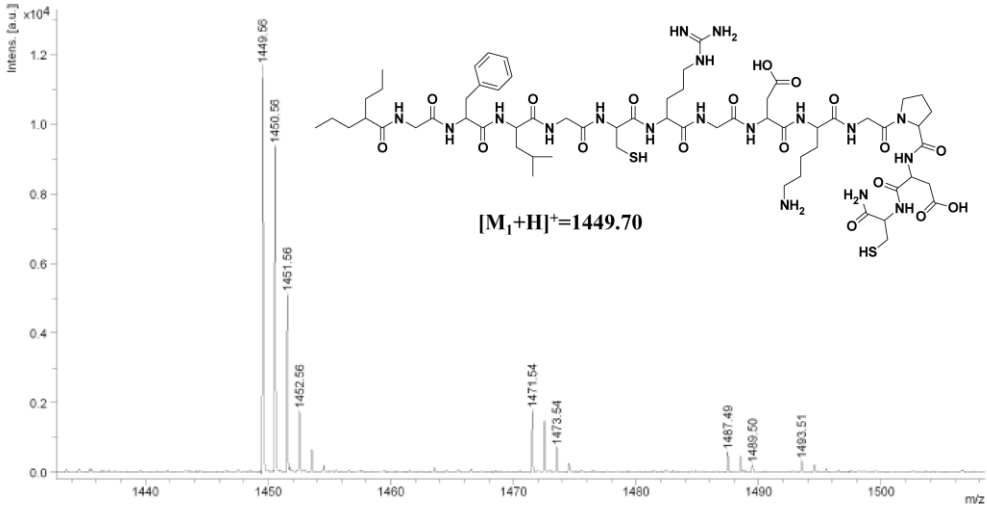

Figure 3.6: Mass spectrum of the reduced product from VPA-GFLG-iRGD.

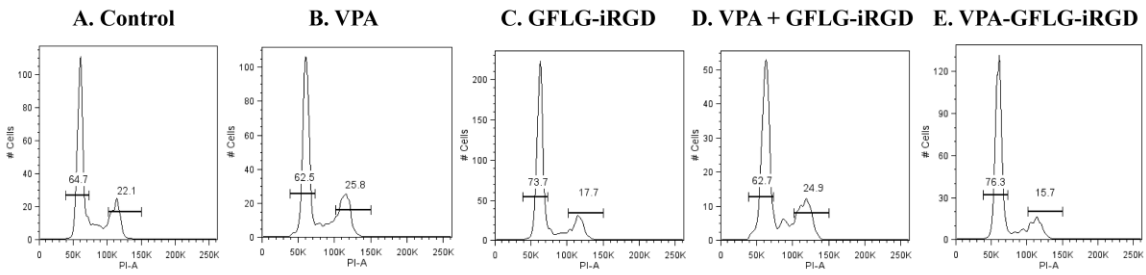

Figure 3.7: Representative flow cytometric pictures and percentages of cells in G1 and G2 phase of the DU-145 cell cycle: (A) control, (B) 1.5 mM VPA, (C) 1.5 mM GFLG-iRGD, (D) 1.5 mM VPA + 1.5 mM GFLG-iRGD, (E) 1.5 mM VPA-GFLG-iRGD.

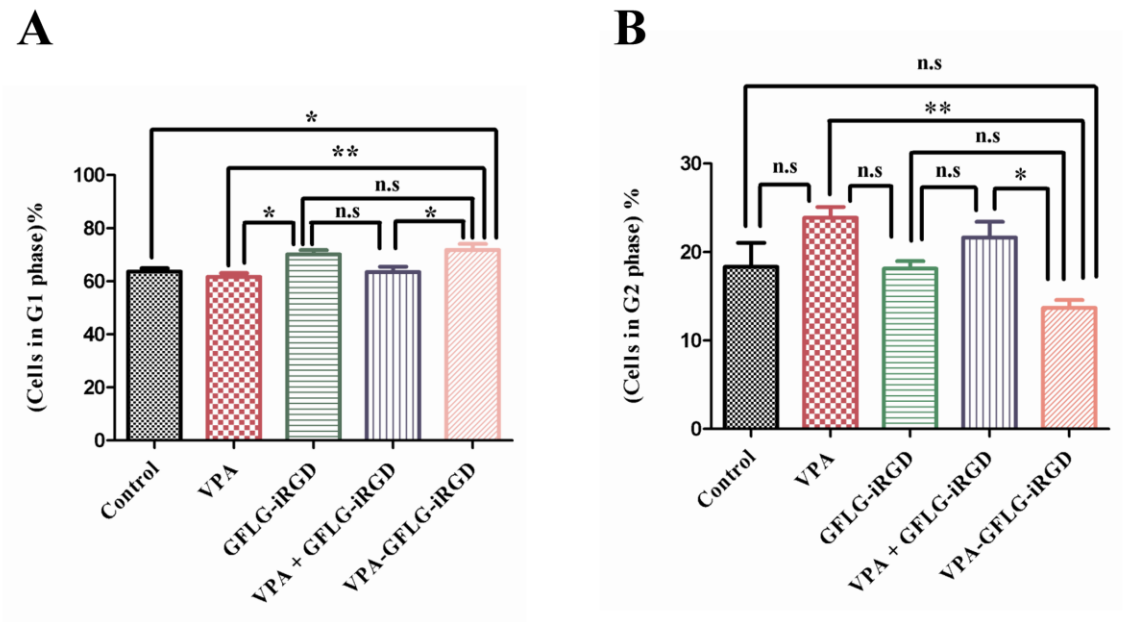

Figure 3.8: Average percentage of cells in G1 (A) and G2 (B) phase of the DU-145 cell cycle. Statistics: One Way ANOVA plus Turkey's post-hoc test (0.001<P<0.01 = **; 0.01<P<0.05 = *; not significant = n.s).

distribution of DU-145 cells in G1 and G2 phase. The treatment with conjugate VPA-GFLG-iRGD resulted in a decreased percentage of DU-145 cells in the G2 phase, whereas the exposure of cells to a mixture of VPA and GFLG-iRGD led to an increased percentage of cells in the G2 phase. The decreased G2 phase cell population in VPA-GFLG-iRGD treated group might be attributed to the blockage of $\alpha_v\beta_3$ and $\alpha_v\beta_5$ on the DU-145 cell surface by RGD (39).

3.4.3 Cell cytotoxicity of VPA-GFLG-iRGD and related controls against DU-145

The average viable cell number in untreated group was set as 100%. The viability % was calculated by dividing the viable cell number in the treated group by the average viable cell number in the untreated group. The results are expressed as (mean ± SEM) %. The results after treatment with 0.5 mM drug or drug equivalents are shown in Figure 3.9.A: control (99.97 ± 0.84), VPA (99.56 ± 7.46), GFLG-iRGD (70.52 ± 2.89), GFLG-iRGD + VPA (57.87 ± 6.01), VPA-GFLG-iRGD (69.30 ± 0.30). Figure 3.9.B shows the results after exposure to 1.5 mM drug or drug equivalent: control (100.00 ± 2.47), VPA (79.87 ± 2.44), GFLG-iRGD (58.67 ± 3.89), GFLG-iRGD + VPA (31.22 ± 1.33), VPA-GFLG-iRGD (38.96 ± 2.76). As shown in Figure 3.9.B, VPA-GFLG-iRGD was significantly more toxic than either VPA or GFLG-iRGD. Although the combination of VPA and GFLG-iRGD seems to possess a slightly higher toxicity than VPA-GFLG-iRGD, the difference is not statistically significant. Interestingly, we found that GFLG-iRGD has cytotoxicity to DU-145 cells at the two concentrations used. The cytotoxicity of GFLG-iRGD may be due to the blockage of $\alpha_v\beta_3$ and $\alpha_v\beta_5$ on the DU-145

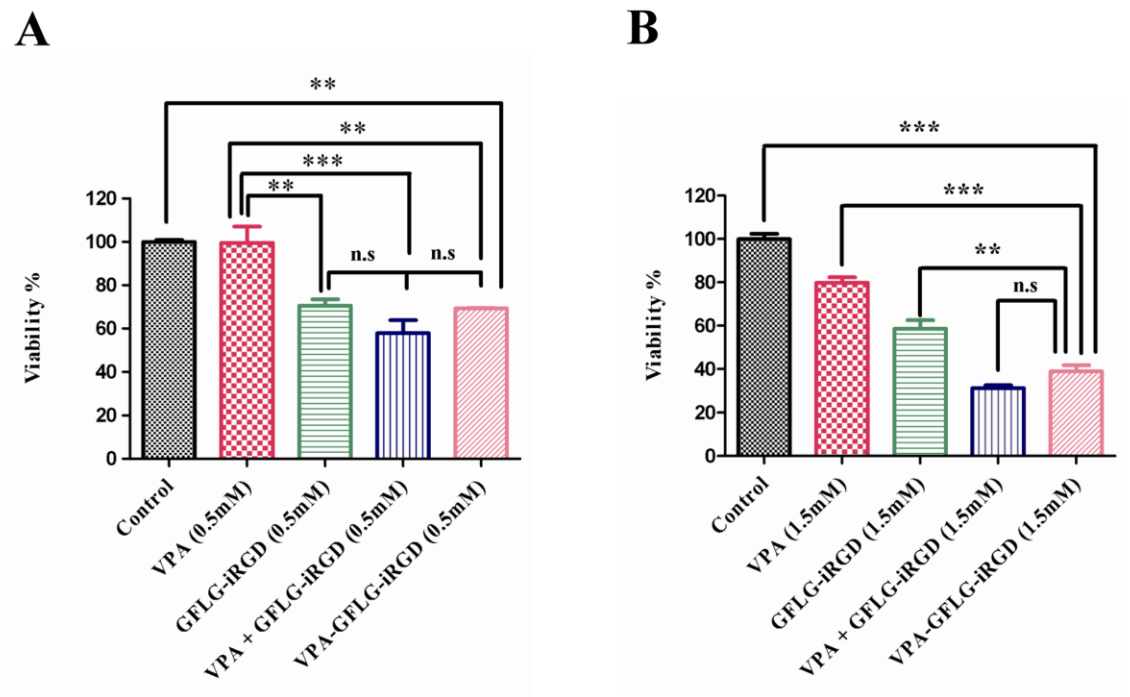

Figure 3.9: Cytotoxicity of VPA, GFLG-iRGD, VPA-GFLG-iRGD, and a mixture of VPA and GFLG-iRGD against DU-145 prostate cancer cells: (A) 0.5 mM; (B) 1.5 mM. Statistics: One Way ANOVA plus Turkey's post-hoc test ($P<0.001$ = ***; $0.001<P<0.01$ = **; not significant = n.s).

cell surface by RGD (40). This blockage could cause the inhibition of integrin-linked kinase activity and phosphorylation of PKB/Akt on serin-473, which inhibited the cell proliferation [39]. The data were analyzed with One-Way ANOVA plus Turkey's post-hoc test by using Prism 5 GraphPad software.

3.5 Conclusion

In summary, we have successfully prepared a tumor cell penetrating peptide iRGD targeted HDAC inhibitor conjugate (VPA-GFLG-iRGD). The conjugate structure was confirmed by both mass spectrometry of cyclized construct and of its reduced product. This synthesis methodology will help to design other iRGD or other cyclic peptide targeted pro-drugs. The cytotoxicity of VPA toward prostate cancer cells was enhanced both by covalent attachment or mixture with iRGD. Both forms of VPA changed the stage of cell cycle arrest: the VPA-GFLG-iRGD conjugate induced the decreased DU-145 cell population in G2 phase, and the combination of VPA and GFLG-iRGD enhanced G2 cell cycle arrest in DU-145 cells. We also found that the iRGD derivative has some cytotoxicity at the tested concentrations. The exact iRGD uptake mechanism is still being evaluated.

3.6 References

1. Dawson MA, Kouzarides T. Cancer epigenetics: from mechanism to therapy. Cell. 2012;150:12–27.

2. Roth SY, Denu JM, Allis CD. Histone acetyltransferases. Annu Rev Biochem. 2001;70:81–120.

3. Xu WS, Parmigiani RB, Marks PA. Histone deacetylase inhibitors: molecular mechanisms of action. Oncogene. 2007;26:5541–52.

4. Bolden JE, Peart MJ, Johnstone RW. Anticancer activities of histone deacetylase inhibitors. Nat Rev Drug Discov. 2006;5:769–84.

5. Thiagalingam S, Cheng K-H, Lee HJ, Mineva N, Thiagalingam A, Ponte JF. Histone deacetylases: unique players in shaping the epigenetic histone code. Ann N Y Acad Sci. 2003;983:84–100.

6. Patra SK, Patra A, Dahiya R. Histone deacetylase and DNA methyltransferase in human prostate cancer. Biochem Biophys Res Commun. 2001;287:705–13.

7. Halkidou K, Gaughan L, Cook S, Leung HY, Neal DE, Robson CN. Upregulation and nuclear recruitment of HDAC1 in hormone refractory prostate cancer. The Prostate. 2004;59:177–89.

8. Weichert W, Röske A, Gekeler V, Beckers T, Stephan C, Jung K, et al. Histone deacetylases 1, 2 and 3 are highly expressed in prostate cancer and HDAC2 expression is associated with shorter PSA relapse time after radical prostatectomy. Br J Cancer. 2008;98:604–10.

9. Sharma NL, Groselj B, Hamdy FC, Kiltie AE. The emerging role of histone deacetylase (HDAC) inhibitors in urological cancers. BJU Int. 2013;111:537–42.

10. Frønsdal K, Saatcioglu F. Histone deacetylase inhibitors differentially mediate apoptosis in prostate cancer cells. The Prostate. 2005;62:299–306.

11. Bradley D, Rathkopf D, Dunn R, Stadler WM, Liu G, Smith DC, et al. Vorinostat in advanced prostate cancer patients progressing on prior chemotherapy (National Cancer Institute Trial 6862): trial results and interleukin-6 analysis: a study by the Department of Defense Prostate Cancer Clinical Trial Consortium and University of Chicago Phase 2 Consortium. Cancer. 2009;115:5541–9.

12. Gryder BE, Akbashev MJ, Rood MK, Raftery ED, Meyers WM, Dillard P, et al. Selectively targeting prostate cancer with antiandrogen equipped histone deacetylase inhibitors. ACS Chem Biol. 2013;8:2550–60.

13. Kim H-J, Bae S-C. Histone deacetylase inhibitors: molecular mechanisms of action and clinical trials as anti-cancer drugs. Am J Transl Res. 2011;3:166–79.

14. Gurvich N, Tsygankova OM, Meinkoth JL, Klein PS. Histone deacetylase is a target of valproic acid-mediated cellular differentiation. Cancer Res. 2004;64:1079–86.

15. Göttlicher M, Minucci S, Zhu P, Krämer OH, Schimpf A, Giavara S, et al. Valproic acid defines a novel class of HDAC inhibitors inducing differentiation of transformed cells. EMBO J. 2001;20:6969–78.

16. Kwiecińska P, Wróbel A, Taubøll E, Gregoraszczuk EŁ. Valproic acid, but not levetiracetam, selectively decreases HDAC7 and HDAC2 expression in human ovarian cancer cells. Toxicol Lett. 2013;

17. Phiel CJ, Zhang F, Huang EY, Guenther MG, Lazar MA, Klein PS. Histone deacetylase is a direct target of valproic acid, a potent anticonvulsant, mood stabilizer, and teratogen. J Biol Chem. 2001;276:36734–41.

18. Han BR, You BR, Park WH. Valproic acid inhibits the growth of HeLa cervical cancer cells via caspase-dependent apoptosis. Oncol Rep. 2013;30:2999–3005.

19. Shirsath N, Rathos M, Chaudhari U, Sivaramakrishnan H, Joshi K. Potentiation of anticancer effect of valproic acid, an antiepileptic agent with histone deacetylase inhibitory activity, by the cyclin-dependent kinase inhibitor P276-00 in human non-small-cell lung cancer cell lines. Lung Cancer Amst Neth. 2013;82:214–21.

20. Li X, Zhu Y, He H, Lou L, Ye W, Chen Y, et al. Synergistically killing activity of aspirin and histone deacetylase inhibitor valproic acid (VPA) on hepatocellular cancer cells. Biochem Biophys Res Commun. 2013;436:259–64.

21. Li Y, Liu T, Ivan C, Huang J, Shen D-Y, Kavanagh JJ, et al. Enhanced cytotoxic effects of combined valproic acid and the aurora kinase inhibitor VE465 on gynecologic cancer cells. Front Oncol. 2013;3:58.

22. Catalano MG, Fortunati N, Pugliese M, Poli R, Bosco O, Mastrocola R, et al. Valproic acid, a histone deacetylase inhibitor, enhances sensitivity to doxorubicin in anaplastic thyroid cancer cells. J Endocrinol. 2006;191:465–72.

23. Chen X, Wong JYC, Wong P, Radany EH. Low-dose valproic acid enhances radiosensitivity of prostate cancer through acetylated p53-dependent modulation of mitochondrial membrane potential and apoptosis. Mol Cancer Res. 2011;9:448–61.

24. Sidana A, Wang M, Shabbeer S, Chowdhury WH, Netto G, Lupold SE, et al. Mechanism of growth inhibition of prostate cancer xenografts by valproic acid. J Biomed Biotechnol. 2012;2012:180363.

25. Xia Q, Sung J, Chowdhury W, Chen C-L, Höti N, Shabbeer S, et al. Chronic administration of valproic acid inhibits prostate cancer cell growth in vitro and in vivo. Cancer Res. 2006;66:7237–44.

26. Zhang L, Wang G, Wang L, Song C, Wang X, Kang J. Valproic acid inhibits prostate cancer cell migration by up-regulating E-cadherin expression. Pharm. 2011;66:614–8.

27. Goun EA, Shinde R, Dehnert KW, Adams-Bond A, Wender PA, Contag CH, et al. Intracellular cargo delivery by an octaarginine transporter adapted to target prostate cancer cells through cell surface protease activation. Bioconjug Chem. 2006;17:787–96.

28. Dubikovskaya EA, Thorne SH, Pillow TH, Contag CH, Wender PA. Overcoming multidrug resistance of small-molecule therapeutics through conjugation with releasable octaarginine transporters. Proc Natl Acad Sci U S A. 2008;105:12128–33.

29. Peng Z-H, Sima M, Salama ME, Kopečková P, Kopeček J. Spacer length impacts the efficacy of targeted docetaxel conjugates in prostate-specific membrane antigen expressing prostate cancer. J Drug Target. 2013;21:968–80.

30. Yang Z, Lee JH, Jeon HM, Han JH, Park N, He Y, et al. Folate-based near-infrared fluorescent theranostic gemcitabine delivery. J Am Chem Soc. 2013;135:11657–62.

31. Vlashi E, Kelderhouse LE, Sturgis JE, Low PS. Effect of folate-targeted nanoparticle size on their rates of penetration into solid tumors. ACS Nano. 2013;7:8573–82.

32. Miura Y, Takenaka T, Toh K, Wu S, Nishihara H, Kano MR, et al. Cyclic RGD-linked polymeric micelles for targeted delivery of platinum anticancer drugs to glioblastoma through the blood-brain tumor barrier. ACS Nano. 2013;7:8583–92.

33. Myrberg H, Zhang L, Mäe M, Langel U. Design of a tumor-homing cell-penetrating peptide. Bioconjug Chem. 2008;19:70–5.

34. Koren E, Apte A, Jani A, Torchilin VP. Multifunctional PEGylated 2C5-immunoliposomes containing pH-sensitive bonds and TAT peptide for enhanced tumor cell internalization and cytotoxicity. J Control Release. 2012;160:264–73.

35. Sugahara KN, Teesalu T, Karmali PP, Kotamraju VR, Agemy L, Greenwald DR, et al. Coadministration of a tumor-penetrating peptide enhances the efficacy of cancer drugs. Science. 2010;328:1031–5.

36. Sugahara KN, Teesalu T, Karmali PP, Kotamraju VR, Agemy L, Girard OM, et al. Tissue-penetrating delivery of compounds and nanoparticles into tumors. Cancer Cell. 2009;16:510–20.

37. Ye Y, Zhu L, Ma Y, Niu G, Chen X. Synthesis and evaluation of new iRGD peptide analogs for tumor optical imaging. Bioorg Med Chem Lett. 2011;21:1146–50.

38. Page K, Hood CA, Patel H, Fuentes G, Menakuru M, Park JH. Fast Fmoc synthesis of hAmylin1-37 with pseudoproline assisted on-resin disulfide formation. J Pept Sci. 2007;13:833–8.

39. Cruet-Hennequart S, Maubant S, Luis J, Gauduchon P, Staedel C, Dedhar S. alpha(v) integrins regulate cell proliferation through integrin-linked kinase (ILK) in ovarian cancer cells. Oncogene. 2003;22:1688–702.

40. Maubant S, Saint-Dizier D, Boutillon M, Perron-Sierra F, Casara PJ, Hickman JA, et al. Blockade of alpha v beta3 and alpha v beta5 integrins by RGD mimetics induces anoikis and not integrin-mediated death in human endothelial cells. Blood. 2006;108:3035–44.

CHAPTER 4

TUMOR-PENETRATING PEPTIDE TARGETED HPMA COPOLYMER DOXORUBICIN CONJUGATES FOR PROSTATE CANCER TREATMENT

4.1 Summary

On-demand drug release systems are important for improving the efficacy and reducing the side effect of drugs. Here, we describe the design, preparation, and biological properties of stimuli-responsive HPMA copolymer drug and tumor-penetrating peptide conjugates. Doxorubicin (DOX) was conjugated to HPMA copolymer via a lysosomally cleavable tetrapeptide spacer (-GFLG-). Tumor-homing and penetrating peptide iRGD was connected to HPMA copolymer through a matrix metalloproteinase 2 (MMP-2) degradable linker (-PLGLAG-). Free iRGD and monomer MA-GG-PLGLAG-iRGD were prepared with solid phase synthesis. HPMA copolymer-DOX conjugates (P-DOX and P-DOX-PLGLAG-iRGD) were prepared via traditional copolymerization. The uptake of DOX conjugates was tested in both monolayer and multilayer DU-145 prostate cancer cells with flow cytometry. The results have shown that P-DOX-PLGLAG-iRGD treated cells had the strongest fluorescence intensity compared to that of other treated groups (Control, iRGD, P-DOX, P-DOX plus iRGD). The cell cycle arrest, in vitro apoptosis, and cytotoxicity of DOX conjugates and related controls were tested against

DU-145 monolayer prostate cancer cells. Consistent with the drug uptake results, the in vitro results show that P-DOX-PLGLAG-iRGD had the strongest activity against DU-145 prostate cancer cells. The penetration ability of DOX conjugates was tested in 3D multicellular tumor cell spheroids. The results show that the conjugate P-DOX-PLGLAG-iRGD penetrated deepest in tumor cell spheroids.

4.2 Introduction

Nanomedicines are promising in cancer treatment due to their ability to improve the pharmacokinetics and efficacy as well as reduce the side effects of free drugs (1–3). However, more and more researchers question the low translation efficiency of nanomedicines from publications to drugs (4–6). One of the major reasons is that more than 95% of the nanomedicine accumulates in undesired organs (4). Most large molecular weight nanomedicines rely on enhanced permeability and retention (EPR) effect to enter into tumor area, but EPR effect is often compromised by the tumor microenvironment (7,8). The increased interstitial fluid pressure (IFP), dense stromal cells, and extracellular matrix (ECM) hamper the convection of nanomedicine into the tumor (9). Furthermore, the EPR effect is usually over-estimated by ignoring the heterogeneity within and between tumor types, and the variance between patients (10,11). Even in a single tumor, the vessel structure difference between regions results in varying degrees of EPR effect (10,11). The inefficiency and heterogeneity of the EPR effect may be responsible for the lack of overall survival benefit from nanomedicines as compared to their small molecule drug counterparts (10,11). Another important reason for the inefficiency of nanomedicines is that they cannot cross more than one or two cell layers because of their

large size, the high IFP, and the tight structure of tumor (12–16). Therefore, there are two potential ways to promote the translation of nanomedicines from research to the clinic. The first method is to increase the accumulation of nanomedicines in tumors and to facilitate the internalization of nanomedicines into tumor cells by attaching targeting moieties on drug carriers (17). The second method is to enhance the tumor penetration ability of nanomedicines by conjugation with cell-penetrating peptides (CPPs) (7,18).

The newly developed internalizing C-end cyclic peptide iRGD can function as both a tumor-homing and penetrating peptide (19,20). Although iRGD significantly enhanced the cell uptake of different size drugs, the short half life (a few minutes) of free iRGD limits its clinical application because it is cleared from the bloodstream quickly due to proteolysis and rapid renal clearance (21,22). Since the size of iRGD (mass 5 kDa) is much smaller than the pore size of glomeruli (diameter, 8 nm), iRGD can be ultra-filtrated by the kidney completely in a few minutes (21). Conjugation to larger polymers or plasma proteins (albumin and immunoglobulin) are two general strategies to prolong the half life of peptide drugs (21). However, both our and other group's results show that the conjugated form of iRGD may lose its cell penetration/targeting ability as compared to its free form (20). Therefore, we aimed to develop a smart drug delivery system that can prolong the half-life of iRGD as well as preserve its penetration ability. The aim of the study in Chapter 3 was to utilize the targeting effect of iRGD by conjugating iRGD to valproic acid via a tetrapeptide spacer (-GFLG-). A –GFLG- spacer was used so that the drug would be released in the lysosome after the drug conjugate was endocytosed into the tumor cells. The aim of this chapter was to enhance the penetration ability of drugs, so iRGD was required to be released in the tumor microenviroment to regain its penetration

ability. Thus, iRGD was conjugated to a drug delivery system via a tumor microenvironment sensitive spacer in this study.

As shown in Figure 4.1, we designed a MMP-2 stimuli-responsive drug delivery system for treatment of prostate cancer. *N*-(2-hydroxypropyl)methacrylamide (HPMA) was used as the drug carrier backbone because it is water soluble and biocompatible (2,3). Doxorubicin (DOX) was selected as the model drug for two major reasons: first, the fluorescence of DOX will make it easy to track its fate; second, DOX is one of the most effective anticancer drug but it has only limited penetration in prostate cancer (23). DOX was conjugated to HPMA copolymer via a well-defined lysosomally cleavable linker (-glycylphenylalanylleucylglycine-, -GFLG-) to limit nonspecific cytotoxicity because the drug is only released from the conjugate after the conjugates are uptaken into cells (24). We conjugated iRGD to HPMA copolymer via a -PLGLAG- peptide spacer, which was able to be cleaved by MMP-2 in the tumor microenvironment (25,26). MMP-2 was selected as the cleavage enzyme because the expression of MMP-2 is associated with the growth and progression of prostate cancer (27–29). More importantly, MMP-2 is an effective enzyme for peptide substrate cleavage, and the ratio of k_{cat}/K_m was between 1.4 x 10^4 $M^{-1}S^{-1}$ and 2 x 10^5 $M^{-1}S^{-1}$ (30). This strategy has at least three potential advantages. First, the conjugation of iRGD to the HPMA copolymer-drug conjugate actively delivers the drug to the tumor, thus enhancing the accumulation of drug conjugates at the tumor site. Second, the large molecular weight of HPMA copolymer iRGD conjugate increases the half-life of iRGD, thus resulting in increased opportunity to interact with integrin on tumor vessel endothelial cells and tumor cells. This also enhances the accumulation of drug conjugates in the tumor. Third, the penetration ability of free iRGD will be regained

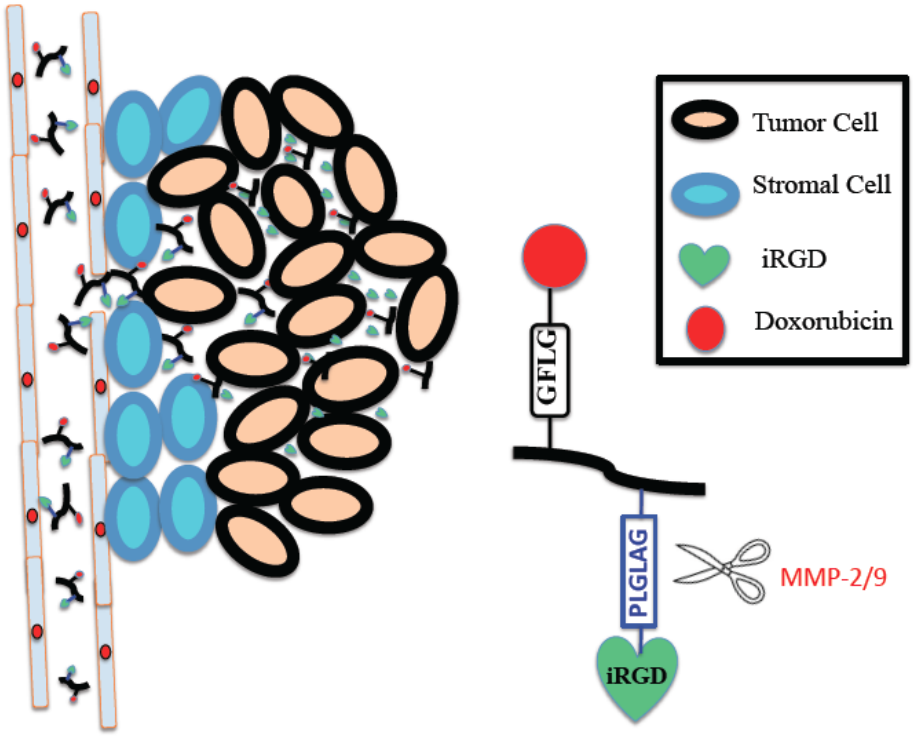

Figure 4.1: Schematic illustration of HPMA copolymer iRGD conjugate delivery.

after the iRGD is released from the HPMA copolymer conjugate in the tumor microenvironment. We hypothesized that the smart iRGD release system will improve the effect of DOX conjugates via the enhanced targeting and penetration effect.

The uptake, penetration, and accumulation of DOX conjugates were tested in DU-145 prostate cancer cell monolayers, multicellular spheroids, and xenograft tumors. The activities of DOX conjugates were evaluated and compared by measuring cell apoptosis and viability.

4.3 Material and Methods

4.3.1 Materials

Doxorubicin hydrochloride was a kind gift from Meiji Seika Kaisha Ltd. (Tokyo, Japan). 1-[Bis(dimethylamino)methylene]-1*H*-1,2,3-triazolo[4,5-*b*]pyridinium 3-oxid hexafluorophosphate (HATU), protected amino acids, and 2-chlorotrytyl chloride resin were purchased from AAPPTEC (Louisville, KY). 2,2'-Azobis(2,4-dimethyl valeronitrile (V-65) was purchased from Wako (Japan). Thallium (III) trifluoroacetate ($Tl(OOCF_3)_3$), *N*-methylmorpholine (NMM), triisopropylsilane (TIPS), *N*,*N*-diisopropylethylamine (DIPEA), and piperidine were purchased from Sigma Aldrich (St. Louis, MO). Tris(2-carboxyethyl) phosphine hydrochloride (TCEP) was purchased from Thermo Scientific (Waltham, MA). General solvents were purchased from Fisher Scientific (Fair Lawn, NJ). Trifluoroacetic acid (TFA) was purchased from Acros (Fair Lawn, NJ). Monomers HPMA (31), MA-GFLG-OH (32), and MA-GG-OH (33) were prepared as described in literature.

4.3.2 Synthesis of monomer MA-GFLG-DOX

The synthesis of monomer MA-GFLG-DOX is shown in Figure 4.2. Doxorubicin hydrochloride (1.16 g, 2 mmol), MA-GFLG-OH (875 mg, 1.9 mmol), NMM (660 μL, 7.1 mmol), DMF (40 mL), and a stirrer bar were added to a 100 mL of round-bottom flask. After the mixture was cooled to -20 ^{o}C, a solution of HATU (760 mg, 2 mmol) in DMF was added slowly into the mixture. The reaction temperature was kept at -20 ^{o}C for 4 h, then slowly increased to room temperature and kept at room temperature for another 20 h. After removing DMF under reduced pressure, the crude product was dissolved in methanol and purified with an LH-20 column. Monomer MA-GFLG-DOX (1.37g, 73%) was obtained after removing the methanol under vacuum.

4.3.3 Preparation of monomer MA-GG-PLGLAG-iRGD and free iRGD

The preparation of monomer MA-GG-PLGLAG-iRGD is shown in Figure 4.3. The synthesis of MA-GG-PLGLAG-iRGD started from manual attachment of the Fmoc-Cys(Acm)-OH to resin by mixing 2-chlorotrityl chloride resin (400 mg, 1.1 mmol/g, 100-200 mesh) with Fmoc-Cys(Acm)-OH (200 μmol, 117 mg) at room temperature for 2 h. The remaining active groups in resin were capped with a mixture solution of dichloromethane (DCM) : methanol (MeOH) : DIPEA = 17 : 2 : 1.

Next, protected amino acids (Fmoc-Asp(OtBu)-OH, Fmoc-Pro-OH, Fmoc-Gly-OH, Fmoc-Lys(Boc)-OH, Fmoc-Asp(OtBu)-OH, Fmoc-Gly-OH, Fmoc-Arg(Pbf)-OH, Fmoc-Cys(Acm)-OH, Fmoc-Gly-OH, Fmoc-Ala-OH, Fmoc-Leu-OH, Fmoc-Gly-OH, Fmoc-Leu-OH, Fmoc-Pro-OH), or MA-GG-OH were loaded to resin sequentially with conventional solid phase synthesis. The general procedure consists of de-protection and

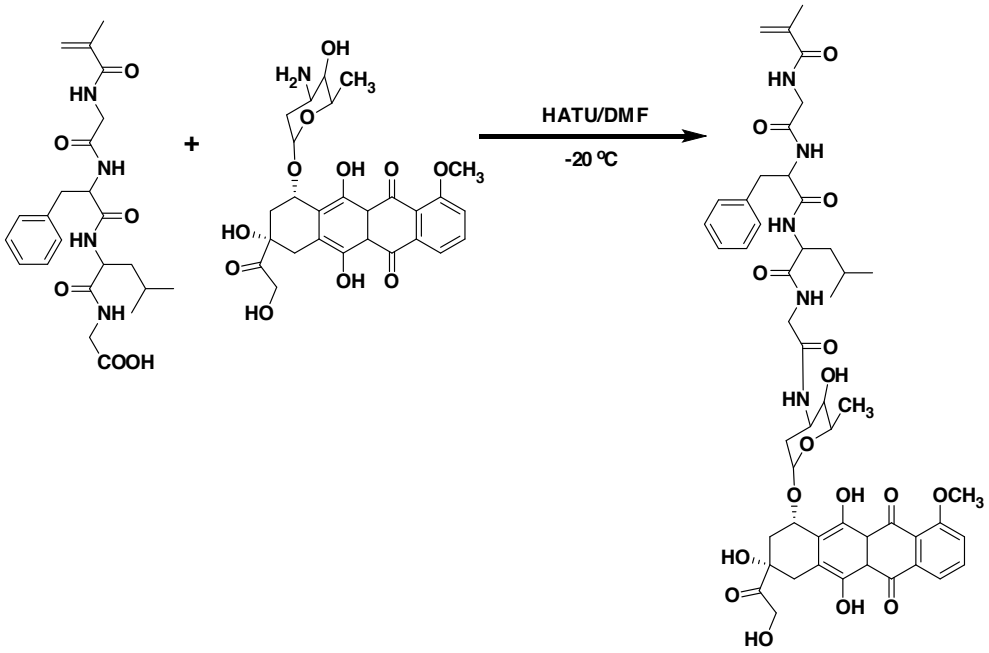

Figure 4.2: Synthetic scheme of monomer MA-GFLG-DOX.

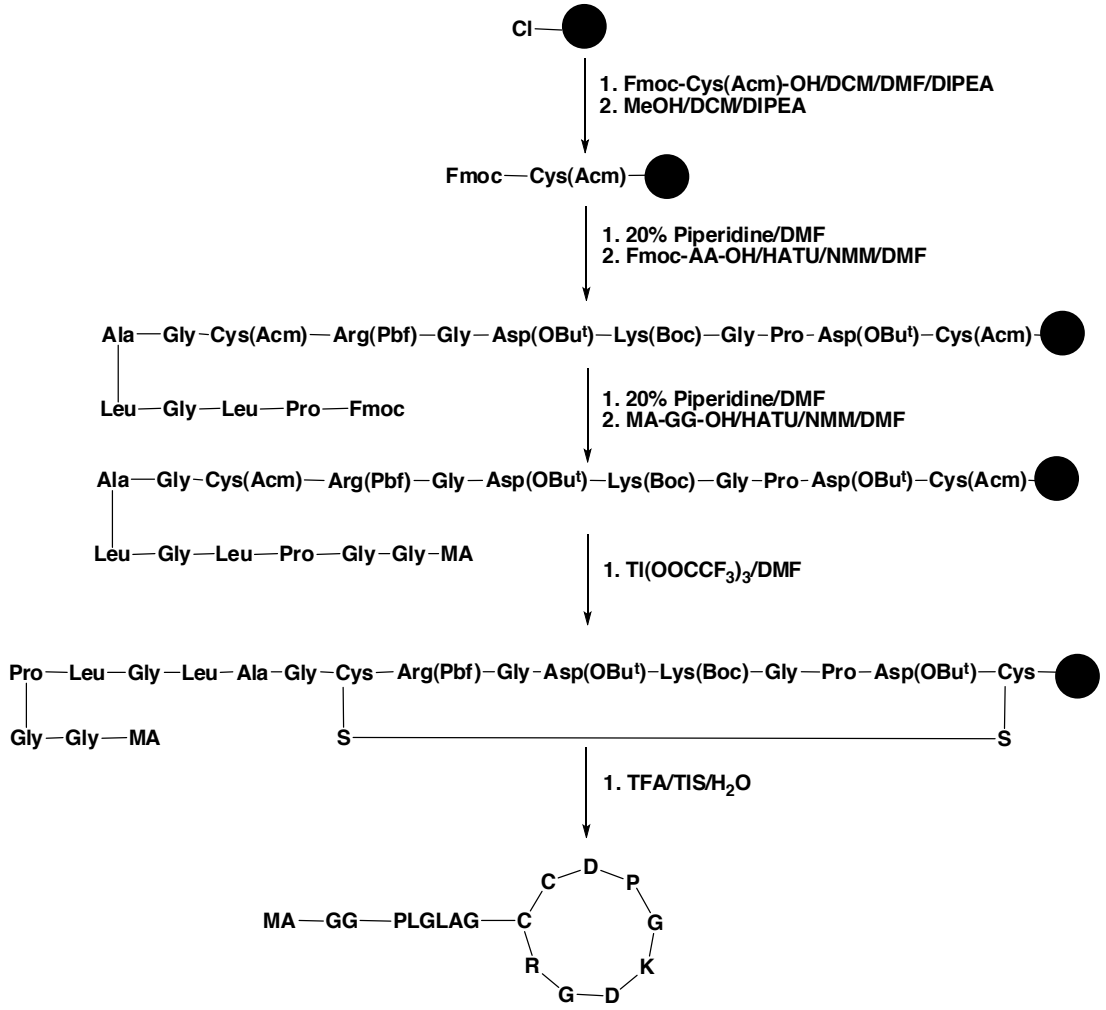

Figure 4.3: Synthetic scheme for monomer MA-GG-PLGLAG-iRGD.

coupling steps: (i) the Fmoc protecting groups were removed by mixing resin bound peptide with 20% piperidine in DMF for 5 min; (ii) the coupling reaction was conducted by mixing three equivalents (600 μmol) of protected amino acid (Fmoc-AA(XXX)-OH) or MA-GG-OH with resin bound peptide in the presence of HATU (228 mg, 600 μmol).

Then, a solution of thallium trifluoroacetate ($Tl(OOCF_3)_3$) (254 mg, 468 μmol) in DMF was added to the resin bound linear peptide and the mixture kept at room temperature under shaking. The $Tl(OOCF_3)_3$ solution was removed by filtration, and the remaining resin was washed with DMF and MeOH, respectively, for three times.

Finally, the crude product MA-GG-PLGLAG-iRGD was obtained by mixing the dried resin bound peptide with 10 mL of cleavage solution (TFA/TIPS/H_2O = 95/2.5/2.5) for 3 h. After removing most of the solvent under vacuum, the remaining residue was added into cold diethyl ether to precipitate the product. After centrifugation, the crude product was dried in air and purified on a HPLC system with detection wavelength (220 nm).

As shown in Figure 4.4, the synthesis procedure of iRGD is similar as that of MA-GG-PLGLAG-iRGD with minor modification.

4.3.4 Preparation and molecular weight (MW) measurement of polymer conjugate P-DOX

The synthetic scheme of P-DOX is shown in Figure 4.5. Monomer HPMA (416 mg, 0.97 mmol), monomer MA-GFLG-DOX (89 mg, 0.03 mmol), initiator V-65 (30 mg, 0.036 mmol), and a mixture of dimethyl sulfoxide (DMSO)/H_2O was added to an ampoule. The mixture was bubbled with nitrogen for 30 min, and the ampoule was sealed. The

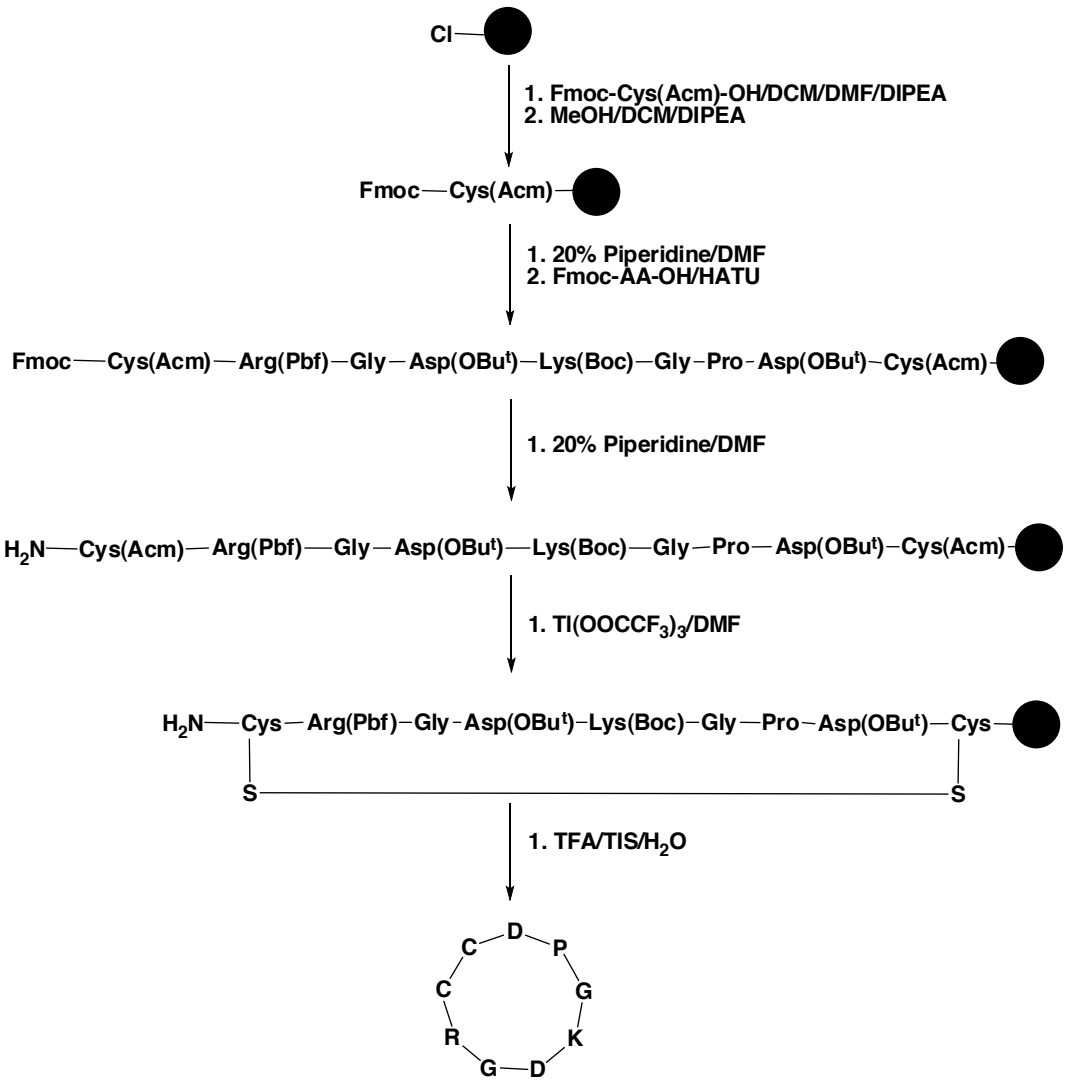

Figure 4.4: Synthetic scheme for free iRGD.

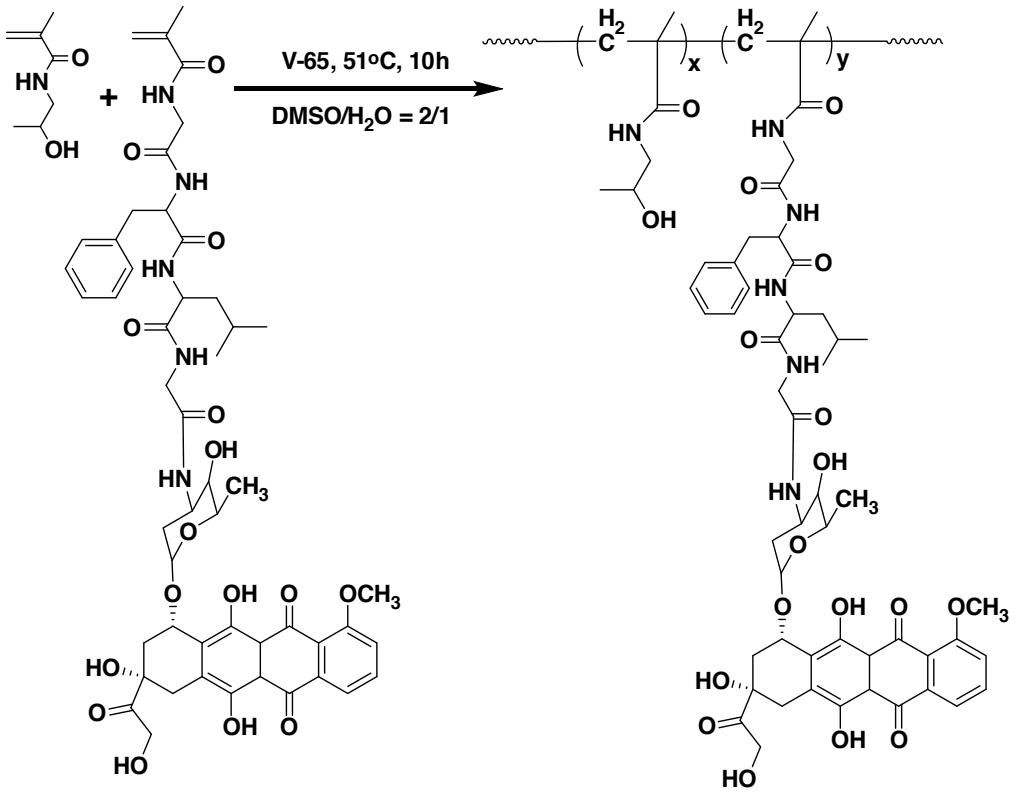

Figure 4.5: Synthetic scheme of polymer conjugate P-DOX

polymerization was conducted at 51 ^{o}C for 10 h. The polymer was precipitated in a mixture of diethyl ether and acetone. The crude product was first purified on an LH-20 column, and further purified on Superose 6 HR10/30 preparative column in an AKTA FPLC system (Pharmacia) equipped with refractive index (Optilab rEX) and light scattering MiniDawn TREOS detectors (Wyatt Technology Inc, Santa Barbara). Sodium acetate (0.1 M) in a mixture of 30% acetonitrile/70% DI water (v/v) (pH = 6.5) was used as the eluent, and the flow rate was 1 mL/min.

The molecular weight of P-DOX was measured on a Superose 6 HR10/30 analytical column，and the flow rate was 0.4 mL/min. HPMA homopolymer fractions were used as molecular weight standards.

4.3.5 Synthesis and MW measurement of polymer conjugate P-DOX-PLGLAG-iRGD

As shown in Figure 4.6, the polymer conjugate P-DOX-PLGLAG-iRGD was prepared by conventional radical polymerization. Briefly, monomer HPMA (70.6 mg, 0.493 mmol), monomer MA-GFLG-DOX (15.1 mg, 0.015 mmol), monomer MA-GG-PLGLAG-iRGD (25 mg, 0.015 mmol) initiator V-65 (5.13 mg, 0.018 mmol), and a mixture of DMSO/H_2O solvent was added to an ampoule. The ampoule was sealed after the mixture was bubbled with nitrogen for 30 min. Then the polymerization was conducted at 51 ^{o}C for 10 h. The purification and MW measurement methods are the same as that of the polymer conjugate P-DOX (Section 4.3.4).

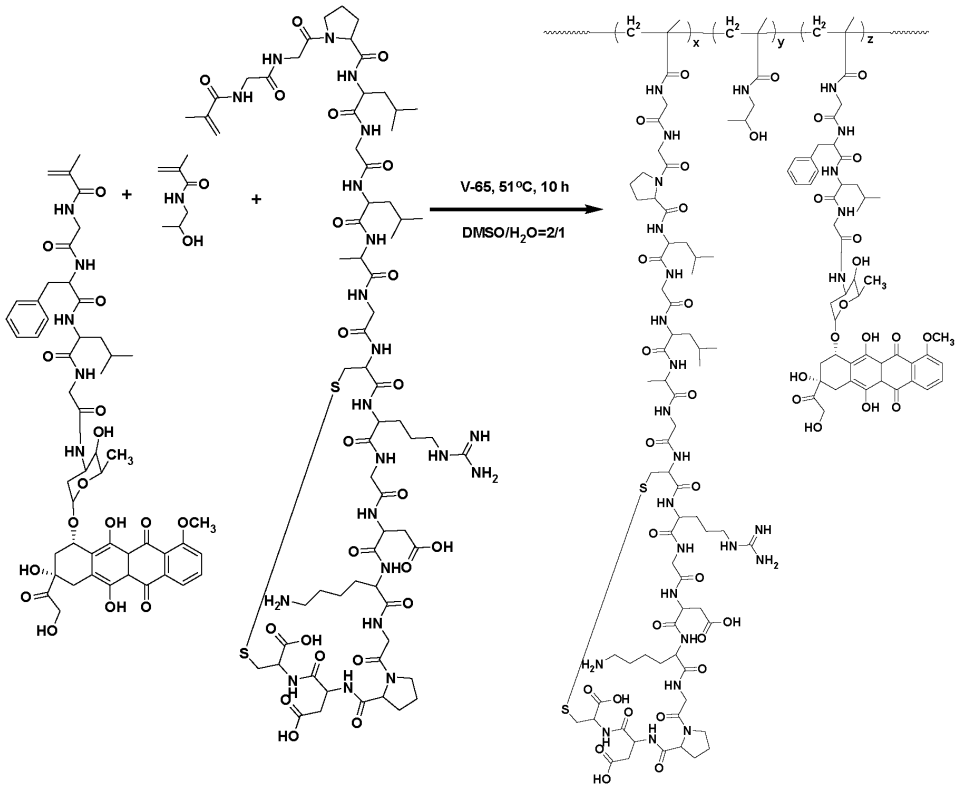

Figure 4.6: Synthetic scheme of polymer conjugate P-DOX-PLGLAG-iRGD

4.3.6 Determination of the DOX content in conjugates P-DOX and P-DOX-PLGLAG-iRGD

The DOX content in conjugates P-DOX and P-DOX-PLGLAG-iRGD was calculated by measuring the DOX UV absorbance in methanol. General procedure for testing DOX UV absorbance in a solution of P-DOX-PLGLAG-iRGD in methanol: (i) P-DOX-PLGLAG-iRGD (2.26 mg) was dissolved in 10 mL methanol; (ii) 1 mL solution was transferred to a spectrophotometer cell and UV absorbance was scanned from 200 nm to 800 nm with Varian UV-Vis spectrophotometers, with blank methanol used as the reference; (iii) the UV absorbance at 482 nm was used for DOX concentration calculation.

4.3.7 Determination of the iRGD content in P-DOX-PLGLAG-iRGD

The iRGD content in conjugate P-DOX-PLGLAG-iRGD was determined by amino acid analysis. The first step was to hydrolyze the peptide by dissolving 2.5 mg of conjugate P-DOX-PLGLAG-iRGD in 0.5 mL of 6 M HCl and heating at 110 ^{o}C for 24 h. The following steps were similar as the procedure for measuring DUPA contents (Chapter 2.3.6). Aspartic acid (1 mM, 2.5 mM, 5 mM) and alanine (0.3 mM, 1 mM, 3 mM) were used for calibration.

4.3.8 Cell culture

Human prostate cancer DU-145 cells (ATCC, Manassas, VA) were grown in RPMI-1640 media (Sigma-Aldrich, St. Louis, MO) containing 10% (v/v) fetal bovine serum (FBS), 100 U/ml penicillin, and 100 μg/mL streptomycin (Gibco, Carlsbad, CA) at

37 ^{o}C in a humidified atmosphere of 5% CO_2 (v/v). Cells were passaged every 2-4 d and stopped at passage 20.

4.3.9 In vitro doxorubicin cellular uptake

DU-145 cells were seeded at a density of $4*10^5$ cells/well in 6-well plates and incubated at 37 ^{o}C for 24 h to allow cell attachment. After removing the media, the cells treated with 9 μM [iRGD] equivalent of free iRGD, 10 μM [DOX] equivalent of P-DOX, 9 μM [iRGD] equivalent of free iRGD plus 10 μM [DOX] equivalent P-DOX, or 9 μM [iRGD] and 10 μM [DOX] equivalents of P-DOX-PLGLAG-iRGD for 24 h. The cells were washed and detached from plates with cold PBS. After being centrifuged and removed the supernatant, the cells were resuspended in PBS and measured with flow cytometry.

4.3.10 Cell cycle arrest

The DU-145 cells were seeded at a density of $4*10^5$ cells/well in 6-well plates and incubated at 37 ^{o}C to allow adherence to plates. After 24 h, the media were replaced with 9 μM [iRGD] equivalent of free iRGD, 10 μM [DOX] equivalent of P-DOX, 9 μM [iRGD] equivalent of free iRGD plus 10 μM [DOX] equivalent P-DOX, or 9 μM [iRGD] and 10 μM [DOX] equivalents of P-DOX-PLGLAG-iRGD for another 24 h. After removing the drug solution, the cells were washed and detached with cold PBS and centrifuged. The supernatant was removed and the cells were fixed with 80% ethanol for at least 2 h. After being washed with PBS, the fixed cells were re-suspended in 500 μL of

propidium iodide (PI) staining solution (50 μg/mL PI, 200 μg/mL RNase) and analyzed on a flow cytometer.

4.3.11 Apoptosis

DU-145 cells were seeded at a density of $4*10^5$ cells/well in 6-well plates and incubated at 37 ^oC for 24 h to allow cell attachment. The media was replaced with 9 μM [iRGD] equivalent of free iRGD, 10 μM [DOX] equivalent of P-DOX, 9 μM [iRGD] equivalent of free iRGD plus 10 μM [DOX] equivalent P-DOX, or 9 μM [iRGD] and 10 μM [DOX] equivalents of P-DOX-PLGLAG-iRGD for another 24 h. The general procedure for preparing samples for measuring apoptosis: (I) the cells were detached from 6-well plates, and transferred to 1.5 mL Eppendorf vials; (II) the cells were centrifuged to remove the supernatant, and washed with 1X binding buffer; (III) the cells were re-suspended in 200 μL of 1X binding buffer; (IV) Annexin V (5 μL) and propidium iodide (10 μL) were added to the cell suspension, and the suspension was incubated at room temperature for 5-15 min in the dark; (V) the cells were analyzed by flow cytometry.

4.3.12 Cell cytotoxicity

Cytotoxicity of DOX conjugates and controls against DU-145 cells was assessed by CCK-8 assay. DU-145 cells were seeded at a density of 3,500 cells/well in a 96-well plate and cultured at 37 ^oC for 24 h. The media was then replaced with fresh culture media containing 9 μM [iRGD] equivalent of free iRGD, 10 μM [DOX] equivalent of P-DOX, or 9 μM [iRGD] equivalent of free iRGD plus 10 μM [DOX] equivalent P-DOX,

or 9 μM [iRGD] and 10 μM [DOX] equivalents of P-DOX-PLGLAG-iRGD and cultured for 12 h or 24 h. The drug solutions were replaced with 100 μL of fresh media and cultured for another 60 h or 48 h. The media were replaced with 100 μL of fresh media and 50 μL of diluted CCK-8 solution. The formazan dye formed was detected at absorbance wavelength 450 nm, and 630 nm was used as a background.

4.3.13 Multicellular tumor spheroid formation

To a 0.5% agar coated, 10-mm diameter Petri-dish was added $2*10^6$ DU-145 cells in 15 mL of RPMI media supplemented with 10% fetal bovine serum (FBS), 50 U/mL penicillin, and 50 μg/mL streptomycin. Cells were grown at 37 ^oC in a humidified atmosphere with 5% CO_2 (v/v). The size of spheroids was monitored with a EVOS fluorescence microscope (AMG).

4.3.14 DOX conjugates accumulation in multicellular tumor spheroids

When most of the spheroids grew to 100-300 μm diameter, the spheroids were transferred to 15 mL conical base plastic tube and allowed to settle for 2 min. The supernatant was removed, and the spheroids were transferred to 24-well plates and incubated with 9 μM [iRGD] and/or 10 μM [DOX] equivalents of iRGD, P-DOX, a mixture of iRGD and P-DOX, or P-DOX-PLGLAG-iRGD for 24 h. After being washed with PBS three times, the spheroids were disassociated with accutase (Invitrogen) to single cells and analyzed on flow cytometer.

4.3.15 DOX conjugates penetration in multicellular tumor spheroids

The DU-145 prostate cancer spheroids were incubated with 9 μM [iRGD] and/or10 μM [DOX] equivalents of iRGD, P-DOX, a mixture of iRGD and P-DOX, or P-DOX-PLGLAG-iRGD for 24 h. After being washed and fixed, the DOX fluorescence in spheroids was measured with Olympus FV1000 confocal microscope. The images were analyzed using ImageJ software.

4.3.16 Statistical analysis

Average results are expressed as mean ± SEM or mean ± SD. The statistical difference between groups was assessed by a one-way analysis of variance (ANOVA) plus post-hoc tests using GraphPad Prism software. P values ≤ 0.05 were considered statistically significant.

4.4 Results and Discussion

4.4.1 Design, synthesis, and characterization of monomer MA-GFLG-DOX

The conventional method to prepare monomer MA-GFLG-DOX from MA-GFLG-OH included two steps: the first step is to prepare MA-GFLG-4-nitrophenyl ester (MA-GFLG-ONp) by the reaction of MA-GFLG-OH and 4-nitrophenol in the presence of *N,N'*-dicyclohexylcarbodiimide (DCC) in DMF; the second step is to react MA-GFLG-ONp with DOX to produce MA-GFLG-DOX (32). This procedure is laborious to remove the dicyclohexyl urea (DCU) side product from the coupling agent DCC. As shown in Figure 4.2, we prepared monomer MA-GFLG-DOX by direct reaction of MA-GFLG-OH with DOX using the coupling agent HATU at low temperature. The coupling

reaction was preferentially induced at the primary amine in DOX by controlling the reaction temperature.

4.4.2 Design, synthesis, and characterization of monomer MA-GG-PLGLAG-iRGD and free iRGD

To incorporate iRGD into the drug carrier system via a MMP-2 degradable spacer -PLGLAG-, two general methods are potentially able to achieve this aim. The first method is to prepare the drug carrier precursor first, then conjugate the iRGD to the drug carrier precursors. The second method is to prepare the monomer form of iRGD first, then incorporate the iRGD into the polymer carrier by direct copolymerization. Because of the presence of disulfide bond, primary amine, and carboxyl group in iRGD, we prefer to use the second method to directly incorporate iRGD into drug carrier system to avoid undesired side reactions. Because iRGD strictly requires the exposure of C terminus to keep its activity, we prepared the monomer by conjugation starting from the *N*-terminus of iRGD (34). As shown in Figure 4.3, we designed a concise method to prepare the monomer form of iRGD (MA-GG-PLGLAG-iRGD) with solid phase synthesis. This procedure is easy to handle because all of the conjugation and cyclization reactions occurred in solid phase when attached to resin. In particular, the cyclization reaction on resin is able to avoid the formation of intermolecular disulfide bond between two iRGDs. The structures of free iRGD and monomer MA-GG-PLGLAG-iRGD were confirmed by MALDI-TOF (matrix-assisted laser desorption ionization, time-of-flight) mass spectroscopy. As shown in Figure 4.7, the peak at m/z 1638.79 corresponds to $[M+H]^+$ of

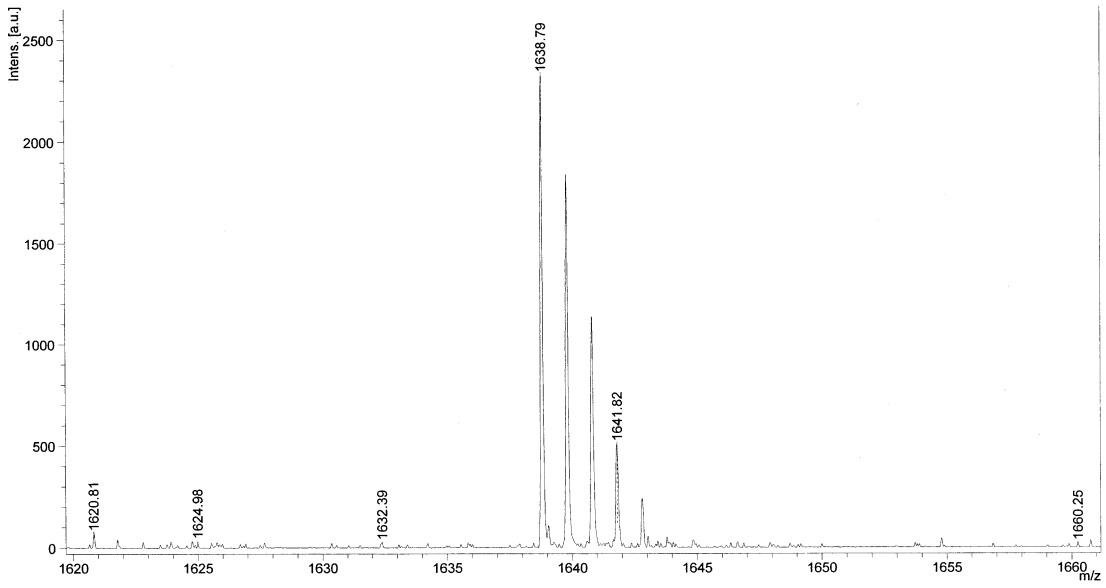

Figure 4.7: Mass spectrum of monomer MA-GG-PLGLAG-iRGD.

the monomer MA-GG-PLGLAG-iRGD. The peak at m/z 948.37 in Figure 4.8 corresponds to $[M+H]^+$ of the free iRGD.

4.4.3 Synthesis and characterization of polymer conjugates

P-DOX and P-DOX-PLGLAG-iRGD

The conjugates P-DOX (Figure 4.5) and P-DOX-PLGLAG-iRGD (Figure 4.6) were prepared by conventional radical polymerization. The monomers MA-GFLG-DOX and MA-GG-PLGLAG-iRGD are soluble in DMSO, but the polymerization rate in DMSO is slow. To balance the solubility of monomers and reaction rate, we chose a mixture of DMSO and DI water (DMSO/water =2/1) as the solvent to prepare the two DOX conjugates with conventional polymerization. By using conventional polymerization, both P-DOX and P-DOX-PLGLAG-iRGD can be prepared in 10 h.

The molecular weight, molecular weight distribution, DOX, and iRGD content in conjugates P-DOX and P-DOX-PLGLAG-iRGD are summarized in Table 4.1. The average number of iRGD units in one polymer chain is 4.6.

4.4.4 Cellular uptake

We used flow cytometry to quantitatively measure DOX uptake in monolayer DU-145 prostate cancer cells after incubation with P-DOX-PLGLAG-iRGD and controls for 24 h (Figure 4.9). Higher fluorescence intensity was detected in P-DOX and P-DOX plus iRGD treated groups compared to control and iRGD treated group. P-DOX-PLGLAG-iRGD treated group shows the largest rightward shift in the histogram, indicating the highest cellular uptake and accumulation of DOX in the P-DOX-

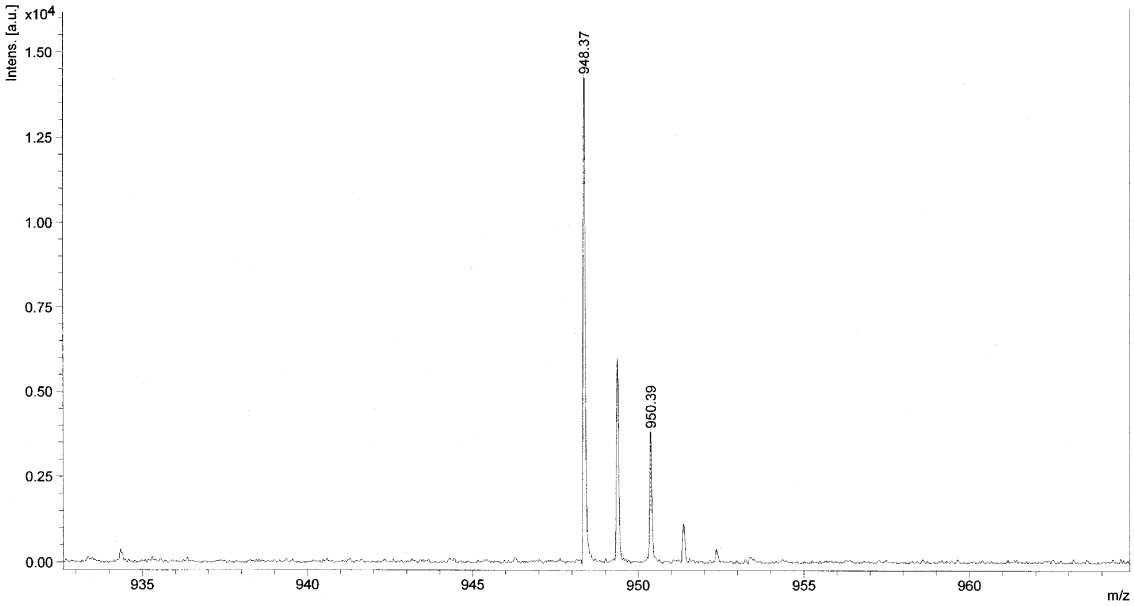

Figure 4.8: Mass spectrum of free iRGD.

Table 4.1 Physicochemical properties of DOX conjugates.

DOX Conjugate	Mn (kDa)	Mw (kDa)	Mw/Mn	DOX (wt%)	iRGD (wt%)
P-DOX	69.8	120.0	1.72	8.35	N/A
P-DOX-PLGLAG-iRGD	71.9	134.3	1.87	3.87	6.05

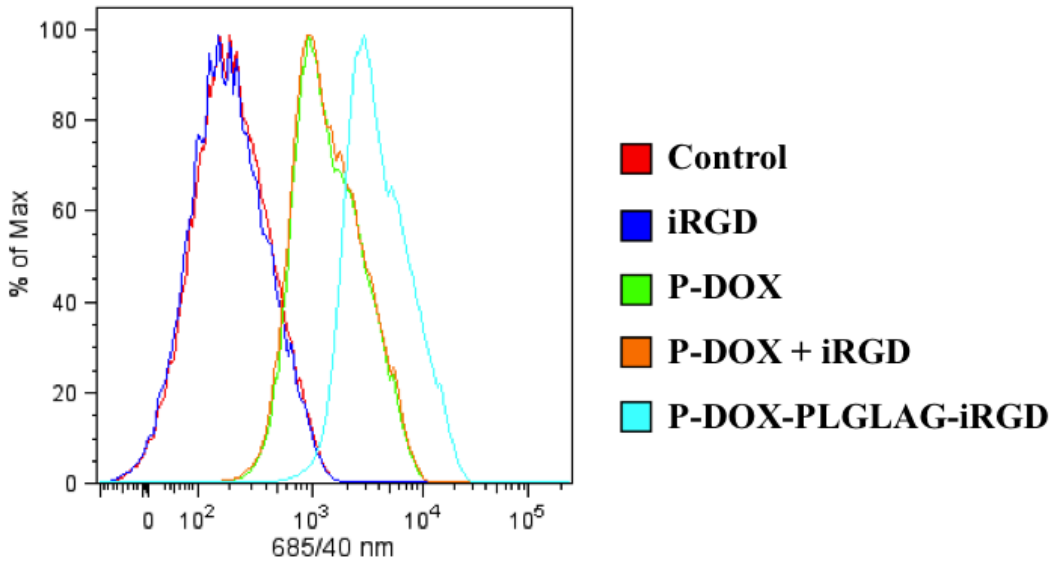

Figure 4.9: Uptake of DOX conjugates and controls in DU-145 cell monolayers by measuring the DOX fluorescence.

PLGLAG-iRGD treated group. In contrast, the mixture of iRGD with P-DOX only resulted in a slight increase of uptake and accumulation of P-DOX in DU-145 cells in the tested concentration and incubation time.

4.4.5 Cell cycle arrest assay

It was reported that the treatment of prostate cancer DU-145 cells with DOX resulted in G2/M arrest (35). We performed cell cycle arrest assay to check whether the enhanced accumulation of DOX in the P-DOX-PLGLAG-iRGD treated group could lead to increased G2/M cell cycle arrest. Consistent with DOX uptake results, the highest percentage ((41.6 ± 7.2)%) of cells in G2/M phase was found in the P-DOX-PLGLAG-iRGD treated group (Figure 4.10). While P-DOX and a mixture of iRGD and P-DOX only induced a mild increase of G2/M arrest ((31.7 ± 7.1)%, (32.9 ± 6.4)%, respectively). These results further demonstrated that the conjugated form of iRGD can enhance the accumulation of DOX conjugates in DU-145 prostate cancer cells.

4.4.6 Apoptosis

The concentrations of DOX and iRGD used in this study were equivalent to those used in the uptake and cell cycle assays to assess whether the uptake and cell cycle arrest were associated with the cell apoptosis. The percentages of late apoptotic, early apoptotic, and live cells were analyzed on flow cytometer after double staining the cells with FITC-Annexin V and PI (Figure 4.11). Annexin V+/PI+ cells were considered as late apoptotic cells, shown in the upper right quadrant. Annexin V+/PI- cells were considered as early

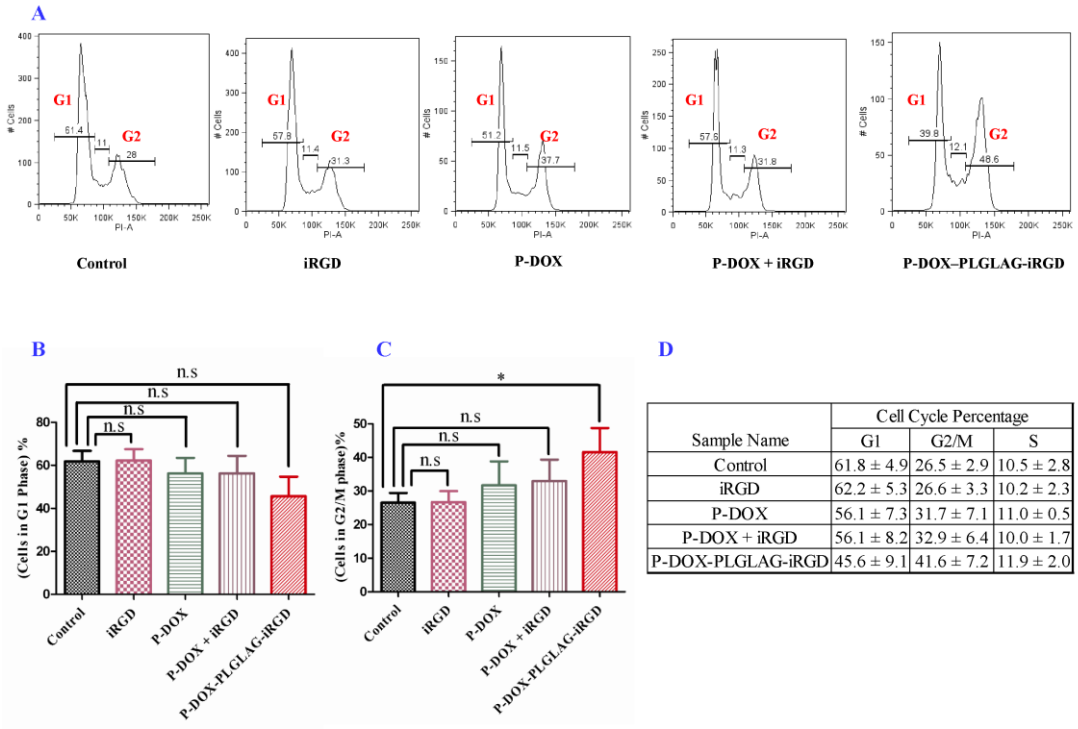

Sample Name	Cell Cycle Percentage		
	G1	G2/M	S
Control	61.8 ± 4.9	26.5 ± 2.9	10.5 ± 2.8
iRGD	62.2 ± 5.3	26.6 ± 3.3	10.2 ± 2.3
P-DOX	56.1 ± 7.3	31.7 ± 7.1	11.0 ± 0.5
P-DOX + iRGD	56.1 ± 8.2	32.9 ± 6.4	10.0 ± 1.7
P-DOX-PLGLAG-iRGD	45.6 ± 9.1	41.6 ± 7.2	11.9 ± 2.0

Figure 4.10: DU-145 cell cycle distribution after treatment with DOX conjugates and related controls. (A) Representative profiles. (B) Percentage of cells in G1 phase. (C) Percentage of cells in G2/M phase. (D) Average percentages of cell cycle distribution. Average data were presented as mean ± SD. Statistics: One Way ANOVA plus Dunnett's post-hoc test ($P<0.05$ = *; not significant = n.s).

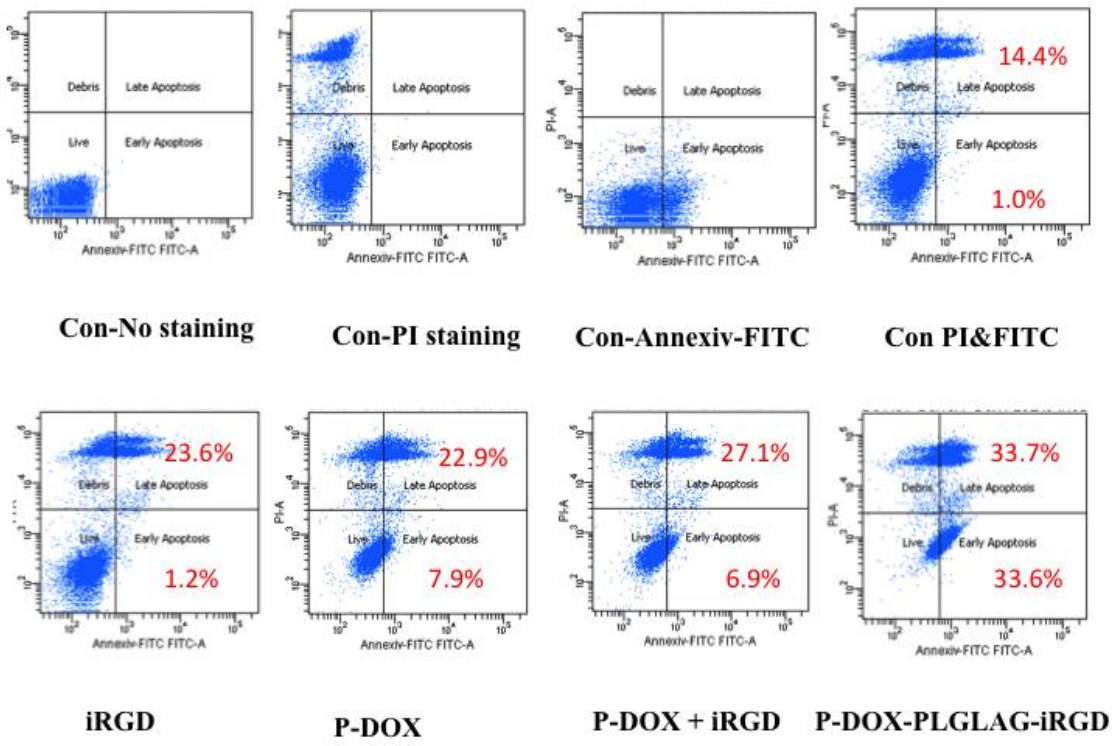

Figure 4.11: Induced apoptosis in DU-145 cells after treatment with DOX conjugates and related controls.

apoptotic cells, shown in the lower right quadrant. Annexin V-/PI- cells shown in the lower left quadrant were considered as live cells. The percentages of early apoptotic DU-145 cells were counted as 1.0%, 1.2%, 7.9%, 6.9%, and 33.6% for control, iRGD, P-DOX, P-DOX plus iRGD, and P-DOX-PLGLAG-iRGD treated groups, respectively. The percentages of late apoptotic DU-145 cells were counted as 14.4%, 23.6%, 22.9%, 27.1%, and 33.7%, respectively. Compared to control and iRGD group, both P-DOX and the mixture of P-DOX and iRGD enhanced early apoptosis. P-DOX-PLGLAG-iRGD treated group showed the highest early and late apoptosis compared to control and other treated groups.

4.4.7 In vitro cellular cytotoxicity assays

We evaluated the cytotoxicity of DOX conjugates and related controls against DU145 prostate cancer cells by determining the viable cells with CCK-8 assay. The cells were incubated with 10 μM [DOX] equivalent and/or 9 μM [iRGD] equivalent of P-DOX-PLGLAG-iRGD, a mixture of P-DOX and iRGD, P-DOX, and iRGD for 12 h or 24 h. As shown in Figure 4.12, the conjugate P-DOX-PLGLAG-iRGD is more toxic to DU-145 prostate cancer cells than P-DOX or the mixture of P-DOX and iRGD. The highest cytotoxicity of P-DOX-PLGLAG-iRGD could be, at least in part, attributed to its fast intracellular uptake. The fact that the conjugate of P-DOX-PLGLAG-iRGD is more toxic than that of the mixture of P-DOX and iRGD further supports the conclusion that the targeting interaction between RGD and integrin on DU-145 cell surface possibly facilitates the drug conjugate internalization.

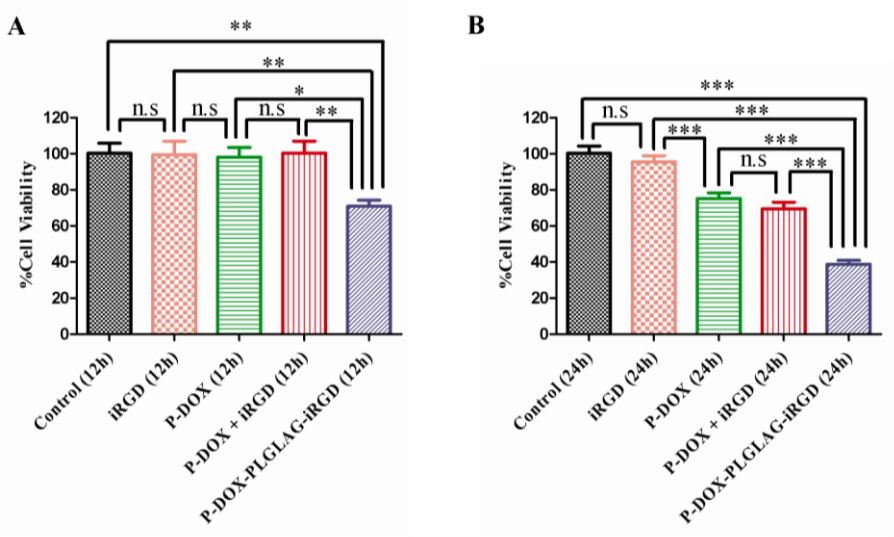

Figure 4.12: In vitro cytotoxicity of P-DOX-PLGLAG-iRGD and related controls against DU-145 prostate cancer cells. (A) 12 h. (B) 24 h. Statistics: One Way ANOVA plus Turkey's post-hoc test ($P<0.001$ = ***, $0.001<P<0.01$ = **, $0.01<P<0.05$ = *, not significant = n.s).

4.4.8 Accumulation of DOX conjugates and related controls in multicellular tumor spheres (MTS)

MTS are more considered as one of the primary tools for drug development (36). Compared to 2D monolayer tumor cells, 3D MTS closely resemble 3D tumor tissues and mimic the tumor microenvironment (37). MTS is an excellent model for drug delivery studies because it mimics the physiological barriers in solid tumors (38). The VEGF production, Ki-67, and gene expression profile in 3D prostate cancer spheres is similar to the solid tumors in immune-derived mice (39). To bridge the gap between cell culture and live tissue, DU-145 MTS were used to investigate the accumulation and penetration of DOX conjugates.

We evaluated DOX conjugates accumulation in DU-145 MTS by analyzing the DOX fluorescence in disassociated cells using flow cytometry. As shown in Figure 4.13, the cells in the P-DOX-PLGLAG-iRGD treated group have the strongest fluorescence intensity. Consistent with monolayer cell uptake results, the cells from spheroids following treatment with a mixture of P-DOX and iRGD, or P-DOX also have enhanced fluorescence intensity compared to control groups.

4.4.9 MTS penetration of DOX conjugates

We evaluated DOX conjugates penetration in DU-145 MTS using confocal microscopy (Figure 4.14). To keep the morphology of tested spheroids intact, we fixed the spheroids with formalin. The presence of DOX within spheroids was visualized by measuring DOX's intrinsic fluorescence. The images were converted to surface plot by using Image-J software. Consistent with flow cytometry results, an enhanced

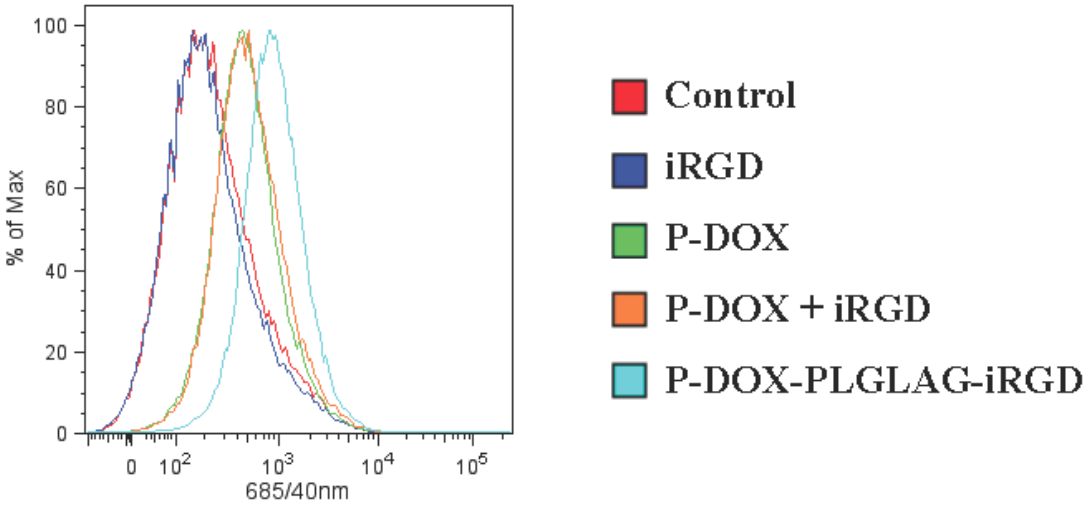

Figure 4.13: Accumulation of DOX conjugates in DU-145 multilayer tumor cell spheroids.

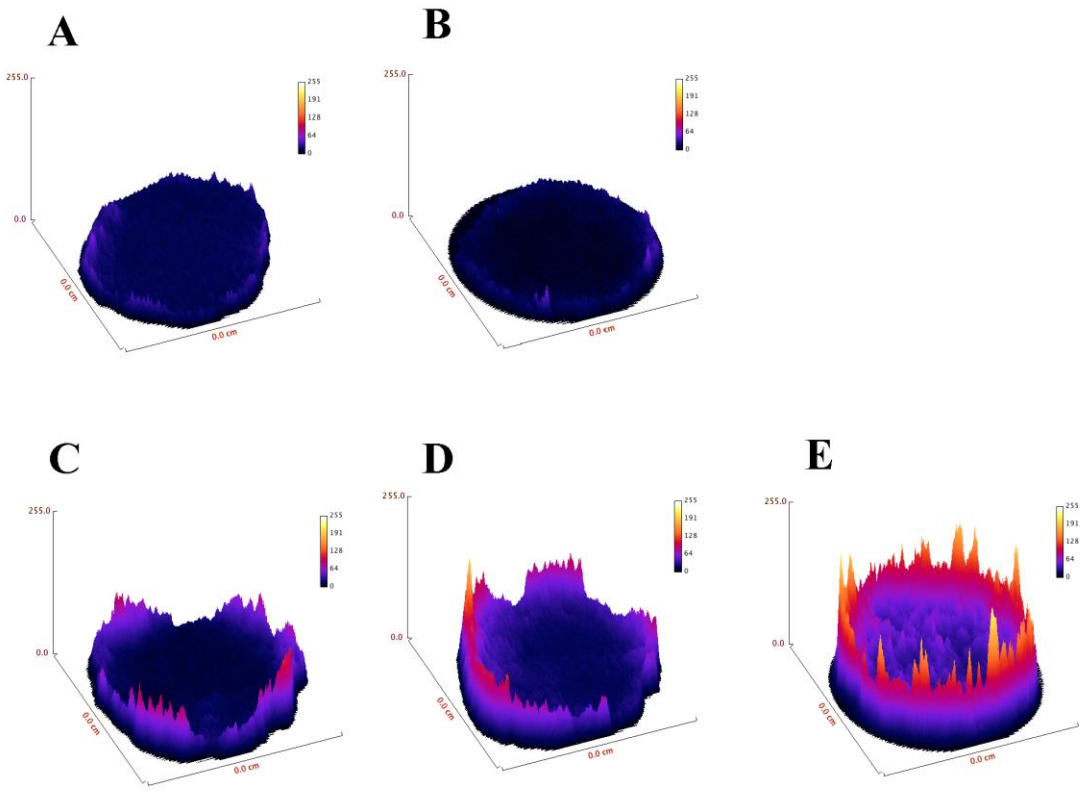

Figure 4.14: Penetration of DOX conjugates or controls in DU-145 MTS (surface plots of images): (A) Control; (B) iRGD; (C) P-DOX; (D) P-DOX + iRGD; (E) P-DOX-PLGLAG-iRGD.

fluorescence intensity in P-DOX-PLGLAG-iRGD treated spheroids over P-DOX treated spheroids was observed.

4.5 Conclusion

In this study, a stimuli responsive drug delivery system with iRGD conjugated to drug carrier via a MMP-2 cleavable spacer was successively developed for prostate cancer treatment. Both confocal fluorescene microscopy and flow cytometry studies demonstrated that the conjugated form of iRGD enhanced the DOX uptake in prostate cancer DU-145 monolayer and multilayer cells. We evaluated the in vitro activity of DOX conjugates on DU-145 cell cycle arrest, cell apoptosis, and cell death. The penetration of DOX conjugates was tested in vitro tumor spheroids. The results demonstrated that the conjugate P-DOX-PLGAGL-iRGD has better penetration ability than P-DOX and a mixture of P-DOX and iRGD. This strategy by conjugating iRGD to drug carrier via a -PLGLAG- spacer enhances the penetration and accumulation of DOX in tumor. Consequently, a lower dosage of DOX in this new formulation has the potential to achieve the same efficacy as reported dosage. This strategy can broaden the application of DOX for cancer treatment through bypassing the dose-limiting cardiotoxicity (40,41). Consistent with the results from other research group, we further demonstrated that tumor spheroids are excellent model for testing drug penetration before moving for in vivo evaluation (42). Together our data demonstrated the advantages of our novel drug delivery system with MMP-2 controlled release of iRGD. This strategy opens up avenues for modifying iRGD to enhance its tumor targeting and penetration ability.

4.6 References

1. Petros RA, DeSimone JM. Strategies in the design of nanoparticles for therapeutic applications. Nat Rev Drug Discov. 2010;9:615–27.

2. Kopeček J, Kopečková P. HPMA copolymers: origins, early developments, present, and future. Adv Drug Deliv Rev. 2010;62:122–49.

3. Kopeček J. Polymer–drug conjugates: Origins, progress to date and future directions. Adv Drug Deliv Rev. 2013;65:49–59.

4. Park K. Facing the truth about nanotechnology in drug delivery. ACS Nano. 2013;7:7442–7.

5. Venditto VJ, Szoka Jr. FC. Cancer nanomedicines: So many papers and so few drugs! Adv Drug Deliv Rev. 2013;65:80–8.

6. Stirland DL, Nichols JW, Miura S, Bae YH. Mind the gap: a survey of how cancer drug carriers are susceptible to the gap between research and practice. J Control Release. 2013;172:1045–64.

7. Markman JL, Rekechenetskiy A, Holler E, Ljubimova JY. Nanomedicine therapeutic approaches to overcome cancer drug resistance. Adv Drug Deliv Rev. 2013;65:1866–79.

8. Tong R, Chiang HH, Kohane DS. Photoswitchable nanoparticles for in vivo cancer chemotherapy. Proc Natl Acad Sci U S A. 2013;110:19048–53.

9. Provenzano PP, Cuevas C, Chang AE, Goel VK, Von Hoff DD, Hingorani SR. Enzymatic targeting of the stroma ablates physical barriers to treatment of pancreatic ductal adenocarcinoma. Cancer Cell. 2012;21:418–29.

10. Prabhakar U, Maeda H, Jain RK, Sevick-Muraca EM, Zamboni W, Farokhzad OC, et al. Challenges and key considerations of the enhanced permeability and retention effect for nanomedicine drug delivery in oncology. Cancer Res. 2013;73:2412–7.

11. Kunjachan S, Pola R, Gremse F, Theek B, Ehling J, Moeckel D, et al. Passive versus active tumor targeting using RGD- and NGR-modified polymeric nanomedicines. Nano Lett. 2014;14:972–81.

12. Dreher MR, Liu W, Michelich CR, Dewhirst MW, Yuan F, Chilkoti A. Tumor vascular permeability, accumulation, and penetration of macromolecular drug carriers. J Natl Cancer Inst. 2006;98:335–44.

13. Popović Z, Liu W, Chauhan VP, Lee J, Wong C, Greytak AB, et al. A Nanoparticle Size Series for In Vivo Fluorescence Imaging. Angew Chem Int Ed. 2010;49:8649–52.

14. Wong C, Stylianopoulos T, Cui J, Martin J, Chauhan VP, Jiang W, et al. Multistage nanoparticle delivery system for deep penetration into tumor tissue. Proc Natl Acad Sci. 2011;108:2426–31.

15. Lammers T, Kiessling F, Hennink WE, Storm G. Drug targeting to tumors: principles, pitfalls and (pre-) clinical progress. J Control Release. 2012;161:175–87.

16. Desoize B, Gimonet D, Jardiller JC. Cell culture as spheroids: an approach to multicellular resistance. Anticancer Res. 1998;18:4147–58.

17. Curnis F, Sacchi A, Corti A. Improving chemotherapeutic drug penetration in tumors by vascular targeting and barrier alteration. J Clin Invest. 2002;110:475–82.

18. Dubikovskaya EA, Thorne SH, Pillow TH, Contag CH, Wender PA. Overcoming multidrug resistance of small-molecule therapeutics through conjugation with releasable octaarginine transporters. Proc Natl Acad Sci U S A. 2008;105:12128–33.

19. Sugahara KN, Teesalu T, Karmali PP, Kotamraju VR, Agemy L, Girard OM, et al. Tissue-penetrating delivery of compounds and nanoparticles into tumors. Cancer Cell. 2009;16:510–20.

20. Sugahara KN, Teesalu T, Karmali PP, Kotamraju VR, Agemy L, Greenwald DR, et al. Coadministration of a tumor-penetrating peptide enhances the efficacy of cancer drugs. Science. 2010;328:1031–5.

21. Pollaro L, Heinis C. Strategies to prolong the plasma residence time of peptide drugs. MedChemComm. 2010;1:319–24.

22. Pang H-B, Braun GB, She Z-G, Kotamraju VR, Sugahara KN, Teesalu T, et al. A free cysteine prolongs the half-life of a homing peptide and improves its tumor-penetrating activity. J Control Release. 2014;175:48–53.

23. Primeau AJ, Rendon A, Hedley D, Lilge L, Tannock IF. The Distribution of the anticancer drug doxorubicin in relation to blood vessels in solid tumors. Clin Cancer Res. 2005;11:8782–8.

24. Liu J, Kopečková P, Pan H, Sima M, Bühler P, Wolf P, et al. Prostate-cancer-targeted N-(2-hydroxypropyl)methacrylamide copolymer/docetaxel conjugates. Macromol Biosci. 2012;12:412–22.

25. Jiang T, Olson ES, Nguyen QT, Roy M, Jennings PA, Tsien RY. Tumor imaging by means of proteolytic activation of cell-penetrating peptides. Proc Natl Acad Sci U S A. 2004;101:17867–72.

26. Zhu L, Wang T, Perche F, Taigind A, Torchilin VP. Enhanced anticancer activity of nanopreparation containing an MMP2-sensitive PEG-drug conjugate and cell-penetrating moiety. Proc Natl Acad Sci U S A. 2013;110:17047–52.

27. Dos Reis ST, Villanova FE, Andrade PM, Pontes J Jr, de Sousa-Canavez JM, Sañudo A, et al. Matrix metalloproteinase-2 polymorphism is associated with prognosis in prostate cancer. Urol Oncol. 2010;28:624–7.

28. Zhong W, Han Z, He H, Bi X, Dai Q, Zhu G, et al. CD147, MMP-1, MMP-2 and MMP-9 protein expression as significant prognostic factors in human prostate cancer. Oncology. 2008;75:230–6.

29. Singh S, Singh UP, Grizzle WE, Lillard JW Jr. CXCL12-CXCR4 interactions modulate prostate cancer cell migration, metalloproteinase expression and invasion. Lab Investig J Tech Methods Pathol. 2004;84:1666–76.

30. Chen EI, Kridel SJ, Howard EW, Li W, Godzik A, Smith JW. A unique substrate recognition profile for matrix metalloproteinase-2. J Biol Chem. 2002;277:4485–91.

31. Kopeček J, Bažilová H. Poly[N-(2-hydroxypropyl)methacrylamide]—I. Radical polymerization and copolymerization. Eur Polym J. 1973;9:7–14.

32. Ulbrich K, Šubr V, Strohalm J, Plocová D, Jelínková M, Říhová B. Polymeric drugs based on conjugates of synthetic and natural macromolecules. I. Synthesis and physico-chemical characterisation. J Control Release. 2000;64:63–79.

33. Rejmanová P, Labský J, Kopeček J. Aminolyses of monomeric and polymeric 4-nitrophenyl esters of N-methacryloylamino acids. Makromol Chem. 1977;178:2159–68.

34. Teesalu T, Sugahara KN, Kotamraju VR, Ruoslahti E. C-end rule peptides mediate neuropilin-1-dependent cell, vascular, and tissue penetration. Proc Natl Acad Sci U S A. 2009;106:16157–62.

35. Tyagi AK, Singh RP, Agarwal C, Chan DCF, Agarwal R. Silibinin strongly synergizes human prostate carcinoma DU145 cells to doxorubicin-induced growth Inhibition, G2-M arrest, and apoptosis. Clin Cancer Res. 2002;8:3512–9.

36. Hirschhaeuser F, Menne H, Dittfeld C, West J, Mueller-Klieser W, Kunz-Schughart LA. Multicellular tumor spheroids: an underestimated tool is catching up again. J Biotechnol. 2010;148:3–15.

37. Yip D, Cho CH. A multicellular 3D heterospheroid model of liver tumor and stromal cells in collagen gel for anti-cancer drug testing. Biochem Biophys Res Commun. 2013;433:327–32.

38. Mehta G, Hsiao AY, Ingram M, Luker GD, Takayama S. Opportunities and challenges for use of tumor spheroids as models to test drug delivery and efficacy. J Control Release. 2012;164:192–204.

39. Takagi A, Watanabe M, Ishii Y, Morita J, Hirokawa Y, Matsuzaki T, et al. Three-dimensional cellular spheroid formation provides human prostate tumor cells with tissue-like features. Anticancer Res. 2007;27:45–53.

40. Zhang S, Liu X, Bawa-Khalfe T, Lu L-S, Lyu YL, Liu LF, et al. Identification of the molecular basis of doxorubicin-induced cardiotoxicity. Nat Med. 2012;18:1639–42.

41. Das A, Durrant D, Mitchell C, Mayton E, Hoke NN, Salloum FN, et al. Sildenafil increases chemotherapeutic efficacy of doxorubicin in prostate cancer and ameliorates cardiac dysfunction. Proc Natl Acad Sci U S A. 2010;107:18202–7.

42. Perche F, Patel NR, Torchilin VP. Accumulation and toxicity of antibody-targeted doxorubicin-loaded PEG-PE micelles in ovarian cancer cell spheroid model. J Control Release. 2012;164:95–102.

CHAPTER 5

HPMA COPOLYMER CXCR-4 ANTAGONIST BKT140 CONJUGATES FOR INHIBITING PROSTATE CANCER CELL MIGRATION

5.1 Summary

In this chapter, we describe the design, synthesis, structure validation, and biological properties of a *N*-(2-hydroxypropyl)methacrylamide (HPMA) copolymer CXCR-4 antagonist (BKT140) conjugate. BKT140 was attached to HPMA backbone via a matrix metallopeptidase 2 (MMP-2) cleavable spacer (-PLGLAG-). Both free BKT140 and monomer MA-GG-PLGLAG-BKT140 were prepared by solid phase synthesis. HPMA copolymer-BKT140 conjugate (P-PLGLAG-BKT140) was prepared via Reversible Addition-Fragmentation Chain Transfer (RAFT) copolymerization of HPMA and MA-GG-PLGLAG-BKT140. The -PLGLAG- spacer was cleaved in prostate cancer cells growth media at a minimum of two sites. The in vitro cell cytotoxicity results show that the free BKT140 and P-PLGLAG-BKT140 have the same activities against PC-3 cells, indicating the conjugation of BKT140 to HPMA did not impact the functionality of BKT140. The migration results shown that both HPMA copolymer BKT140 conjugate and free BKT140 inhibited the CXCL12 induced PC-3 prostate cancer cell migration. The conjugate P-PLGLAG-BKT140 has great impact than that of free BKT140.

5.2 Introduction

Metastasis accounts for 90% of cancer-associated mortality, and the 5-year survival of metastatic prostate cancer is only about 30% (1,2). Prostate cancer can metastasize to lymph nodes, liver, and thorax, but the most common metastatic site is bone (84% of 74,826 patients) (3,4). More and more evidence has demonstrated prostate cancer cells use CXCR4/CXCL12 pathway to migrate from primary tumor to bone (5,6). CXCR4 was detected in most (94.2%) of metastatic prostate cancer. In addition, CXCR4 and CXCL12 were significantly elevated in localized and metastatic prostate cancer in samples of over 600 patients (7,8). The overexpression of CXCR4 accelerates prostate cancer metastasis by promoting the migration and invasion ability of prostate cancer cells toward CXCL12 (9,10). Blocking or inhibiting the CXCL12/CXCR4 interaction by anti-CXCR4 antibody or CXCR4 antagonists impairs the migration and invasion potential of prostate cancer cells (9,11,12).

In this study, we aim to develop a *N*-(2-hydroxypropyl)methacrylamide (HPMA) copolymer CXCR-4 antagonist conjugate to block the migration of prostate cancer cells. 4F-benzoyl-TN14003 (BKT140) was chosen as the CXCR4 antagonist to develop new therapeutics based on two major reasons: (i) BKT140 has a high binding affinity (1 nM) toward CXCR4 (13), and (ii) BKT140 is safe in vivo (14). However, two factors hinder the in vivo application of BKT140. First, BKT140 is sensitive to enzymatic degradation in the circulation because it is a peptide. Second, the renal clearance of BKT140 is fast because the mass of BKT140 is less than 5 kDa (15). The most common strategy to prolong the plasma residence time of peptide is to conjugate the peptide to a water-soluble polymer (15).

BKT140 was conjugated to HPMA copolymer via a MMP-2 cleavable spacer (-PLGLAG-) (16,17). MMP-2 was selected as the cleavage enzyme because MMP-2 is highly expressed in prostate cancer cells (9,18,19). We hypothesized that the conjugation of BKT140 to HPMA copolymer will prolong the plasma residence time of BKT140 during circulation. Once HPMA copolymer-BKT140 conjugates reach the tumor area, the BKT140 will be released from the conjugate after the spacer (-PLGLAG-) is cleaved by MMP-2.

5.3 Material and Methods

5.3.1 Materials

Recombinant human CXCL12 was purchased from PeproTech (Rocky Hill, NJ). 1-[Bis(dimethylamino)methylene]-1*H*-1,2,3-triazolo[4,5-*b*]pyridinium 3-oxid hexafluoro -phosphate (HATU), protected amino acids, and Rink amide MBHA resin were purchased from AAPPTEC (Louisville, KY). 4,4'-Azobis(4-cyanopentanoic acid) (V-501) was purchased from Wako (Japan). Tris(2-carboxyethyl) phosphine hydrochloride (TCEP) was purchased from Thermo Scientific (Waltham, MA). General solvents were purchased from Fisher Scientific (Fair Lawn, NJ). Trifluoroacetic acid (TFA) was purchased from Acros (Fair Lawn, NJ). HPMA (20), MA-GG-OH (21), and 4-cyanopentanoic acid dithiobenzoate (CPAD) (22) were prepared as described in literature. All other chemicals were purchased from Sigma Aldrich (St. Louis, MO) unless otherwise noted.

5.3.2 Synthesis of free CXCR4 antagonist BKT140

The resin bound linear peptide BKT140 was prepared by solid phase synthesis using a PS-3 peptide synthesizer (Protein Technologies, Inc). As shown in Figure 5.1, the synthesis started from the deprotection of Fmoc group on Resin by mixing the Rink amide MBHA resin (300 mg, 0.52 mmol/g, 156 μmol) with 20% piperidine in DMF. Then the protected amino acids (Fmoc-Arg(Pbf)-OH, Fmoc-Cys(Acm)-OH, Fmoc-Cit-OH, Fmoc-Arg(Pbf)-OH, Fmoc-Tyr(tBu)-OH, Fmoc-Pro-OH, Fmoc-D-Lys(Boc)-OH, Fmoc-Lys(Boc)-OH, Fmoc-Cit-OH, Fmoc-Tyr(tBu)-OH, Fmoc-Cys(Acm)-OH, Fmoc-Nal-OH, Fmoc-Arg(Pbf)-OH, Fmoc-Arg(Pbf)-OH), and 4-fluorobenzoic acid were sequentially attached to the resin in the presence of HATU (169 mg, 444.6 μmol).

The MBHA resin bound linear peptides were suspended in a solution of $Tl(OOCF_3)_3$ (254mg, 468 μmol) in DMF and shaken for 2h. After the $Tl(OOCF_3)_3$ solution was removed by filtration, the remaining resin was washed with DMF and methanol respectively for three times, and then dried.

A mixture solution (TFA/TIPS/H2O = 95/2.5/2.5) (10 mL) was added to the dried resin and shaken at room temperature for 3 h. Then the solution was filtered, and concentrated under vacuum. The remaining solution was added slowly into cold diethyl ether. The suspension obtained was centrifuged at 4000 RPM, and the crude solid products were obtained after removing the supernatant.

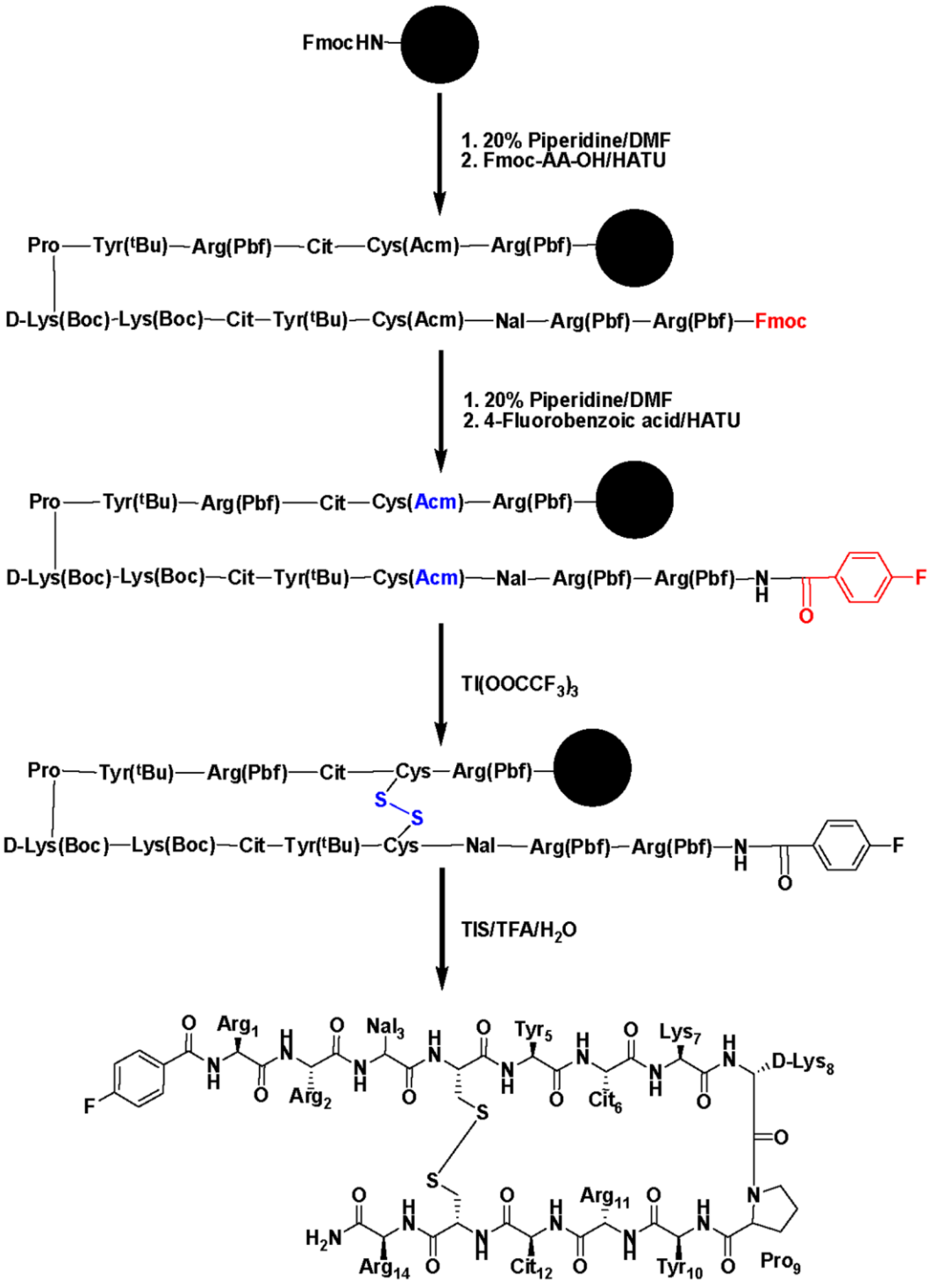

Figure 5.1: Synthetic scheme of free BKT140.

5.3.3 Reduction of free CXCR4 antagonist BKT140

The scheme for reduction of BKT140 is shown in Figure 5.2. BKT 140 (0.2 mg) was added to 0.5 mL of 10 mM tris(2-carboxyethyl) phosphine hydrochloride (TCEP) in phosphate buffered saline (PBS) (10 mM) with 1 mM ethylene diamine tetra acetic acid (EDTA), and incubated at 37 ^{o}C for 2 h.

5.3.4 Synthesis of monomer MA-GG-PLGLAG-BKT140

The synthetic scheme of monomer MA-GG-PLGLAG-BKT140 is shown in Figure 5.3. The first step was to prepare the Rink amide MBHA bound protected linear BKT140 peptide. This procedure was similar as the procedure in the synthesis of free BKT140; the only difference was that Fmoc-D-Lys(Dde)-OH was used instead of Fmoc-D-Lys(Boc)-OH.

The second step was to selectively remove the 1-(4,4-dimethyl-2,6-dioxocyclohex-1-ylidene)-3-ethyl (Dde) protecting group from the D-Lys^{8} amino acid residue by mixing the Rink amide MBHA bound protected linear BKT140 peptide with 2% hydrazine in DMF for 10 min.

The next step was to sequentially attach protected amino acids (Fmoc-Gly-OH, Fmoc-Ala-OH, Fmoc-Leu-OH, Fmoc-Gly-OH, Fmoc-Leu-OH, Fmoc-Pro-OH) and MA-GG-OH to resin.

The following step was to cyclize the linear peptide by mixing the resin bound linear BKT 140 peptide with a solution of $Tl(OOCF_3)_3$ (254 mg, 468μmol) in DMF for 1.5 h, and the resin bound peptides were washed with methanol and DMF twice.

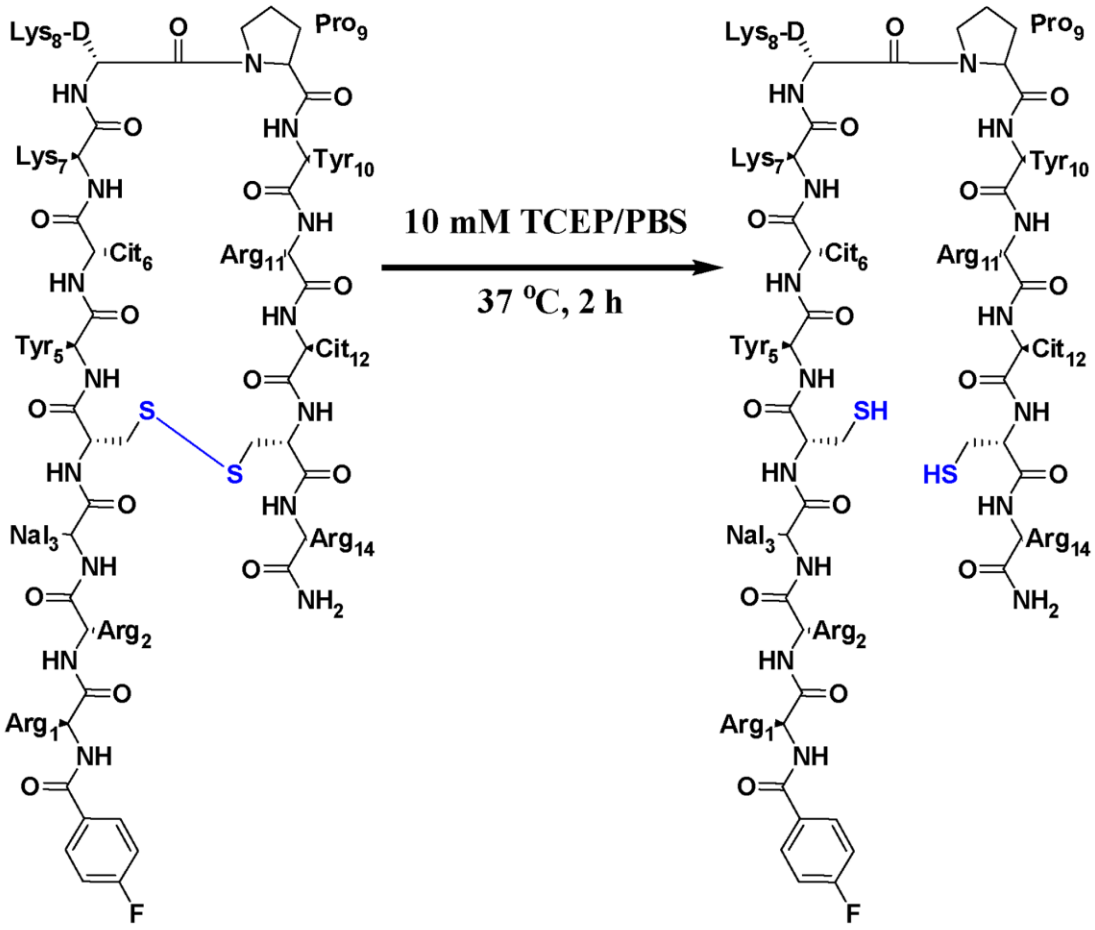

Figure 5.2: Scheme for reduction of free BKT140.

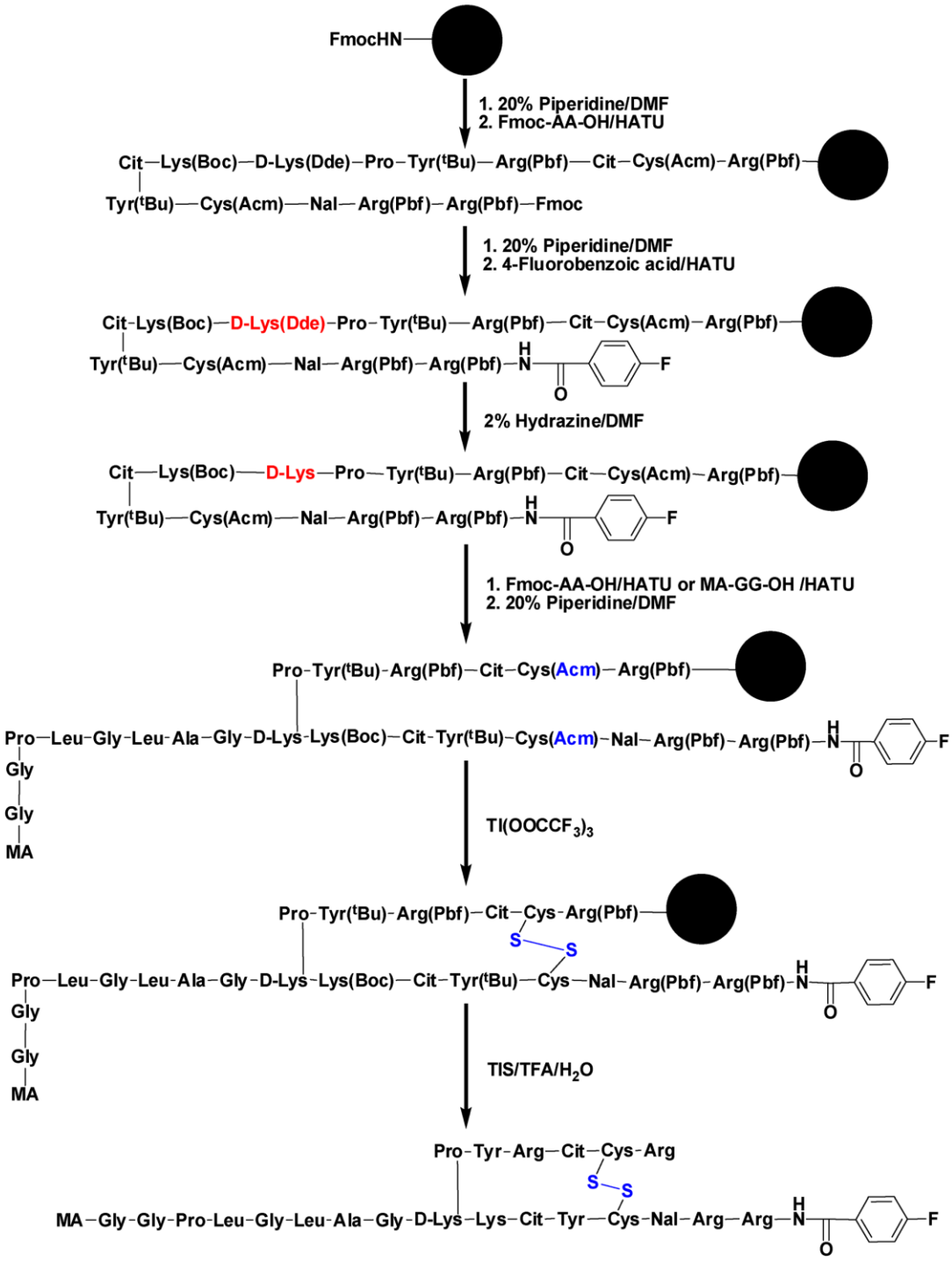

Figure 5.3: Synthetic scheme of monomer MA-GG-PLGLAG-BKT140.

The final step was to cleave the peptide from the resin with a mixture of TFA (9.5 mL), TIS (0.25 mL), and H_2O (0.25 mL) for 3 h. The acid liable protecting groups were also removed in this step. After concentrating under vacuum, the remaining residue was added into cold diethyl ether to precipitate the crude product. The crude MA-GG-PLGLAG-BKT140 was obtained after removing the supernatant.

5.3.5 Purification and characterization of BKT140 and monomer MA-GG-PLGLAG-BKT140

The free BKT140 and monomer MA-GG-PLGLAG-BKT140 were purified by RP-HPLC (Agilent 1100 series) equipped with a semipreparative ZORBAX 300SB-C18 column (5 μm, 9.4*250 mm) from Agilent Technologies (Santa Clara, CA). Buffer A (0.1% TFA in DI water) and Buffer B (0.1% TFA in acetonitrile) were used as the elution agents. The structure of BKT140 and MA-GG-PLGLAG-BKT140 were analyzed by matrix-assisted laser desorption/ionization time of flight (MALDI-TOF) mass spectrometry (Voyager-DE STR Biospectromety Workstation, Perseptive Biosystems, Framingham, MA).

5.3.6 Preparation of HPMA copolymer-BKT140 conjugate

As shown in Figure 5.4, the HPMA copolymer-BKT140 conjugate P-PLGLAG-BKT140 was prepared via RAFT polymerization. Briefly, monomer HPMA (86 mg), monomer MA-GG-PLGLAG-BKT140 (35 mg), chain transfer agent 4-cyanopentanoic acid dithiobenzoate (CPAD) (0.172 mg), initiator V501 (0.172 mg), and a mixture of DMSO and DI water were added to a 2 mL ampoule. After being bubbled with nitrogen

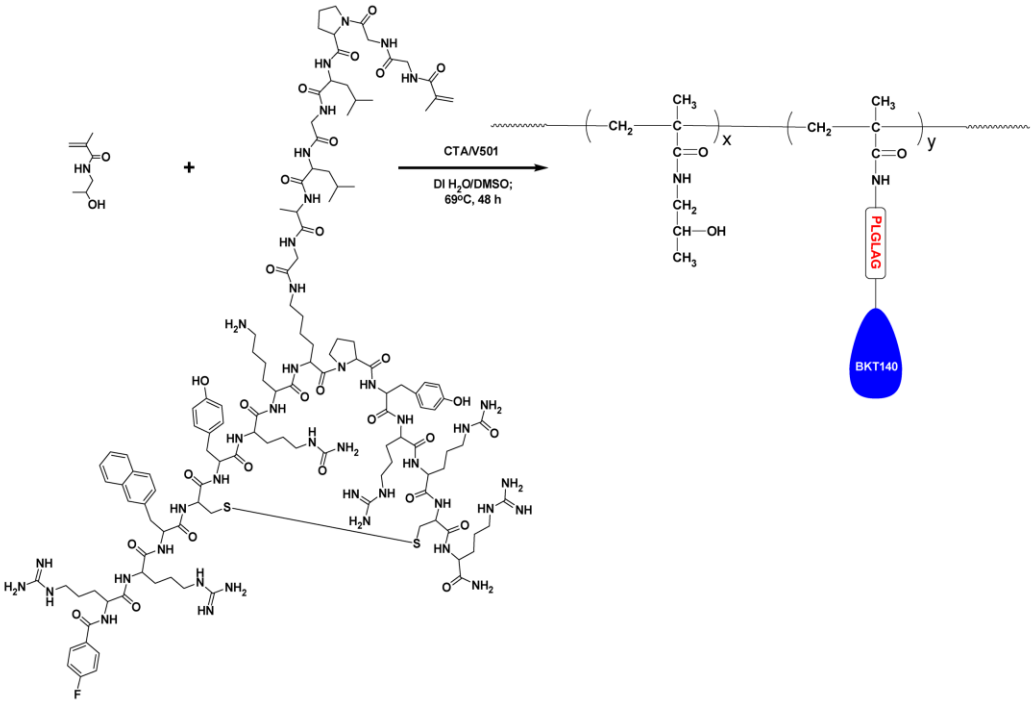

Figure 5.4: Synthetic scheme of polymer conjugate P-PLGLAG-BKT140.

for 30 min, the ampoule was sealed and the mixture was incubated at 69 ^{o}C for 48 h. The reaction mixture was cooled to room temperature and added into a mixture of acetone and diethyl ether. The precipitate was collected after removing the supernatants by centrifugation.

5.3.7 Purification and characterization of P-PLGLAG-BKT140

The polymer conjugate P-PLGLAG-BKT140 was purified by size exclusion chromatography using a Superose 6 HR10/30 preparative column on an AKTA FPLC system (Pharmacia) equipped with refractive index (RI) and UltraViolet (UV) detectors. The buffer with 0.1 M of sodium acetate in a mixture of 30% acetonitrile in DI water (v/v) (pH = 6.5) was used as the eluant, and the flow rate was 1 mL/min.

The number average molecular weight (M_n), weight average molecular weight (M_w) and polydispersity (M_w/M_n) of P-PLGLAG-BKT140 were measured on a Superose 6 HR10/30 analytical column using the same instrument and buffers as for purification. The flow rate was 0.4 mL/min. HPMA homopolymer fractions were used for molecular weight calibration.

The BKT140 content in P-PLGLAG-BKT140 was determined by amino acid analysis. The general procedure was similar as the procedure for measuring DUPA content in DUPA targeted HPMA copolymer-DTX conjugates (Chapter 2.3.6). Tyrosine (0.3, 1, 3 mM) and alanine (0.1, 0.3, 1 mM) were used for standard curve calibration.

5.3.8 Cell culture

PC-3 prostate cancer cells (ATCC) were grown in RPMI-1640 media supplemented with 10% fetal bovine serum (FBS), 100 U/ml penicillin, and 100 μg/mL streptomycin (Gibco, Carlsbad, CA) at 37 ^{o}C in a humidified atmosphere of 5% CO_2 (v/v). Cells were passaged every 3-4 d and stopped at passage 20.

5.3.9 In vitro cleavage study

When PC-3 prostate cancer cells grew to 90% confluence, the cell culture media was collected. To PC-3 cell culture media (10 mL) was added 0.05 mL of monomer MA-GG-PLGLAG-BKT140 in tris(hydroxymethyl)aminomethane (Tris) solution (1 mg/mL) and kept at 37 ^{o}C for 2 h. Acetonitrile (10 mL) was added to the above mixture and centrifuged to remove the precipitate. The collected solution was concentrated until dry, and the residue was redissolved in 1.5 mL of acetonitrile and DI water mixture (v/v = 1/1). After filtration, the mixture was checked with MALDI-TOF mass spectrometry.

5.3.10 Cell cytotoxicity assay

PC-3 cells were seeded at a density of 3,500 cells/well in a 96-well plate for 24 h. Then the media was replaced with various concentrations (25 μM, 10 μM, 5 μM, 5 μM, 0.05 μM) of free BKT140 and of BKT140 equivalent of P-BKT140 in RPMI-160 media with supplements. After being incubated at 37 ^{o}C for 72 h, the drug solutions were aspirated and replaced with 100 μL fresh culture media and 50 μL of diluted CCK-8 solution. Then the UV absorbance of the mixture was measured at 450 nm, with a reference of 630 nm.

5.3.11 In vitro cell migration assay

To the bottom chamber of 6.5 mm transwell (Corning, Corning, NY) with 8 μm pore polycarbonate membrane was added 0.65 mL of RPMI-1640 serum free media with or without 400 ng CXCL12/mL. To the top chamber of transwell was added PC-3 cells ($1*10^5$ cells in 0.1 mL) and incubated at 37 ^oC in a humidified atmosphere of 5% CO_2 (v/v). After 24 h, the nonmigratory cells on upper membrane surface were removed. The cells on bottom surface were stained with DAPI. The cells that migrated through to the lower membrane surface were stained with 4',6-diamidino-2-phenylindole (DAPI, 1 μg/mL, Sigma). Migrating cells were quantified by manually counting 15 representative fields, using an AMG inverted microscope.

5.3.12 Statistical analysis

Data are expressed as mean ± SEM or mean ± SD. Statistical comparisons of means between groups were performed by a one-way analysis of variance (ANOVA) plus post-hoc tests using GraphPad Prism software. P values ≤ 0.05 were considered statistically significant.

5.4 Results and Discussion

5.4.1 Design, synthesis, and characterization of BKT140 and monomer MA-GG-PLGLAG-BKT140

All the conjugation reactions were conducted on solid phase support. The D-Lys at position 8 was chosen for conjugation because the conjugation at this position does not interfere with the binding affinity of BKT140 toward CXCR4 [28–30]. To make sure that

the reaction could be selective at D-Lys^{8} and rather than L-Lys^{7}, we selected Fmoc-D-Lys(Dde)-OH and Fmoc-L-Lys(Boc)-OH for preparing the monomer MA-GG-PLGLAG-BKT140. The Dde protecting group can be selectively removed with 2% hydrazine, while other protecting groups (tBu, Boc, Pbf, Acm) are stable at this condition. The structure of monomer MA-GG-PLGLAG-BKT140 was validated by MALDI-TOF mass spectrometry. The calculated mass of monomer MA-GG-PLGLAG-BKT140 $[M+H]^+$ is 2849.45, and the found mass is 2849.30 (Figure 5.5).

For preparing free BKT140, Fmoc-D-Lys(Boc)-OH was used because it is cheaper than Fmoc-D-Lys(Dde)-OH. The BKT140 structure was confirmed by measuring the mass of BKT140 and its reduced product. As shown in Figure 5.2, the reduction of the disulfide bond in BKT140 produced two sulfhydryl groups in linear BKT140. The mass of the linear BKT140 is 2 Da higher than that of original BKT140. The peak at 2159.17 corresponds to the mass of the BKT140 ($[M+H]^+$) (Figure 5.6). The peak at 2161.14 corresponds to the mass of the reduced product from BKT140 ($[M_1+H]^+$) (Figure 5.7).

5.4.2 Preparation and characterization of P-PLGLAG-BKT140

The obvious advantages of 'Green' RAFT polymerization are controlling polymer structures and functionality (26). The homopolymer HPMA can be prepared in aqueous media (27). The P-PLGLAG-BKT140 was prepared by RAFT polymerization of monomers HPMA and MA-GG-PLGLAG-BKT140. 4-cyano-pentanoic acid dithiobenzoate (CPAD) and 4,4′-azobis(4-cyanopentanoic acid) (V-501) were used as the

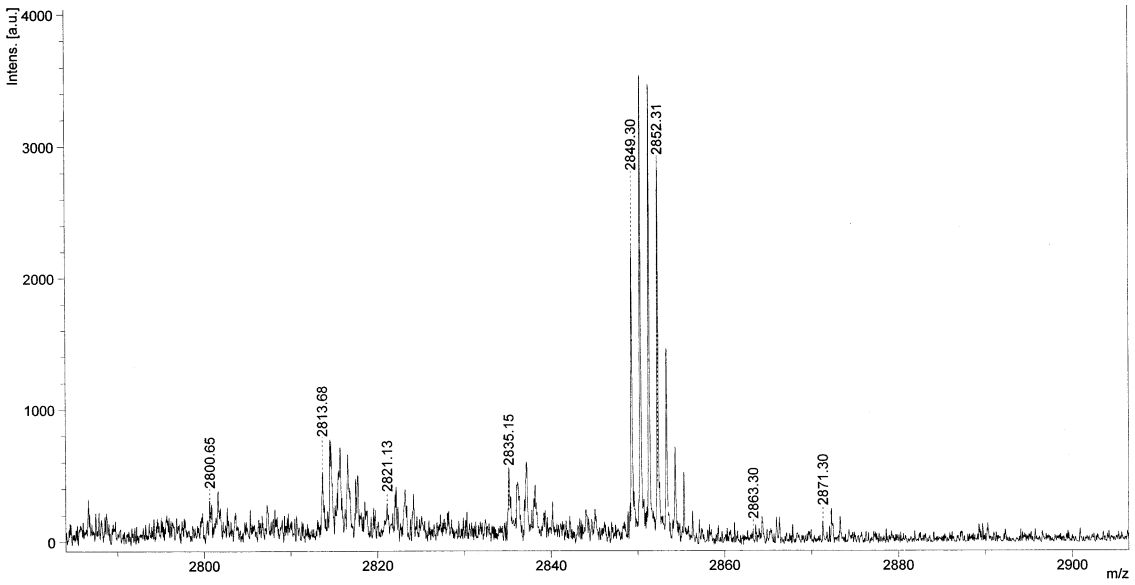

Figure 5.5: Mass spectrum of monomer MA-GG-PLGLAG-BKT140.

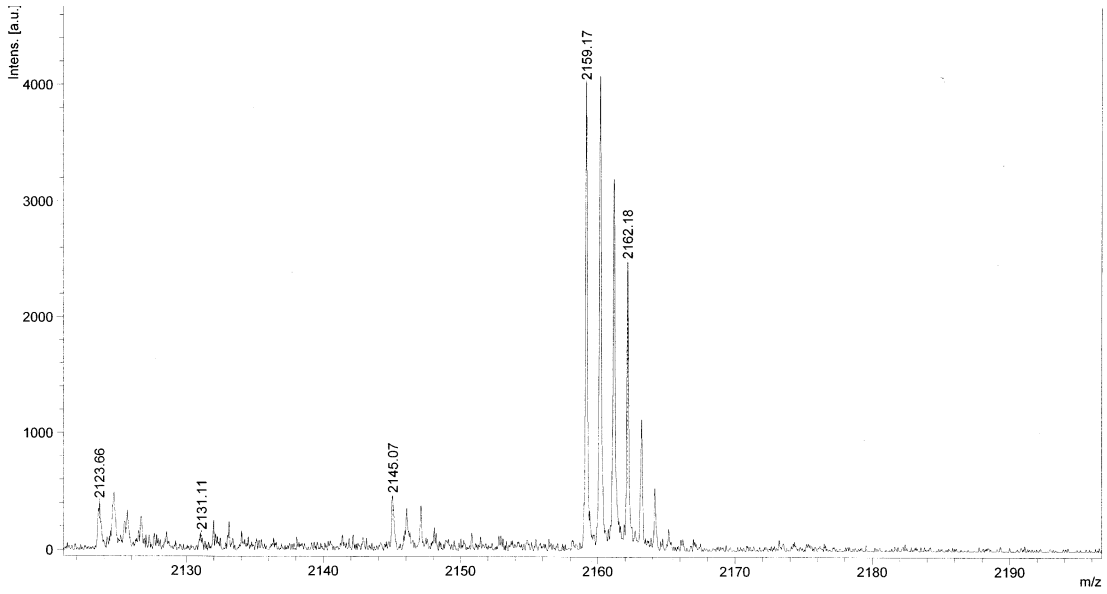

Figure 5.6: Mass spectrum of free BKT140.

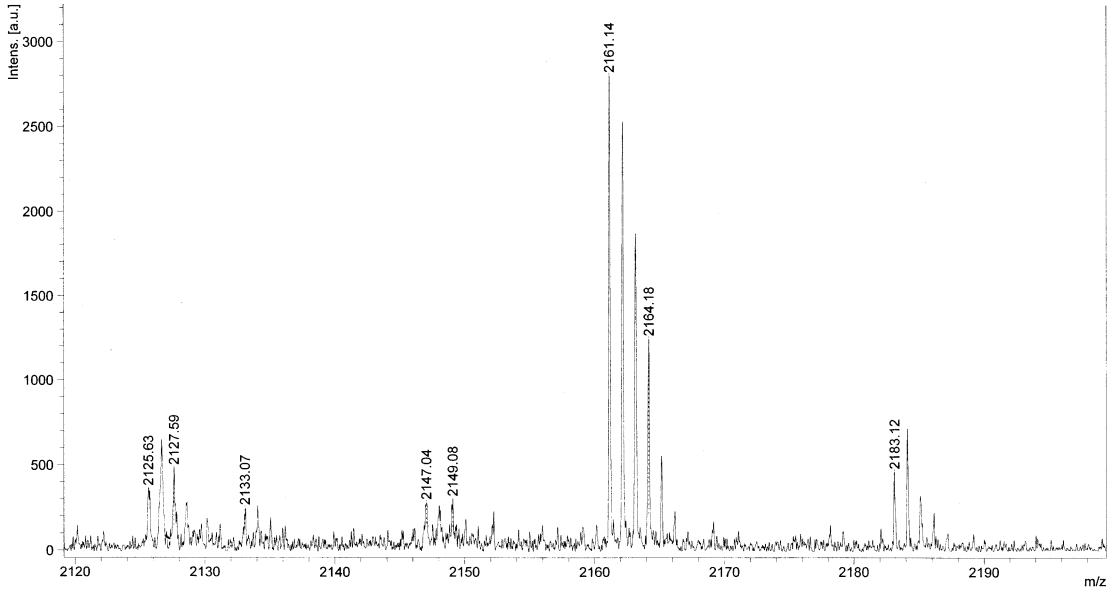

Figure 5.7: Mass spectrum of reduced product from free BKT140.

chain transfer agent (CTA) and initiator, respectively. A small amount of DMSO was added to enhance the solubility of monomer MA-GG-PLGLAG-BKT140 and initiator V-501 in the reaction mixture.

The molecular weight and molecular weight distribution of P-PLGLAG-BKT140 were analyzed by size exclusion chromatography. The number average, weight average molecular weights, and polydispersity (Mw/Mn) of P-PLGLAG-BKT140 were $1.00 * 10^5$ Da, $1.23 * 10^5$ Da, and 1.23, respectively.

The content of BKT140 in the polymer conjugate P-PLGLAG-BKT140 was measured by amino acid analysis. The measured content was 68.6 nmol BKT140/mg polymer, and the weight percent was 14.8% (BKT140/polymer). Alanine and tyrosine were used for calibration.

5.4.3 In vitro cleavage results

It has previously been demonstrated that peptide -PLGLAG- can be cleaved by MMP-2 (16,17,28). In order to check whether BKT140 could be released from the carrier in tumor microenvironment, we incubated MA-GG-PLGLAG-BKT140 with PC-3 prostate cancer cell growth media because the active MMP-2 concentration in PC-3 cell growth media is up to 2000 pg/mL (9). The mass spectrum of the mixture was checked with MALDI-TOF mass spectrometry, and the result is shown in Figure 5.8. The peaks at 2849.46 and 2871.36 correspond to the mass of monomer MA-GG-PLGLAG-BKT140 ($[M+H]^+$, $[M+Na]^+$). From the results in Figure 5.8, at least two cleavage sites were found in MA-GG-PLGLAG-BKT140. Two cleavage sites are proposed in Figures 5.9 and 5.10. In Figure 5.9, it is shown that MA-GG-PLGLAG-BKT140 was cut between

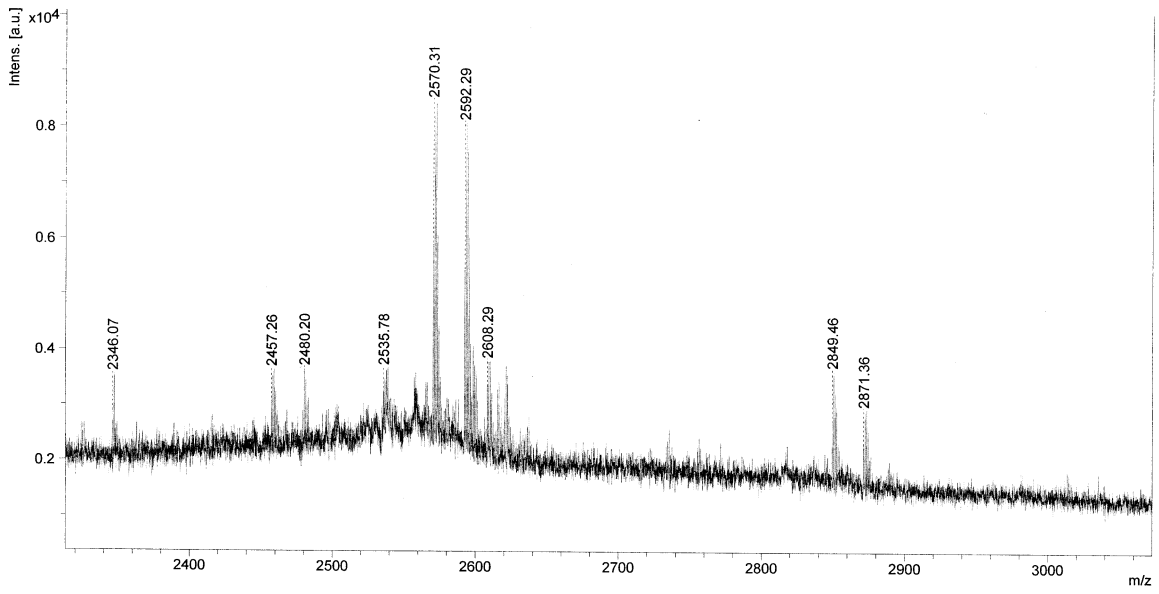

Figure 5.8: Mass spectrum of cleavage product from monomer MA-GG-PLGLAG-BKT140 after incubation with PC-3 cell culture media.

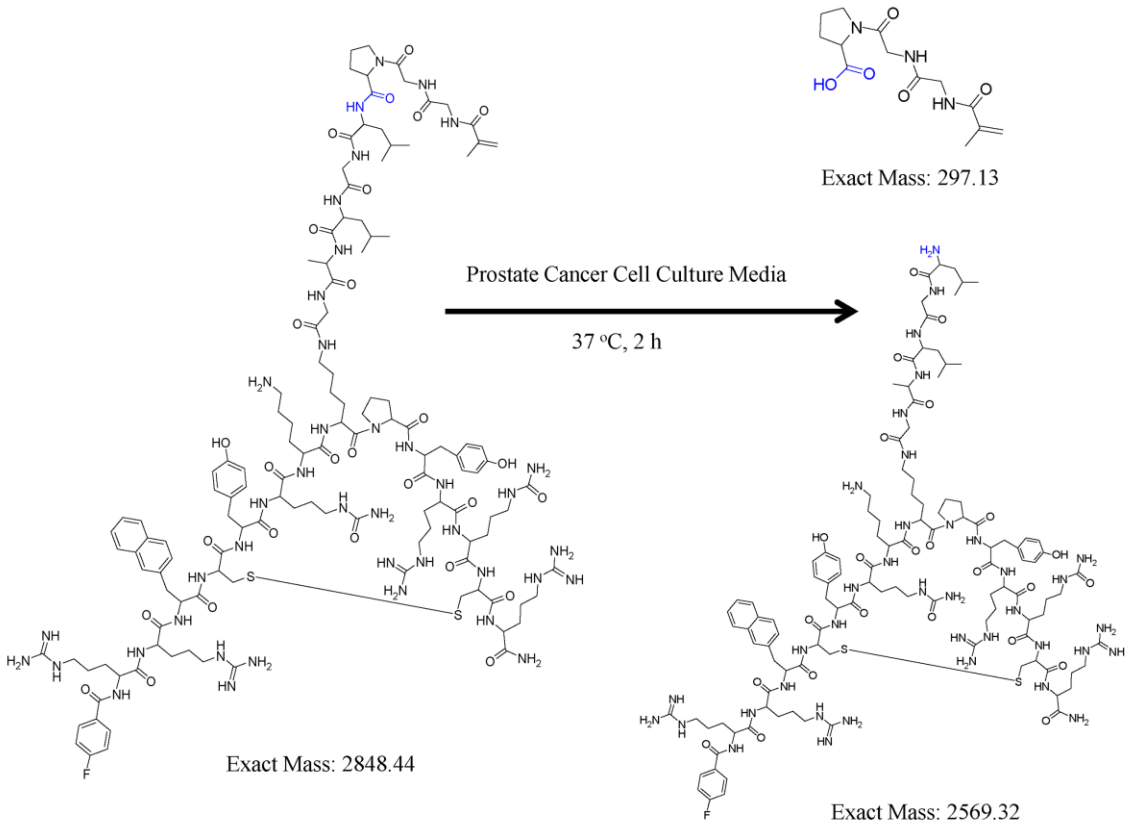

Figure 5.9: Proposed cleavage site 1 of monomer MA-GG-PLGLAG-BKT140 after incubation with PC-3 cell culture media.

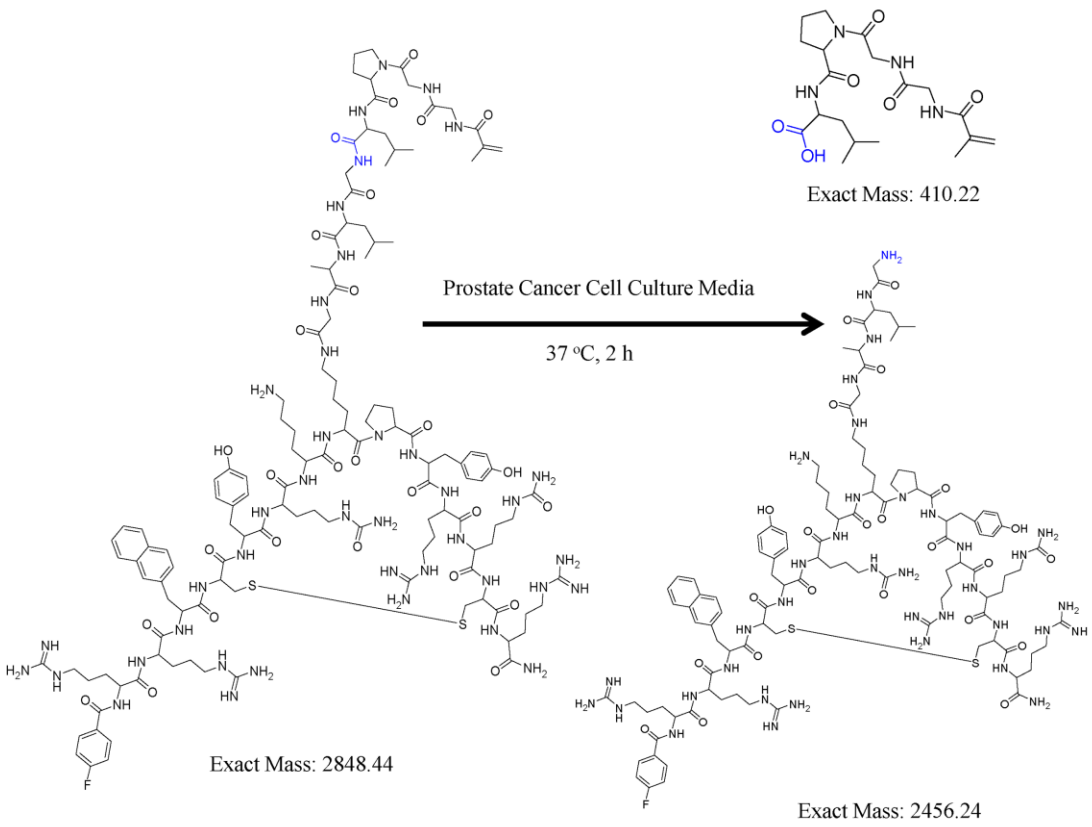

Figure 5.10: Proposed cleavage site 2 of monomer MA-GG-PLGLAG-BKT140 after incubation with PC-3 cell culture media.

proline and leucine residues. The peaks at 2570.31, 2592.29, 2608.29 in Figure 5.8 correspond to the mass of one cleaved product in Figure 5.9 ($[M_1+H]^+$, $[M_1+Na]^+$, $[M_1+K]^+$. In Figure 5.10, it is shown that MA-GG-PLGLAG-BKT140 was also cleaved between leucine and glycine residues. The peaks at 2457.26, 2480.20 in Figure 5.8 correspond to the mass of one cleaved product in Figure 5.10 ($[M_2+H]^+$, $[M_2+Na+H]^+$.

5.4.4 In vitro cytotoxicity results

In order to rule out that the inhibition of cell motility is due to nonspecific cytotoxic effects, we conducted an in vitro cytotoxicity assay to find the appropriate concentrations of BKT140 for migration and invasion study. Five different concentrations (25 μM, 10 μM, 5 μM, 0.5 μM, 0.05 μM) of BKT140 or BKT140 equivalent of P-PLGLAG-BKT140 were tested against PC-3 prostate cancer cells, and the cell cytotoxicity results are summarized in Figure 5.11. P-PLGLAG-BKT140 has similar cytotoxicity of as free BKT140, and both BKT140 and P-PLGLAG-BKT140 have only minor cytotoxicity against PC-3 prostate cancer cells when the concentration is less than 10 μM. Thus, concentrations lower than10 μM will be used for migration studies.

5.4.5 In vitro migration results

Based on the above cytotoxicity results, we used 5 μM of BKT140 or BKT140 equivalent of P-PLGLAG-BKT140 for migration study. As shown in Figure 5.12, CXCL12 enhanced the migration of PC-3 prostate cancer cells. Both BKT140 and P-PLGLAG-BKT140 inhibited the CXCL12 induced migration of PC-3 prostate cancer cells, and the conjugate P-PLGLAG-BKT140 worked much better than free BKT140.

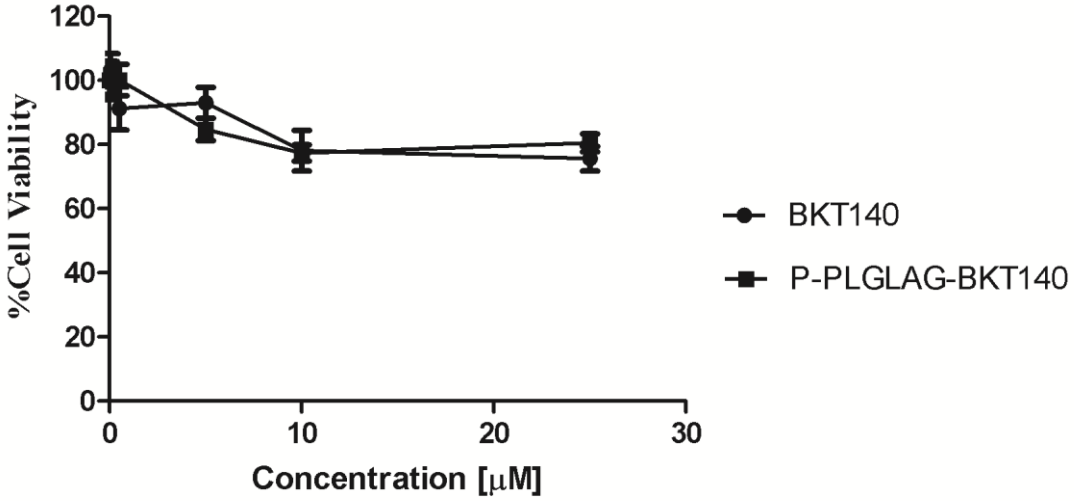

Figure 5.11: In vitro cytotoxicity of BKT140 and P-PLGLAG-BKT140 against PC-3 prostate cancer cells.

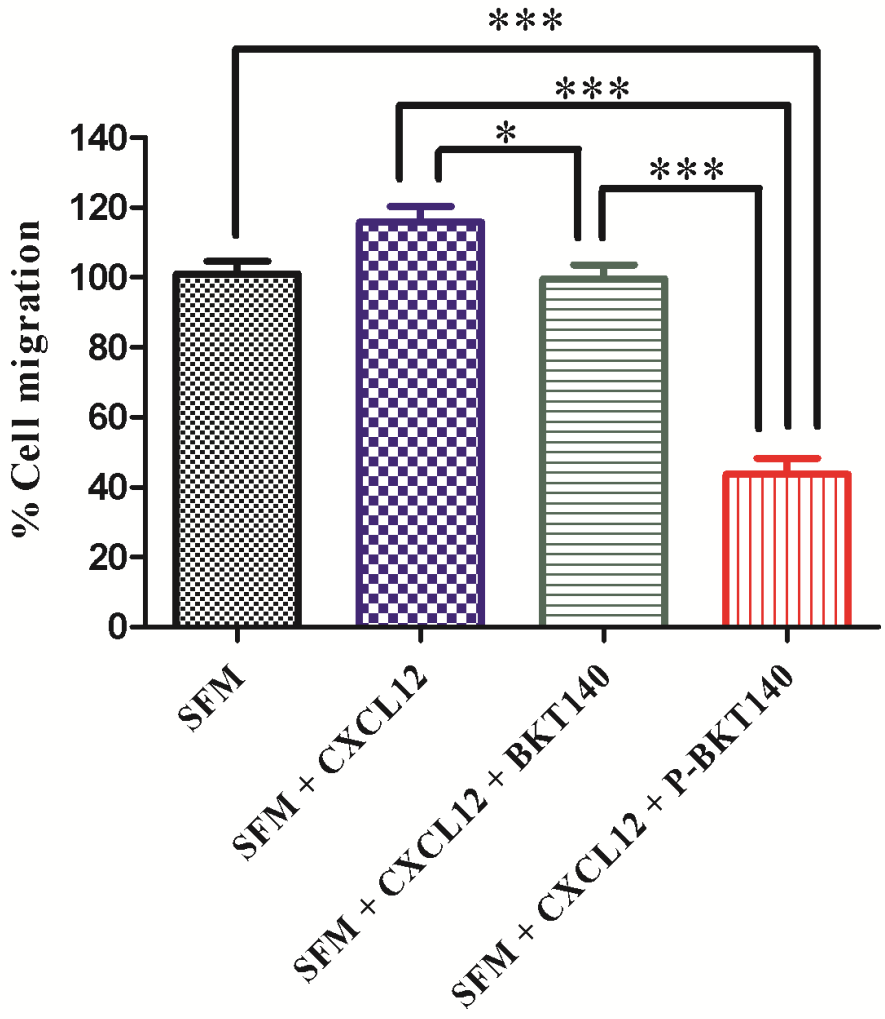

Figure 5.12: Effects of BKT140 and P-PLGLAG-BKT140 on CXCL12 induced migration of PC-3 prostate cancer cells.

5.5 Conclusion

We have successfully prepared a prostate cancer tumor microenvironment responsive *N*-(2-hydroxypropyl)methacrylamide (HPMA) copolymer CXCR-4 antagonist conjugate (P-PLGLAG-BKT140) via RAFT copolymerization of monomer HPMA and MA-GG-PLGLAG-BKT140. We designed a concise scheme to prepare the monomer MA-GG-PLGLAG-BKT140. All the conjugation reactions of MA-GG-PLGLAG-BKT140 were conducted on MBHA resin for easy handling. Fmoc-D-Lys(Dde)-OH and Fmoc-L-Lys(Boc)-OH were chosen for the synthesis of the monomer MA-GG-PLGLAG-BKT140 in order to make sure the reaction selectively occurred at D-Lys^{8} rather than L-Lys^{7}. The structures of free BKT140 and monomer MA-GG-PLGLAG-BKT140 were confirmed by mass spectrometry. The synthesis methodology for P-PLGLAG-BKT140 can be used to design other formulation of BKT140 conjugates. The spacer (-PLGLAG-) was cleaved by prostate cancer growth media at a minimum of two sites. Both free BKT140 and P-PLGLAG-BKT140 have shown the same cytotoxicity against PC-3 cells, indicating that the conjugation of BKT140 to HPMA copolymer retains the functionality of free BKT140. The migration results shown that both HPMA copolymer BKT140 conjugate and free BKT140 inhibited the CXCL12 induced PC-3 prostate cancer cell migration. The conjugate P-PLGLAG-BKT140 has great impact than that of free BKT140. The activities of BKT140 and P-PLGLAG-BKT140 for blocking the invasion of prostate cancer cells toward CXCL12 will be investigated further.

5.6 References

1. Chaffer CL, Weinberg RA. A perspective on cancer cell metastasis. Science. 2011;331:1559–64.

2. Jemal A, Siegel R, Xu J, Ward E. Cancer statistics, 2010. CA Cancer J Clin. 2010;60:277–300.

3. Gandaglia G, Abdollah F, Schiffmann J, Trudeau V, Shariat SF, Kim SP, et al. Distribution of metastatic sites in patients with prostate cancer: A population-based analysis. The Prostate. 2014;74:210–6.

4. Hess KR, Varadhachary GR, Taylor SH, Wei W, Raber MN, Lenzi R, et al. Metastatic patterns in adenocarcinoma. Cancer. 2006;106:1624–33.

5. Taichman RS, Cooper C, Keller ET, Pienta KJ, Taichman NS, McCauley LK. Use of the stromal cell-derived factor-1/CXCR4 pathway in prostate cancer metastasis to bone. Cancer Res. 2002;62:1832–7.

6. Arya M, Patel HRH, McGurk C, Tatoud R, Klocker H, Masters J, et al. The importance of the CXCL12-CXCR4 chemokine ligand-receptor interaction in prostate cancer metastasis. J Exp Ther Oncol. 2004;4:291–303.

7. Sun Y-X, Wang J, Shelburne CE, Lopatin DE, Chinnaiyan AM, Rubin MA, et al. Expression of CXCR4 and CXCL12 (SDF-1) in human prostate cancers (PCa) in vivo. J Cell Biochem. 2003;89:462–73.

8. Akashi T, Koizumi K, Tsuneyama K, Saiki I, Takano Y, Fuse H. Chemokine receptor CXCR4 expression and prognosis in patients with metastatic prostate cancer. Cancer Sci. 2008;99:539–42.

9. Singh S, Singh UP, Grizzle WE, Lillard JW Jr. CXCL12-CXCR4 interactions modulate prostate cancer cell migration, metalloproteinase expression and invasion. Lab Investig J Tech Methods Pathol. 2004;84:1666–76.

10. Darash-Yahana M, Pikarsky E, Abramovitch R, Zeira E, Pal B, Karplus R, et al. Role of high expression levels of CXCR4 in tumor growth, vascularization, and metastasis. FASEB J. 2004;18:1240–2.

11. Dubrovska A, Elliott J, Salamone RJ, Telegeev GD, Stakhovsky AE, Schepotin IB, et al. CXCR4 Expression in Prostate Cancer Progenitor Cells. PLoS ONE. 2012;7:e31226.

12. Cho KS, Yoon SJ, Lee JY, Cho NH, Choi YD, Song YS, et al. Inhibition of tumor growth and histopathological changes following treatment with a chemokine receptor CXCR4 antagonist in a prostate cancer xenograft model. Oncol Lett. 2013;6:933–8.

13. Beider K, Begin M, Abraham M, Wald H, Weiss ID, Wald O, et al. CXCR4 antagonist 4F-benzoyl-TN14003 inhibits leukemia and multiple myeloma tumor growth. Exp Hematol. 2011;39:282–92.

14. Peled A, Abraham M, Avivi I, Rowe JM, Beider K, Wald H, et al. The high-affinity CXCR4 antagonist BKT140 is safe and induces a robust mobilization of human CD34+ cells in patients with multiple myeloma. Clin Cancer Res Off J Am Assoc Cancer Res. 2014;20:469–79.

15. Pollaro L, Heinis C. Strategies to prolong the plasma residence time of peptide drugs. MedChemComm. 2010;1:319–24.

16. Jiang T, Olson ES, Nguyen QT, Roy M, Jennings PA, Tsien RY. Tumor imaging by means of proteolytic activation of cell-penetrating peptides. Proc Natl Acad Sci U S A. 2004;101:17867–72.

17. Zhu L, Wang T, Perche F, Taigind A, Torchilin VP. Enhanced anticancer activity of nanopreparation containing an MMP2-sensitive PEG-drug conjugate and cell-penetrating moiety. Proc Natl Acad Sci U S A. 2013;110:17047–52.

18. Dos Reis ST, Villanova FE, Andrade PM, Pontes J Jr, de Sousa-Canavez JM, Sañudo A, et al. Matrix metalloproteinase-2 polymorphism is associated with prognosis in prostate cancer. Urol Oncol. 2010;28:624–7.

19. Zhong W, Han Z, He H, Bi X, Dai Q, Zhu G, et al. CD147, MMP-1, MMP-2 and MMP-9 protein expression as significant prognostic factors in human prostate cancer. Oncology. 2008;75:230–6.

20. Kopeček J, Bažilová H. Poly[N-(2-hydroxypropyl)methacrylamide]—I. Radical polymerization and copolymerization. Eur Polym J. 1973;9:7–14.

21. Rejmanová P, Labský J, Kopeček J. Aminolyses of monomeric and polymeric 4-nitrophenyl esters of N-methacryloylamino acids. Makromol Chem. 1977;178:2159–68.

22. Mitsukami Y, Donovan MS, Lowe AB, McCormick CL. Water-soluble polymers. 81. Direct synthesis of hydrophilic styrenic-based homopolymers and block copolymers in aqueous solution via RAFT. Macromolecules. 2001;34:2248–56.

23. Grunbeck A, Huber T, Sachdev P, Sakmar TP. Mapping the ligand-binding site on a G protein-coupled receptor (GPCR) using genetically encoded photocrosslinkers. Biochemistry (Mosc). 2011;50:3411–3.

24. Oishi S, Masuda R, Evans B, Ueda S, Goto Y, Ohno H, et al. Synthesis and application of fluorescein- and biotin-labeled molecular probes for the chemokine receptor CXCR4. ChemBioChem. 2008;9:1154–8.

25. Nomura W, Tanabe Y, Tsutsumi H, Tanaka T, Ohba K, Yamamoto N, et al. Fluorophore labeling enables imaging and evaluation of specific CXCR4-ligand interaction at the cell membrane for fluorescence-based screening. Bioconjug Chem. 2008;19:1917–20.

26. Semsarilar M, Perrier S. “Green” reversible addition-fragmentation chain-transfer (RAFT) polymerization. Nat Chem. 2010;2:811–20.

27. Scales CW, Vasilieva YA, Convertine AJ, Lowe AB, McCormick CL. Direct, controlled synthesis of the nonimmunogenic, hydrophilic polymer, poly(N-(2-hydroxypropyl)methacrylamide) via RAFT in aqueous media. Biomacromolecules. 2005;6:1846–50.

28. Li L, Ge J, Wu H, Xu Q-H, Yao SQ. Organelle-specific detection of phosphatase activities with two-photon fluorogenic probes in cells and tissues. J Am Chem Soc. 2012;134:12157–67.

CHAPTER 6

RESULTS, CONCLUSIONS, AND FUTURE PROSPECTS

Stimuli-responsive targeted drug release systems are important for improving the efficacy and reducing the side effect of drugs. Prostate cancer is the most frequently diagnosed cancer in men and has the second highest mortality rate in United States. In this thesis, we developed stimuli-responsive targeted therapeutics for inhibiting primary and metastatic prostate cancer growth.

In Chapter 2, we describe the design, synthesis, structure validation, and biological properties of targeted and nontargeted *N*-(2-hydroxypropyl)methacrylamide (HPMA) copolymer docetaxel (DTX) conjugates. Docetaxel was conjugated to HPMA copolymer via a tetrapeptide spacer (-GFLG-). 3-(1,3-dicarboxypropyl)-ureido]pentanedioic acid (DUPA) was used as the targeting moiety to actively deliver DTX for treatment of Prostate-Specific Membrane Antigen (PSMA) expressing prostate cancer. Short and long spacer DUPA monomers were prepared, and four HPMA copolymer-DTX conjugates (nontargeted, two targeted with different molecular weight with short spacer, and targeted with long spacer) were prepared via Reversible Addition-Fragmentation Chain Transfer (RAFT) copolymerization. Following confirmation of PSMA expression on C4-2 cell line, the DTX conjugates' in vitro cytotoxicity was tested against C4-2 tumor cells and their anticancer efficacies were assessed in nude mice

bearing *s.c.* human prostate adenocarcinoma C4-2 xenografts. The in vivo results showed that the spacer length between targeting moieties and HPMA copolymer backbone could significantly affect the treatment efficacy of DTX conjugates against C4-2 tumor bearing nu/nu mice. Moreover, histological analysis indicated that the DUPA targeted DTX conjugate with longer spacer had no toxicity in major organs of treated mice.

In order to further confirm the importance of spacer length between targeting moiety DUPA and HPMA backbone, binding affinity of DUPA targeted conjugates with different spacer length against PSMA (+) prostate cancer cells should be tested and compared. We hypothesize that the similar in vitro toxicities of the DUPA targeted and nontargeted conjugates are the result of free DTX being released from the drug conjugate in cell culture conditions and subsequently dominating the toxicological profile. To test this hypothesis, other HPMA-drug conjugates with acid-liable (and basic stable) bonds should be prepared and tested. To maximize the targeting effect of DUPA, the impact of DUPA distribution and number conjugated to HPMA copolymer chain on targeting effect should be further investigated.

In Chapter 3, a conjugate of the tumor homing peptide iRGD and histone deacetylase inhibitor valproic acid (VPA-GFLG-iRGD) was developed and its activities were evaluated in DU-145 prostate cancer cells. Conjugates VPA-GFLG-iRGD and GFLG-iRGD were prepared by solid phase synthesis. The activities of VPA-GFLG-iRGD and related controls against DU-145 prostate cancer cells were tested by both cell cytotoxicity and cell cycle arrest assays. The conjugate VPA-GFLG-iRGD and a mixture of VPA and GFLG-iRGD have shown similar cytotoxicity against DU-145 prostate cancer cells. However, the treatment of DU-145 cells with conjugate VPA-GFLG-iRGD

resulted in a decreased percentage of cells in the G2 phase, whereas the exposure of a mixture of VPA and GFLG-iRGD led to an increased percentage of cells in the G2 phase. We also found that GFLG-iRGD possessed cytotoxicity at the tested concentrations.

More experiments are needed to investigate the uptake mechanism of VPA-GFLG-iRGD conjugate into DU-145 prostate cancer cells. In the present work, VPA was conjugated to iRGD via a lysosomally cleavable spacer based on the hypothesis that this conjugate enters cells via endocytosis. Other drug-iRGD conjugates, which are formed by linking drug with iRGD via a disulfide spacer should be investigated and compared with the conjugate VPA-GFLG-iRGD. As GFLG-iRGD is toxic to DU-145 prostate cancer cells at the tested concentrations, other more potent drugs should be chosen to prepare the iRGD-drug conjugate in order to minimize the cytotoxicity of iRGD. In addition, experiments are needed to explain the cytotoxicity of GFLG-iRGD.

In Chapter 4, we describe the design, preparation, and biological properties of stimuli-responsive HPMA copolymer drug and tumor-penetrating peptide conjugates. Doxorubicin (DOX) was conjugated to HPMA copolymer via a lysosomally cleavable tetrapeptide spacer (-GFLG-). Tumor homing and penetrating peptide iRGD was connected to HPMA copolymer through a MMP-2 degradable linker (-PLGLAG-). Free iRGD and monomer MA-GG-PLGLAG-iRGD were prepared with solid phase synthesis. HPMA copolymer-DOX conjugates (P-DOX and P-DOX-PLGLAG-iRGD) were prepared via conventional radical copolymerization. The uptake of DOX conjugates was tested in both monolayer and multilayer DU-145 prostate cancer cells with flow cytometry. The results have shown that P-DOX-PLGLAG-iRGD treated cells had the strongest fluorescence intensity compared to that of other treated groups (Control, iRGD,

P-DOX, P-DOX plus iRGD). The cell cycle arrest, in vitro apoptosis, and cytotoxicity of DOX conjugates and related controls were tested against DU-145 monolayer prostate cancer cells. Consistent with the drug uptake results, the in vitro activity results show that P-DOX-PLGLAG-iRGD had the strongest activity against DU-145 prostate cancer cells. The penetration ability of DOX conjugates was tested in 3D multicellular tumor cell spheroids. The results show that the conjugate P-DOX-PLGLAG-iRGD penetrated deepest in tumor cell spheroids.

The conjugation of iRGD to HPMA copolymer DOX conjugate via a MMP-2 cleavable spacer increased the accumulation of DOX conjugates in mono- and multi-layer DU-145 prostate cancer cells. More in vivo experiments including a bio-distribution and efficacy study should add to further prove the advantages of conjugation of iRGD to HPMA copolymer drug conjugates. To demonstrate the importance of a cleavable spacer between iRGD and drug carriers, one more control conjugate that links the iRGD to HPMA copolymer drug conjugate via a nondegradable spacer should be prepared and tested. As integrin is also expressed on tumor vascular endothelial cells, iRGD will likely interact with tumor vascular endothelial cells. As the conjugation of iRGD to HPMA copolymer DOX conjugate enhanced the accumulation in prostate cancer cells, its accumulation in tumor vascular endothelial cells should also be examined to determine if a similar effect can be observed.

In Chapter 5, a HPMA copolymer CXCR-4 antagonist (BKT140) conjugate was designed, synthesized, characterized, and its activities were tested against PC-3 prostate cancer cells. BKT140 was attached to HPMA backbone via a matrix metallopeptidase 2 (MMP-2) cleavable spacer (-PLGLAG-). Both free BKT140 and monomer MA-GG-

PLGLAG-BKT140 were prepared by solid phase synthesis. Fmoc-D-Lys(Dde)-OH and Fmoc-L-Lys(Boc)-OH were chosen for the synthesis of the monomer MA-GG-PLGLAG-BKT140 in order to make sure the reaction selectively occurred at D-Lys^{8} rather than L-Lys^{7}. HPMA copolymer-BKT140 conjugate (P-PLGLAG-BKT140) was prepared via Reversible Addition-Fragmentation Chain Transfer copolymerization of monomer HPMA and MA-GG-PLGLAG-BKT140. The -PLGLAG- spacer was cleaved in prostate cancer cells growth media at a minimum of two sites. The in vitro cell cytotoxicity results showed that the free BKT140 and P-PLGLAG-BKT140 had the same activities against PC-3 cells, indicating that the conjugation of BKT140 to HPMA did not impact the functionality of BKT140. The migration results showed that both HPMA copolymer BKT140 conjugate and free BKT140 inhibited the CXCL12 induced PC-3 prostate cancer cell migration. The conjugate P-PLGLAG-BKT140 had great impact than that of free BKT140.

Our present results showed that the conjugation of BKT140 to HPMA copolymer enhanced its ability to inhibit the CXCL12 induced prostate cancer migration. However, more experiments are required to demonstrate the mechanism of BKT140 conjugate. For example, what is the conformation of BKT140 in the conjugate? What is the morphology of HPMA copolymer BKT140 conjugate? How does the conjugate interact with CXCR4 receptor on the tumor cell surface? In addition, further optimization of the structure of BKT140 conjugate is necessary to maximize the inhibition effect of BKT140. Other structures such as the star, dendrimer shape of BKT140 conjugates deserve to be prepared and tested. More HPMA copolymer BKT40 conjugates with different molecular weight and/or varied BKT140 distribution in the polymer chain should be prepared and assessed.

Furthermore, the ultimate goal of this part study is to develop new therapeutics for inhibiting prostate cancer metastasis. Cancer metastasis is a multistage process including invasion from the extracellular matrix and adherence to bone marrow endothelial cells. Whether the HPMA copolymer BKT140 conjugate can inhibit the invasion and adherence of prostate cancer cells should also be examined.